



# **Subduction Zone Metasomatism and its Consequences for Potassium-rich Magmatism and Deep Nitrogen Cycling**

Michael W. Förster

ARC Centre of Excellence of Core to Crust Fluid Systems  
and Department of Earth and Planetary Sciences,  
Macquarie University, Sydney, Australia

A Thesis submitted to Macquarie University for the Degree  
of Doctor of Philosophy

Supervision:

Professor Stephen F. Foley

January 2019

*Für Doris.*

© Copyright by Michael W. Förster, 2019  
All Rights Reserved

## Statement of Originality

I (Michael Werner Förster) declare, that I have written the research presented in this thesis “Subduction Zone Metasomatism and its Consequences for Potassium-rich Magmatism and Deep Nitrogen Cycling”, independently by myself, without using source materials or aids, other than stated as referenced quotations within this work. I further declare that this thesis has not previously been submitted for a degree nor has it been submitted as part of requirements for a degree to any other university or institution.

Sydney, 18/01/2019

# Table of Contents

Statement of Originality .....	III
Table of Figures .....	VII
List of Tables .....	X
List of Publications .....	XI
Acknowledgements .....	XII
List of Abbreviations .....	XIV
Key Contributions of this PhD to the Field of Research .....	XV
Abstract .....	XVI
<b>I. Introduction</b>	
i. Mantle metasomatism .....	17
ii. Metasomatized mantle xenoliths .....	18
iii. Ultrapotassic lavas .....	18
iv. Deep nitrogen cycling .....	20
v. Research approach and aim of study .....	22
vi. Structure of the thesis .....	25
<b>Chapter 1: Sediment-Peridotite Reaction Controls Fore-Arc Metasomatism and Arc-Magma Geochemical Signatures</b>	
1.1 Introduction .....	27
1.2 Materials and Methods .....	29
1.3 Results .....	31
1.3.1 Textural observations .....	31
1.3.2 Phase compositions .....	33
1.4 Discussion .....	35
1.4.1 Progressive replacement of peridotites by phlogopite-pyroxenites in the fore-arc .....	35
1.4.2 Rates of metasomatism .....	36
1.5 Conclusions .....	37
<b>Chapter 2: Melting of Sediments in the Deep Mantle Produce Saline Fluid Inclusions in Diamonds</b>	
2.1 Introduction .....	40
2.2 Materials and Methods .....	41
2.3 Results .....	42
2.3.1 Mass balance calculations .....	44
2.4 Discussion .....	48
2.5 Conclusion .....	54



**Chapter 3: Two-stage Formation of K-enrichment in Ultrapotassic Magmatism Confirmed by a Novel Experimental Approach**

3.1 Introduction .....	56
3.2 Experimental strategy .....	57
3.3 Materials and Methods .....	58
3.3.1 Starting materials.....	58
3.3.2. Experimental and analytical techniques .....	59
3.4 Results .....	60
3.4.1 First-stage experiments.....	60
3.4.2 Second-stage experiments.....	62
3.5 Discussion.....	64
3.5.1 Comparison with previous experimental studies .....	64
3.5.2 First stage experiments: formation of Si-rich potassic melts.....	67
3.5.3 Second stage experiments: formation of high K/Na ultrapotassic melts.....	68
3.5.4 Implications for the formation of post-collisional lavas .....	70
3.6 Conclusions .....	71

**Chapter 4: An Experimental Study of the Role of Partial Melts of Sediments *versus* Mantle Melts in the Sources of Potassic Magmatism**

4.1 Introduction .....	75
4.2 Materials and Methods .....	77
4.2.1 Experimental techniques .....	77
4.2.2 Analytical techniques.....	78
4.3 Results .....	79
4.3.1 Structural observations.....	79
4.3.2 Major element compositions.....	80
4.3.3 Trace element composition .....	84
4.4 Discussion.....	87
4.4.1 Sediment/dunite reaction .....	87
4.4.2 Hydrous-basanite/dunite reaction .....	88
4.4.3 Trace element partitioning .....	88
4.4.4 Trace elements as indicators for recycling- and mantle melting processes .....	90
4.4.5 Melts of sediment- <i>versus</i> mantle melt-metasomatism .....	93
4.5 Conclusion.....	94

<b>Chapter 5: Melting Phlogopite-rich MARID: Lamproites and the Role of Alkalis in Olivine-Liquid Ni-partitioning</b>	
5.1 Introduction .....	97
5.2 Materials and Methods.....	99
5.2.1 Starting materials.....	99
5.2.2 Experimental techniques.....	99
5.2.3 Analytical techniques.....	100
5.3 Results.....	101
5.3.1 Textural observations .....	101
5.3.2 Melt compositions in the reaction experiments .....	102
5.3.3 Trace element composition of melts and olivine .....	104
5.3.4 Composition of the mineral phases .....	105
5.4 Discussion.....	106
5.4.1 Constraints on the formation of cratonic ultrapotassic magmas.....	106
5.4.2 Ni-partitioning in olivine and ultrapotassic melts .....	108
5.4.3 Ni-partitioning in olivine/liquid as a geothermometer .....	111
5.4.4 Geothermometry on natural glass-olivine pairs .....	115
5.5 Conclusion.....	116
<b>Chapter 6: Partitioning of Nitrogen during Slab-melting and Recycling in Subduction Zones</b>	
6.1 Introduction .....	119
6.2 Materials and Methods.....	121
6.3 Results.....	123
6.3.1 Structural observations.....	123
6.3.2 Nitrogen concentration and -speciation in experimental phases .....	124
6.4 Discussion.....	126
6.4.1 Partitioning of nitrogen in subduction zones.....	126
6.4.2 Subduction zone N budgets.....	129
6.4.3 Evolution of pN <sub>2</sub> in Earth's atmosphere .....	132
6.5 Conclusion.....	134
<b>II. Thesis Conclusion</b>	
i. Metasomatism of the shallow lithosphere and the formation of ultrapotassic lavas.....	136
ii. Metasomatism of the cratonic lithosphere and its relation to kimberlite magmatism .....	138
iii. Nitrogen enrichment of the lithospheric mantle .....	138
<b>References.....</b>	<b>140</b>
<b>Appendices.....</b>	<b>165</b>
Appendix 1: Supplementary materials .....	165
Appendix 2: Published paper in journal format .....	182

# Table of Figures

## Introduction:

**Fig. I:** Distribution of lamproites (stars) within the Mediterranean region .....24

**Fig. II:** Alignment of the 6 research chapters to the 3 topics of this thesis.....25

## **Chapter 1:** Sediment-Peridotite Reaction Controls Fore-Arc Metasomatism and Arc-Magma Geochemical Signatures

Fig. 1.1: Schematic image of a subduction zone.....29

Fig. 1.2: EPMA WDX- and LA-ICP-TOFMS maps of an experiment at 3 GPa/850 °C .....32

Fig. 1.3: Element fractionation within the reaction zone .....34

Fig. 1.4: Rates of metasomatism .....37

## **Chapter 2:** Melting of Sediments in the Deep Mantle Produce Saline Fluid Inclusions in Diamonds

Fig. 2.1: Backscattered electron images of experimental charges .....43

Fig. 2.2: K/Na ratios of experimental chlorides and saline micro-inclusions in diamonds .....44

Fig. 2.3: Modal proportions of phases in the reaction experiments .....46

Fig. 2.4: K/Na and Cl/F in mica, melt, fluid, and halides.....47

Fig. 2.5: Composition of silicate phases in reaction experiments .....48

Fig. 2.6: Pressure-temperature stability of Na-K chlorides.....51

Fig. 2.7: Ternary diagram of experimental phases.....52

## **Chapter 3:** Two-stage Formation of K-enrichment in Ultrapotassic Magmatism Confirmed by a Novel Experimental Approach

Fig. 3.1: Backscattered electron images of reaction zones .....59

Fig. 3.2: Melt (A) and clinopyroxene (B) compositions from reaction experiments .....61

Fig. 3.3: K<sub>2</sub>O (A), Na<sub>2</sub>O (B), Al<sub>2</sub>O<sub>3</sub> (C), and CaO (D) *versus* SiO<sub>2</sub>.....63

Fig. 3.4: K/Na (A) and K<sub>2</sub>O mass fractions (B) of melts *versus* experimental run temperature .....66

Fig. 3.5: N-MORB normalized trace element compositions .....68

Fig. 3.6: Model for the genesis of post-collisional UP magmatism. ....72

**Chapter 4: An Experimental Study of the Role of Partial Melts of Sediments versus Mantle Melts in the Sources of Potassic Magmatism**

Fig. 4.1: Backscattered electron images (Comp) and WDX elemental maps .....	80
Fig. 4.2: Total alkali <i>versus</i> silica (A) K/Na <i>versus</i> SiO <sub>2</sub> (B), and K <sub>2</sub> O <i>versus</i> SiO <sub>2</sub> (C) .....	81
Fig. 4.3: Compositions of pyroxenes from reaction experiments .....	82
Fig. 4.4: Compositions of phlogopites from experiments.....	83
Fig. 4.5: Trace element compositions of starting materials.....	85
Fig. 4.6: C1-Chondrite normalized REE patterns of clinopyroxene (A) and garnet (B) .....	86
Fig. 4.7: Concentration of compatible trace elements in phlogopite .....	89
Fig. 4.8: Partition coefficients for trace elements.....	90
Fig. 4.9: Trace element compositions of experimental melts.....	92
Fig. 4.10: Subduction zone (A) and mantle melt-metasomatism in a rifting scenario (B).....	95

**Chapter 5: Melting Phlogopite-rich MARID: Lamproites and the Role of Alkalis in Olivine-Liquid Ni-partitioning**

Fig. 5.1: Composition (Backscattered electron - BSE) images of polished sectioned capsules ....	102
Fig. 5.2: Major element composition of melts in the experimental charges .....	103
Fig. 5.3: Trace element composition of melts.....	104
Fig. 5.4: Major element composition of phlogopites from start materials.....	108
Fig. 5.5: Ni-partitioning of melt/olivine .....	109
Fig. 5.6: D <sub>Ni</sub> of olivine/melt <i>versus</i> melt-viscosity.....	110
Fig. 5.7: D <sub>Ni</sub> dependencies of our melts (black circles) and test datasets.....	112
Fig. 5.8: Glass-based geothermometers showing deviations of calculated- from measured T ...	114
Fig. 5.9: Application of the thermometer to olivine-glass pairs from lavas.....	115

**Chapter 6: Partitioning of Nitrogen during Slab-melting and Recycling in Subduction Zones**

Fig. 6.1: Backscattered electron image of the 3 GPa/850 °C experiment.....	124
Fig. 6.2: Raman spectra of A) phlogopite and B) glass of the 3 GPa/850 °C experiment .....	126
Fig. 6.3: Partition coefficients for N and K for phengite/melt and phlogopite/melt .....	127
Fig. 6.4: Partition coefficients for N between fluid and melt <i>versus</i> experimental T.....	128
Fig. 6.5: Partition coefficients for N between fluid and bulk <i>versus</i> experimental T .....	129

Fig. 6.6: Mass-balance calculations showing the distribution of nitrogen .....	130
Fig. 6.7: Total mass fraction of recycled atmospheric nitrogen.....	131
Fig. 6.8: Nitrogen retention within global subduction zones.....	133
<b>Thesis conclusion:</b>	
Fig. II: Schematic section through subduction, craton-, and continental rift.....	139
<b>Supplementary for chapter 1:</b>	
Supplementary Fig. 1.1: LA-ICP-TOFMS map of vanadium .....	165
Supplementary Fig. 1.2: Metasome thicknesses and infiltrated melt distances .....	167
Supplementary Fig. 1.3: Reaction zone phases .....	168
<b>Supplementary for chapter 2:</b>	
Supplementary Fig. 2.1: Chloride map of 5 GPa/1000 °C experiment.....	170
Supplementary Fig. 2.2: Backscattered electron image of the 6 GPa/1100 °C experiment.....	171
<b>Supplementary for chapter 3:</b>	
Supplementary Fig. 3.1: Residual sediment of the 3 GPa/900 °C experiment .....	172
Supplementary Fig. 3.2: Orthopyroxene-veines in dunite of the 3 GPa/900 °C experiment .....	172
<b>Supplementary for chapter 5:</b>	
Supplementary Fig. 5.1: Synthetic MARID glass in San Carlos Olivine capsule .....	173
Supplementary Fig. 5.2: A) Correlation of $D_{Ni}$ in olivine/melt <i>versus</i> MgO-content .....	174
Supplementary Fig. 5.3: A) Model parameters B <i>versus</i> C of melt-viscosity model .....	174
Supplementary Fig. 5.4: A) $D_{Ni}$ <i>versus</i> temperature and B) $D_{Ni}$ <i>versus</i> molar contents.....	175
Supplementary Fig. 5.5: Correlation of $D_{Ni}$ in olivine/melt <i>versus</i> CaO-content.....	175
Supplementary Fig. 5.6: Calculated temperature <i>versus</i> measured temperature.....	176
Supplementary Fig. 5.7: Thermometer based on Ni-part. and molar constituents of melt .....	176
<b>Supplementary for chapter 6:</b>	
Supplementary Fig. 6.1: Raman spectra of $NH_4$ -feldspar (buddingtonite).....	177
Supplementary Fig. 6.2: Measurement parameters for N at the EPMA.....	178
Supplementary Fig. 6.3: Linear correlation of N <i>versus</i> $K_2O$ in phengite .....	179
Supplementary Fig. 6.4: Nitrogen mass fraction of glasses (A) and mica (B) <i>versus</i> T.....	179
Supplementary Fig. 6.5: Mass fraction of atmospheric nitrogen <i>versus</i> time.....	180
Supplementary Fig. 6.6: Nitrogen retention within subduction zones.....	181

# List of Tables

## **Chapter 3:** Two-stage Formation of K-enrichment in Ultrapotassic Magmatism Confirmed by a Novel Experimental Approach

Table 3.1: Melting phase relations of reaction experiments and 2<sup>nd</sup> stage melting experiment....62

## **Chapter 4:** An Experimental Study of the Role of Partial Melts of Sediments versus Mantle Melts in the Sources of Potassic Magmatism

Table 4.1: Composition, temperature, pressure, and duration of each experiment.....78

Table 4.2: Average composition of starting materials and high-pressure experiment melts .....81

Table 4.3: Average analyses for silicate phases in the experiments .....83

## **Chapter 5:** Melting Phlogopite-rich MARID: Lamproites and the Role of Alkalis in Olivine-Liquid Ni-partitioning

Table 5.1: Composition, temperature, pressure, and duration of each experiment.....100

Table 5.2: Representative analysis for MARID composition and experiment melts .....104

Table 5.3: Ni-contents of melt and olivine and  $D_{Ni}$  of experimental charges.....105

Table 5.4: Representative analyses for silicate phases in the experiments.....106

Table 5.5: Correlation coefficients of various combinations of constituents *versus*  $D_{Ni}$  and T. ...109

## **Chapter 6:** Partitioning of Nitrogen during Slab-melting and Recycling in Subduction Zones

Table 6.1: Composition of the synthetic buddingtonite.....122

Table 6.2: Thermobaric conditions and phases present in experimental runs .....123

Table 6.3: Results of nitrogen mass-balance between experimental phases .....126

Table 6.4: Mass fraction of N in the oceanic lithosphere .....131

Table 6.5: Parameters for N recycling budgets.....131

### **Supplementary for chapter 1:**

Supplementary Table 1.1: Phase relations of reaction experiments.....166

Supplementary Table 1.2: Major element composition of starting materials [wt%].....168

### **Supplementary for chapter 2:**

Supplementary Table 2.12: Phase relations of experiments .....169

### **Supplementary for chapter 5:**

Supplementary Table 5.1: Reference materials for electron-microprobe routines.....173

# List of Publications

## Peer-reviewed publications:

Förster, M. W., Buhre, S., Xu, B., Prelević, D., Mertz-Kraus, R., Foley, S. F. Two-stage formation of K-enrichment in ultrapotassic magmatism confirmed by a novel experimental approach. Contributions to Mineralogy and Petrology, under review: 15/01/2019

Förster, M. W., Bussweiler, Y., Prelević, D., Daczko, N. R., Buhre, S., Mertz-Kraus, R., Foley, S. F. Sediment-peridotite reaction controls fore-arc metasomatism and arc-magma geochemical signatures. Scientific Reports, minor revisions, revisions send to journal: 06/03/2019

Förster, M. W., Prelević, D., Buhre, S., Mertz-Kraus, R., Foley, S. F. An experimental study of the role of partial melts of sediments versus mantle melts in the sources of potassic magmatism. 2019. Journal of Asian Earth Sciences: Magmatic Evolution and Crustal Growth of the Mediterranean Region: New Geochemical and Geochronological Perspectives (special issue) 177, 76-88.

Förster, M. W., Foley, S. F., Marschall, H. R., Alard, O., Buhre, S. Melting of sediments in the deep mantle produce saline fluid inclusions in diamonds. Science Advances, accepted manuscript.

Huong, L. T. T., Otter, L. M., Förster, M. W., Hauzenberger, C. A., Krenn, K., Alard, O., Macholdt, D. S., Weis, U., Stoll, B., Jochum, K. P. 2018. Femtosecond-laser ablation-ICP-mass spectrometry and CHNS elemental analyzer reveal trace element characteristics of danburite from Mexico, Tanzania, and Vietnam. MDPI Minerals, 8(6), 234, 1-15.

Förster, M.W., Prelević, D., Schmück, H.R., Buhre, S., Marschall, H.R., Mertz-Kraus, R., Jacob, D.E., 2018. Melting phlogopite-rich MARID: Lamproites and the role of alkalis in olivine-liquid Ni-partitioning. Chemical Geology 476, 429–440.

## Conference abstracts:

Förster, M. W., Prelević, D., Buhre, S., Foley, S. F. Nitrogen partitioning in subduction zone processes. IMA2018, Melbourne, 08/2018

Förster, M. W., Prelević, D., Buhre, S., Foley, S. F. Partitioning of nitrogen during partial melting of phlogopite-rich metasomes. Goldschmidt2017, Paris, France, 08/2017

Förster, M. W., Prelević, D., Buhre, S., Schmück, H. R., Veter, M., Foley, S. F., Jacob, D. E. Reaction Experiments of Glimmerite + Harzburgite at 3-5 GPa and Genesis of low-SiO<sub>2</sub> Ultrapotassic Magmas, EMPG XV, Zurich, 06/2016

Förster, M. W., Prelević, D., Buhre, S., Schmück, H. R., Veter, M., Mertz-Kraus, R., Foley, S. F., Jacob, D. E. Reaction Experiments of Glimmerite + Harzburgite at 1-2 GPa and Genesis of Orogenic Ultrapotassic Magmas, EMPG XV, Zurich, 06/2016

# Acknowledgements

First, I would like to express my respect to the traditional owners of the land – the Wattamattagal clan of the Darug people – that Macquarie University is built on.

I kindly thank Stephen Foley, Nathan Daczko, Simon Clark, and Dejan Prelević for supervising my thesis. Especially to Steve I wish to extend my greatest gratitude as he gave me this challenging project and allowed me to travel overseas to do my experiments and analysis in Mainz and Frankfurt during the time of the lab shutdown at Macquarie University.

I am grateful to all laboratories at Johannes Gutenberg-University, Mainz: Stephan Buhre, Nora Groschopf, Regina Mertz-Kraus, Harald Schmück, Fatma Gülmez, Jennifer Günther, Anastasia Zemlitskaya, and Marina Veter, the high-pressure group at the Goethe University, Frankfurt: Thomas Kautz, Kevin Klimm, Laura Uenver-Thiele, Vladimir Matjuschkin, Sonja Aulbach, and Horst Marschall, the Macquarie University Faculty of Science and Engineering Microscope Facility (MQFoSE MF): Sue Lindsay and Chao Shen, the Environmental Quality Laboratory: Russel Fields and Damien Gore, the Macquarie GeoAnalytical Unit (MQGA): Steve Craven, George Amulele, John Adam, Tracy Rushmer, Elena Belousova, Olivier Alard, Lauren Gorojovsky, Lauren Robinson, Bruce Schaefer, Tim Murphy, Yi-Jen Lai, Nigel Wilson, Yoann Greau, Peter Wieland, and Dorrit Jacob as well as Macquarie's Geophysics and Geodynamics Group: Juan Carlos Afonso, Kate Selway, Steven Hansen, and Beñat Oliveira-Bravo. All provided skilful advice and tireless support.

I gratefully acknowledge Dan Frost and Ananya Mallik for inviting me to present my research at the Bayerisches Geoinstitut (BGI) and the input they gave me for further experiments.

Further, I acknowledge Sue O'Reilly, Bill Griffin, Summer Luo, Sally Ann-Hodgekiss and the whole CCFS team for supporting my research, challenging my work and allowing me to be part of this world-class research group.

I thank the former and current EPS administration team, Wendy Southwell, Alarnah Jade-Cullen, Jen Rowland, Aida Pujol, Phil Dartnell, Fiona Yang, Jenny Fang, and Amid Shresta for all the help in organizational and financial questions.

I would also like to acknowledge Hossai Gul as well as all convenours and participants of the inaugural year of "Future STEMM Leaders".



Big thanks to all my peers at the Macquarie high-pressure petrology group “DEEP MQ”: Zsanett Pintér, Chunfei Chen, Zairong Liu, Mingdi Gao, Joshua Shea, Chengyuan Wang, Anthony Lanati, and Yu Wang.

I thank my friends and colleagues Marina Veter, Zhongxuan Li, Thusitha Nimalsiri, Sarath Kumara, Dilmi Herath, Alexander Wellhäuser, Christoph Lenz, Shucheng Wu, Kui Han, Hindol Ghatak, Francesca Mirolo, Jonathan Munnikhuis, Rosa Didonna, Sinan Özeydin, Oluwatoosin Agbaje, Xiong Wang, Milena Schönhofen, Bo Xu, Stephanie Greene, Jonathan Wasiliev, Hadrien Henry, Maria Manassero, and many more for the various coffee breaks, cinema Mondays, and roof-top Fridays.

A big thank also to Gudrun Daniels who welcomed Laura and me to Australia and helped us settle in and find our first apartment.

I give my greatest gratitude to Tanya Chapman who is our current landlady since the second half of our PhDs and supported us with great geology related discussions, heaps of wonderful food, and great company.

I also thank Laura, my partner, not only for your love, support, and assistance but also for all help regarding proofreading and editing of this thesis. Without your out-of-this-world time management skills I wouldn't have made the deadline! To my families in Waldbrunn and Heidelberg, Doris, Heinz, my brother Ramon, Ron, Elke, Anne, and Wolf, thank you all for the love and support you give me.

# List of Abbreviations

## General:

AHOB:	Alpine-Himalayan Orogenic Belt
EPMA:	Electron-probe microanalyzation
$fO_2$ :	Oxygen fugacity
Ga:	Giga-annum
GeoReM:	Geological and Environmental Reference Materials
GLOSS:	Global average subducting sediments
GPa:	Giga-pascal
IODP:	International Ocean Discovery Project
LA-ICP-MS:	Laser ablation-inductively coupled plasma-mass spectrometry
MARID:	Mica-amphibole-rutile-ilmenite-diopside association of xenoliths
MORB:	Mid ocean ridge basalt
OIB:	Ocean island basalt
TOFMS:	Time of flight mass spectrometry
UP:	Ultrapotassic
LILE:	Large ion lithophile element (Rb, Cs, Ba, Sr)
HFSE:	High field strength element (Th, U, Zr, Hf)
REE:	Rare earth element (La, Ce, Pr, Nd, Sm, Eu, Gd, Tb, Dy, Ho, Er, Tm, Yb, Lu)

## Minerals:

Cc:	Calcite
Coe:	Coesite
Cpx:	Clinopyroxene
Dol:	Dolomite
Gt:	Garnet
Ky:	Kyanite
Mgs:	Magnesite
Ol:	Olivine
Opx:	Orthopyroxene
Phe:	Phengite
Phl:	Phlogopite
Qtz:	Quartz

## Key Contributions of this PhD to the Field of Research

- High-pressure experiments reacting sediment with dunite at 1-3 GPa show that the fore-arc of a subduction zone is enriched in K, and metasomes show a continental crust-like trace element pattern.
- Melting of the metasomatized mantle produces melts with >6 wt% K<sub>2</sub>O, and trace element signatures comparable to those found in post-collisional potassic lavas with K/Na >2.
- High-pressure reaction experiments of hydrous basanite with dunite indicate that post-collisional lavas with K/Na 0.5-1 originate from a mantle-melt metasomatized lithosphere.
- Silicate network modifiers, namely Na, K, and Al, as well as temperature, strongly influence the Ni-partitioning between olivine and melt.
- The changes in melt composition as well as Ni-partitioning between olivine and melt are combined to calibrate a sensitive, novel geothermometer applicable from 1100 to 1600 °C specifically developed for basaltic melts.
- High-pressure experiments reacting sediment and dunite at 4-6 GPa produce magnesite and high K/Na chlorides similar to highly saline fluid inclusions in diamonds. These alkaline chlorides are equivalent to those believed to occur in the formation of salty kimberlites such as Udachnaya East.
- The reaction of sediment with depleted peridotite leads to a redistribution of organic N into K-bearing minerals such as mica; N is also enriched in melt and fluid phases.
- Partitioning of N between fluid and melt increases with temperature and retention of N in Earth's mantle is favored under cold subduction conditions.
- The efficiency of N recycling is higher now than in the Earth's past and exceeds the rate of degassing of mantle N, thus pN<sub>2</sub> of the atmosphere is currently slowly decreasing.

## Abstract

In total, subduction zones span 40,000 km across Earth's surface and recycle an average thickness of 500 m of sediment. During burial and heating these sediments eventually start melting at  $T > 675^{\circ}\text{C}$ , following which Si-rich hydrous melts infiltrate the peridotites of the mantle wedge above the subducting slab.

In this thesis, a high-pressure experimental approach is used to examine the reaction of sediments and peridotites at 2-6 GPa in subduction zones and its consequences on the generation of K-rich magmatism and on deep nitrogen cycling. All experiments are conducted in a layered arrangement, where the depleted peridotite is placed above the sediments in a 1:1 ratio. At 2-3 GPa, the reaction of melts of sediment with depleted peridotite, simulating the fore-arc of a subduction zone, leads to the formation of layered phlogopite pyroxenites and selective incorporation of major and trace elements in these metasomatic layers. Partial melting of these phlogopite pyroxenites produces melts rich in  $\text{K}_2\text{O}$  ( $>9 \text{ wt\%}$ ) with  $\text{K/Na} \gg 2$  and a trace element pattern comparable to "orogenic lamproites".

At similar pressures, the reaction of hydrous mantle melts with depleted peridotites produces metasomatic layers that show  $\text{K/Na} \sim 1$  and a trace element pattern that closely resembles "anorogenic lamproites". In both cases, K-enrichment is facilitated by the crystallization of an eclogitic residue rich in Na, poor in K, and consequently with low  $\text{K/Na}$ .

At 4-6 GPa, the reaction of melts of sediment with depleted peridotite does not produce mica, instead resulting in alkali chlorides with  $\text{K/Na}$  ratios similar to saline fluid inclusions in diamonds. Besides the chlorides, magnesite also crystallises in the peridotite. Both phases are important ingredients for the generation of salty kimberlites such as Udachnaya East.

The change in metasomatic style from mica- to chloride formation between 3 to 4 GPa corresponds to the depth of the mid-lithospheric discontinuity, a zone of low seismic velocities that is found intermittently beneath all continents at a depth of 80–100 km.

The subduction of sediment is the main mechanism that recycles nitrogen back to Earth's mantle. The partitioning of nitrogen between fluid and melt ( $D_{\text{N(Fluid/Melt)}}$ ) and fluid and bulk residue (melt+mica) ( $D_{\text{N(Fluid/Bulk)}}$ ) was found to increase linearly with temperature normalized to pressure. Using the new partition coefficients, the amount of N recycled to Earth's mantle since the onset of subduction is calculated as  $50 \pm 6 \%$ .

# I. Introduction

## i. Mantle metasomatism

The chemical change of rock by the interaction with fluids is described as metasomatism (Harte, 1987). It ranges from changes in trace- to major element composition and occurs within the crust and uppermost (lithospheric) mantle (Harte, 1987). Generally, metasomatic processes are considered to have taken place when a specific mineral assemblage of a rock cannot be derived by simple melting and crystallization processes (Dawson, 1984; Harte, 1987). Mantle metasomatism and the chemical changes and reactions of pre-existing minerals with infiltrating fluids were first described at the beginning of the last century (Goldschmidt, 1922; Lindgren, 1912). Since the early 1970s, the concept of mantle metasomatism has been accepted and is invoked as a possible precursor of alkaline magmatism (Bailey, 1982). Uncertainties remain of whether metasomatism is precursory to melt formation or if it is merely a consequence of it.

Metasomatism is divided into three types: 1. Modal metasomatism describes major changes in bulk rock chemistry, which lead to mineral alteration and formation of new minerals such as amphibole, mica, clinopyroxene, Fe-Ti-oxides, apatite, sulphide, and zircon, usually in form of veins within less metasomatized host-rock (Dawson, 1984; Harte, 1987). 2. Cryptic metasomatism, which describes the enrichment of the rock phases in trace elements without changes in mineral textures as well as minor to major elements (Dawson, 1984). 3. Stealth metasomatism, which is characterised by the addition of new phases that are indistinguishable from common phases of the previously un-metasomatized rock (O'Reilly and Griffin, 2013). Metasomatic agents are likely (1) liquids that either rise from the deeper (asthenospheric) mantle, where the presence of volatile components such as  $\text{H}_2\text{O}+\text{CO}_2$  lower the solidus of peridotite by  $<400^\circ\text{C}$  and produce 'incipient' amounts of melt (Foley and Pintér, 2018), or (2) liquids that rise from subducted oceanic and continental crustal rocks as well as sediments that may eventually melt and react with arc mantle (Bebout, 2013). While the first mode of metasomatism is characteristic for intraplate settings such as rift zones and mantle plumes (Foley and Fischer, 2017), the latter is found at convergent plate margins of oceanic and continental subduction (Prelević et al., 2010; Prelević et al., 2013; Prouteau et al., 2001).

## **ii. Metasomatized mantle xenoliths**

Fragments of Earth's mantle transported to the surface by rapidly rising magmas and are referred to as mantle xenoliths (Nixon, 1987). Several different styles of metasomatism have been recognized from metasomatized mantle xenoliths, depending on the tectonic setting (cratonic, non-cratonic) and composition of the metasomatizing agent (O'Reilly and Griffin, 2013). Xenoliths of metasomatized mantle are generally found within alkaline lavas and are sampled above the region of melt generation, since the melt first pools to a certain quantity before it rises rapidly and entrains xenoliths (Schmincke, 2007). Modally metasomatized xenoliths carry hydrous minerals such as amphibole and mica and range from kaersutite/pargasite-dominated to pyroxenite and phlogopite-pyroxenite (glimmerite) assemblages (Dawson, 1984; Harte, 1987). The latter group also includes the mica-amphibole-rutile-ilmenite-diopside (MARID) association of xenoliths and was first described from xenoliths in Kimberley, South Africa (Dawson and Smith, 1977) were soon also found in other parts of the world (Downes, 2001). Since individual volcanoes erupt xenoliths with various stages of metasomatism, from modally metasomatized to un-metasomatized, the xenoliths likely represent fragments of the vein-wall rock melting relationship (Foley, 1992c). Numerous recent studies confirmed the vein-wall rock melting relationship and established a source-melt kinship of modally metasomatized mantle and ultrapotassic lavas (Förster et al., 2017; Giuliani et al., 2015; Rosenthal et al., 2009; Tappe et al., 2008).

## **iii. Ultrapotassic lavas**

Ultrapotassic lavas are “alkaline igneous rocks”. This umbrella term describes all igneous rocks that are generally enriched in the oxide species  $\text{Na}_2\text{O}$  and  $\text{K}_2\text{O}$  relative to sub-alkaline (tholeiitic) rocks at similar  $\text{SiO}_2$  (Le Maitre et al., 2005). The alkaline rocks include sodic and potassic series, depending on the dominant oxide species. The sodic series is generally more common/abundant and includes nephelinites, basanites, alkali-olivine-basalts (AOB) and their differentiates (Le Maitre et al., 2005). Potassic rocks are defined by comprising  $\text{K}_2\text{O} > \text{Na}_2\text{O}$  in wt% and include compositional ranges from leucite-bearing basanites to K-enriched rock variants like leucitites, lamprophyres, orangeites, as well as shoshonites and lamproites (Mitchell and Bergman, 1991). The term “ultrapotassic” was introduced by Carmichael et al. (1974) and Bergman (1987) for rock

compositions with  $K_2O/Na_2O$  ratios  $>3$ . However, this is in contrast to the work of Bogatikov et al. (1985), who suggested that only ratios of  $K_2O/Na_2O >10$  should be termed ultrapotassic, thereby excluding a large proportion of previously classified “ultrapotassic” rocks (Carmichael et al., 1974). Furthermore, Bogatikov et al. (1985) referred to rocks with  $K_2O/Na_2O$  ratios of 5-10 as “highly potassic”, while those with ratios of only 1-5 were called simply “potassic”. Later, the terminology characterizing all types of potassic rocks was thoroughly revised by Foley et al. (1987). They suggested that rocks are “ultrapotassic” when  $K_2O >3$  wt%, while  $K_2O/Na_2O$  and  $MgO$  are  $>2$  and  $>3$  wt%, respectively. Depending on the present phases, K-rich rocks are distinguished into Kamafugites, Lamprophyres, Leucitites, Shoshonites, Kimberlites, and Lamproites:

- Kamafugites are known from Uganda (Tappe et al., 2003) as well as Italy and Serbia (Prelević et al., 2005). These extremely silica-undersaturated lavas show melilite and kalsilite, a feldspathoid which forms in place of leucite at extreme silica deficiency (Foley et al., 1987).
- Lamprophyre is not a rigid classification but describes a group of magmatic rocks that mainly occur on intraplate settings (Mitchell & Bergman, 1991). It is a collective term that includes lavas of diverse characters such as shoshonitic lamprophyres, alkaline lamprophyres, and ultramafic lamprophyres (ailikites, Veter et al., 2017). They are mildly potassic with  $K/Na$  values of 1-1.5 and contain phenocrystic phlogopite in a matrix of sanidine or plagioclase as well as kaersutite, melilite, monticellite, nepheline, grossular-andradite garnet and carbonates.
- Leucitites are potassic rocks that are found in intraplate settings (e.g. Eifel, Mertes & Schmincke, 1985) and subduction zones (e.g. Turkey, Akal, 2004). They contain clinopyroxene, leucite, melilite, and olivine as well as sodic feldspathoids such as nepheline which are absent in lamproites. (Mitchell & Bergman, 1991).
- Shoshonites are K-feldspar-bearing alkaline rocks that are typically found on active continental margins and island arcs behind subduction-zone volcanoes of andesitic composition (Morrison, 1980). They contain olivine and augite phenocrysts in a groundmass of labradorite, olivine and leucite. Shoshonites show  $Na_2O + K_2O >5$  wt% and  $K/Na >1$  and can be silica-oversaturated as well as silica-undersaturated (Morrison, 1980).

- Kimberlites are ultramafic lavas which are restricted to cratons. They are distinguished into two groups depending on their mineral assemblage: Group-I kimberlites are not ultrapotassic and show phenocrysts of olivine, phlogopite, monticellite, spinel, perovskite, calcite and primary serpentine. In addition they contain upper-mantle derived megacrysts of Ti-pyroxene, Mg-ilmenite, subcalcic diopside, and enstatite (Mitchell & Bergman, 1991). Orangeites, former known as Group-II kimberlites are ultrapotassic and show phlogopite, which occur both as phenocrysts and groundmass phases as well as diopside and carbonates (Mitchell & Bergman, 1991).
- Lamproites are peralkaline ultrapotassic rocks that contain phlogopite, amphibole, clinopyroxene, olivine, leucite, K-Feldspar, as well as spinel, rutile, and ilmenite. They are strongly enriched in K, Rb, Sr, Ba, F, Cr, Ni and LREE. Lamproites are depleted in Na, Ca, and Al, when compared to other alkaline magmas, which likely result from deficiencies within the source material (Mitchell & Bergman, 1991). Lamproites often occur after continental collisions and their generation involve strongly depleted peridotites, combined with a high-extend of crustal-derived enrichment (Prelević et al., 2013).

Direct melting of the primitive mantle, which has a  $K_2O/Na_2O$  of  $\sim 0.1$  (Hofmann, 1988) and thus contains ca. 10 times lower amounts of  $K_2O$  compared to  $Na_2O$ , cannot produce potassic alkaline magmas with  $K_2O > Na_2O$  (e.g. Novella and Frost, 2014). Instead,  $K_2O$  has to be enriched and the source of potassic alkaline magmas likely lies within the lithospheric mantle which is metasomatically overprinted.

#### **iv. Deep nitrogen cycling**

Nitrogen is the fifth most abundant element in the solar system and a key nutrient to life (Elser et al., 2007). Surficial nitrogen cycling is well understood today (Boyd, 2001; Holloway and Dahlgren, 2002; Kelly, 2000), however, little is known about its quantities and distribution within the Earth (Johnson and Goldblatt, 2015). The geological nitrogen cycle begins with sedimentation of organic matter and the formation of ammonium ( $NH_4^+$ ) by organic decay and hydrolysis within the sediment (Hall and Matson, 1999). In silicates, N is generally present in its reduced form as ammonium ( $NH_4^+$ ) and hydrothermally formed N-silicates such as  $NH_4$ -feldspar (Buddingtonite) are examples of minerals with N as a major constituent. However, most N is incorporated in the form of trace amounts of  $NH_4^+$  substituting for  $K^+$  (e.g. Itihara and Honma, 1979). The ionic radius



of  $\text{NH}_4^+$  is about 0.2 Å larger than the  $\text{K}^+$  radius (1.61-1.69 Å for 10,11 coordination *versus* 1.46-1.63 Å for 8-10 coordination) and thus can easily substitute into K-bearing minerals (Khan and Baur, 1972; Whittaker and Muntus, 1970) and for Na and Ca in plagioclase feldspars (Honma and Itihara, 1981). Hence, all K-bearing minerals such as clay minerals, feldspars, and micas are able to accommodate  $\text{NH}_4^+$  (Johnson and Goldblatt, 2015). When these minerals are subducted, N is recycled back into the mantle. At plate boundaries with slow and hot subduction, N escapes as  $\text{N}_2$  back into the atmosphere via volcanic gases (Elkins et al., 2006). In contrast, faster and colder subduction is capable of transferring N back into the mantle (Mitchell et al., 2010).

The speciation of nitrogen in the mantle strongly depends on redox, thermobaric and pH conditions as well as the prevailing oxygen fugacity ( $f\text{O}_2$ ) (Frost, 1991; Libourel et al., 2003). Oxygen fugacity buffered by fayalite-magnetite-quartz (FMQ) leads to the dominance of  $\text{N}_2$  among the N-species as evident from fluid inclusions in oceanic basalts (Marty, 1995), while  $\text{NH}_3$  is found under reduced conditions ( $f\text{O}_2$  buffered by iron-wustite (IW)); (Li and Keppler, 2014; Libourel et al., 2003). Nitrogen is soluble in metal alloys at a variety of pressures (Kadik et al., 2011; Roskosz et al., 2013). According to Roskosz et al. (2013), N may be present in Earth's core and also in Fe-Ni alloys in the transition zone and lower mantle. In the transition zone these are considered to contain <10 wt% in FeNi-metals and <0.5 wt% in silicates (Roskosz et al., 2013). At  $f\text{O}_2$  below IW, the lower mantle and core probably contain N in form of metal nitrides (Adler and Williams, 2005). Differences in pH also influence the speciation of N (Mikhail and Sverjensky, 2014). Budgeting of total N in Earth has been challenging due to the lack of knowledge about mass fractions and behaviour of N during formation of the planets and moon (Johnson and Goldblatt, 2015). The concentration of N present during Earth's formation is derived from chondrites (Halliday, 2013; Marty, 2012), which show strongly heterogeneous concentrations of N that range from  $605 \pm 206 \mu\text{g}\cdot\text{g}^{-1}$  in enstatite chondrites (EC) to up to  $1235 \pm 440 \mu\text{g}\cdot\text{g}^{-1}$  in carbonaceous chondrites (CC) (Marty, 2012). This range of values is used to estimate the concentration of N in bulk Earth. However, it also depends on the compatibility and partitioning of N during accretion: If, on one hand, N behaves in a strongly volatile manner similar to Ar, bulk Earth concentration would be  $34 \pm 12 \mu\text{g}\cdot\text{g}^{-1}$  and  $55 \pm 20 \mu\text{g}\cdot\text{g}^{-1}$  for EC and CC, respectively (Johnson and Goldblatt, 2015). Reduced conditions, on the other hand, would lead to N concentrations from around 145 to  $864 \mu\text{g}\cdot\text{g}^{-1}$  under the assumption that it is present as  $\text{NH}_4^+$  and behaves

similarly to  $K^+$ . Since N behaviour is thought to be more volatile than K, the latter result is likely an upper threshold for N in bulk Earth (Johnson and Goldblatt, 2015).

The mass fraction of N within the different endogenic reservoirs in Earth is difficult to determine due to the lack of knowledge of the behaviour of nitrogen in the mantle and core (Johnson and Goldblatt, 2015). The continental crust has the highest mass fraction of N in Earth (about  $120 \mu\text{g}\cdot\text{g}^{-1}$ ), while all mantle rocks have generally only  $<1 \mu\text{g}\cdot\text{g}^{-1}$  (Johnson and Goldblatt, 2015). As mantle rocks are mostly not exposed at the surface and thus cannot be analysed directly for their N content, most analyses are performed on upper mantle xenoliths and oceanic basalts where N is present in its strongly incompatible state of  $\text{N}_2$  (Goldblatt et al., 2009; Marty and Humbert, 1997; Marty and Zimmermann, 1999). Accordingly, N mass fractions of mantle rocks are likely to be underestimated because of early N degassing during magma formation (Libourel et al., 2003). K-rich rocks such as lamproites with N mass fractions of up to  $394 \mu\text{g}\cdot\text{g}^{-1}$  (Jia et al., 2003), as well as an average of  $794 \mu\text{g}\cdot\text{g}^{-1}$  N in diamonds (Johnson and Goldblatt, 2015), suggest that there may be hidden N-rich reservoirs within Earth's mantle.

Determining the source of nitrogen within a given sample by stable isotopes remains inconclusive since chondrites show both negative and positive  $\delta^{15}\text{N}$  values (Grady et al., 1986; Javoy et al., 1986; Pearson et al., 2006). However, there is a consensus that positive  $\delta^{15}\text{N}$  are a signature of recycled, surficial nitrogen since primitive mantle rocks generally have negative  $\delta^{15}\text{N}$  (-35 to -5 ‰). Recycled continental crustal materials, on the other hand, have positive  $\delta^{15}\text{N}$  (0 to +20 ‰) (Grady et al., 1986; Javoy et al., 1986).

## **v. Research approach and aim of study**

In this thesis, a high-pressure experimental approach is used to examine the fate of recycled sediments in subduction zones and the enrichment of potassium and nitrogen in the lithospheric mantle. The experiments were conducted on natural marine sediments from the Mediterranean (acquired from the International Ocean Discovery Project: ODP 161-976 B 18 X3 105-106.5) (Fig. I) that were reacted with depleted peridotite in a 2-layer arrangement as well as on mica-rich pyroxenites (glimmerites). The experimental capsules were imaged and analysed for major and trace elements to determine the compositions of newly grown mineral or glass phases. The motivation of using K-rich rocks and sediments is founded on the circumstance that K-rich metasomatized mantle is a viable reservoir for nitrogen. The substitution of the potassium ion by

ammonium and the presence of N-rich ultrapotassic lavas is tightly linked to nitrogen enrichment of the lithospheric mantle and K-rich metasomes (Jia et al., 2003; Johnson and Goldblatt, 2015). Hence, the study of metasomatic processes within the uppermost mantle is a vital precondition for understanding the deep cycling of nitrogen. However, the origin of ultrapotassic magmas is still a matter of debate and two rivalling theories are currently discussed: one side favours the direct melting of crustal rocks hybridized with mantle peridotites (Campbell et al., 2014; Ersoy et al., 2010), while the other side favours a strong contribution of K-rich mantle metasomes (e.g. Conticelli et al., 2015; Prelević et al., 2008b). While the reaction of K-rich mantle metasomes with depleted peridotites in a vein-wall rock melting scenario produces various magmas with ultrapotassic composition (Foley, 1992c; Förster et al., 2017), direct melting of crustal rocks hybridized with mantle peridotites leads only to mildly K-enriched rocks, which are too low in potassium to satisfy the composition of ultrapotassic magmas (Wang et al., 2017a; Wang and Foley, 2018). However, the vein-wall rock melting scenario requires that the mantle has already been metasomatized, previously enriched by a K-rich melt (e.g. Harte, 1987), leading to a ‘chicken and egg’ dilemma. Previous studies suggested that metasomes composed of phlogopite-enriched pyroxenites formed by reaction of hydrous slab-derived melt with peridotite (Sekine and Wyllie, 1982a, 1983; Wyllie and Sekine, 1982), but a direct link between subduction and ultrapotassic magmatism has yet to be established. In this thesis we compare the experimental melts to K-rich rocks of the Mediterranean, which have been studied extensively during the recent decades (Avanzinelli et al., 2007; Conticelli et al., 2013, 2015; Fritschle et al., 2013; Prelević et al., 2008a,b; Prelević et al., 2013). They include kamafugites, leucitites, as well as orogenic and anorogenic lamproites. The latter two types of lavas are distinguished by their isotopic- and geochemical signatures of which ‘orogenic’ lamproites show strong  $^{87}\text{Sr}/^{86}\text{Sr}$  enrichment trace element signatures of recycled crustal material, while ‘anorogenic’ lamproites are low in  $^{87}\text{Sr}/^{86}\text{Sr}$  and are derived from an asthenospheric source (Prelević et al., 2008a). Both ‘orogenic’ and ‘anorogenic’ K-rich lavas are of ‘post-collisional’ origin, meaning that K-rich magmatism is induced during the later stages of subduction and continental collision, when processes such as slab rollback or -break off induce melting of metasomatized mantle by upwelling and heat transfer (Prelević et al., 2013).

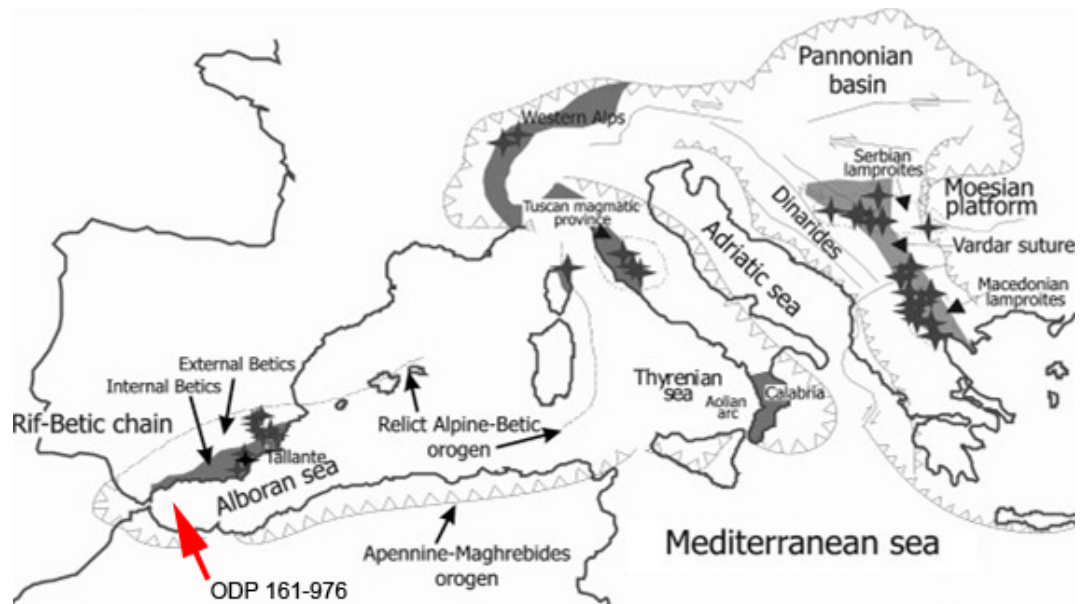


**Fig. I:** Distribution of lamproites (stars) within the Mediterranean region (modified from Prelević et al., (2008)). Major faults are indicated by toothed lines and grey highlights orogenic belts. Red arrow indicates the sample location of the sediment used in this study (acquired from the International Ocean Discovery Project: ODP 161-976 B 18 X3 105-106.5).

The overall goal of this thesis is to increase our understanding of potassium and nitrogen enrichment during mantle metasomatism. To achieve this, the following aims need to be addressed:

- 1) Define a model of fore-arc mantle metasomatism in subduction zones and its effects on K-rich ultrapotassic igneous rocks.
- 2) Investigate the necessity of K-rich ultrapotassic magmas to form via a multistage enrichment process to produce ultrapotassic rocks with  $K_2O > 6$  wt%.
- 3) Determine the differences that melts of sediment *versus* mantle melts have on metasomatism.
- 4) Clarify how mantle metasomatism at cratonic depths ( $> 120$  km) differs from metasomatic reactions within the shallow lithospheric mantle (30-90 km).
- 5) Investigate if reaction experiments of MARID with harzburgite in a vein-wall rock melting setting are a plausible source for the formation of ultrapotassic magma.
- 6) Determine the influences of alkaline and earth-alkaline elements on Ni-partitioning in olivine and melt.
- 7) Investigate if subduction related metasomatism enriches the lithospheric mantle in N. The subducted N of previously organic origin has to be subsequently released and partially metasomatizes the lithospheric arc mantle.

## vi. Structure of the thesis

This thesis consists of 6 chapters published or submitted for publication as research articles which belong to three topics: (1) 'Mantle Metasomatism', (2) 'K-rich Magmatism', and (3) 'Deep Nitrogen Cycling' (Fig. II).

Chapters 1 and 2 "Sediment-Peridotite Reaction Controls Fore-Arc Metasomatism and Arc-Magma Geochemical Signatures" and "Melting of Sediments in the Deep Mantle Produce Saline Fluid Inclusions in Diamonds" belong to topic (1) 'Mantle Metasomatism' and discuss metasomatic reactions between hydrous sediment melts and depleted peridotites in the shallow lithosphere and cratonic mantle, respectively.

Chapters 3-5 "Two-stage Formation of K-enrichment in Ultrapotassic Magmatism Confirmed by a Novel Experimental Approach", "An Experimental Study of the Role of Partial Melts of Sediments *versus* Mantle Melts in the Sources of Potassic Magmatism", and "Melting Phlogopite-rich MARID: Lamproites and the Role of Alkalis in Olivine-Liquid Ni-partitioning" belong to topic (2) 'K-rich Magmatism' and discuss processes from metasome melting to K-rich magmatism.

Chapter 6 "Partitioning of Nitrogen during Slab-melting and Recycling in Subduction Zones" belongs to topic (3) 'Deep Nitrogen Cycling' and discusses the enrichment of the lithospheric mantle in nitrogen by subduction-zone metasomatism.

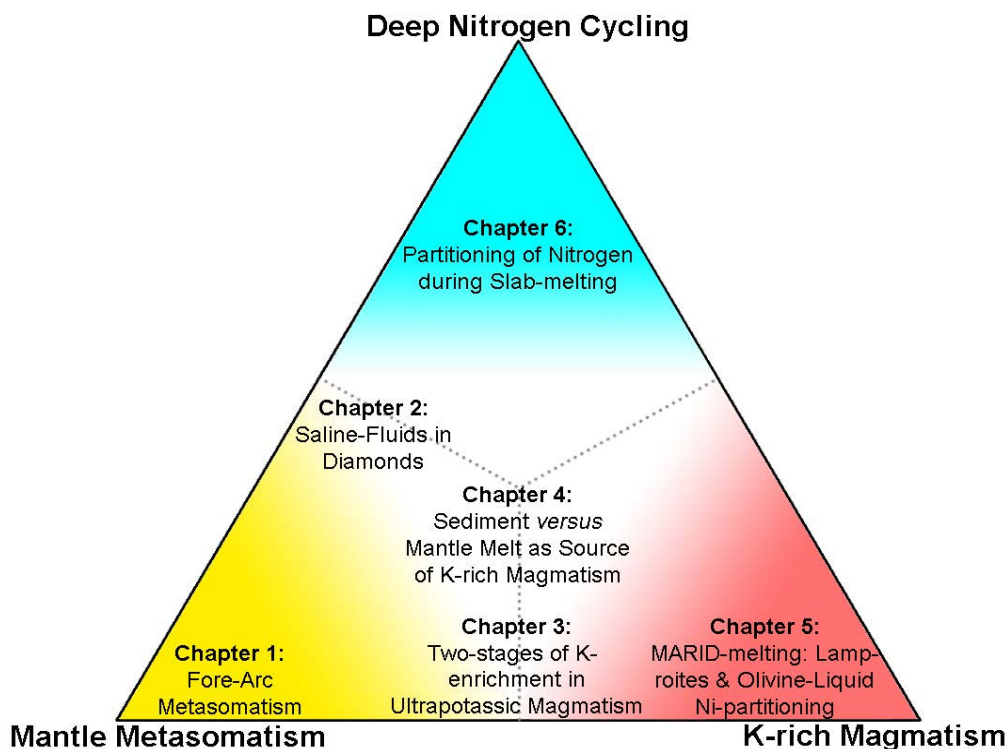


Fig. II: Alignment of the 6 research chapters to the 3 topics of this thesis.

# Chapter 1:

## Sediment-Peridotite Reaction Controls Fore-Arc Metasomatism and Arc-Magma Geochemical Signatures

Michael W. Förster<sup>1</sup>, Yannick Bussweiler<sup>2,3</sup>, Dejan Prelević<sup>4</sup>, Nathan R. Daczko<sup>1</sup>, Stephan Buhre<sup>4</sup>,  
Regina Mertz-Kraus<sup>4</sup>, Stephen F. Foley<sup>1</sup>

<sup>1</sup>ARC Centre of Excellence of Core to Crust Fluid Systems and Department of Earth and Planetary Sciences, Macquarie University, NSW 2109, Sydney

<sup>2</sup>TOFWERK AG, 3600 Thun, Switzerland

<sup>3</sup>Institut für Mineralogie, Universität Münster, 48149 Münster, Germany

<sup>4</sup>Institut für Geowissenschaften, Johannes Gutenberg Universität, 55099 Mainz, Germany

This chapter is in review as an article for Scientific Reports.

### Abstract

Subduction of oceanic crust buries an average of 300–500 m of sediment that eventually dehydrates or partially melts. Progressive release of fluid metasomatizes the fore-arc mantle to serpentinite at low temperatures and to phlogopite-bearing pyroxenite where slab surface temperatures reach 700–900 °C, sufficiently high to partially melt subducted sediments before they approach the depths where arc magmas are formed. Here, we present experiments on reactions between sediments and peridotite at 2–6 GPa/750–1100 °C, which are the thermobaric conditions corresponding to the surface of a subducting slab beneath the fore-arc. Novel LA-ICP-TOFMS element mapping visualizes the processes of metasomatism in the high temperature fore-arc mantle. The reaction of hydrous partial melts derived from sediments with depleted peridotite leads to element separation and a layered arrangement involving metasomatic phases such as phlogopite, clinopyroxene, orthopyroxene, and magnesite. The selective incorporation of major and trace elements in these metasomatic layers closely resembles chemical patterns found in post-collisional K-rich magmas, resolving an enigmatic magmatic suite. Experiments of different duration enabled the calculation of rates of migration of the metasomatic front that range from 1–5 m/ky and are about one order of magnitude lower than plate subduction rates.

## 1.1 Introduction

In the plate tectonic cycle, oceanic crust is continuously subducted and remixed into the mantle. Along with basaltic oceanic crust, an average thickness of 300–500 m of sediment is recycled to mantle depths (Fischer et al., 2002). Rising pressure and temperature during burial drives progressive metamorphism of the sediments and hydrothermally altered oceanic crust, causing the release of fluids (Schmidt and Poli, 1998). Partial melting of the subducted sedimentary material begins at temperatures  $>675^{\circ}\text{C}$ , depending on pressure and chemical composition of the sediment (Hermann et al., 2006; Spandler et al., 2007). Partial melts of the subducted and metamorphosed sedimentary rocks eventually separate from their source, rise, and react and hybridize with the mantle wedge beneath arcs to generate subduction-related magmatism. These arc magmas are generally known for their strong depletion in high field strength elements (HFSE), which is thought to result from residual rutile during sediment de-volatilization (Stolz et al., 1996), trace element filtering by amphibole in the mantle wedge (Foley et al., 2000), mantle-magma interaction (Kelemen et al., 1990), or multiple melt-depletion events (Woodhead et al., 1993).

A plethora of studies have been conducted on subduction zone and arc magmatism that can be summarized as showing that the mantle wedge beneath arcs can be divided into three domains (Fig. 1.1): The cool region of the fore-arc mantle is strongly metasomatized by hydrous fluids to form serpentinite, as evident from geophysical studies and the abundance of serpentinite in seamounts (Bostock et al., 2002; Brocher et al., 2003; Fryer et al., 1985; Hyndman and Peacock, 2003) (“A”, Fig. 1.1). The deeper, hotter part of the fore-arc mantle contains phlogopite-bearing pyroxenites, formed by infiltration and reaction of sediment-derived hydrous melts (“B”, Fig. 1.1) that can be activated through slab-roll back (Gülmez et al., 2016). These phlogopite-bearing pyroxenites are a likely source for post-collisional lavas of exotic potassic to ultrapotassic composition which are strongly enriched in large ion lithophile elements (LILE), high field strength elements (HFSE), and rare earth elements (REE) (Avanzinelli et al., 2009; Prelević et al., 2008b; 2013; Su et al., 2017). In addition to potassic magmas from post-collisional settings, the formation of phlogopite-pyroxenites within the fore-arc mantle is reported from Mexico (Vigouroux et al., 2008) and likely a common phenomenon to subduction zones (Wyllie and Sekine, 1982), though, only visible when activity shifts from the arc into the fore-arc and potassic magmas are erupted.

Most studies have focused on the magmatic arc ("[C](#)", [Fig. 1.1](#)), where models suggest magmas are formed either by volatile- and sediment melt-fluxed melting of peridotite (Bulatov et al., 2014; Mallik et al., 2015; 2016; Mitchell and Grove, 2015; Rapp and Watson, 1995; Woodland et al., 2018) or *mélange* melting (Bebout and Barton, 2002; Cruz-Urbe et al., 2018; Marschall and Schumacher, 2012). While high-pressure studies (Cruz-Urbe et al., 2018) reproduce the low HFSE contents of arc magmas by producing an HFSE-enriched residue, the experimental designs have not considered the modification of subducted components during fore-arc metamorphism and metasomatism that occurs before the sediment component reaches the sub-arc zone. Eclogites, depleted in LILE, HFSE, and LREE, are reported (John et al., 2004), but as yet are interpreted as residuals to fluid-metasomatism beneath the volcanic arc. However, the occurrence of trace element-enriched ultrapotassic magmas (Gülmez et al., 2016; Vigouroux et al., 2008) sourced from metasomatized fore-arc mantle strongly suggests that subducted sedimentary components experience element depletion before they reach the common depths of arc magma sources (100–120 km). Therefore, the sediment-derived components of arc magmas are supplied by the residues of partial melting and not the unmodified sediments as commonly assumed. This focusses attention on a gap in earlier research, namely experiments on the interaction between sedimentary rocks and peridotite in the fore-arc of subduction zones ("[B](#)", [Fig. 1.1](#)) where pressures <3 GPa and temperatures <1000 °C prevail. Depending on the rate of subduction and the age of the subducting crust, slab-surface temperatures reach 700–900 °C in the fore-arc (Syracuse et al., 2010), and therefore, subducted sedimentary components may partially devolatilize and melt to infiltrate and metasomatize the lithospheric mantle in the fore-arc. Element fractionation during these fore-arc processes will change the fundamental geochemical character of the sediment component that proceeds to depths where arc magmas are generated.

In this study, we simulate metasomatism in the fore-arc by reacting clastic sediments from the Mediterranean Sea from the International Ocean Discovery Project (IODP) site ODP 161-976 with melt-depleted peridotite (dunite) at 2–6 GPa and 750–1100 °C ([Supplementary Table 1.1](#)). We employ newly developed LA-ICP-TOFMS element mapping to visualize and quantify the redistribution of trace elements during this reaction, which corresponds to fore-arc mantle metasomatism.



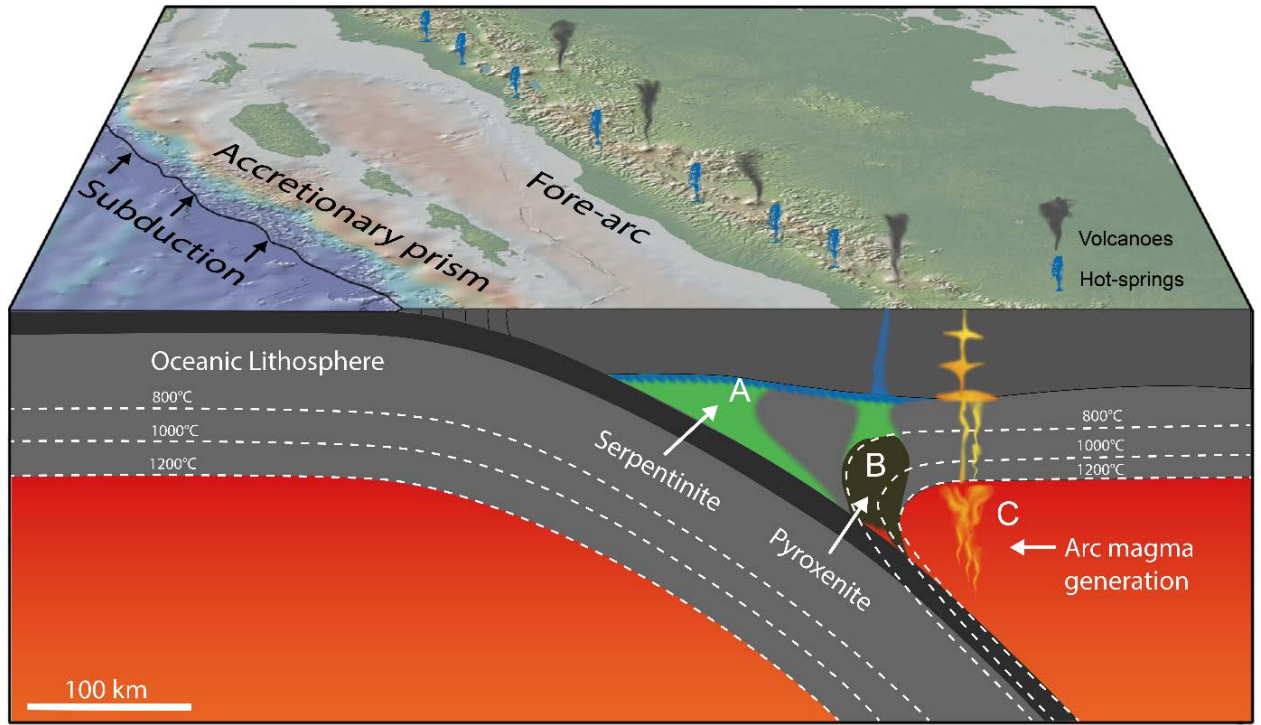


**Fig. 1.1:** Schematic image of a subduction zone and the region of fore-arc mantle metasomatism. At  $<800$  °C, the fore-arc mantle is mainly serpentinized by low density hydrous fluids (A). At  $>800$  °C, sediment-derived hydrous partial melts of dacitic-rhyolitic composition infiltrate the lithospheric fore-arc mantle to produce pyroxenite (this study; B). Arc magmas form beyond the fore-arc lithospheric mantle (grey) where hybridization of residual sedimentary rock and asthenospheric mantle occurs (C). Map modified from GeoMapApp, [www.geomapapp.org/](http://www.geomapapp.org/) with Global Multi-Resolution Topography (GMRT) (Ryan et al., 2009).

## 1.2 Materials and Methods

The experiments used a sediment from the International Ocean Discovery Project (ODP 161-976 B 18 X3 105-106.5) which is a carbonate-bearing ( $<10\%$ ) siliciclastic marine sediment (Supplementary Table 1.2). The depleted peridotite is a clinopyroxene-bearing dunite (sample ZD11-53) containing olivine ( $>97\%$ ), spinel ( $\sim 2\%$ ), and clinopyroxene ( $<1\%$ ) from the Zedang ophiolite (south Tibet, China). It occurs as a lens-shaped body within harzburgite (Supplementary Table 1.2).

Experiments were carried out using a piston cylinder apparatus at the University of Mainz at 1-3 GPa, and a belt apparatus at Goethe University Frankfurt at 4–6 GPa. Sediment and peridotite powders were placed as two separate layers in an inner carbon capsule, which controls  $f_{O_2}$  via the  $C + CO$  equilibrium and then sealed into an outer platinum capsule. For the piston cylinder experiments, the assembly of the experiments consisted of a pressure cell made of  $Al_2O_3$  spacers, a graphite furnace, B-type thermocouple, and a  $CaF_2$  spacer outside the capsule. For belt

apparatus experiments, the materials were mostly similar to piston-cylinder experiments. However, the spacer and capsule holder consisted of natural polycrystalline calcium fluoride. All cell assemblies were first pressurized and subsequently heated at a rate of 50 °C/min. Thermobaric conditions were kept constant for 2–14 days. At the end of each experiment, charges were quenched by switching off the heating. Quench times to temperatures below 500 °C were approx. 6 s for the piston-cylinder runs (Ziaja et al., 2014), and 8 s for the belt runs.

Major element contents of experimental run products were acquired using a JEOL JXA 8200 Superprobe electron-probe microanalyzer equipped with 5 wavelength dispersive spectrometers at the University of Mainz using the methods described in Förster et al., (2017).

Trace element analyses (Supplementary Table 1.3, 1.4) were carried out using laser ablation-inductively coupled plasma mass spectrometry (LA-ICP-MS) at the University of Mainz. An ESI NWR193 ArF Excimer laser ablation system (193 nm wavelength) equipped with a TwoVol2 ablation cell was used for the formation of a dry aerosol from the samples. Ablation was performed with a repetition rate of 10 Hz at 3 J/cm<sup>2</sup>. The sample was transferred to an Agilent 7500ce mass spectrometer by a He-Ar mixed gas flow. Synthetic glass NIST SRM 610 was used as calibration material using published values (Jochum et al., 2011) and <sup>29</sup>Si was selected as internal standard for silicates, using the SiO<sub>2</sub> data determined by electron microprobe. For quality control, synthetic NIST SRM 612 and basaltic USGS BCR-2G were measured as unknowns in each run (Supplementary Table 1.3). Results for NIST SRM 610 and USGS BCR-2G were within 10 % of the data tabulated in the GeoReM database (<http://georem.mpch-mainz.gwdg.de/>, Jochum et al., 2005). For each analysis, background signals were acquired for 20 s, followed by a dwell time of 30 s with spot sizes of 20 µm. Data processing was carried out using GLITTER 4.4.1 (Griffin, 2008).

LA-ICP-TOFMS, performed at TOFWERK AG in Thun, Switzerland, was used to map trace elements of the experiments using a spot size of 5 µm, repetition rate of 30 Hz, and a laser fluence of 3 J/cm<sup>2</sup> (193 nm Excimer laser). Each pixel represents the signal from a single laser shot (Bussweiler et al., 2017). The count rates for each element measured by LA-ICP-TOFMS were used to compare element abundances in the reaction zone to the metapelite and dunite. For each element, the count rates were averaged from an equal sized area (10,000 µm<sup>2</sup>) within the reaction zone and the dunite (Supplementary Fig. 1.1).

## 1.3 Results

### 1.3.1 Textural observations

The experiments produced a reaction zone between the sediment and depleted peridotite with thicknesses of 30–1000  $\mu\text{m}$  (Supplementary Fig. 1.2), which increased with temperature and experiment duration. Phases present within the reaction zone include phlogopite, clinopyroxene, orthopyroxene, and magnesite at 2–3 GPa (Supplementary Table 1.1), whereas experiments at 4–6 GPa and  $<1100^\circ\text{C}$  differed by the presence of Na-K chlorides and absence of phlogopite, while all other phases were identical. The metamorphosed sediment partially melted, leaving a residue dominated by garnet and clinopyroxene; the residue additionally contains silica-rich glass in experiments at  $\leq 4$  GPa, phengite and apatite at  $\leq 850^\circ\text{C}$ , as well as coesite at  $\leq 800^\circ\text{C}$ . Figure 1.2 A shows backscattered electron images and WDX maps of the reaction zone of a representative experiment (3 GPa/ $850^\circ\text{C}$ ). Generally, the reaction leads to enrichment of K, Ca, Al, and Si within the depleted peridotite in all experiments and the formation of three layers that are sandwiched between the two starting materials (Fig. 1.2 A): (1) Orthopyroxenite: thickness 50–500  $\mu\text{m}$  and in contact with the depleted peridotite; (2a) Phlogopite-clinopyroxenite (in experiments at  $\leq 3$  GPa): forming a symplectite and measuring 50–200  $\mu\text{m}$  thickness; (2b) Pyroxenite (in experiments at  $>3$  GPa): forming a symplectite of clinopyroxene and orthopyroxene, measuring  $\sim 100$   $\mu\text{m}$  thickness; (3) Clinopyroxenite: thickness  $\sim 100$   $\mu\text{m}$  and in contact with the residual melt-depleted sediment. The orthopyroxenite zone is seen most clearly in the Mg map, in which orange orthopyroxene contrasts with the red of dunitic olivine. Almost all K is concentrated in phlogopite of zone 2, whereas the clinopyroxene of zone 3 is seen in the orange in the Si map and blue in the Al map, contrasting with the high Al of the adjacent former sediment layer.

Element mapping by laser ablation inductively coupled plasma time-of-flight mass spectrometry (LA-ICP-TOFMS) reveals selective incorporation of minor and trace elements in the reaction zone (Fig. 1.2 B): sulphur is enriched in the reaction zone, where it combines with Ni and Fe from olivine of the dunite to form Fe-Ni-sulphides. The former contact between sediment and dunite is clearly seen in the strong decrease in Ni and the composite image (Fig. 1.2 B). Elements of the LILE and HFSE groups are strongly incorporated into and trapped in the reaction zone, exemplified by Rb, Cs, Th, and Zr, whereas the Ce and Lu maps indicate strong fractionation of the REE.



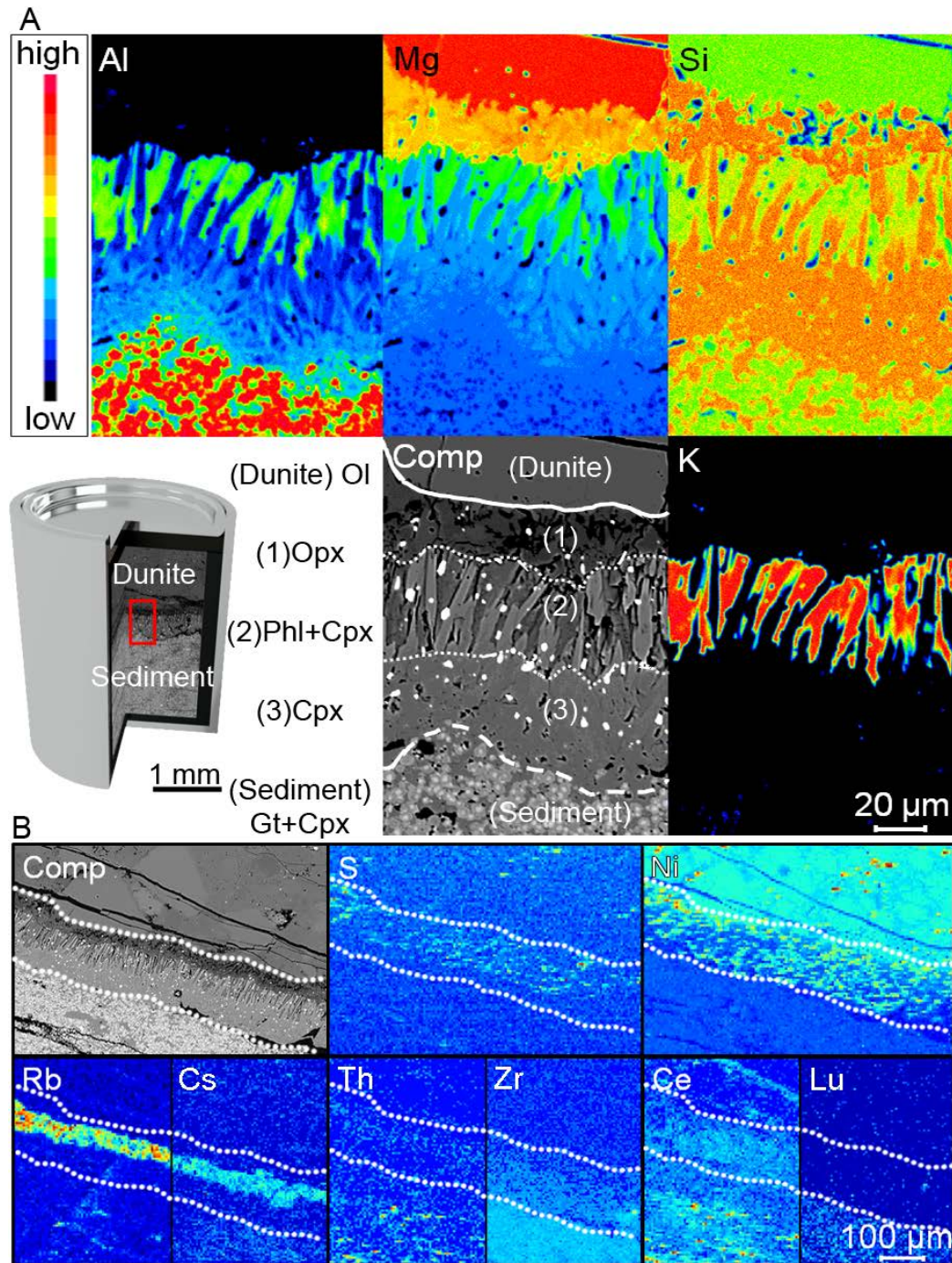


**Fig. 1.2:** EPMA WDX- and LA-ICP-TOFMS maps of an experiment at 3 GPa/850 °C. (A) Backscattered electron image (Comp) and qualitative WDX maps showing the distribution of Al, Mg, Si, and K in the reaction zone between dunite and partially melted sediment. Al is highest in garnet grains of the residual sediment (red in Al map) and in phlogopite grains in the reaction zone (green), while clinopyroxene grains show a gradual increase in Al towards the residual sediment (blue gradient in Al map). Mg shows a gradual decrease away from the dunite and is higher in phlogopite than in adjacent diopside. Si is high in clinopyroxene and orthopyroxene (orange in Si map). K is strongly enriched in phlogopite (red in K map), where it forms a symplectite with diopside (dark blue in Al map). (B) Trace element maps recorded by LA-ICP-TOFMS show the distribution of S, Ni, Rb, Cs, Th, Zr, Ce, and Lu in relation to the mineralogy shown in the backscattered electron (Comp) image. Rb, Cs and S are enriched in the reaction zone in phlogopite and sulphides. The sulphides also host Ni, explaining its heterogeneous occurrence inside the reaction zone. Th, Zr, and Ce are present within the reaction zone, while Lu is confined to the residual sediment.

### 1.3.2 Phase compositions

In all experiments the original sedimentary section now contains Na-Al-rich clinopyroxene (2–4 wt% Na<sub>2</sub>O, 7–14 wt% Al<sub>2</sub>O<sub>3</sub>) and Ca-rich garnet (12–16 wt% CaO). Garnet is chemically zoned (Mg, Fe, and Ca), with increasing Mg from core to rim, while Ca and Fe decrease (Fig. 1.2 A). The sediment layer in experiments at ≤3 GPa also contains 10–40 % hydrous silicate glass with 4–6 wt% K<sub>2</sub>O and 55–75 wt% SiO<sub>2</sub>. The reaction zone layers 1–3 are generally enriched in K, Ca, Al, Si, CO<sub>2</sub> and H<sub>2</sub>O. Clinopyroxene shows a chemical zonation across the reaction zone whereby the Na-Al-component is highest at the contact with the partially melted sediment and gradually decreases from 10 to 3 wt% Al<sub>2</sub>O<sub>3</sub> and 3 to 1 wt% Na<sub>2</sub>O across layer 3 to 2 (Fig. 1.2 A). Orthopyroxene is the major phase in layer 1, occurring as veins within the dunite, and contains low amounts of Al<sub>2</sub>O<sub>3</sub> (0.5–1 wt%).

Trace element count rates from LA-ICP-TOFMS of the reaction zone were normalized to count rates in the dunite (Fig. 1.3 A) to give an estimate of element partition coefficients (D). These coefficients are indicative of the element transfer during metasomatism as they compare the element composition of the metasomatic layers to the unreacted dunite. The metasome in the 3 GPa/850 °C experiment shows that trace elements are enriched in a descending order from LILE (6–20 times), HFSE (2–9 times), light REE (2–6 times), and heavy REE (<3 times) (Fig 3a). The composition of the sediment, the melt in the reaction zone, and the residue are shown relative to N-MORB and compared to the composition of Mediterranean lamproites and arc-magmas in Fig. 1.3 B. The composition of the melt which infiltrated the dunite to form the metasome was calculated using the fractional melting equation (Shaw, 1970) for a 10 % melt, using the element coefficients between reaction zone and dunite derived above (Fig. 1.3 A).

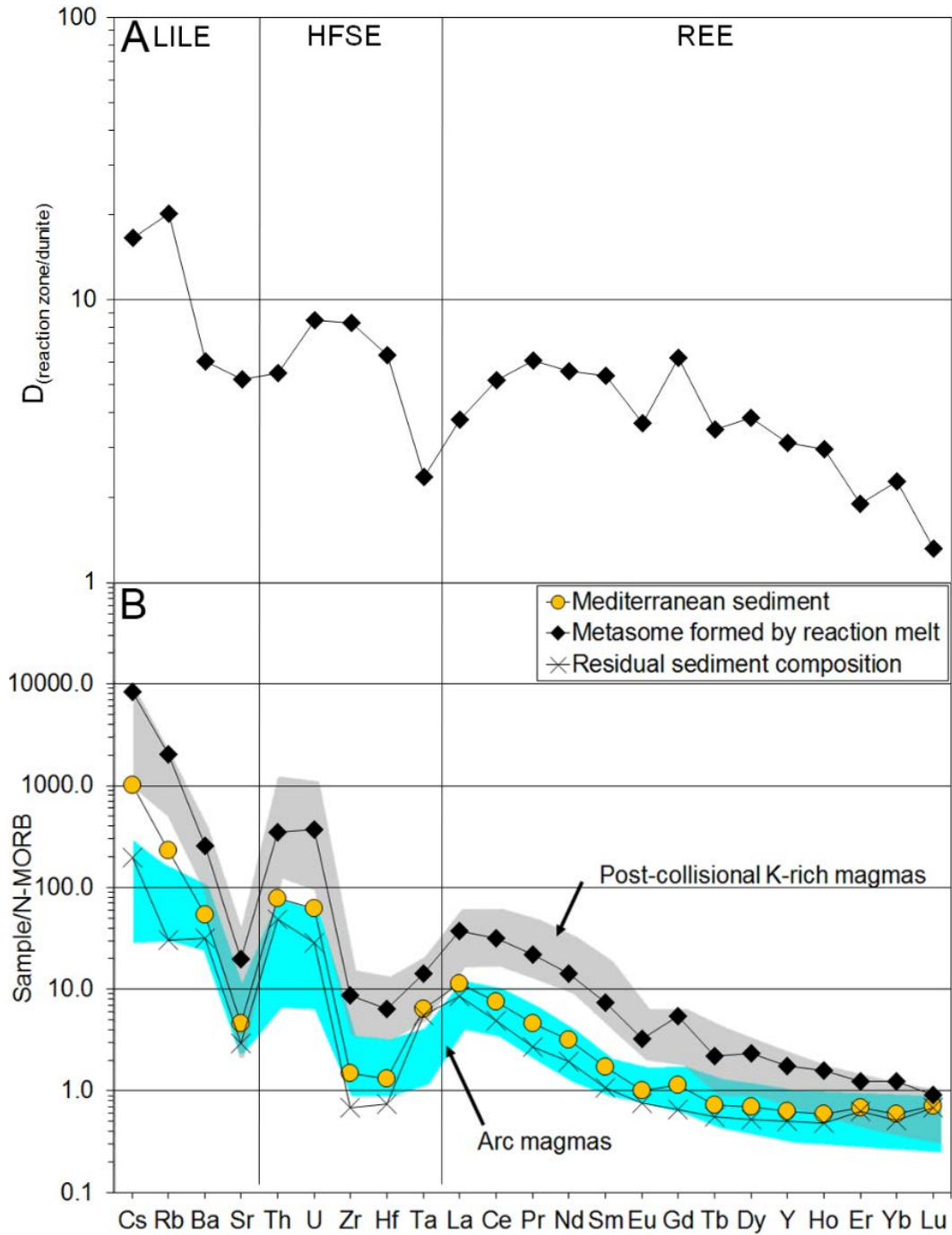


**Fig. 1.3:** Element fractionation within the reaction zone. (A) Element distribution plot, showing element partition coefficients ( $D$ ) calculated from LA-ICP-TOFMS raw counts in the reaction zone normalized to the depleted peridotite (dunite). Trace elements are heterogeneously distributed: LILE are strongly enriched (6–20x), followed by HFSE (2–9x), and LREE (2–6x), while HREE show no significant enrichment (1–3x). (B) N-MORB normalized trace element contents (Sun and McDonough, 1989) of ODP sediment and the calculated metasome composition compared to post-collisional K-rich magmas (Prelević et al., 2008b; 2013). The element partition coefficients from (A) were used with the fractional melting equation<sup>31</sup> to calculate the trace element mass fraction within the metasome. A 10 % fractional melt from the sediment-dunite reaction successfully explains the trace elements in the source of post-collisional K-rich magmas, while the residue of this reaction plots within the compositional range of arc magmas (Luhr and Carmichael, 1985; Pearce and Peate, 1995).

## 1.4 Discussion

Although the fore-arc mantle is widely interpreted to be hydrated from geophysical measurements (Bostock et al., 2002; Brocher et al., 2003; Hyndman and Peacock, 2003), it remains unclear to what degree its major and trace element composition is modified by infiltrating hydrous partial melts derived from sediments. We propose that these partial melts rise from the slab surface and metasomatize the lithospheric fore-arc mantle within domain B of Figure 1, based on the following observations: (1) the eruption of trace-element enriched ultrapotassic lavas that form during slab-rollback and fore-arc mantle melting (Gülmez et al., 2016; Vigouroux et al., 2008); (2) the strong HFSE-depletion of arc magmas (Foley et al., 2000; Kelemen et al., 1990; Stolz et al., 1996) that suggest sediments either retain HFSE during the formation of arc magmas or that redistribution of HFSE to the fore-arc mantle occurs before the sediment component proceeds to the depths of arc magma sources; (3) the presence of an extensive magnetotelluric low resistivity zone stretching from mantle to shallow crustal depths 30–80 km in front of the volcanic arc (McGary et al., 2014; Pommier and Evans, 2017; Worzewski et al., 2011) that coincides with hot springs on the surface that discharge Cl- and CO<sub>2</sub>-bearing fluids (Kawamoto et al., 2013).

### 1.4.1 Progressive replacement of peridotites by phlogopite-pyroxenites in the fore-arc mantle

The reaction of hydrous partial melts derived from sediments with dunite leads to the formation of a metasomatically enriched zone that consumes dunite. This is illustrated by orthopyroxene which formed from the dunite and is preserved as relict in the clinopyroxene in layer 3 (Supplementary Fig. 1.3), which originate from the former dunite layer. Over the whole range of experiments from 2–6 GPa, the reaction zone always contains pyroxene, while phlogopite is absent at  $P > 4$  GPa and replaced by Na-K chlorides. The growth of phlogopite pyroxenites at 2–3 GPa/800–1000 °C is in accordance with previous studies (Massonne, 1992).

LA-ICP-TOFMS mapping shows that trace elements are heterogeneously redistributed throughout the reaction zone. LILE, HFSE, and light REE are enriched in the reaction zone (layers 1–3) and controlled by the growth of phlogopite, clinopyroxene, and accessory apatite as well as sulphides (Fig. 1.2). The reaction zone remains devoid of heavy REE because they are retained in garnet in the residue of the partially melted sediment. Since the element distribution between reaction zone and dunite is controlled by mineral growth, the coefficients represent the metasomatic enrichment of depleted peridotite by hydrous partial melts derived from the sedimentary layer (Fig. 1.3 A).



Assuming subducted sedimentary material is involved in creating the trace element patterns in ultrapotassic magmas, the mechanism of their formation must enrich LILE, HFSE, and LREE more than HREE to satisfy the observed trace element patterns. Using the fractional melting equation (Shaw, 1970), and a melt fraction of 10 %, the observed patterns of LILE, HFSE, and light REE in the migrating melts in the experiments are identical to those of ultrapotassic magmas in post-collisional settings (Peccherillo and Martinotti, 2006; Prelević et al., 2008b) (Fig. 1.3 B). The residue of this reaction is depleted in decreasing order from LILE to heavy REE compared to the sedimentary starting material. The incorporation of this residue into the arc magma source at deeper levels successfully explains the characteristic depleted HFSE and REE <1 (Sm-Lu) (Lühr and Carmichael, 1985; Pearce and Peate, 1995) signature ascribed to subducted sediments in arc magmas (Fig. 1.3 B).

#### 1.4.2 Rates of metasomatism

The thickness of the reaction zone in the experiments was found to increase with temperature and experiment duration. Calculated growth rates exhibit an exponential dependency on temperature ( $R^2 = 0.91$ ) (Fig. 1.4). Infiltration of ultramafic potassic melt (Förster et al., 2017; 2018) exhibits a similar exponential dependency on temperature ( $R^2 = 0.66$ ) and is in accordance with experiments that examined percolation of basaltic melts within peridotite (Connolly et al., 2009; Watson, 1982). Both styles of metasomatism, i.e. by hydrous silicic partial melts derived from sediments, and by ultramafic potassic melts, follow a similar trend with temperature ( $R^2 = 0.91$ ). The extrapolation of reaction zone growth rates translates to rates of metasomatism that cover a range of 3–500 m/ky for temperatures of 750–1450 °C (Fig. 1.4). For a cool fore-arc environment, metasome growth rates are <5 m/ky for temperatures <900 °C to <1 m/ky for temperatures <700 °C. These growth rates are about one order of magnitude below the rate of subduction which varies between 10–100 m/ky. Therefore, replenishment of the sediment seems to be faster than the consumption of the hydrous partial melts by reaction and metasomatism. However, if melt extraction and supply to the fore-arc mantle is channelized, percolation rates (Aharonov et al., 1995) could increase significantly and likely be similar to extraction of silica-rich melt within migmatites (Sawyer, 1991) that reaches rates of up to ~20 m/ka. Hence, the percolation rate estimated for silica-rich melt in channelized melt flow equals the supply by subduction and can be taken as a maximum for melt infiltration within the fore-arc mantle. Assuming that no subduction erosion of this metasome happens, it may reach a thickness of >1 km within <1 million years.



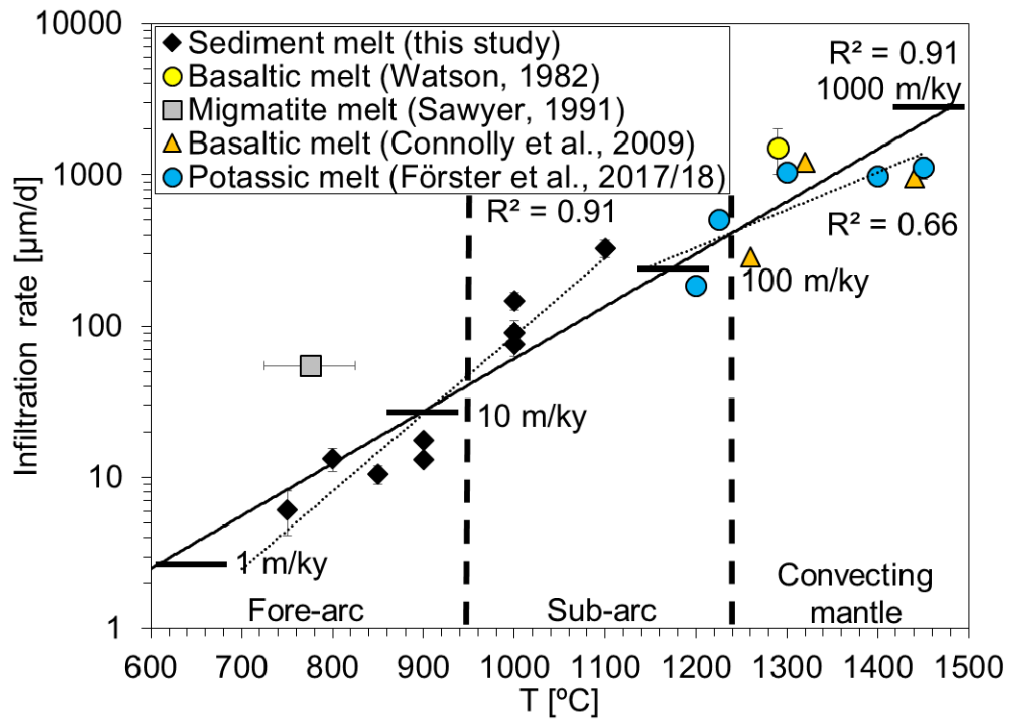


**Fig. 1.4:** Rates of metasomatism. Thickness of metasome growth (black diamonds, this study) and distance of melt infiltration (blue circles: Förster et al., 2017; 2018) in other reaction experiments correlates exponentially with temperature. Rates of metasomatism are about 10–300  $\mu\text{m/d}$  which translates to 3–100 m/ky. At fore-arc temperatures (<950 °C), typical rates of infiltration of reacting siliceous melt are 3–5 m/ky, which is an order of magnitude lower than values for melt extraction in migmatites during regional metamorphism (grey square: Sawyer, 1991). Infiltrating potassic melt lies about 1–2 magnitudes higher and reaches 200–500 m/ky, in accordance with values determined for basaltic melts (orange triangles: Connolly et al., 2009; yellow circle: Watson, 1982).

## 1.5 Conclusions

Our results provide the first direct experimental evidence of metasome growth within the fore-arc mantle (Fig. 1.1) and reveal the following key insights into subduction-related mantle metasomatism: (1) The low solidus of hydrous clastic sediments (~675 °C) (Hermann et al., 2006; Spandler et al., 2007) compared to depleted peridotites and hydrous partial melts derived from them, will lead to infiltration in the fore-arc mantle wedge long before the hydrous solidus of peridotite is reached in the source regions of arc magmas. The large difference in solidus temperatures leads to reaction and crystallization as well as trapping of infiltrating melt, while low amounts of sediment-derived melt may be retained in the eclogite-like residue. (2) All experiments comprised a layered reaction zone where the redistribution of major and trace elements was controlled by mineral growth, which effectively separates distinct sets of elements according to the mineral compositions. Trace element enrichment was highest for LILE, followed

by HFSE, and light REE, while the reaction zone was devoid of HREE. (3) Whereas the dunite was heavily metasomatized by infiltrating and reacting hydrous partial melts, the residual sediment was transformed to eclogite-like mineralogy, comprising mainly garnet and clinopyroxene. (4) Calculation of the metasome composition shows that a 10 % fractional melt of the sediment successfully explains the sediment-signature within the source for post-collisional K-enriched magmas, while the depleted residue from this reaction corresponds to the geochemical characteristics of the sediment component in arc magmas. The general depletion in HFSE of arc magmas results from loss of these elements to the fore-arc metasome, since these elements are also enriched into the reaction zone (Fig. 1.2 B). Thus, the sediment component in arc magmas is delivered by the residue following partial melting of sedimentary rocks, rather than bulk subducted sediment. (5) For a temperature range of 700–900 °C, fore-arc metasomatism rates are in the order of 1–5 m/ky, which is 1–2 orders of magnitude lower than rates of subduction. After <1 million years of subduction, the metasome may grow to an aggregated thickness of >1 km.

### **Author contributions**

MF performed all experiments and processed and interpreted the data. MF wrote the manuscript. YB performed the LA-ICP-TOFMS measurements. SB and RMK assisted in analysis and evaluation of the datasets. SF, ND, and DP supervised the work, helped in data interpretation and manuscript evaluation. MF handles the correspondence of the submitted manuscript version of this chapter.

### **Acknowledgments**

This work is part of the PhD thesis of MF, supported by an Australian Government International Postgraduate Research Scholarship (IPRS) and Macquarie Postgraduate Research Fund (PGRF). The International Ocean Discovery Project (IODP) supported this study in providing the Mediterranean marine sediment. YB gratefully acknowledges support through a Marie Skłodowska-Curie Fellowship (Project ID 746518). Thomas Kautz of the Goethe University, Frankfurt assisted with the belt apparatus experiments.

## Chapter 2:

# Melting of Sediments in the Deep Mantle Produce Saline Fluid Inclusions in Diamonds

Michael W. Förster<sup>1</sup>, Stephen F. Foley<sup>1</sup>, Horst R. Marschall<sup>2</sup>, Olivier Alard<sup>1,3</sup>, Stephan Buhre<sup>4</sup>

<sup>1</sup>ARC Centre of Excellence of Core to Crust Fluid Systems and Department of Earth and Planetary Sciences, Macquarie University, NSW 2109, Sydney, Australia

<sup>2</sup> Institute for Geosciences, Goethe University, 60438 Frankfurt am Main, Germany

<sup>3</sup>Géosciences Montpellier, UMR 5243, CNRS & Université Montpellier, 34095 Montpellier, France.

<sup>4</sup>Institute for Geosciences, Johannes Gutenberg University, 55099 Mainz, Germany

This chapter is in review as an article for Science Advances.

### Abstract

Diamonds growing in the Earth's mantle often trap inclusions of fluids that are highly saline in composition. These fluids are thought to emerge from deep in subduction zones and may also be involved in the generation of some of the kimberlite magmas that transport diamonds to the surface. However, the source of these fluids and the mechanism of their transport into the mantle lithosphere are unresolved. Here, we present experimental results showing that alkali chlorides are stable phases in the mantle lithosphere below 110 km along cold, continental thermal gradients. These alkali chlorides are formed by the reaction of subducted marine sediments with peridotite and show identical K/Na ratios to fluid inclusions in diamond. At temperatures >1100 °C and low pressures the chlorides are unstable: here, potassium is accommodated in mica, while chlorine is distributed between mica, melt, and a fluid-phase. The reaction of subducted sediments with peridotite explains the occurrence of magnesite and the highly saline fluids found in diamonds and in chlorine-enriched kimberlite magmas. This process leads to phlogopite formation at around 3 GPa, corresponding to depths of the mid-lithospheric seismic discontinuity.

## 2.1 Introduction

The lithospheric mantle beneath the cratons (Griffin et al., 2008) contains a complex record of geochemical depletion by ancient melting events that are overprinted by later re-fertilization by infiltrating liquids (Foley and Fischer, 2017; Weiss et al., 2015). Fast-growing fibrous diamonds, and less often gem-quality diamonds (Jablon and Navon, 2016), trap and preserve fluids that are present during their formation, providing insights into the chemical environment of diamond formation (Eldridge et al., 1991; Pal'Yanov et al., 1999). The encapsulated fluids may be highly saline, with K/Na ratios (by mass) of 0.5–9, siliceous, or low- or high Mg- carbonatitic in composition (Izraeli et al., 2001; Tomlinson et al., 2006; Weiss et al., 2015). However, the source of these exotic fluids within the lithospheric mantle has remained ambiguous (Izraeli et al., 2001; Jablon and Navon, 2016; Tomlinson et al., 2006): Weiss et al. (2015) argue that the saline component in diamond micro-inclusions originates from subducted seawater in altered oceanic crust, but the mechanism of fluid transport and the fractionation of K from Na remains enigmatic.

Diamonds (Haggerty, 1999) are transported to the surface by kimberlites, which are rapidly emplaced magmas with exotic, H<sub>2</sub>O- and CO<sub>2</sub>-rich compositions and whose origin is still a matter of debate (Harris et al., 2004; Kjarsgaard et al., 2009; Mitchell, 2013; Ringwood et al., 1992). Melting experiments on peridotite with H<sub>2</sub>O and CO<sub>2</sub> can explain the carbonate component in kimberlites, but cannot reproduce the high K/Na unless the starting composition is pre-enriched in K<sub>2</sub>O (Foley et al., 2009). The most recent models explain kimberlites as hot (>1400 °C) melts of peridotite (Kopylova et al., 2013; Stamm and Schmidt, 2017), whereas other authors argue for cooler primary melts from a carbonated peridotite and Na-carbonatite-chloride compositions with low emplacement temperatures (<800 °C) (Kamenetsky et al., 2014). The models that advocate primary kimberlite magmas similar to carbonatites suggest that kimberlitic melts are similar to the high-Mg saline, carbonatitic micro-inclusions in diamonds (Kamenetsky et al., 2014; Weiss et al., 2011). However, the micro-inclusions show higher contents of alkalis, even when compared to the most alkaline kimberlite, Udachnaya-East (Kamenetsky et al., 2014) and highly saline fluids may play only a restricted role in shaping the source of kimberlites. This kimberlite is also globally prominent for its abundant chloride phases and may have been formed from an unusual chloride-rich source (Kamenetsky et al., 2014). In addition to fluid inclusions, diamonds contain mineral inclusions with compositions indicative of the rock type in which they formed (Tomlinson et al., 2006). These include olivine, chromite, orthopyroxene, clinopyroxene, and Cr-

rich garnet sourced from mantle peridotites, as well as omphacite and Ca-Mg-Fe garnet (E-type garnet), characteristic phases of eclogite, which results from basalt or gabbro being metamorphosed at high pressures (Jacob et al., 1994).

## 2.2 Materials and Methods

The sediment sample used as a starting material in experiments was acquired from the International Ocean Discovery Project (ODP 161-976 B 18 X3 105-106.5) and is a carbonate-bearing (<10 %) siliciclastic marine sediment (Supplementary Table 1.2) similar to global subducting sediment (GLOSS) composition (Plank and Langmuir, 1998), but with higher contents of carbonate. For the depleted peridotite we used a clinopyroxene-bearing dunite (sample ZD11-53) containing olivine (>97 %), spinel (~2 %), and clinopyroxene (<1 %) from the Zedang ophiolite (south Tibet, China), which occurs as a lens-shaped body within harzburgite. The dunite was chosen since it represents the most depleted endmember of peridotites that are present within the lithospheric mantle and all metasomatic phases that grow during the experiment are easy to recognize and cannot be confused with phases that are already present in less depleted peridotite. Both samples were ground to powders in an agate mortar.

Experiments were carried out using a piston cylinder apparatus at the University of Mainz at 3 GPa, and a belt apparatus at Goethe University Frankfurt at 4–6 GPa. Sediment and peridotite powders were placed as separate layers in an inner carbon capsule, which controls  $f_{\text{O}_2}$  via the C + CO equilibrium. The inner carbon capsule was sealed in an outer platinum capsule. For the piston cylinder experiments, the experimental assembly consisted of a pressure cell made of  $\text{Al}_2\text{O}_3$  spacers, a graphite furnace, B-type thermocouple, and a  $\text{CaF}_2$  spacer outside the capsule. For belt apparatus experiments, most of the materials were similar to piston-cylinder experiments, but the spacer and capsule holder consisted of natural polycrystalline calcium fluoride. All cell assemblies were first pressurized and subsequently heated at a rate of 50 °C/min. Thermobaric conditions were kept constant for 2–14 days. At the end of each experiment, charges were quenched by switching off the heating. Quench times to temperatures below 500 °C were approx. 6 s for the piston-cylinder runs, and 8 s for the belt runs.

Major element compositions of experimental run products were acquired using a JEOL JXA 8200 Superprobe electron-probe microanalyzer (EPMA) equipped with 5 wavelength dispersive spectrometers at the University of Mainz, Germany (Supplementary Tables 2.1-2.11). Micas,

silicates, and glasses were analysed with 15 kV accelerating voltage and a beam current of 12 nA. Peak counting times were 20–30 seconds for melts and silicate minerals. The beam diameter was set to 2  $\mu\text{m}$ . Element maps and semi-quantitative EDX analysis were performed using a nanoScience Instruments Phenom XL benchtop electron microscope. Three aliquots of the sediment were analyzed for H, C, and N in an automated vario EL cube elemental analyzer (Elementar, Langenselbold, Germany) using the method described in Le Huong et al. (2018). Analyses of SDO-1 (USGS reference material - shale) yielded H =  $1.57 \pm 0.14$  wt%; C =  $9.11 \pm 0.01$  wt% and N =  $0.36 \pm 0.01$  wt%, within error of the GeoReM (<http://georem.mpch-mainz.gwdg.de/>, Jochum et al., 2005) compiled values for H and C (H = 1.34 wt%; C = 9.95 wt%).

## 2.3 Results

Here we present the results of an experimental study that simulates the reaction of subducted marine sediments with mantle peridotite at pressures corresponding to the mid- to lower cratonic lithosphere. The results shed light on the origin of exotic diamond fluid compositions. We conducted two types of experiments: melting experiments on marine sediments, and reaction experiments employing a two-layer arrangement in which marine sediment and a geochemically depleted peridotite (dunite) were loaded as distinct blocks in single experimental capsules. Experiments were conducted at 3–6 GPa and 800–1100 °C, corresponding to 100–200 km depth in the mantle (Supplementary Table 2.12). This approach simulates a setting in which subducted sediments partially melt and react with mantle peridotites resulting in mantle metasomatism at cratonic depths.

Generally, subducted crustal rocks have solidus temperatures as low as 675 °C, which depend on pressure and particularly on volatile contents (Hermann and Spandler, 2007; Spandler et al., 2003). The experiments were all conducted above the sediment solidus, while the experiment at 3 GPa/800 °C is close to the solidus as indicated by the small melt fraction of ~10 %. In subduction zones, slab-surface temperatures vary strongly with age, speed, and angle of subduction (Syracuse et al., 2010). As such, the deep subduction of sediments to cratonic mantle depths is most probable in the case of an old, cold slab. Since significant element transport from subducted sediments to the mantle wedge only occurs above the solidus (Hermann and Spandler, 2007), sediment subduction to the deep mantle is feasible in a cold slab. The experiments



presented here trace this scenario, simulating the reaction of sediments that melt after rapid subduction to cratonic depths.

All reaction experiments resulted in a reaction zone situated between the two rock types (Fig. 2.1 A,B); these reaction zones contain Na-K chlorides in experiments at pressures at and above 4 GPa (Fig. 2.1 A,C,D, Supplementary Fig. 2.1, 2.2). Most of the analysed chlorides contain 5–15 wt% Na and 30–45 wt% K, with K/Na ratios between 2 and 9 (by mass; Fig. 2.2). In contrast, all experiments at 3 GPa and the higher temperature experiments at 4 GPa are devoid of chlorides. In these experiments, potassium and sodium are contained in Mg-rich mica (phlogopite) and melt (Fig. 2.1 B,E,F). The melts are silica-rich (>55 wt% SiO<sub>2</sub>), containing 0.2–0.4 wt% chlorine and exhibiting K/Na ratios of 3 to 7 (Fig. 2.2). However, melt and mica do not account for all chlorine in the starting sediment composition, just as the low abundance of Na-K chlorides of ~0.5 % does not contain all Na and K in mica- and melt-free experiments.

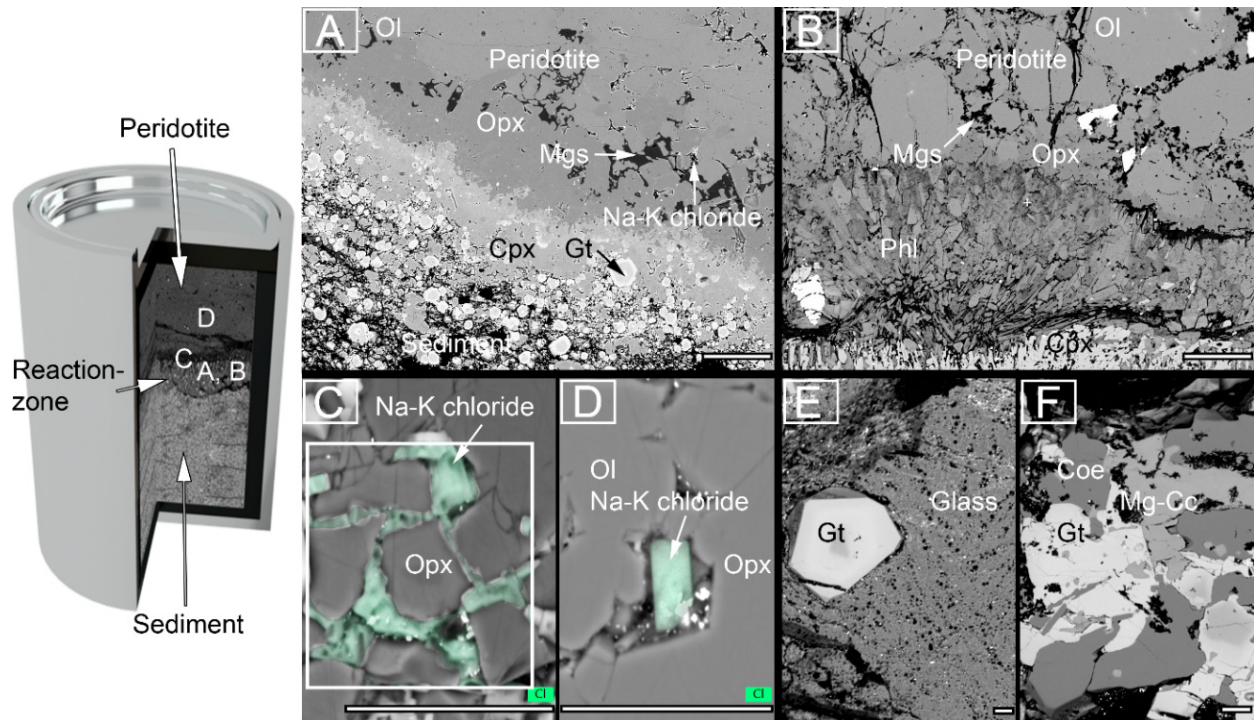


**Fig. 2.1:** Backscattered electron images of experimental charges. Locations of images A-D from sediment-peridotite reaction experiments shown in capsule on left. A, C, D: reaction experiments at 4-6 GPa and 900-1000 °C with superimposed EDX maps of chlorine (green in C, D). The sediment half of two-layer experiments recrystallized to garnet and clinopyroxene, whereas orthopyroxene, magnesite and Na-K chlorides formed at the leading edge of the reaction zone against the peridotite. B: Peridotite layer in reaction experiment at 3 GPa/900 °C contained phlogopite behind the magnesite + orthopyroxene zone, and Na-K chlorides were absent. E, F: melting experiment at 4 GPa/1000 °C showing silicate melt (E) in equilibrium with garnet, coesite, and mg-calcite shown in (F). Scale-bar in A, B = 100 μm and C, D, E, F = 20 μm.

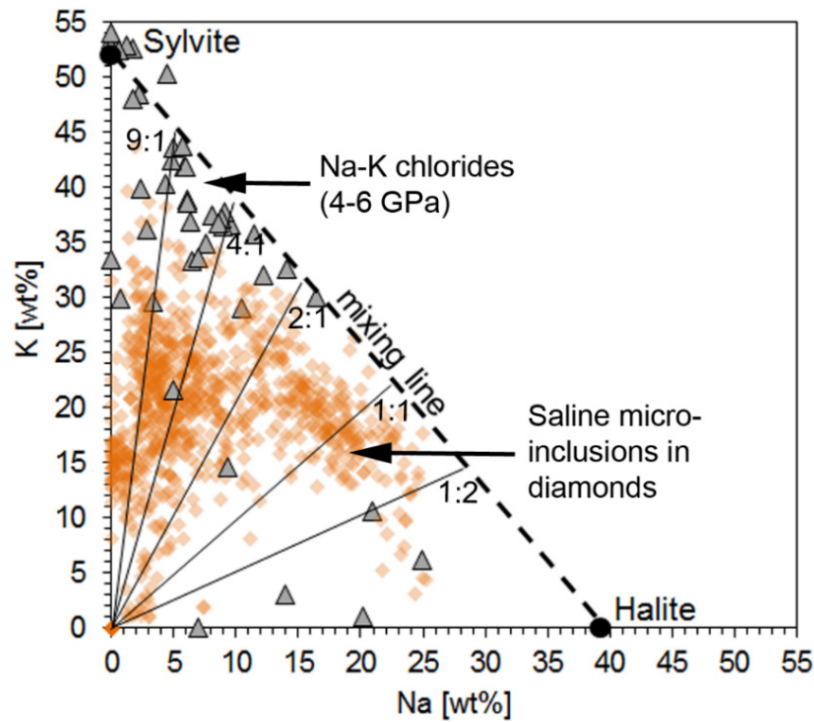


**Fig. 2.2:** K/Na ratios of experimental chlorides and saline micro-inclusions in diamonds. Most saline micro-inclusions (orange diamonds, Tomlinson et al., 2006; Weiss et al., 2015; 2018) have a K/Na ratio between 0.5 and 9, similar to the ratios found in the experimental Na-K chlorides of this study (grey diamonds). Full analyses of chlorides given in [Supplementary Tables 2.8-2.11](#).

### 2.3.1 Mass balance calculations

To determine the modal phase proportions, the bulk composition of the capsule has to correspond to the equations:

Sediment + Dunite = Mineral(s) + (Melt) +/- Fluid, for the reaction experiments, and

Sediment = Mineral(s) + Melt +/- Fluid for the melting experiment.

Here, "sediment" and "dunite" refer to the amounts that are involved in the reaction, as opposed to the amounts originally included in the capsule at the start of the experiments. Since the composition of the fluid phase cannot be determined in our experiments, it is not part of the equation. However, we can estimate the fluid composition by subtracting the modal proportions of the measured phases from the bulk composition. The mass balance calculation is iterative; the left side of the equation has to match the proportions of the phases on the right side of the equation. With increase in pressure and temperature, the sediment increasingly reacts with dunite to a maximum where 50 % sediment reacts with 50 % dunite ([Fig. 2.3](#)). The proportion of dunite involved in the reaction on the educt side of the equation is determined by the composition of the product: a high proportion of reacted dunite leads to low mass fractions of oxides such as CaO and Al<sub>2</sub>O<sub>3</sub> (which are absent in the dunite) but greatly increased MgO within the reacted



products strongly increases. The least-squares best fit of the mass balance calculation is taken to correspond to the best solution for the amount of sediment and dunite involved in the reaction. The increase of the proportion of dunite involved in the reaction, and thus addition of more MgO from the dunite to the sediment layer, leads to a high modal proportion of garnet and pyroxene at the expense of melt and mica. This is clearly seen when the sediment melting experiment is compared with the reaction experiments: without the addition of MgO from the dunite, the sediment melting experiment lacks pyroxene and shows a higher melt fraction.

The chloride-bearing experiments show the highest contents of garnet (25%) and pyroxenes (47% Opx, 17% Cpx) and are distinguished from chloride-free experiments by the absence of hydrous phases such as melt and mica. In contrast, the sediment melting experiment is devoid of chlorides and pyroxenes and contains the highest mass fraction of melt (65%). The main difference between this and the reaction experiment is its low MgO (1.5% in the melt), which inhibits the crystallization of pyroxene and therefore the melt is not consumed, but remains as the most abundant phase. The correlation of oxide species (+Cl, F) on both sides of the equation gives the coefficient of determination ( $R^2$ ). All mass balance calculations ([Supplementary Tables 2.13-2.18](#)) achieve an  $R^2$  of >0.99 and each oxide species of the balanced reaction phases resembles that of the starting condition within ~15 % deviation except for FeO, which can be lost to the metal capsule during the experiment, and Na<sub>2</sub>O, K<sub>2</sub>O, Cl, and F that are interpreted to be accommodated in a fluid phase. While the fluid probably also contains other elements, they cannot be estimated since the mass balanced compositions are within <15 % deviation from the starting composition. The calculated fluid phase for mica- and melt-bearing experiments shows an opposed trend of high Cl/F and low K/Na with increasing pressure and temperature which contrasts with chloride-bearing experiments that comprise high K/Na in the fluid phase, while Cl and F are depleted ([Fig. 2.4](#)).

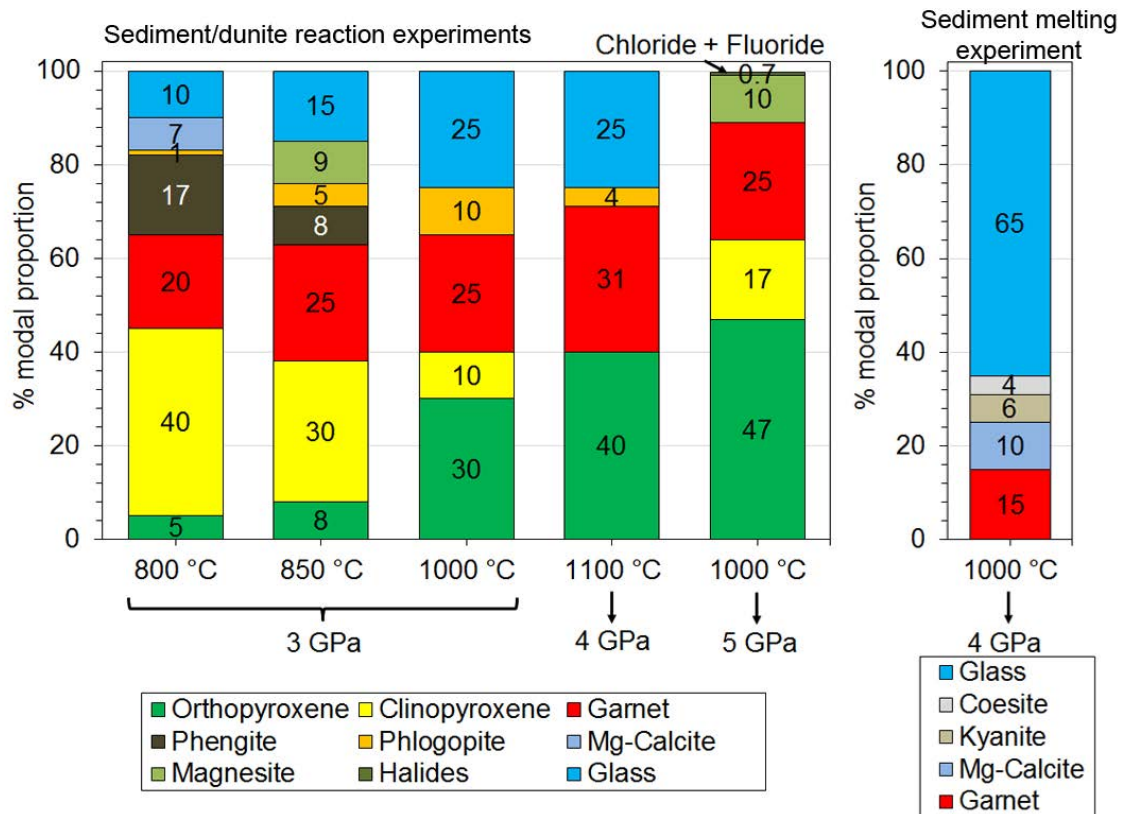


**Fig. 2.3:** Modal proportions of phases in the reaction experiments and the melting experiment. From 3-5 GPa and 800-1100°C, the sedimentary rock reacts with an increasing amount of peridotite (3 GPa: 800°C – 15 %, 850°C – 25 %, 1000°C – 30 %; 4 GPa/1100°C – 40 %; 5 GPa/1000°C – 50 %) which leads to an increase in modal pyroxene and garnet in place of mica and melt. The sediment melting experiment contains the highest melt fraction and is devoid of phases such as pyroxenes that are characteristic for the reaction experiments. Unlike the reaction experiments it did not contain peridotite and therefore remains depleted in MgO, inhibiting pyroxene crystallization.

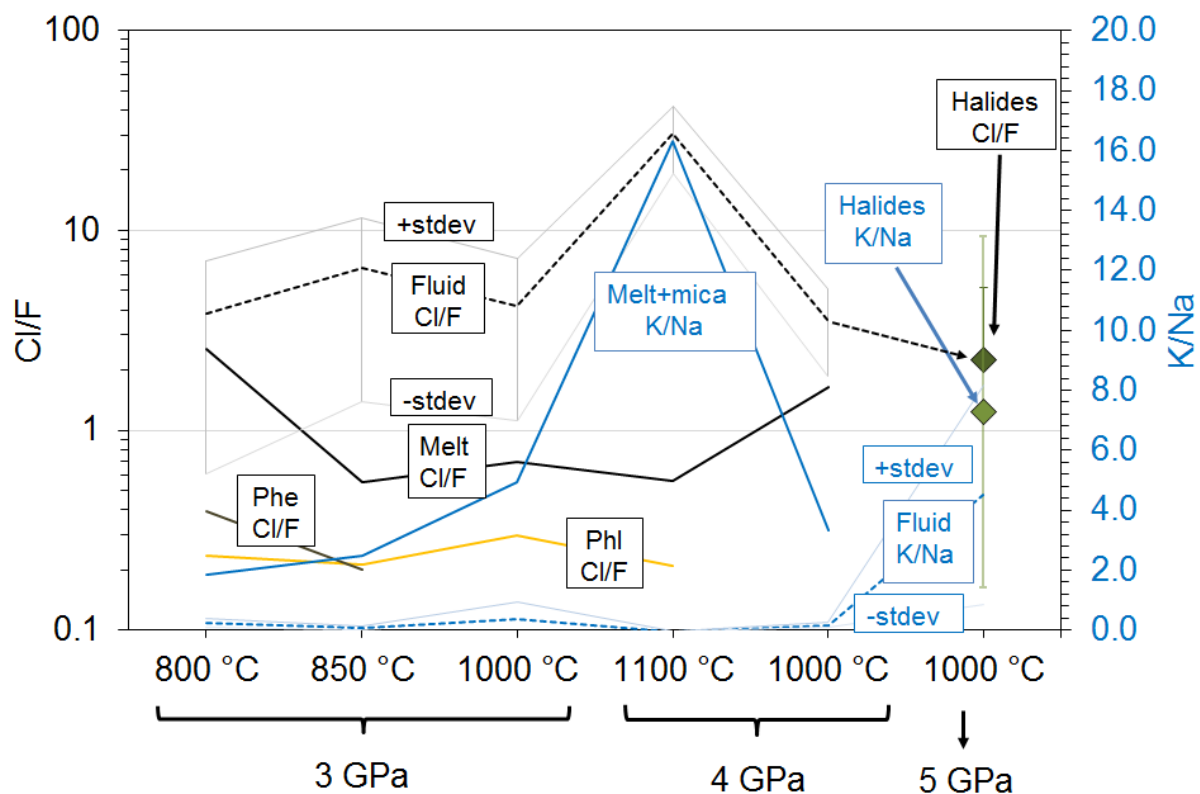


**Fig. 2.4:** K/Na and Cl/F in mica, melt, fluid, and solid halide phases (chlorides + fluorides). The ratio of Cl/F in mica and melt decreases with increasing pressure and temperature, while K/Na increases. In contrast, the fluid shows high Cl/F and low K/Na in the presence of melt and mica, while fluids in chloride-bearing experiments are depleted in halogens and show high K/Na.

Light-element analysis of the sedimentary starting material shows C, H, and N mass fractions of  $8.18 \pm 0.10$ ,  $1.83 \pm 0.15$ , and  $0.35 \pm 0.01$  wt%, respectively, which are sourced from carbonate, clay minerals, and organic material. The loss on ignition of 15.3 wt% gives an oxygen mass fraction of  $\sim 6.9$  wt% by subtracting carbon, hydrogen, and nitrogen and addition of oxygen from  $\text{SO}_3$  and  $\text{Fe}_2\text{O}_3$  reduction. The breakdown of carbonate, clay, and organic material would thus produce a mixed  $\text{H}_2\text{O} \pm \text{H}_2 \pm \text{CO}_2 \pm \text{CO} \pm \text{CH}_4$  fluid, the speciation of which depends strongly on pressure, temperature, and oxygen fugacity. Given the carbon saturation, the decomposition of the sediment follows the reaction:  $\text{CH}_4 + \text{H}_2\text{O} = 3 \text{H}_2 + \text{CO}$  (Chiodini and Marini, 1998). Since equilibrium constants are undetermined for the experimental pressure range, the measured mass fractions of 8.2 wt% C, 1.8 wt% H, and 6.9 wt% O will fall within a range for each species at the beginning of the reaction: 4.0-5.3 wt%  $\text{CH}_4$ , 9.7-12.0 wt% CO, 0-1.5 wt%  $\text{H}_2\text{O}$ , 0-0.5 wt%  $\text{H}_2$ . Due to the graphite inner capsule, which provides excess C, the C-species change during the experiments. The graphite inner capsule also buffers the oxygen fugacity at C-CO and the equilibrium  $2 \text{CO} = \text{C} + \text{CO}_2$  leads to  $\text{CO}_2$  formation at all relevant thermobaric conditions (Jakobsson and Oskarsson, 1994). At  $T < 1000$  °C,  $\text{CO}_2$  reacts with olivine to form magnesite and

orthopyroxene:  $\text{Mg}_2\text{SiO}_4 + \text{CO}_2 = \text{MgCO}_3 + \text{MgSiO}_3$ , which is in accordance with the presence of <7 wt% magnesite (Fig. 2.2).

Besides magnesite, the reaction zone in all experiments at <1100 °C is also enriched in clinopyroxene (Fig. 2.1 A,B). These clinopyroxenes exhibit a gradual change in composition from high Na<sub>2</sub>O (~5 wt%) and Al<sub>2</sub>O<sub>3</sub> (~10 wt%) in the former sedimentary rock to low Na<sub>2</sub>O (~0.6 wt%) and Al<sub>2</sub>O<sub>3</sub> (~3 wt%) in the peridotite (Fig. 2.5 A). Micas also fall into two groups based on their Al and Ti contents: those from experiments at 1000 to 1100 °C contain 13–16 wt% Al<sub>2</sub>O<sub>3</sub>, 1–2 wt% TiO<sub>2</sub>, whereas in experiments at lower temperatures they contain lower Al<sub>2</sub>O<sub>3</sub> (8–13 wt%) and TiO<sub>2</sub> (0.5–1 wt%) (Fig. 2.5 B).

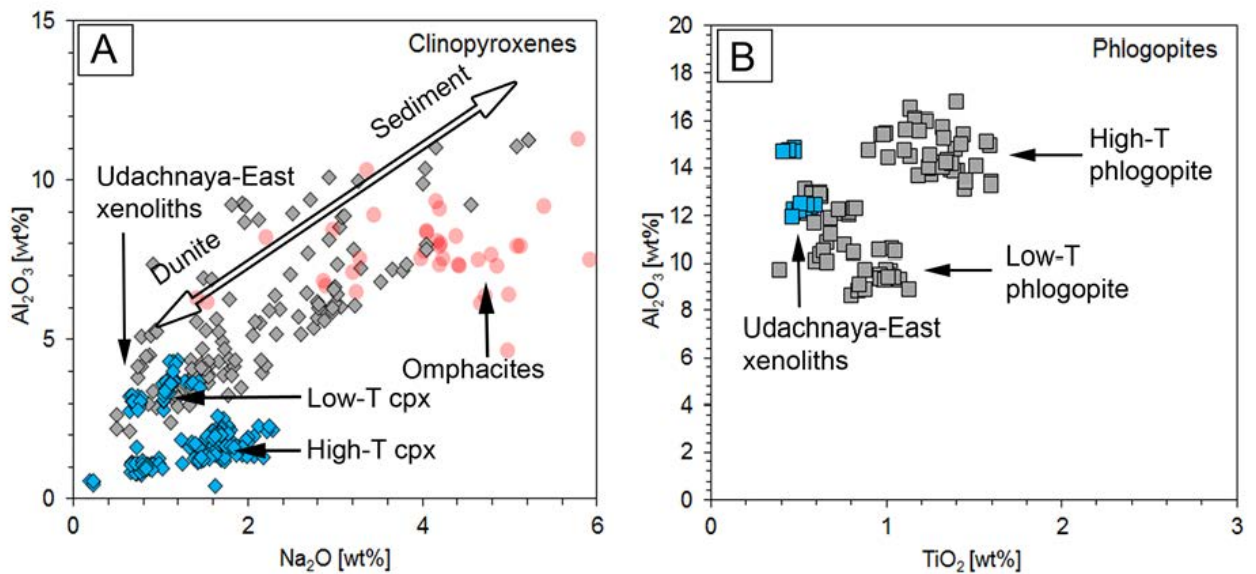


**Fig. 2.5:** Composition of silicate phases in reaction experiments. A) Clinopyroxenes from experiments at 3–6 GPa (grey diamonds) show a gradual decrease in Na<sub>2</sub>O (5 to 0.2 wt%) and Al<sub>2</sub>O<sub>3</sub> (12 to 2 wt%) across the reaction zone towards the peridotite layer. Mantle xenoliths from the Udachnaya-East pipe contain two types of clinopyroxenes, an Al-rich (low-T) metasomatic and an Al-poor (high-T) peridotite suite (blue diamonds, Ionov et al., 2010). Omphacite inclusions in diamonds (red circles, Weiss et al., 2015) are similar to the Na-Al-rich clinopyroxene in the experiments. B) Phlogopites from experiments at 3–4 GPa (grey squares) form a low-temperature group (800–900 °C) with low Ti and Al, and a high-temperature group (1000–1100 °C) with high Ti and Al. Udachnaya-East mantle xenoliths (blue squares, Ionov et al., 2010) contain phlogopites similar to the low-T group. Full analyses of silicates are found in [Supplementary Tables 2.1–2.10](#).

## 2.4 Discussion

If the fluids found as micro-inclusions in diamond ultimately originated from seawater in subducting sediments, then a process that very efficiently fractionates Na<sup>+</sup> from K<sup>+</sup> is required to explain their high K/Na ratios of 1–9. Weiss et al. (2015) postulated that Na<sup>+</sup> is consumed during

low-temperature alteration of seafloor basalts and that K/Na is increased further by the formation of Cl-rich phengite. Our experimental results show that the fractionation of Na<sup>+</sup> from K<sup>+</sup> can also occur at high pressures in liquids that originate from the reaction between subducted marine sediments and peridotite; this is in accordance with previous results that show a gradual increase of K/Na in fluids and melts with pressure and temperature (Hermann and Spandler, 2007). The Na-K chlorides formed only in reaction experiments at 4–6 GPa and <1100 °C, giving way to Cl-bearing mica and silicate melt at lower pressure and higher temperature (Fig. 2.6). The restriction of chlorides to the reaction experiments shows that these phases are only stable in an ultramafic, high-pressure environment, since the silica-rich melts produced by direct melting of the same sedimentary rock alone in the melting experiments were devoid of chlorides. The euhedral appearance of cubic chloride crystals is indicative of equilibrium growth from highly saline fluids rather than forming as a quench phase (Fig. 2.1 D), which would result in a mat of interlocking crystals at random angles as seen in many high-pressure experiments (Foley et al., 2009). While the capsule setup in this study does not allow for direct measurement of the fluid composition, the mass balance calculation estimates K/Na of the fluid to be  $4.5 \pm 3.6$ , which is within the average K/Na of  $7.3 \pm 5.9$  of the Na-K chlorides. The fluid has to be enriched in K since Na is sequestered in abundant, coexisting Na-rich clinopyroxene and K is absent in any other phase besides the Na-K chlorides in the reaction experiments at 4–6 GPa (Fig. 2.3). Since the Na-K chlorides only account for ~20 % of the total mass fraction of K in the experiments, a K/Na-rich fluid has to be present during the crystallization of the chlorides. It has to be emphasised that all chloride-bearing experiments are devoid of any hydrous phase. It is thus likely that the process of chloride formation is restricted to a reducing environment and a shift in fluid species which consumes H<sub>2</sub>O following the reactions:  $\text{CH}_4 + \text{H}_2\text{O} = 3 \text{H}_2 + \text{CO}$  and  $2 \text{CO} = \text{C} + \text{CO}_2$ . The reaction also produces C, since the removal of CO<sub>2</sub> shifts the equilibrium on the product side of the second equation. The co-existence of elemental C with CO<sub>2</sub> and magnesite has been previously observed in diamond inclusions (Wang et al., 1996). Thus, the sequestration of CO<sub>2</sub> in magnesite is related to the consumption of CH<sub>4</sub> + H<sub>2</sub>O until H<sub>2</sub>O is exhausted. Hence, Na-K chlorides form by precipitation from an oversaturated solution:  $\text{Na/K}^+(\text{aq}) + \text{Cl}^-(\text{aq}) = (\text{Na,K})\text{Cl}$ .

The crystallization of Na-K chlorides is induced by the reducing conditions in the inner graphite capsule and any experimental buffer material at  $f\text{O}_2$  equal to or below CCO will lead to chloride formation. In contrast, at any  $f\text{O}_2$  above CCO, H<sub>2</sub>O will not be exhausted and Na, K and

Cl stay in solution to form the known highly saline fluids. Given the low  $fO_2$  that is needed for chloride precipitation, magnesite and  $H_2$  should equilibrate:  $MgCO_3 + H_2 = Mg(OH)_2 + CO$ . However, the process of carbonate reduction is known to be kinetically slow, especially at high pressure (Martirosyan et al., 2016; Scott et al., 2004). Since the dehydration of the fluid is only observed in reaction experiments at >3 GPa, the sequence leading to chloride precipitation has to be: (1) melting of the sediment and reaction with dunite, (2) total consumption of the melt phase by anhydrous phases (garnet and pyroxene) as evident from mass balance calculations (Fig. 2.3, 2.4) that drives all  $H_2O$  into a fluid phase, and (3) dehydration of the fluid by reaction of  $H_2O$  to  $H_2$  and precipitation of chloride from a fluid saturated in K, Na and Cl. If  $fO_2$  is above CCO, Na-K chlorides will not precipitate, but instead be dissolved in highly saline hydrous fluids. The absence of hydrous crystalline phases such as mica in all chloride-bearing experiments is thought to be a direct result of the depletion of the fluid in  $H_2O$ , although depletion of Al by the increasing modal abundance of garnet at >3 GPa cannot be discounted.

The K/Na ratios of the chlorides (0.5 to 9) largely overlap with those of saline fluids included in diamonds (1 to 9; Fig. 2.2). However, the fluid micro-inclusions in diamond show lower total mass fractions of  $Na^+$  and  $K^+$  (Tomlinson et al., 2006; Weiss et al., 2015; 2018), and thus may represent diluted equivalents of the chlorides (Fig. 2.2). Silicate melts in experiments at 3 GPa attain K/Na ratios of 3 to 7, indicating that the process of Na separation and K-enrichment in the melt is equal to the processes that lead to high K/Na chlorides. All reaction experiments contain clinopyroxene, which shows an increase in Na and Al across the reaction zone from the peridotite towards the sediment (Fig. 2.5 A). We argue that the enrichment of K/Na in melts and chlorides is caused by the contemporaneous crystallization of Na-Al-rich clinopyroxene within the sediment, transforming it to a Na-enriched residuum with low K/Na ratios. Similar clinopyroxenes rich in Na and Al are found in natural mantle xenoliths that occur in kimberlites such as Udachnaya-East (Ionov et al., 2010). These sodic, aluminous clinopyroxenes are of metasomatic origin and are geochemically distinct from peridotite clinopyroxenes (Fig. 2.5 A). In the 3 GPa experiments clinopyroxene coexists with mica, which is also comparable to mica found in the metasomatic Udachnaya-East xenoliths (Ionov et al., 2010) (Fig. 2.5 B).



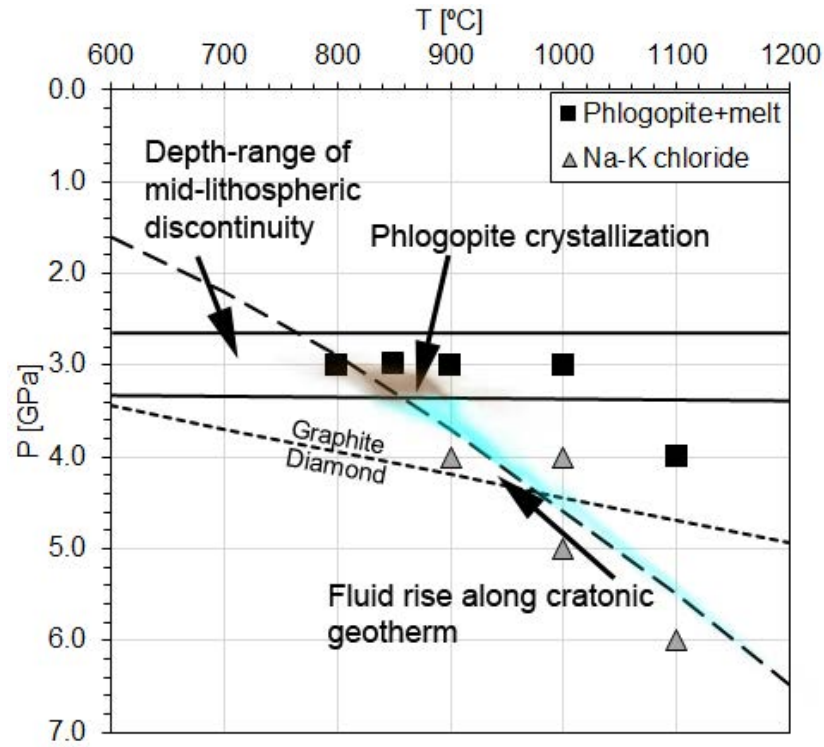


**Fig. 2.6:** Pressure-temperature stability of Na-K chlorides. Na-K chlorides are restricted to the reaction experiments at 4-6 GPa, while at 3 GPa and 4 GPa, 1100 °C, K is sequestered in phlogopite. When mobile, highly saline fluids rise to lower pressures along the cratonic geotherm, they stall and react to form phlogopite-bearing metasomes. The depth of phlogopite crystallization coincides with the mid-lithospheric discontinuity (Selway et al., 2015).

The formation of magnesite, and of chlorides with high K/Na, demonstrates that the reaction between sediment and peridotite may cause a type of mantle metasomatism vital for the formation of some diamonds. When compared to peridotite minerals, metasomatic carbonate, and chloride phases, the compositions of saline micro-inclusions in diamonds are distributed between four end-members: a Na-K chloride-enriched composition, low- and high Mg carbonatitic-, and silicic compositions (Fig. 2.7). Weiss et al. (2015) interpret this to represent mixing of highly saline fluids from the subducting slab with melts of carbonated peridotite. From our experimental observations, we argue that the carbonate is also derived from the sediment and forms by the reaction of CO<sub>2</sub>-bearing saline fluids with mantle peridotite. This process consumes CO<sub>2</sub>, which is incorporated into magnesite that grows at the expense of olivine at the reaction front (Fig. 2.1 A,B). Since magnesite is the only observed carbonate phase within the peridotite, the metasomatically overprinted mantle would preferentially produce high-Mg carbonatitic melt. In a natural setting diamonds would grow during this reaction and enclose fluids from various stages of this interaction. If “most diamonds were created equal” (Jablon and

Navon, 2016), it would follow that reaction between sedimentary rocks and peridotite during subduction is the main mechanism for the formation of diamonds and mantle carbonates.

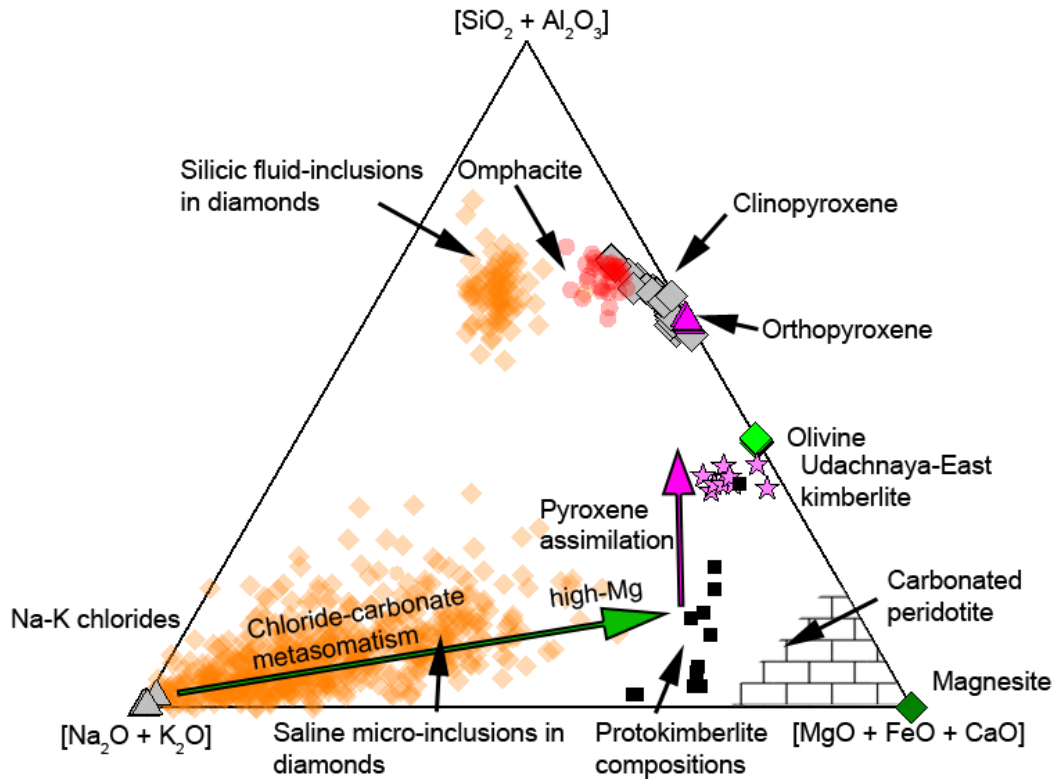


**Fig. 2.7:** Ternary diagram of experimental phases compositions compared to diamond inclusions. Composition of saline and silicic diamond micro-inclusions (orange diamonds, Tomlinson et al., 2006; Weiss et al., 2015; 2018) and omphacite mineral inclusions in diamonds (red circles, Weiss et al., 2015) compared to clinopyroxenes (light grey diamonds), orthopyroxenes (pink triangles), olivines (green diamonds), magnesite (olive diamonds), and Na-K chlorides (grey triangles) from this study. The “carbonated peridotite” field represents various mixtures of magnesite and silicates. Saline micro-inclusions are mixtures between the Na-K chloride and carbonated peridotite. The source for protokimberlitic melts of Udachnaya-East (black squares, Sharygin et al., 2015) is enriched in Na and K relative to carbonated peridotite and trends towards bulk kimberlite composition (pink stars, Russell et al., 2012) by assimilating pyroxenes, as indicated by the pink arrow.

The high mobility of saline fluids provides an effective mechanism to metasomatize the cratonic lithosphere. Na-K chlorides and carbonates are widely distributed within the reaction zone and the peridotite in the experiments, whereas the growth of mica in chloride-free experiments was restricted to the reaction zone (Fig. 2.1 B). This demonstrates that Na-K chlorides and carbonates crystallized from highly mobile fluids. Our experimental delineation of alkali chloride stability restricts this to depths greater than approximately 120 km, spreading to shallower depths where temperatures are lowest. Fluids that move far from their source are strongly depleted in all major elements except for the highly fluid-soluble alkalis and magnesium, since only magnesite and chlorides are observed within the peridotite layer (Fig. 2.1 A,C,D). This



means that the radiogenic isotope and geochemical signature of sediment probably remains sequestered in clinopyroxene in the reaction zone. Hence, if Sr and Eu are similarly retained in clinopyroxene to Ca, the fluid that progresses into the peridotite should gradually flatten positive Sr and Eu anomalies as well as evolve to lower  $^{87}\text{Sr}/^{86}\text{Sr}$  ratios (Weiss et al., 2015).

The change of metasomatic overprinting of the depleted peridotite from highly saline fluids and chlorides at  $\geq 4$  GPa to melt infiltration and mica formation below 4 GPa has further consequences for the cratonic mantle: fluids that rise to mantle levels shallower than the stability of Na-K chlorides will stall and crystallize mica, as evident from reaction experiments at 3 GPa (Fig. 2.6). The depth at which these highly saline fluids will stall is characteristic for the seismic mid-lithosphere discontinuity, a zone of low seismic velocities that is widespread in the continental lithospheric mantle, and is found intermittently beneath all continents at a depth of 80–100 km. The mid-lithosphere discontinuity has been suggested to be related to the occurrence of hydrous assemblages (Hansen et al., 2015; Selway et al., 2015), which is consistent with the formation of mica in our experiments.

Kimberlite magmas are generally considered to originate by partial melting of a carbonated peridotite source (Mitchell, 2004; Sokol et al., 2013). The occurrence of Na-rich mineral- and fluid inclusions in magmatic olivine rims in kimberlites (Giuliani et al., 2012; 2013; Mernagh et al., 2011) is consistent with the presence of primary Na-Ca carbonatite melts. The loss of sodium is thought to occur after emplacement by rapid weathering of the kimberlite matrix (Kamenetsky et al., 2012; 2014). The Udachnaya-East kimberlite is a very fresh chlorine-rich kimberlite that has been used to propose that chloride-rich carbonatite may be a common protokimberlitic composition (Kamenetsky et al., 2012; 2014). Our experimental observation of Na-K chlorides coexisting with carbonate in the reaction zone between sedimentary rock and peridotite may thus be directly relevant for the source of some kimberlites. Melting experiments on chloride-rich Udachnaya-East kimberlites (Sharygin et al., 2015) at 4.5–6.5 GPa/1000–1100 °C within the carbonated peridotite field have produced melts close to the composition of diamond micro-inclusions (Fig. 2.7). Hence, our experiments provide evidence that the reaction between sediment-derived melts and mantle peridotite at  $>120$  km can produce the same fluids that are trapped in diamonds. These fluids precipitate chlorides as a direct result of migrating into the strongly reduced environment of the lower cratonic mantle, producing sources that can later melt to form exotic alkali chloride-bearing kimberlites such as those found at Udachnaya-East.

## 2.5 Conclusion

In this study we performed high pressure experiments from 3-6 GPa and 800-1100 °C to simulate the reaction of melts of sediment with depleted peridotite within the cratonic lithospheric mantle. The reaction lead to different styles of metasomatic reactions depending on the thermobaric conditions:

1. At >4 GPa and <1100 °C, the reaction of melts of sediment and depleted peridotite leads to the formation of saline fluids similar to those found in diamond inclusions.
2. Under reducing conditions, H<sub>2</sub>O dehydrates to H<sub>2</sub>, and thus, leads to the precipitation of Na-K chlorides from oversaturated saline fluids.
3. Besides Na-K chlorides, magnesite forms by the reaction of sediment-derived CO<sub>2</sub> with olivine. Magnesite and Na-K chlorides are constituents necessary for the formation of “salty kimberlites” such as Udachnaya-East.
4. At <4 GPa, Na-K chlorides were absent from the experimental phases and K was contained in mica and melt. The thermobaric conditions of this change in phase assemblage coincides with the mid-lithospheric continuity, a seismic low-velocity zone that is found intermittently beneath all continents at a depth of 80–100 km.

## Author contributions

MF performed all experiments and processed and interpreted the data. MF wrote the manuscript. OA and SB assisted in analysis and evaluation of the datasets. SF and HRM helped in data interpretation and manuscript evaluation. MF handles the correspondence of the submitted manuscript version of this chapter.

## Acknowledgments

The authors acknowledge the Macquarie University Faculty of Science and Engineering Microscope Facility (MQFoSE MF) for access to its instrumentation and support from its staff. Thomas Kautz (Goethe Universität Frankfurt) assisted with belt apparatus experiments. Dorrit Jacob and Bill Griffin are gratefully acknowledged for proof-reading this manuscript. This work is part of the PhD thesis of MWF, supported by an Australian Government International Postgraduate Research Scholarship (IPRS), Macquarie Postgraduate Research Fund (PGRF), and the ARC Centre of Excellence for Core to Crust Fluid Systems (CCFS). HRM acknowledges support from the Wilhelm und Else Heraeus Stiftung. The International Ocean Discovery Project (IODP) provided the Mediterranean marine sediment.

# Chapter 3:

## Two-stage Formation of K-enrichment in Ultrapotassic Magmatism Confirmed by a Novel Experimental Approach

Michael W. Förster<sup>1</sup>, Stephan Buhre<sup>2</sup>, Bo Xu<sup>1,3</sup>, Dejan Prelević<sup>2,4</sup>, Regina Mertz-Kraus<sup>2</sup>, Stephen F. Foley<sup>1</sup>

<sup>1</sup>ARC Centre of Excellence of Core to Crust Fluid Systems and Department of Earth and Planetary Sciences, Macquarie University, NSW 2109, Sydney, Australia

<sup>2</sup>Institute für Geowissenschaften, Johannes Gutenberg Universität, 55099 Mainz, Germany

<sup>3</sup>State Key Laboratory of Geological Processes and Mineral Resources, China University of Geosciences, Beijing 10083, China

<sup>4</sup>Faculty of Mining and Geology, University Belgrade, 11000 Belgrade, Serbia

This chapter is in review as an article for Contributions to Mineralogy and Petrology.

### Abstract

The generation of strongly potassic melts in the mantle requires the presence of phlogopite in the melting assemblage, while isotopic and trace element analyses of ultrapotassic rocks frequently indicate the involvement of subducted crustal lithologies in the source. However, phlogopite-free experiments that focus on melting of sedimentary rocks and subsequent hybridization with mantle rocks have not successfully produced melts with K<sub>2</sub>O >5-6 wt%, while ultrapotassic igneous rocks reach up to 12 wt% K<sub>2</sub>O. Accordingly, a two-stage process that enriches K<sub>2</sub>O and increases K/Na in intermediary assemblages the source prior to ultrapotassic magmatism seems likely. Here, we simulate this two-stage formation of ultrapotassic magmas using a novel experimental approach that involves melting of parts of an experimental product in a second experiment. In the first stage, reaction experiments containing layered sediment and dunite at 3 GPa and 800-1000 °C produced a modally metasomatized reaction zone at the border of a depleted peridotite. Melts of sediment have generally <6 wt% K<sub>2</sub>O and 70-79 wt% SiO<sub>2</sub> from 800-900 °C to 53-58 wt% SiO<sub>2</sub> at 1000 °C. At 900 °C the metasomatized product was characterized by

high contents of phlogopite and K/Na of ~8.9. For the second stage experiment, the metasomatized dunite was cut out, thoroughly removed from the residue of the sedimentary rock and melted at 2 GPa and 1200 °C. Melts contained 8-8.5 wt% K<sub>2</sub>O with K/Na of 6-7, which are a result from 20 % batch melting of the metasomatized dunite. This is the first time that extremely K-enriched ultrapotassic melts have been generated experimentally from metasomatized mantle lithologies in a process that is applicable to post-collisional and intraplate magmatism.

### 3.1 Introduction

Potassium-rich magmatism is a common feature in the post-collisional stage of orogenic belts and exhibits compositions ranging from basic to silica-rich. Generally, ultrapotassic (UP) lavas (*sensu stricto*) exhibit unusually high K<sub>2</sub>O mass fractions from 3 to 12 wt% at MgO >3 wt% (Mitchell and Bergman, 1991) and high K/Na ratios of >>2, coupled with extreme trace element and isotopic enrichment. Two models try to clarify this enrichment: (A) a two-stage metasome melting model (vein+wall rock model of Foley (1992b)), and (B) a single-stage recycled sediment/crust melting model (e.g. Campbell et al., 2014).

(A) The metasome melting model is a two-stage model that proposes that the UP lavas are produced by melting of modally metasomatized mantle source that has been enriched in phlogopite and pyroxene in a first stage (Conticelli et al., 2015; Lustrino, 2011; Prelević et al., 2008b; Xu et al., 2017). These phlogopite-rich “metasomes” may be pyroxenites or glimmerites, most likely formed when K-rich liquids react with peridotite to form layers and veins (Foley, 1992b; Prelević et al., 2013). Experimental studies have successfully produced melts of UP composition from phlogopite-bearing and phlogopite-veined peridotites (Condamine et al., 2016; Förster et al., 2017). This explanation often does not specify the ultimate origin of the glimmeritic metasomes and the K-rich liquids that generated them.

(B) Contrasting with the above model, other studies propose direct melting of subducted sediments (Mallik et al., 2016) and/or continental crustal material (Wang et al., 2017b), which mix with peridotite to form mélanges that melt and form UP rocks (Campbell et al., 2014) in a single stage. Subducted crustal rocks have in general low solidus temperatures of >675 °C, which strongly depend on pressure and volatile contents (Hermann et al., 2006; Hermann and Spandler, 2007; Wang et al., 2017b). Therefore, when the felsic crustal material is buried to mantle depths, it will preferentially melt and react with surrounding peridotitic matrix. Since continental lithologies are usually K-rich compared to mantle rocks (K/Na 1-2), they can provide the K-

enrichment for the potassic-ultrapotassic melts (Sekine and Wyllie, 1983; Wyllie and Sekine, 1982). The conception of a single-stage formation of UP lavas from recycled crustal components lies in the isotopic and geochemical composition of post-collisional lavas, which are enriched in  $^{87}\text{Sr}/^{86}\text{Sr}$  and show trace element patterns which are similar to the average composition of globally subducted sediment (GLOSS) (Plank and Langmuir, 1998). Other studies have suggested other recycled crustal components, including blueschists (Tommasini et al., 2011), terrigenous siliciclastic sediments (Prelević et al., 2008b), and marly sediments (Avanzinelli et al., 2007).

However, recycled crustal components do not necessarily have to melt directly to produce UP melts in a single stage, but may produce an intermediate pyroxenitic component as in model (A). This is evident from olivines within post-collisional lavas that comprise extreme Fo of 90-94 and NiO >0.5 wt%, which indicate a role for ultra-depleted peridotites (Foley et al., 2013; Prelević et al., 2013). To account for the crust-like geochemical composition of the post-collisional lavas, these pyroxenites must be phlogopite-rich and be characterized by high  $^{87}\text{Sr}/^{86}\text{Sr}$  isotopic and sediment-like trace element compositions. Given the widespread occurrence of post-collisional lavas, there also has to be a commonly occurring mechanism that produces pyroxenites with crust-like isotopic and trace element compositions within the lithospheric mantle. Furthermore, experiments on sediment and peridotite hybridization produce melts that are restricted to <6 wt% K<sub>2</sub>O on average (Wang et al., 2017a; Wang and Foley, 2018).

In this study, we simulate the metasome melting model (A) for the formation of UP melts using a novel two-stage experimental approach in which parts of an experimental product are re-used in a second experiment. The two experimental stages are (1) heating of two-layer charges consisting of carbonate-bearing siliciclastic marine sediment and dunite, resulting in a phlogopite-rich pyroxenite metasomatic reaction layer, and (2) partial melting of the phlogopite-rich pyroxenite synthesized in the first experiment to generate UP melts with K<sub>2</sub>O >6 wt%.

### **3.2 Experimental strategy**

Our hypothesis is that the formation of extremely K-enriched UP lavas requires a two-stage process, including i) metasomatism resulting in production of phlogopite-rich pyroxenites within the fore-arc mantle wedge of long-lived subduction zones; in our view this is a widespread result of normal subduction processes; ii) re-melting of the vein ± the wallrock, which may considerably postdate the metasomatic event. This scenario is based on the following observations:

1. An increasing number of studies imply that fore-arc regions of long-lived volcanic arcs with abundant calc-alkaline volcanism may act as an important host for phlogopite-rich pyroxenites (Gülmez et al., 2016; Vigouroux et al., 2008). Trenchward migration of volcanism leads to extreme potassium and trace element enrichment in the erupted lavas, indicating that the fore-arc mantle is strongly metasomatized to a phlogopite-bearing pyroxenite. Enrichment of the fore-arc probably takes place during subduction of sediments that melt, depending on pressure and volatile-contents, at temperatures as low as 675 °C to produce Si-rich melts (Hermann et al., 2006; Hermann and Spandler, 2007). These Si-rich melts rise from the slab surface and immediately react with peridotite to produce phlogopite-pyroxenites (Massonne, 1992; Sekine and Wyllie, 1982b; Sekine and Wyllie, 1983). Since phlogopite pyroxenites, as well as phlogopite peridotites, have solidi of ~1100-1200 °C (Condamine et al., 2016; Förster et al., 2017), far above the melting temperatures of sedimentary rocks, the melts within the fore-arc are completely consumed in this process.

2. Trace element and isotope compositions of post-collisional volcanic rocks indicate thorough mixing of recycled crustal components in the source region (e.g. Conticelli et al., 2009).

3. Trace element signatures of olivine phenocrysts indicate the presence of pyroxenite in the source (Foley et al., 2013; Prelević et al., 2013).

4. UP lavas have to be produced by the reaction of a melt of a low solidus vein and wall-rock peridotite with higher solidus since multiple saturation points including Ol, Opx, Cpx, and Gt/Sp are absent in liquidus experiments (Foley, 1992a).

5. Direct melting of sediments and hybridization with peridotite is unable to generate melts having K<sub>2</sub>O mass fractions that exceed on average 6 wt% (e.g. Wang et al., 2017a).

6. UP magmatism shows a prolonged activity of several million years duration within a given region, indicating that the recycled component is able to reside for a long time within the mantle lithosphere (e.g. Guo et al., 2006).

### **3.3 Materials and Methods**

#### **3.3.1 Starting materials**

The sedimentary starting material is a hydrous, carbonate-bearing, siliciclastic marine sediment with <10% carbonate and 5-10 wt% H<sub>2</sub>O as estimated by difference to 100 wt% in glasses and a melt fraction of ~40 %, which was acquired from the International Ocean Discovery Project (IODP) site ODP 161-976 B 18 X3 105-106.5 ([Supplementary Table 3.2](#)). A dunite (sample ZD11–

53) from the Zedang ophiolite (south Tibet, China) containing olivine (>97%), spinel (~2%), and clinopyroxene (<1%) was used as the depleted peridotite ([Supplementary Table 3.2](#)). Both samples were powdered in an agate mortar.

### 3.3.2. Experimental and analytical techniques

Experiments were carried out using a piston cylinder apparatus at the University of Mainz, which produces exceptionally well-preserved glasses. For the first stage experiments, which were conducted at 3 GPa and 800-1000 °C, the dunite was placed as a distinct layer on top of the sediment in a 30 % dunite to 70 % sediment ratio and sealed in 4 mm diameter capsules. Thermobaric conditions correspond to the fore-arc setting of a subduction zone (Gonzalez et al., 2016). After the experiment, the capsule was cut in half longitudinally; one half was embedded in epoxy and polished for characterization of the charges, and the other half was prepared for the second stage melting experiment. For the second-stage metasome melting experiment, half of the completed first stage experiment was dissected with a scalpel to separate the metasomatized dunite from the reacted sediment. The experiment at 900 °C was used for this purpose because the dunite contained the thickest phlogopite layer. The size of the cut out is highlighted by the blue box in [Fig. 3.1](#). During this mechanical extraction process, the sample material disintegrated into smaller pieces, which were sealed together in a capsule measuring 2 mm in diameter.

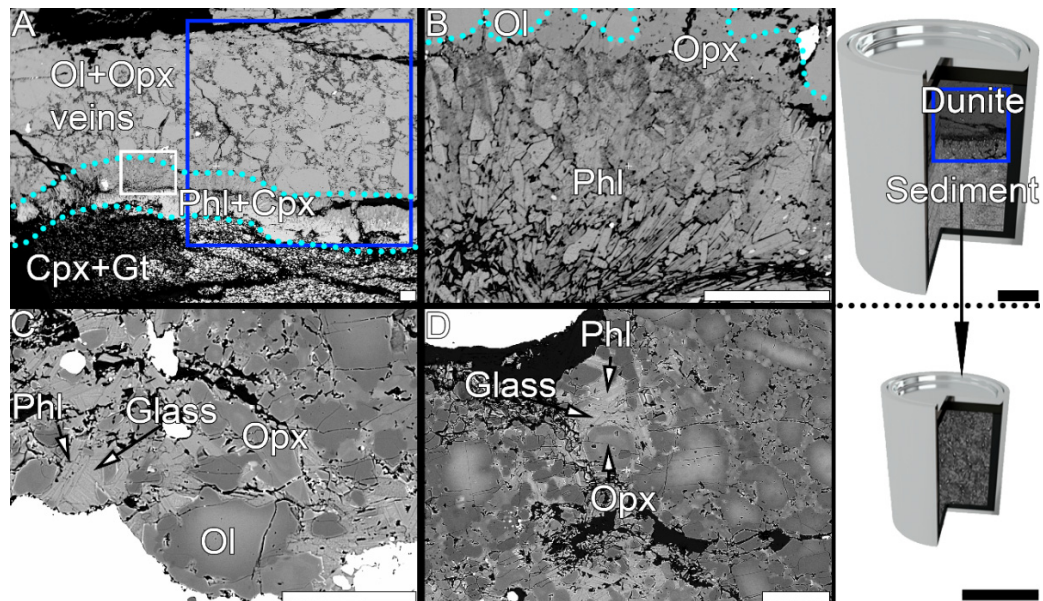


**Fig. 3.1:** Backscattered electron images of reaction zones in high-pressure experiments. (A) Reaction experiment at 3 GPa/900 °C with dunite upper layer and sediment lower layer. Light blue dotted line highlights the extent of a 300-400 µm thick reaction zone composed of phlogopite and clinopyroxene. Blue square indicates the portion extracted for the 2<sup>nd</sup> stage experiment. (B) Close-up of the upper part of the reaction zone (white box in A). (C) and (D) 2<sup>nd</sup> stage experiment in which the metasomatized dunite (blue square: reaction zone and dunite) of the experiment in (A) was melted at 2 GPa/1200 °C. All white scale bars (A-D) are 100 µm, while black scale bars for both capsules are 1 mm.



Major element contents of experimental run products were acquired using a JEOL JXA 8200 Superprobe electron-probe microanalyzer (EPMA) equipped with 5 wavelength dispersive spectrometers at the University of Mainz, Germany. Analyses are presented in [Supplementary Tables 3.1-3.10](#). Trace element mass fractions ([Supplementary Tables 3.11-3.14](#)) were determined using laser ablation-inductively coupled plasma mass spectrometry (LA-ICP-MS) at the University of Mainz and solution ICP-MS at Macquarie University, Sydney. Glass and mica of the 3 GPa/1000 °C experiment was ablated to a dry aerosol by using an ESI NWR193 ArF Excimer laser ablation system (193 nm wavelength) equipped with a TwoVol2 ablation cell. The ablation rate was set to 10 Hz at 3 J/cm<sup>2</sup>. Following its formation, the dry aerosol was transferred to an Agilent 7500ce mass spectrometer by a He-Ar mixed gas flow. Background signals were acquired for 20 s, followed by a dwell time of 30 s with spot sizes of 20 µm at each analysed spot. For calibration, synthetic NIST SRM 612 was used with published values (Jochum et al., 2011) and <sup>29</sup>Si was selected as the internal standard using the SiO<sub>2</sub> mass fractions determined by EPMA. USGS BCR-2G was analyzed as an unknown in each run for quality control and measured values were within 10 % of the data tabulated in the GeoReM database ([http:// georem.mpch-mainz.gwdg.de/](http://georem.mpch-mainz.gwdg.de/), Jochum et al., 2005). Data processing and reduction were carried out using the commercial software GLITTER 4.4.1 (Griffin, 2008). Trace-element mass fractions in the sediment were measured by solution ICP-MS. For quality control, USGS BHVO-1 and BIR-1 were measured as unknowns and values are within 10 % of the data tabulated in the GeoReM database (Jochum et al., 2005).

### 3.4 Results

#### 3.4.1 First-stage experiments

Four first stage reaction experiments were performed at 3 GPa at temperatures ranging from 800 to 1000 °C to form a metasomatic reaction zone in depleted peridotite (Table 1). The sedimentary starting material contained 2.57 wt% K<sub>2</sub>O with a K/Na ratio of 1.85 ([Supplementary Table 3.2](#): K<sub>2</sub>O/Na<sub>2</sub>O = 1.65). All experiments show a reaction zone (80-400 µm) sandwiched between the sediment and dunite layers ([Fig. 3.1 A,B](#)). This reaction zone contains mainly phlogopite (~40-80 vol%) and clinopyroxene (~20-50 vol%), as well as minor amounts of orthopyroxene (<10 vol%), and garnet (<5 vol%), while accessory minerals include apatite and Fe-Ni-sulphides. Experiments at 800, 850, and 900 °C also contain veins of orthopyroxene with minor amounts of magnesite



extending into the dunite layer from the reaction zone along olivine grain boundaries. The sedimentary rock fraction contains Mn-rich garnet (spessartine, ~15-22 vol%), Na-Al-rich clinopyroxene (omphacite, ~40-50 vol%), and glass (~20-40 vol%) in all experiments, while at 850 °C phengite, and at 800 °C coesite, were also found. All first stage reaction experiments produced silica-rich glasses which were observed to be a result of 20-40 % melting of the sediment (Supplementary Table 3.8), ranging from 70-79 wt% SiO<sub>2</sub> (Fig. 3.2 A, 3.3 A) for temperatures at 800-900 °C to 53-58 wt% SiO<sub>2</sub> at 1000 °C. All glasses have <6 wt% K<sub>2</sub>O, <16 wt% Al<sub>2</sub>O<sub>3</sub>, <4 wt% CaO, and <2 wt% Na<sub>2</sub>O (Fig. 3.3 A-D), while K/Na ranges from 2.8 to 6.4 (Fig. 3.4 A). Clinopyroxene shows a continuous range of compositions across the reaction zone with increasing Na<sub>2</sub>O (0.6 to 4 wt%) and Al<sub>2</sub>O<sub>3</sub> (2-10 wt%) towards the sediment, while the average mass fraction of Na<sub>2</sub>O decreases with temperature from 3 to 1 wt% (Fig. 3.2 B).

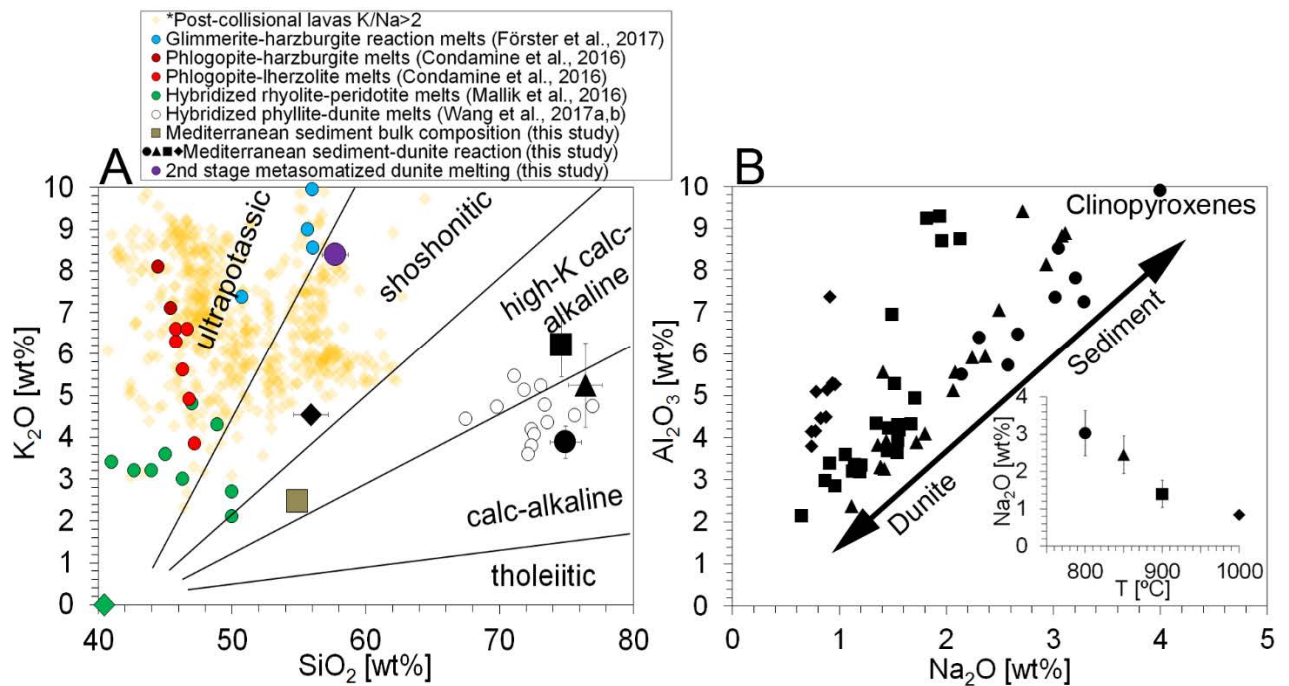


**Fig. 3.2:** Melt (A) and clinopyroxene (B) compositions from reaction experiments (black circle 800 °C; triangle 850 °C; square 900 °C; diamond 1000 °C) and 2<sup>nd</sup>-stage melts (purple circle) of this study, compared to the sedimentary rock starting material (brown square), and published data. Data for melts of phlogopite harzburgite and -lherzolite (dark red and red circles, Condamine et al., 2016), hybridized rhyolite-peridotite (green circles, Mallik et al., 2016), glimmerite-harzburgite (blue circles, Förster et al., 2017), hybridized phyllite-dunite (open white circles, Wang et al., 2017b; 2017a), and post-collisional lavas with K/Na >2 (orange diamonds, Prelević et al., 2008b) are shown for comparison. Melts from reaction experiments at 3 GPa/800-1000 °C are SiO<sub>2</sub>-rich and have moderately high K<sub>2</sub>O. In contrast, 2<sup>nd</sup> stage experiments result in melts (purple dot) with higher K<sub>2</sub>O and lower SiO<sub>2</sub>, similar to natural UP magmas. (B) Clinopyroxenes from reaction experiments show a range of compositions across the reaction zone with higher Na<sub>2</sub>O and Al<sub>2</sub>O<sub>3</sub> towards the former sedimentary rock. Symbols correspond to the experimental temperatures as in (A).

**Table 3.1:** Melting phase relations of reaction experiments and 2<sup>nd</sup> stage melting experiment.

#	Composition	T [°C]	P [GPa]	% Melt	Phases (+ Ol + Opx)	Duration
1	Sediment/Dunite reaction	800	3	~10	Cpx + Phl + Mgs + Gt + Phe + Coe + Si-rich melt	7 d
2	Sediment/Dunite reaction	850	3	~15	Phl + Cpx + Mgs + Gt + Phe + Si-rich melt	13 d
3	Sediment/Dunite reaction	900	3	~40	Phl + Cpx + Mgs + Gt + Si- rich melt	14 d
4	Sediment/Dunite reaction	1000	3	~40	Cpx + Gt + (Phl) + Si-rich melt	4 d
5	Metasome melting (Reaction zone of Exp 3)	1200	2	~23	Phlog + melt	6 h

Trace element compositions of melts derived from the sediment were acquired from the 3 GPa/1000 °C experiment, which contained large pools of melt that were easily measurable by LA-ICP-MS. The melt of the sediment is strongly enriched in large ion lithophile (LILE), high field strength (HFSE), and rare earth elements (REE) and show negative anomalies at Nb, P, and Ti, which are inherited from the bulk sediment composition (Fig. 3.5).

#### 3.4.2 Second-stage experiments

The second stage melting experiment was conducted on the metasomatized dunite from the first-stage experiment at 3 GPa/900 °C (Fig. 3.1 A, Supplementary Table 3.2) which showed the thickest metasome layer of all reaction experiments. Since the metasomatized dunite disintegrated to pieces upon transfer to the new capsule, the second stage experiment was free of layering (Fig. 3.1 C,D). The second stage experiment was performed at 2 GPa/1200 °C, which are thermobaric conditions at which phlogopite pyroxenites are known to be partially molten (Förster et al., 2017). At these thermobaric conditions, a mixture of phlogopite, clinopyroxene, and orthopyroxene breaks down to form olivine and melt (Förster et al., 2017). After the second stage melting, the hydrous glass contains ~57.7 wt% SiO<sub>2</sub>, ~8.4 wt% K<sub>2</sub>O, ~17.8 wt% Al<sub>2</sub>O<sub>3</sub>, 9.36 wt% CaO, and 1.33 wt% Na<sub>2</sub>O (Fig. 3.3 A-D), with K/Na ~7 (Fig. 3.4 A): this was calculated to result from 20 % batch melting of the metasome containing 21 wt% phlogopite, 71 wt% orthopyroxene, and 8 wt% clinopyroxene (Supplementary Table 3.2, 3.9).

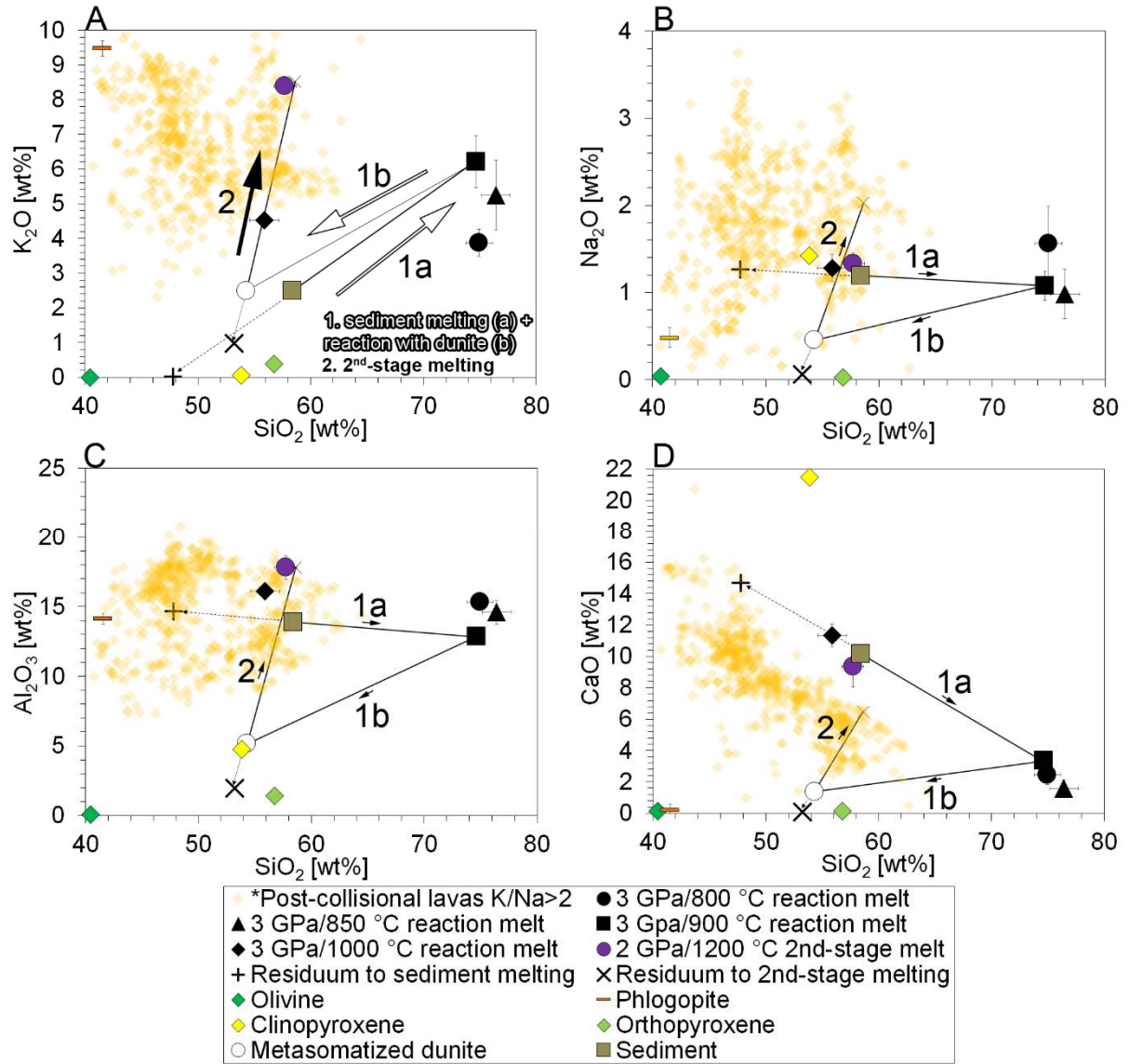


**Fig. 3.3:** K<sub>2</sub>O (A), Na<sub>2</sub>O (B), Al<sub>2</sub>O<sub>3</sub> (C), and CaO (D) *versus* SiO<sub>2</sub> showing the melt evolution of the 3 GPa/900 °C reaction and 2 GPa/1200 °C 2<sup>nd</sup>-stage experiment as calculated by mass balance. In the first stage (white arrows) 40% melting of the sediment (brown square) generates a Si-rich melt (black square), leaving a residuum (black plus) comprising 40% garnet and 60 % clinopyroxene (Supplementary Fig. 3.1), a Ca-rich, and K-poor composition. The Si-rich melt (black square) immediately reacts with olivine (green diamond), metasomatizing the adjacent dunite to phlogopite-pyroxenite (open circle). In the 2<sup>nd</sup>-stage the metasomatized dunite melts to 23 % crystallizing a residuum (black cross) comprising 16 wt% olivine, 56 wt% orthopyroxene, and 5 wt% phlogopite. Note that the calculated 2<sup>nd</sup>-stage melt composition is close to its measured values (purple circle) for K<sub>2</sub>O, Al<sub>2</sub>O<sub>3</sub>, and SiO<sub>2</sub> (A) and (C). However, Na<sub>2</sub>O and CaO are over- and underestimated, respectively, which is likely due to contamination by residual sediment during transfer of the metasomatized dunite to the 2<sup>nd</sup>-stage experiment. Other symbols: melts of sediment (black-circle 800 °C; triangle 850 °C; square 900 °C; diamond 1000 °C), 2<sup>nd</sup>-stage melt (purple circle) metasome (black star), reaction zone phases (phlogopite, orange rectangle; olivine, green diamond; orthopyroxene, lime diamond; clinopyroxene, yellow diamond), and post-collisional lavas with K/Na > 2 (orange diamonds, Prelević et al., 2008b).

### 3.5 Discussion

The generation of UP melts with 8.2-8.7 wt% K<sub>2</sub>O, representing a >4 fold enrichment with respect to the ultimate sediment source, by melting of metasomatized dunite is demonstrated unequivocally in our second stage experiment. This is the first study that has generated UP melts with K<sub>2</sub>O >6 wt% from recycled crustal lithologies with K<sub>2</sub>O contents as low as 2.57 wt%, thus confirming the applicability of this two-stage process of K-enrichment. In the following discussion we first compare our study with previous experiments in similar systems, and then discuss to what extent our experiments are applicable to the origin of post-collisional lavas such as those occurring in the Alpine-Himalayan belt.

#### 3.5.1 Comparison with previous experimental studies

The recycling of crustal rocks into the mantle is a normal consequence of subduction and collision in the global tectonic cycle, constantly juxtaposing Si-oversaturated crustal rocks with Si-deficient mantle rocks. Isotopic and geochemical compositions of orogenic lavas in the Alpine-Himalaya Orogenic Belt (AHOB) undoubtedly document the effective recycling of crustal rocks to mantle depths (Conticelli et al., 2009; Prelević et al., 2010; 2012). The role of crustal recycling in the generation of UP post-collisional lavas differs between the two competing models presented above, with major uncertainties in terms of the process of hybridization and melt generation as follows:

(A) UP lavas form by melting of phlogopite pyroxenites and phlogopite peridotites; this model is successfully simulated by experimental melts with high-K UP compositions (Fig. 3.2), K<sub>2</sub>O of >6 to 12 wt%, MgO >3 wt%, and intermediate SiO<sub>2</sub> (Condamine et al., 2016; Förster et al., 2017; 2018). This model explains K-enrichment in the mantle as taking place in an earlier stage when sediments or continental rocks are subducted to mantle depths (Gao et al., 2007; Prelević et al., 2008b; 2013; Tommasini et al., 2011). Infiltrating melts derived from sediments form phlogopite-bearing pyroxenites at the expense of peridotites following the reaction melt + olivine → phlogopite + pyroxene (Sekine and Wyllie, 1982a; 1982b; Sekine and Wyllie, 1983). The metasomatism probably takes place within the fore-arc of a subduction zone, where hydrous sediments are able to melt and infiltrate the mantle wedge because of their low solidus temperatures and high volatile contents (Massonne, 1992). However, the processes of K-enrichment of the lithospheric mantle by metasomatism due to melts from sediments and the formation of reservoirs producing melts with high K/Na of >>2 have not been clear to date and will be discussed below in Sections 3.5.2-3.5.4.

(B) UP lavas form by direct melting and hybridization of crustal rocks with mantle peridotites “*mélanges*” in a single stage at mantle depths (Campbell et al., 2014; Ersoy et al., 2010). In this scenario, either the subducted crustal rocks mix with peridotites to form *mélanges* and melt to form UP rocks or melts of subducted crustal rocks percolate and react with peridotites to form UP melts. Previous studies of Mallik et al. (2015; 2016) mixed a rhyolitic melt with as much as 6.4 wt% K<sub>2</sub>O with harzburgite, while Wang et al. (2017a) hybridized a phyllite (1.9 wt% K<sub>2</sub>O) with dunite. In both cases, experimental melts contain on average K<sub>2</sub>O <6 wt%, and K/Na ratios of up to 4-5, still too low to explain UP magmas which reach up to 12 wt% K<sub>2</sub>O and K/Na up to 10 (Mitchell and Bergman, 1991). It is noteworthy that crustal lithologies have a solidus up to 500 °C lower than that of peridotite (Wang et al., 2017b). At mantle temperatures of >1200 °C, crustal lithologies, therefore, generate Si-rich high degree melts in which K<sub>2</sub>O is diluted. This is evident from experiments hybridizing rhyolite and peridotite at 1200-1350 °C (Mallik et al., 2015; 2016), where the maximum K<sub>2</sub>O mass fraction of the melt (~7.4 wt%) is close to that of the rhyolite component in the starting material (6.4 wt%). Even though the studies of Mallik et al. (2015; 2016) did not aim to reveal the origin of high-K UP lavas, their work demonstrates that even high mass fractions of K<sub>2</sub>O in the starting material do not lead to UP melts in the experiment. In addition, K/Na ratios, a necessary criterion for the discrimination of UP magmas, are below the composition of the bulk starting material at >1100 °C, since melting of crustal rocks at high mantle temperatures does not form any Na-bearing phases that can cause an increase in K/Na ratios of the melt. All experimental melt compositions of sediment/peridotite hybridization so far fit this pattern (Mallik et al., 2015; 2016; Wang et al., 2017a; Wang and Foley, 2018), with K/Na values of 1-2 at ≥1100 °C (Fig. 3.4 A). In contrast, at <1100 °C, where temperatures are below that of ambient mantle, experimental melts of either sedimentary rocks alone, or melts due to sediment/peridotite reaction, reach K/Na values that exceed those of the starting material. This difference in behaviour is induced by the interaction between phengite stability and Na<sub>2</sub>O in residual clinopyroxene in the sediment layer: as in the case of melting of phlogopite, the highest K/Na are reached after phengite breakdown (at 900 °C; Fig. 3.4 A) where all potassium is accommodated within the melt. However, at <1100 °C, the melts are generally Si-rich with SiO<sub>2</sub> contents of up to >70 wt%, thus, high K/Na are bound to a high Si- and low-Mg content, and thus, unlike in composition to UP lavas. These results are in accordance with experiments by Wang et al. (2017a) and Wang and Foley (2018), showing that experimental melts products of sediment + peridotite hybridization produce are mildly potassic and Si-rich, and may explain the origin of high-K calc-alkaline to shoshonitic lavas as described by Campbell et al. (2014). However, hybridization and melting of



sediment and peridotite fail to explain the origin of the most K-enriched lavas, lamproites, which form side-by-side with mildly potassic lavas (Prelević et al., 2008b).

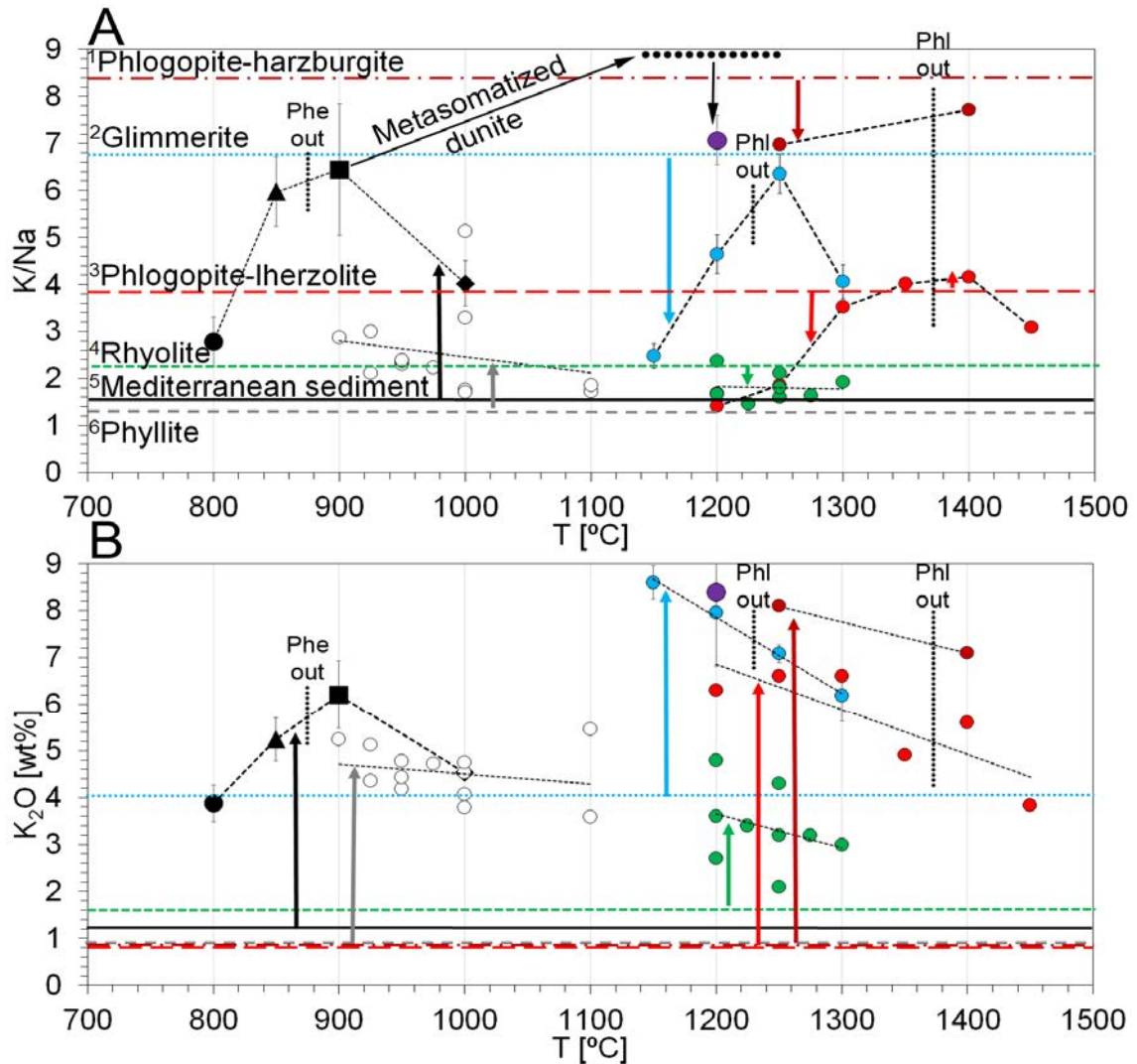


**Fig. 3.4:** K/Na (A) and K<sub>2</sub>O mass fractions (B) of melts *versus* experimental run temperature (black circle 800 °C; triangle 850 °C; square 900 °C; diamond 1000 °C) and 2<sup>nd</sup>-stage melts (purple circle) of this study and published data for phlogopite harzburgite and -lherzolite (dark red and red circles, Condamine et al., 2016), hybridized rhyolite/peridotite (green circles, Mallik et al., 2016), glimmerite/harzburgite (blue circles, Förster et al., 2017), hybridized phyllite/dunite (open white circles, Wang et al., 2017b; 2017a). A) Horizontal lines represent starting materials and are colour-matched to the symbols for the same experiments. K/Na in melts shows peaks related to phengite breakdown at ca. 900°C and phlogopite breakdown at >1100°C. Only experiments at <1100 °C generate melts where K/Na ratios exceed those of the starting materials (upward facing arrows). At >1100 °C, the highest K/Na ratios approach those of the starting material (downward facing arrows). The arrow labelled “Metasomatized dunite” connects the 900 °C reaction experiment and the calculated starting composition (thick dotted line: [Supplementary Table 3.2](#)) of the 2<sup>nd</sup> stage experiment at 1200°C. (B) K<sub>2</sub>O mass fractions of experimental charges generally decrease with temperature. Phengite-buffered K<sub>2</sub>O mass fractions in siliceous melts first increase with temperature and then decrease after phengite breakdown. Maximum mass fractions of K<sub>2</sub>O are <6 wt% for silica-rich melts (black symbols, white and green circles), while those buffered by phlogopite reach <9 wt% K<sub>2</sub>O (blue, purple, and red circles).

3.5.2 First stage experiments: formation of Si-rich potassic melts from a phlogopite-free source

Melting of sedimentary rocks in the first stage experiments and reaction of these melts with depleted peridotite produced Si-rich melts with  $K/Na > 2$ , while total  $K_2O$  never exceeded  $\sim 6$  wt%, consistent with hybridization experiments in previous studies that used continental crust material (Wang et al., 2017a; Wang and Foley, 2018). The melt derived from the sediment is highly enriched in LILE, HFSE, and REE, and plots within the field of post-collisional lavas with  $K/Na > 2$  (Fig. 3.5) (Prelević et al., 2008b). It shows negative anomalies at Nb, P, and Ti, which are inherited from the bulk sediment composition. The formation of this Si-rich melt is explained by 40 % batch melting of the bulk sediment composition (Supplementary Table 3.8):

100 wt% sediment  $\rightarrow$  40 wt% Si-rich melt + 35 wt% clinopyroxene + 25 wt% garnet ( $R^2 = 0.98$ ) (I)

The residue after melting of the sediment (clinopyroxene + garnet) of this first-stage process attains a composition rich in Na and Ca (Fig. 3.3 B,D). Clinopyroxenes from all first-stage reaction experiments are strongly zoned in Na across the reaction zone and reach highest  $Na_2O$  mass fractions on the sediment side of the assemblage (Fig. 3.2 B). Additionally, the lower the melting temperature of the experiment, the more effectively is Na retained in the residue as clinopyroxene shows a continuous decrease in  $Na_2O$  with temperature (Fig. 3.2 B), corresponding to a decrease of  $Na_2O$  partitioning from  $D_{Na(cpx/melt)} \sim 2$  at 3 GPa/800 °C to  $D_{Na(cpx/melt)} \sim 0.8$  at 3 GPa/1000 °C. The formation of residual Na-rich clinopyroxene and the breakdown of phengite produce melt with high  $K/Na$  ratios that peak at  $\sim 6.5$  at 900 °C (Fig. 3.4 A). However, melts from the first stage experiments at  $< 1000$  °C are silica-rich in composition (up to 79 wt%  $SiO_2$ ), which does not match the composition of a UP magma with  $Na_2O + K_2O$  of 5-8 wt% but is common for melts from crustal lithologies (Wang et al., 2017a). Thus, UP melt generation requires a process that first increases the  $K/Na$  ratio of the melt at  $< 1000$  °C, which is facilitated by residual Na-rich clinopyroxene and high  $D_{Na(cpx/melt)}$ , and then reduction of the silica content by reaction with an ultramafic mineral such as olivine. However, at 900-1000 °C, hybridized melts are still Si-rich and show  $MgO$  contents  $< 1$  wt%, and hence do not satisfy the definition of ultrapotassic (Wang et al., 2017a; Wang and Foley, 2018).

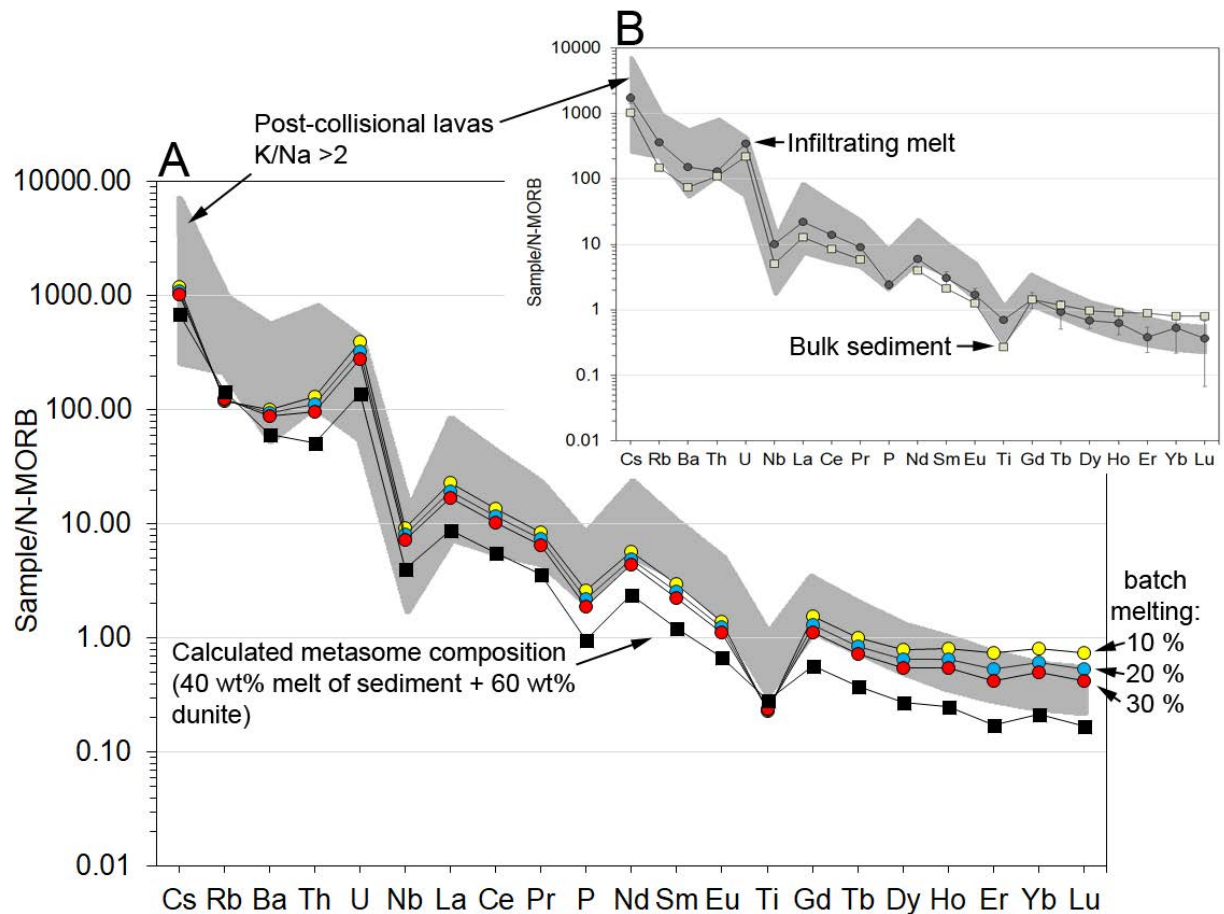


**Fig. 3.5:** N-MORB normalized trace element compositions of (A) modelled batch melt compositions and (B) starting materials (Sun and McDonough, 1989) (grey squares, sediment) compared to experimental melts (grey circles, 3 GPa/1000 °C) and post-collisional lavas (shaded area) (Prelević et al., 2008b). The sediment/dunite reaction melts (B) are high in Cs, Rb, Ba, and show negative anomalies at Nb, P, and Ti, similar to post-collisional lavas with K/Na > 2. (A). 40 wt% melt of sediment reacts with 60 wt% dunite to form the calculated metasome composition. Batch melting of the metasome (10-30%) increases the trace element mass fractions to values observed within post-collisional lavas.

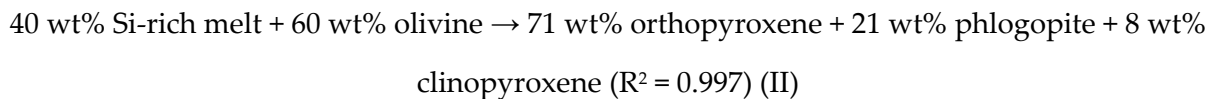
### 3.5.3 Second stage experiments: formation of high K/Na ultrapotassic melts from a metasomatized, phlogopite bearing mantle

Since hybridized melts of peridotite and crustal material are too low in MgO, K<sub>2</sub>O, K/Na, and too high in SiO<sub>2</sub>, the formation of UP magma with MgO >3 wt%, K/Na >2, and K<sub>2</sub>O of 8-12 wt% from subducted crustal rocks must go beyond a single-stage mixing and melting process. Hence, a minimum of two stages are required: (1) Sediments or crustal rocks are subducted to mantle depth within a cool subduction setting where they melt and the melt reacts with dunite. At <1000 °C the SiO<sub>2</sub>-rich melts are consumed as they react with olivine to form phlogopite in an incongruent crystallization reaction (Fig. 3.1 A,B): melt + olivine → phlogopite. (2) In the process of subduction and collision, phlogopite-bearing peridotite is separated from the K-poor residue and melts at >1100 °C to produce UP melts with MgO >3 wt%, K/Na >2, and K<sub>2</sub>O of 8-12 wt%.



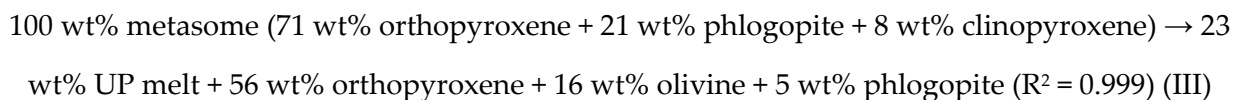
One has to note here that the 2<sup>nd</sup>-stage experiment represents melting of the metasome at one specific thermobaric point which likely explains the overlap with a certain group of the post-collisional lavas with K/Na >2 but does not represent the whole entity of post-collisional lavas with K/Na >2 as shown in [Fig. 3.2A](#).

The phlogopite-bearing metasome forms in the first stage by reaction of melt of sediment and dunite ([Fig. 3.3](#)): since the melt is silica-oversaturated, the reaction with olivine forms pyroxene in addition to phlogopite to account for excess SiO<sub>2</sub> (Wyllie and Sekine, 1982). According to mass balance calculations ([Supplementary Table 3.9](#)), melt infiltration in the 3 GPa/900 °C experiment leads to the reaction:



However, the spatial separation of phlogopite from orthopyroxene in the experimental reaction zones implies that this reaction occurs stepwise: the incongruent crystallization of phlogopite leads to the emergence of a SiO<sub>2</sub>-rich fluid that migrates and reacts with olivine to cause the crystallization of orthopyroxene beyond the phlogopite-enriched layer. Compared to the initial silica-rich melt, this fluid is much more mobile and infiltrates more quickly along olivine grain boundaries. This fits the observation that orthopyroxene veins protrude beyond the metasome into the dunite ([Fig. 3.1 A,B](#); [Supplementary Fig. 3.2](#)).

The UP melt of the 2nd-stage experiment can be calculated as a ~20 % batch melt of the metasome within the dunite ([Supplementary Table 3.10](#)):



Reaction (III) produces UP melt and olivine by consuming phlogopite, clinopyroxene, and orthopyroxene. While olivine is also part of the metasome, it does not melt and is net-positively produced by the melting reaction. The melting of phlogopite produces melts with potassium contents similar or higher than the modal abundance of phlogopite in the source rock since partition coefficients for K<sub>2</sub>O between phlogopite and melt are close to unity and decrease with increasing pressure (Förster et al., 2017; 2018). Incongruent melting of phlogopite produces olivine or orthopyroxene depending on pressure (Foley et al., 1999), which itself causes an increase in K<sub>2</sub>O in the melt (Foley, 1989). Besides this effect of phlogopite, the trend of increasing K/Na with the degree of melting is also controlled by clinopyroxene. While phlogopite buffers the melt at ~7-9 wt% K<sub>2</sub>O, clinopyroxene controls Na<sub>2</sub>O in the melt as it changes its composition from Na-enriched to Na-depleted with increasing temperature (Förster et al., 2017). As a result,

the highest K/Na values in the melt are achieved at intermediate temperatures when phlogopite breaks down and clinopyroxene is a residual phase (Fig. 3.4 A). Hence, high K/Na ratios in UP magmas are inherited from their metasomatized source and reflect the relative proportions of clinopyroxene and phlogopite.

The dotted black line (Fig. 3.4 A) shows the calculated K/Na content of ~8.9 for the metasomatized dunite that was estimated from the modal abundance of phlogopite and clinopyroxene within the reaction zone (Supplementary Table 3.2). Since the metasome formed by reaction of melt with olivine, which contains neither K nor Na, its K/Na ratio is inherited entirely from the infiltrating melt which reaches K/Na ~6.4. The difference between K/Na values of 6.4 and 8.9 is a result of loss of clinopyroxene during transfer to the second stage capsule. This transfer is depicted by the “metasomatized dunite” arrow in Fig. 3.4 A, which symbolizes the metasome formation and mechanical separation. Melting of the metasome produced UP melts with K/Na of ~7 and K<sub>2</sub>O mass fractions of ~8 wt%. While the K/Na ratio is similar to that in the silica-rich melt that metasomatized the dunite, the extreme enrichment of K<sub>2</sub>O during second stage melting (III) was facilitated by physical separation from the K-poor residual sediment that formed by reaction (I).

Due to the small scale of the melt pools within the low-T first stage experiments (800-900 °C) and the second stage experiment, trace elements could only be obtained from the 3 GPa/1000 °C experiment, which had melt pools beneath the reaction zone that were large enough for analysis by LA-ICP-MS. However, since the metasome formed by a reaction of 40 wt% melt of sediment with 60 wt% olivine (reaction II), bulk trace element concentrations of the metasome can be calculated (Fig. 3.5 A, Supplementary Table 3.14). Also, trace element concentrations of the second stage melt (reaction III) can be modelled using the non-modal batch melting equation of Shaw (1970) with partition coefficients determined from partial melting of phlogopite pyroxenite (Förster et al., 2017). While the bulk metasome composition shows concentrations below those observed in post-collisional lavas (Prelević et al., 2008b), 10-30 % batch melts of it lie within the observed compositional range (Fig. 3.5 A).

#### 3.5.4 Implications for the formation of post-collisional lavas

The sediment/dunite reaction of the first stage experiments produced melts with 3-6 wt% K<sub>2</sub>O and SiO<sub>2</sub> varying from 55-79 wt% with decreasing temperature from 1000 to 800 °C. Their major element (Fig. 3.2,3.3) and trace element concentrations (Fig. 3.5 B) are in accordance with the formation of post-collisional lavas as proposed by model (B) that are Si-rich and show K<sub>2</sub>O concentrations similar to shoshonites and high-K calc-alkaline lavas (Prelević et al., 2008b).

However, none of these experiments produced K-rich melts that are comparable to lamproites which coexist with shoshonites and high-K calc-alkaline lavas, nor have other experiments that investigated sediment-peridotite hybridization (Wang et al., 2017a; Wang and Foley, 2018). The most K-enriched crustal rocks, rhyolites and granites, will also produce only mildly potassic lavas if they hybridize with peridotites, as demonstrated previously (Mallik et al., 2015; 2016). Hence, the direct melting of crustal lithologies and hybridization with mantle rocks proposed in model (B) is only able to explain the formation of mildly potassic, Si-rich, post-collisional lavas.

However, it must be emphasised that post-collisional lavas of shoshonitic and high-K calc-alkaline composition occur concurrently in time and space with extremely K-enriched lamproites in volcanic provinces of the AHOB (Prelević et al., 2010; 2013). In two well-documented examples, extremely K-enriched lavas were erupted in a fore-arc setting, induced by slab-rollback, and indicate a strongly metasomatized lithospheric fore-arc mantle (Gülmez et al., 2016; Vigouroux et al., 2008). Accordingly, the simultaneous appearance of lamproites with other K-rich lavas suggest that they share a similar source and represent an end-member with the highest proportion of metasomatized mantle (phlogopite pyroxenite) in their source. Melts of phlogopite pyroxenites, as demonstrated by the second-stage melting experiment, produce melts with a high K<sub>2</sub>O mass fraction of 8-9 wt% and high K/Na of ~7 that are comparable to post-collisional lavas with lamproitic composition (Fig. 3.2,3.4). These results are in accordance with previous studies on phlogopite pyroxenite melting (Förster et al., 2017). Batch-melting modelling of the second-stage experiments shows that 20 % melting of phlogopite pyroxenite satisfies major and trace element composition of high-K post-collisional lavas (Fig. 3.2,3.5). The high degree of melting (20 %) contrasts with the extremely low-degree melts (<2 %) that are required to form high-K alkaline magmas from a peridotitic source (e.g. Novella and Frost, 2014) but better explains high-volumes of K-rich lavas such as those observed in the Roman Province (e.g. Peccerillo, 2017).

### 3.6 Conclusions

Our novel experimental approach confirms that two-stage formation can account for UP magmatism with K<sub>2</sub>O >6 wt% involving significant contributions from silicic crustal components, as seen in almost all post-collisional UP magmas. As established by previous studies, extremely K-enriched magmas require a modally metasomatized mantle enriched in phlogopite (Conticelli et al., 2015; Gülmez et al., 2016; Lustrino, 2011; Prelević et al., 2008b). This enrichment probably takes place during subduction when sediment starts to melt at ~800 °C, forming high K/Na

dacitic/rhyolitic melts that react with wall-rock peridotite. Phlogopite is formed by incongruent crystallization during this reaction, consuming the melt (Fig. 3.6 A). The residue of the melted sediment attains a low K/Na ratio and crystallizes Na-Al rich clinopyroxene, releasing melt with correspondingly high K/Na. The low K/Na residue is subducted to greater depths and temperatures where it may contribute to arc magmas with  $K/Na < 1$  (Fig. 3.6 A).

After subduction ceases, slab rollback and/or break-off allows access of hot asthenospheric mantle to shallow levels of the fore-arc mantle, thereby heating the modally metasomatized peridotite (Fig. 3.6 B). Partial melting of the phlogopite-enriched metasome now produces UP melts with  $K_2O$  contents of 6 to 12 wt%. In addition, large amounts of subducted crustal lithologies incorporated into newly-formed lithosphere (Prelević et al., 2013) may directly melt to produce siliceous potassic rocks with lower  $K_2O$  (<6 wt%; Fig. 3.6 B).

However, if the rise of the hot asthenospheric mantle fails to induce melting of the metasomes, they may reside within the lithospheric mantle until they are “activated” at a much later stage. This later activation could be induced by geodynamic processes different to the post-collisional setting, including heat introduction by mantle plumes, or rifting and associated decompression melting. Potassic magmatism that exhibits the involvement of subducted sediments remote to young orogens in locations such as Gaussberg, Antarctica (Foley and Jenner, 2004) or West Kimberley, Australia (Jaques and Foley, 2018; Nelson, 1992) would fit this scenario.

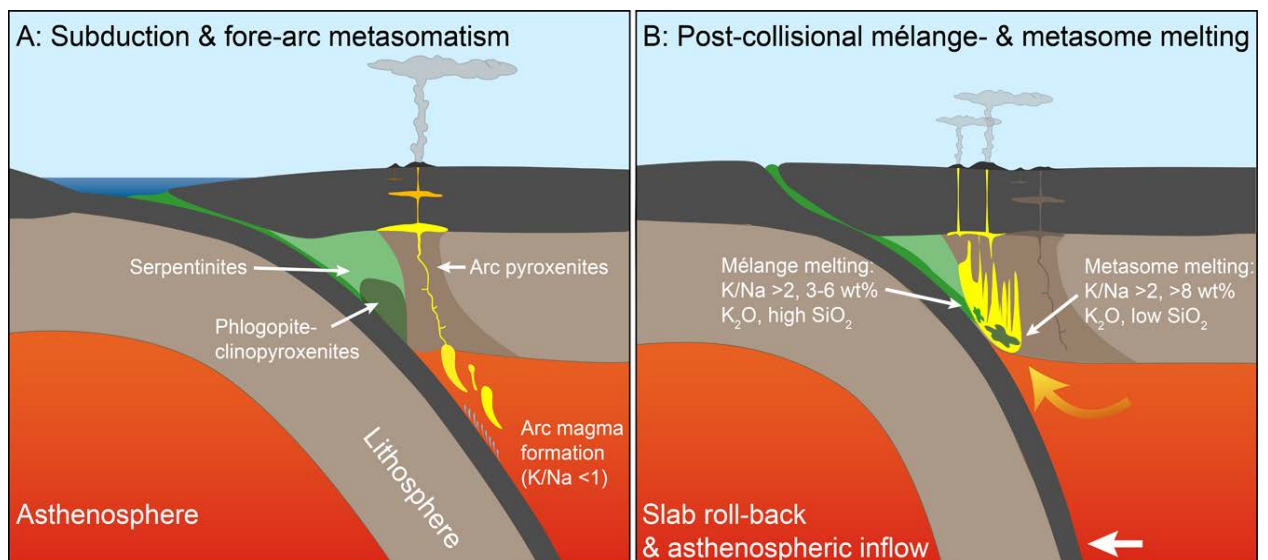


**Fig. 3.6:** Model for the genesis of post-collisional UP magmatism. (A) fore-arc mantle is metasomatized by melts of subducting sedimentary rocks; melts have  $K/Na$  ratios  $> 2$  and react with depleted mantle to form phlogopite clinopyroxenites, leaving a K-depleted residuum that contributes at deeper levels to arc magmas with low  $K/Na$  ratios of  $< 1$ . (B) After continental collision and slab roll-back, upwelling asthenosphere introduces heat and melts the metasomes and mélanges. These second-stage magmas are UP in composition ( $K/Na > 2$ ,  $K_2O$  3-6 wt% from crust and mélanges and up to  $> 8$  wt% for metasome melts).

## **Author contributions**

MF performed all experiments and processed and interpreted the data. MF wrote the manuscript. SB and RMK assisted in analysis and evaluation of the datasets. SF, BX, and DP helped in data interpretation and manuscript evaluation. MF handles the correspondence of the submitted manuscript version of this chapter.

## **Acknowledgements**

We gratefully acknowledge Qing Xiong for providing the dunite sample ZD11-53 used in the experiments. The International Ocean Discovery Project (IODP) supported this study in providing the Mediterranean marine sediment sample from sampling site 161-976. This work is part of the lead author's PhD thesis supported by an Australian Government International Postgraduate Research Scholarship (IPRS) and Postgraduate Research Fund (PGRF). DP was supported through the Deutsche Forschungsgemeinschaft (DFG) project PR 1072/9-1.

## Chapter 4:

# An Experimental Study of the Role of Partial Melts of Sediments *versus* Mantle Melts in the Sources of Potassic Magmatism

Michael W. Förster<sup>1</sup>, Dejan Prelević<sup>2,3</sup>, Stephan Buhre<sup>2</sup>, Regina Mertz-Kraus<sup>2</sup>, Stephen F. Foley<sup>1</sup>

<sup>1</sup>ARC Centre of Excellence of Core to Crust Fluid Systems and Department of Earth and Planetary Sciences, Macquarie University, NSW 2109, Sydney

<sup>2</sup>Institute of Geosciences, Johannes Gutenberg University, 55099 Mainz, Germany

<sup>3</sup>Faculty of Mining and Geology, University Belgrade, 11000 Belgrade, Serbia

This chapter is in review as an article for *Journal of Asian Earth Sciences: Magmatic Evolution and Crustal Growth of the Mediterranean Region: New Geochemical and Geochronological Perspectives* (special issue).

## Abstract

Potassium-rich lavas with K/Na of >2 are common in orogenic and anorogenic intraplate magmatic provinces. However, in the primitive mantle, the concentration of Na exceeds that of K by 10 times. The source of K-rich lavas thus needs to be either K-enriched or Na-depleted to account for high K/Na ratios. The geochemical and isotopic compositions of high <sup>87</sup>Sr/<sup>86</sup>Sr post-collisional lavas show that their mantle source contains a recycled crustal component. These highly K-enriched lavas with crustal like trace element patterns are termed “orogenic lamproites” and are compositional distinct from K-rich “anorogenic lamproites” that show lower <sup>87</sup>Sr/<sup>86</sup>Sr and a trace element pattern that resembles that of primary mantle melts. For both groups the processes of K-enrichment within their source are uncertain and are thought to be linked to melts of sedimentary rocks for “orogenic lamproites” and low-degree melts of ultramafic mantle rocks for “anorogenic lamproites”. In both cases, metasomatism of the mantle lithosphere is the precursor to K-rich magmatism. In this study we experimentally determine the effects of mantle metasomatism by sediment- and hydrous mantle melts. The experiments simulate the interaction of depleted lithospheric mantle and metasomatizing melt in a 2-layer reaction experiment. The

sediment/dunite reaction experiments lead to formation of a strongly K-enriched phlogopite-pyroxenite layer sandwiched between the two starting materials. The low temperature of the sediment/dunite reaction runs at <1000 °C simulate a fore-arc subduction environment, in which the melts of sediment is consumed during interaction with dunite as the temperature is below the solidus of the forming phlogopite-pyroxenites. The hydrous mantle melt/dunite reaction run is simulated by reacting a hydrated basanite with dunite. Since the temperature of the reaction is higher than the solidus of the resulting phlogopite-pyroxenites (1200 °C), the hydrous melt is not consumed but flows further, increasing in K<sub>2</sub>O and K/Na as it reacts with the depleted peridotite. In both cases, melts are enriched in K and gain K/Na by crystallizing a low K and low K/Na eclogitic residue. Compositions of glass and phlogopite from both types of reactions are comparable to glasses and phlogopites found within post-collisional lavas. Since the enrichment of K within the reaction zone is strongly controlled by the formation of low K/Na and low-K residues, metasomatic enrichment of the mantle lithosphere in K does not need a highly K-enriched metasomatic agent.

#### **4.1 Introduction**

Lavas formed in post-collisional settings are geochemically extremely heterogeneous and show Si-undersaturated to Si-oversaturated compositions. Within the Alpine-Himalayan belt, post-collisional lavas usually have >4 wt% K<sub>2</sub>O to up to 9 wt% and K/Na >2. The array of lavas present within the Alpine-Himalayan belt comprise all four major groups of K-rich rock compositions including shoshonites, voluminous Roman-type lavas, as well as lamproites and kamafugites (Foley et al., 1987). Since low-degree melting experiments of peridotite have not been able to produce high contents of K and high K/Na, and liquidus experiments have not produced multiple saturation points for olivine, orthopyroxene, clinopyroxene and garnet/spinel (Edgar and Mitchell, 1997; Foley, 1992a; Mitchell and Edgar, 2002; Sato, 1997), an alternative explanation for K-rich magmatism has been established that involves the presence of phlogopite pyroxenites ("metasomes") in the lithospheric mantle (Foley, 1992b). While lavas with K<sub>2</sub>O <5 wt% and SiO<sub>2</sub> >55 wt% may form by direct melting of mixed crustal/mantle rocks without phlogopite in the source (Campbell et al., 2014; Mallik et al., 2015; 2016; Wang et al., 2017b; 2017a; Wang and Foley, 2018), extremely K-enriched lavas are thought to require modally metasomatized mantle, enriched in phlogopite (Conticelli et al., 2007; Conticelli et al., 2015; Conticelli and Peccerillo, 1992;



Lustrino, 2011; Prelević et al., 2008a). Experimental studies of melting of phlogopite-veined depleted peridotite and phlogopite-peridotite successfully produced melts with K<sub>2</sub>O 8-12 wt% and indicate the importance of phlogopite within the source of ultrapotassic lavas (Condamine et al., 2016; Condamine and Médard, 2014; Förster et al., 2017; 2018). Phlogopite-enriched metasomatized mantle is generally thought to be formed when K-enriched liquids percolate and react with depleted peridotite, re-fertilizing it and producing veins (Conticelli et al., 2013; Foley, 1992b; Prelević et al., 2013). The source of the K-enriched liquids comprises recycled materials, including blueschists (Tommasini et al., 2011), terrigenous siliciclastic sediments (Prelević et al., 2008b), and marly sediments (Avanzinelli et al., 2007). Recycling and metasomatism takes place during subduction, where sediments melt at temperatures as low as 675 °C, depending on pressure and volatile contents and metasomatize the lithospheric mantle (Hermann et al., 2006; Hermann and Spandler, 2007). Melts of sediment, which are strongly enriched in Si, react with Si-poor peridotites to form phlogopite pyroxenites (Sekine and Wyllie, 1983; Wyllie and Sekine, 1982). The phlogopite pyroxenites which are formed at low temperatures within a subduction setting are able to produce K-enriched melts if they are activated by a temperature increase which might be induced by asthenospheric upwelling i.e. by slab rollback or detachment (Gülmez et al., 2016; Vigouroux et al., 2008).

All previously presented rocks share an ‘orogenic’ origin, which is characteristic of strong crustal isotopic signatures (e.g. high <sup>87</sup>Sr/<sup>86</sup>Sr) and geochemical signatures of recycled crustal materials. However, there are also ‘anorogenic’ K-rich rocks, which show low <sup>87</sup>Sr/<sup>86</sup>Sr isotopic and geochemical signatures of a mantle origin (Prelević et al., 2008a). These ‘anorogenic lamproites’ suggest that besides metasomatism induced by melting of recycled crustal lithologies, metasomatism by low-degree mantle melts may also lead to K-enrichment of the lithospheric mantle. While the recycling of crustal lithologies brings K-rich rocks into the mantle, melts of peridotites are generally enriched in Na over K, given the composition of primitive mantle which contains only 0.026 wt% K but 0.246 wt% Na, resulting in a K/Na of ~0.1 (Hofmann, 1988). In the presence of volatiles such as CO<sub>2</sub> and H<sub>2</sub>O, the melting point of peridotite is depressed to up to <400 °C and forms low-degree melts. Low-degree ‘incipient’ melts of peridotite are, depending on the presence and amount of volatiles, highly alkaline and Si-poor with compositions such as melilitites, kimberlites, lamprophyres, and carbonatites (Foley and Pintér, 2018). At <1 % melting of a phlogopite-free garnet-peridotite, K<sub>2</sub>O is enriched to up to 2 wt% while Na<sub>2</sub>O attains ~3 wt% (Erlank, 1987; Novella and Frost, 2014). While these low-degree melts are likely not erupted due

to their overall low volume, they are certainly suitable agents for metasomatism of the lithospheric mantle. The quaternary Eifel Volcanic Fields are an example of 'anorogenic' mildly potassic intraplate magmatism in a rift-setting that show K/Na of ~1 and are interpreted as a result of partially melting of a metasomatized lithospheric mantle enriched in phlogopite (Mertes and Schmincke, 1985; Schmincke, 2007). Particularly for the Quaternary Eifel volcanic fields is a spatial overlap with the older Eocene Hocheifel volcanic fields which comprised sodic magmatism with low K/Na of <0.5 (Fekiacova et al., 2007). Thus, the lithospheric mantle was metasomatized and enriched in K after the formation of the Eocene Hocheifel volcanic fields and during or before the formation of the Quaternary Eifel volcanic fields.

In this study we react layered sediment/dunite and hydrous basanite/dunite in high-pressure experiments to investigate the behaviour of major and trace elements during mantle metasomatism. The sediment/dunite reaction experiments were performed at thermobaric conditions of 1-4 GPa/800-1000 °C that correspond to the fore-arc setting of a subduction zone. A melting experiment of pure sediment was performed at 4 GPa/1000 °C to examine phases that crystallize in absence of the reacting dunite. The hydrous basanite/dunite reaction experiment was performed at 3 GPa/1200 °C and represents an environment within the non-cratonic lithospheric mantle. Both reaction experiments lead to the growth of metasomatic phases in a layer between the starting materials.

## **4.2 Materials and Methods**

### **4.2.1 Experimental techniques**

Experiments were performed with a piston cylinder apparatus at the University of Mainz for experiments performed at 1-3 GPa and a belt apparatus at the University of Frankfurt for experiments at 4 GPa. The experimental charges consisted of layers of dunite (sample ZD11-53) and either sediment (ODP 161-976 B 18 X3 105-106.5; a siliciclastic marine sediment with <10% carbonate and 5-10 wt% H<sub>2</sub>O as estimated by difference to 100 wt% in glasses and a melt fraction of ~40 %) or a sodic basanite (Arensberg, Hocheifel, Germany). The basanite has K/Na ~0.4 and plots on the border between basanite and trachybasaltic compositions. The basanite was powdered and mixed with 10 wt% oxalic acid (C<sub>2</sub>H<sub>2</sub>O<sub>4</sub>) as a volatile source for 4 wt% H<sub>2</sub>O. Experimental charges were filled into a carbon capsules to control *f*O<sub>2</sub> via the C + CO equilibrium, and these were placed into platinum capsules. For piston cylinder experiments, assemblies

consisted of Al<sub>2</sub>O<sub>3</sub> spacers, a graphite furnace, b-type thermocouple, and a sintered CaF<sub>2</sub> outer spacer. For experiments in the belt apparatus, the spacer and capsule holder consisted of natural polycrystalline calcium fluoride, while other materials were identical to those used in the piston-cylinder experiments. All assemblies were pressurized first and heated at a rate of 50 °C/min. Both apparatuses were cooled by a water circuit at approximately 13 °C and pressure and temperature were kept constant for 2-14 days (Table 4.1). All charges were quenched to temperatures below 500 °C within 8 s in the piston-cylinder runs (Ziaja et al., 2014), and within 10 s in the belt runs.

**Table 4.1:** Composition, temperature, pressure, and duration of each experiment.

#	Experiment	P [GPa]	T [°C]	% Melt	Phases	Duration
1	Sediment/dunite reaction	1	900	~40	Ol + Opx + Cpx + melt	4 d
2	Sediment/dunite reaction	2	900	~40	Ol + Opx + Cpx + Gt + melt	4 d
3	Sediment/dunite reaction	3	800	~10	Ol + Opx + Cpx + Phl + Mgs + Gt + Phe + Coe + melt	7 d
4	Sediment/dunite reaction	3	900	~40	Ol + Opx + Phl + Cpx + Mgs + Gt + melt	14 d
5	Sediment/dunite reaction	3	1000	~40	Ol + Opx + Cpx + Gt + (Phl) + melt	4 d
6	Sediment melting	4	1000	~70	Ky + Gt + Cc + Coe + melt	4 d
7	Basanite/dunite reaction	3	1200	~40	Ol + Opx + Cpx + Gt + Phl + melt	2 d

#### 4.2.2 Analytical techniques

Major element mass fractions of experimental phases were acquired using a JEOL JXA 8200 Superprobe electron-probe micro-analyser (EPMA) equipped with five wavelength dispersive spectrometers at the University of Mainz, Germany. All samples were measured using 15 kV accelerating voltage, a spot size of 2 µm, and a beam current of 12 nA with peak counting times of 20-30 seconds. A range of synthetic materials were used as reference materials. Major element analysis of experimental charges are presented in [Supplementary Tables 4.1-4.6](#). Trace element concentrations have been obtained by laser ablation-inductively coupled plasma mass spectrometry (LA-ICP-MS) at the University of Mainz. Using an ESI NWR193 ArF Excimer laser ablation system (193 nm wavelength) equipped with a TwoVol2 ablation cell, samples were ablated to a dry aerosol. Following ablation at 10 Hz and 3 J/cm<sup>2</sup>, the dry aerosol was transferred to an Agilent 7500ce mass spectrometer by a He-Ar mixed gas flow. Synthetic NIST SRM 610 was used with published values (Jochum et al., 2011) for external calibration material. As internal standard <sup>29</sup>Si was used applying for the samples SiO<sub>2</sub> mass fractions determined by EPMA. For quality control, USGS BCR-2G was analysed as an unknown in each run and measured values

were within 10 % of the data tabulated in the GeoReM database ([http:// georem.mpch-mainz.gwdg.de/](http://georem.mpch-mainz.gwdg.de/), Jochum et al., 2005). Background signals were acquired for 20 s, followed by a dwell time of 30 s with spot sizes of 20  $\mu\text{m}$  at each analysed spot. Data processing and reduction was carried out using the commercial software GLITTER 4.4.1 (Griffin, 2008). The whole dataset of reference material- and sample analysis can be found in [Supplementary Tables 4.7-4.14](#).

## 4.3 Results

### 4.3.1 Structural observations

The reaction experiments of sediment/dunite and basanite/dunite show strong enrichment of K, Al, and Si in a reaction zone within the original dunite half of the capsule ([Fig. 4.1 A,B](#)). Generally, WDX-maps reveal the metasomatic growth of phlogopite, clinopyroxene, and orthopyroxene at the expense of olivine. Metasomatic phases generally show grain sizes of 20-50  $\mu\text{m}$ . The basanite/dunite reaction experiment, which was performed at 3 GPa/1200 °C ([Fig. 4.1 A](#)), shows 3 compositionally distinct layers.

The uppermost layer is dunite, which is metasomatically enriched in orthopyroxene, clinopyroxene, and phlogopite. Beneath the contact zone, the basanite crystallized to a layer of clinopyroxene and garnet, which forms the central part of the map images. Individual clinopyroxene and garnet grains attain sizes of <50  $\mu\text{m}$ . The lowermost layer consists of quenched basanitic glass with needles of quenched phlogopite, which is recognizable by its higher content of K and Mg when compared to the surrounding glass. The sediment/dunite experiment shown in [Fig. 4.1 B](#) was performed at 3 GPa/900 °C and shows 4 compositionally distinct layers. The dunite is metasomatically enriched in orthopyroxene, which is recognizable in veins along olivine grain boundaries. The second layer is nearly entirely composed of phlogopite with a small amount of clinopyroxene. Beneath the phlogopite layer follows a layer nearly entirely composed of clinopyroxene. Some of these clinopyroxenes show inclusions of orthopyroxene. Since orthopyroxene formed by reaction with olivine, the dunite layer extended to layer 3 clinopyroxenes as the reaction started. The lowermost layer consists of clinopyroxene and garnet and shows interstitial glass. The sediment melting experiment at 4 GPa/1000 °C is devoid of layering and comprises glass, garnet, kyanite, Mg-calcite, and coesite.

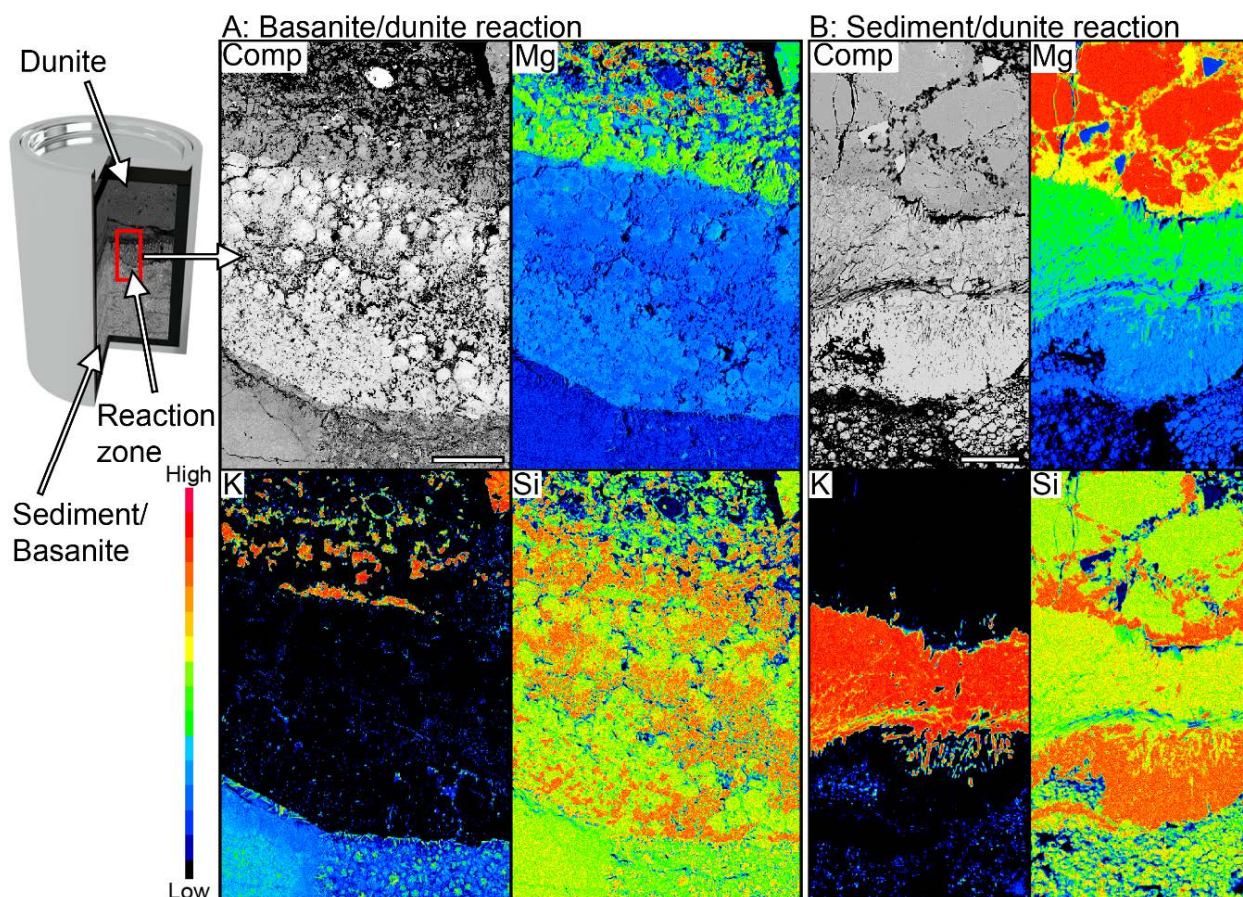


**Fig. 4.1:** Backscattered electron images (Comp) and WDX elemental maps of Mg, K, and Si of (A) basanite/dunite reaction at 3 GPa/1200 °C and (B) sediment/dunite reaction at 3 GPa/900 °C. The basanite/dunite reaction experiment (A) consists of three compositionally distinct layers, the uppermost is the former dunite, enriched in phlogopite and orthopyroxene as seen by the red colour in the K and Si maps. The middle layer consists of clinopyroxene and garnet, has the brightest grey scale in the backscattered electron image (Comp) and appears blue in the Mg map. Domains of garnet (green) and clinopyroxene (red) can be distinguished in the Si map. The lowermost layer is composed of glass and appears blue in the K map; the green needles are phlogopite crystals that formed during quenching. The sediment/dunite reaction experiment (B) shows four compositionally distinct layers: the uppermost represents the metasomatized dunite, enriched in orthopyroxene only (red in the Si map). The second layer forms a belt solely composed of phlogopite (red in K map) and is followed by a pure clinopyroxene layer (blue on Mg, red on Si map). The lowermost layer is composed of garnet, clinopyroxene, and interstitial melt (blue on K map). Scale bar 500  $\mu\text{m}$  (A) and 100  $\mu\text{m}$  in (B).

#### 4.3.2 Major element compositions

Melts formed during the reaction of sediment and dunite are moderate to high in  $\text{SiO}_2$  (50-76 wt%) with moderate  $\text{K}_2\text{O}$  contents of 3-6 wt% and K/Na of 1-5 (Table 4.2, Fig. 4.2 A-C). The melts from basanite/dunite reaction are lower in  $\text{SiO}_2$ , have  $\text{K}_2\text{O}$  of 2.5-3.5 wt%, and low K/Na of 0.5-1.2 but higher than the bulk basanite starting composition with K/Na of 0.4 at  $\text{K}_2\text{O}$  of 1.4 wt%. Experimental clinopyroxenes show a zonation towards omphacite (Fig. 4.3 A) across the reaction zone towards the sediment and basanite capsule half. Omphacitic clinopyroxenes from the



sediment show higher Al(VI) per f.u. (0.2-0.5) at lower Ti per f.u. (<0.015) than those from basanite which attain Al(VI) per f.u. of 0.1-0.2 at Ti per f.u. of 0.01-0.03 (Fig. 4.3 B), while total contents of Al<sub>2</sub>O<sub>3</sub> and Na<sub>2</sub>O are similar between sediment and basanite clinopyroxenes across the reaction zone (Fig. 4.3 C).

**Table 4.2:** Average composition of starting materials and high-pressure experiment melts normalized to 100 % (oxides in wt%).

Sample	Na <sub>2</sub> O	K <sub>2</sub> O	MnO	SiO <sub>2</sub>	MgO	FeO	Al <sub>2</sub> O <sub>3</sub>	Cr <sub>2</sub> O <sub>3</sub>	CaO	TiO <sub>2</sub>	Total
Sediment bulk	1.78(6)	2.46(9)	2.17(9)	54.9(4)	3.93(6)	3.6(2)	17.8(1)	-	13.5(2)	0.82(3)	101
Basanite bulk	3.9(1)	1.46(7)	0.21(5)	46.5(4)	9.3(6)	10.6(2)	13.9(3)	-	12.0(3)	2.54(9)	100
1 GPa/900 °C	2.4(6)	3.3(9)	1.4(6)	54(1)	4(1)	3(1)	19(4)	0.10(1)	13(1)	0.5(2)	100
Sediment/Dunite reaction	1.7(5)	5.4(0.6)	0.1(1)	69(1)	0.4(1)	0.8(2)	17.4(5)	0.01(2)	3.0(7)	0.30(2)	100
2 GPa/900 °C	2(1)	4.2(3)	0.5(1)	64(2)	1.6(4)	1.9(4)	14.3(6)	-	10(2)	0.9(2)	100
Sediment/Dunite reaction	2.8 (4)	2.6 (4)	0.18(4)	46(1)	11(1)	7.1(6)	14.4(5)	0.03(2)	13(2)	3.3(2)	100
4 GPa/1000 °C Sediment melting											
3 GPa/1200 °C											
Basanite/Dunite reaction											

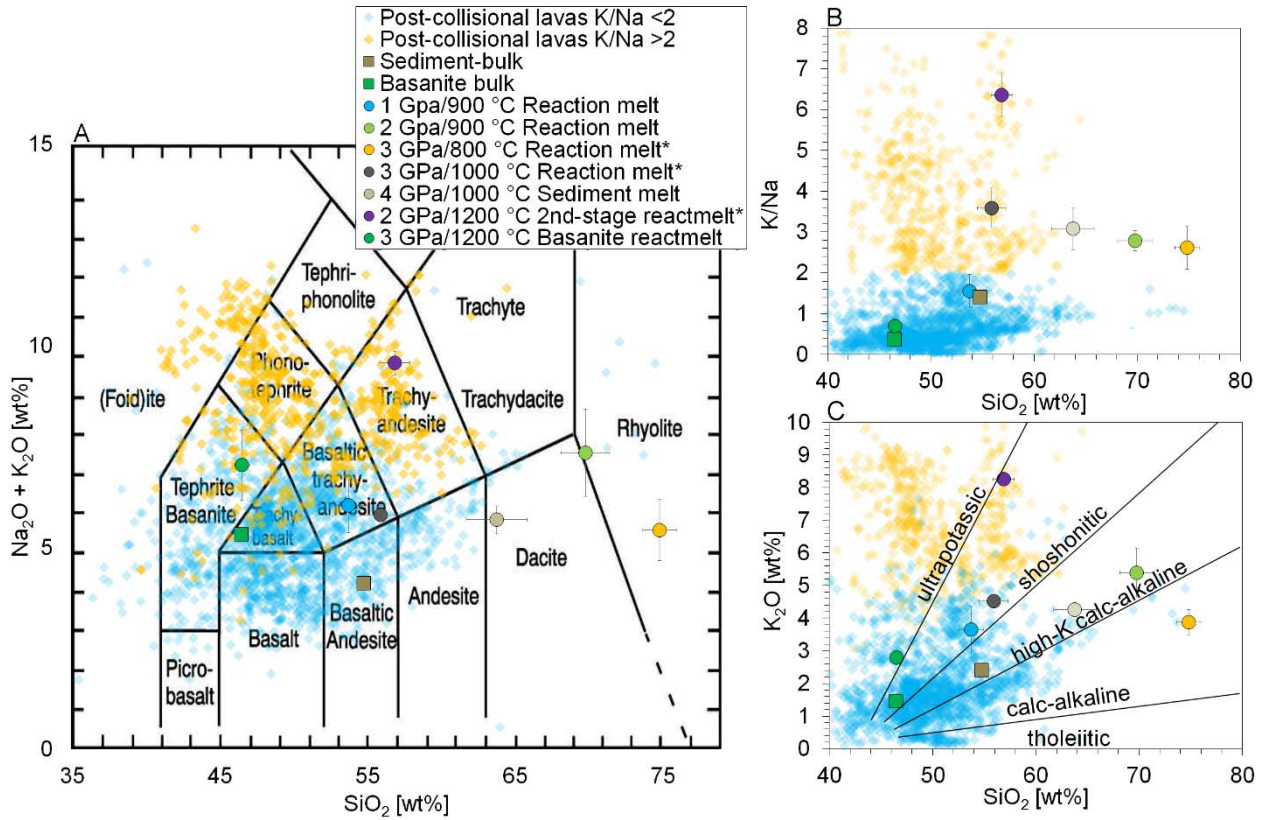


**Fig. 4.2:** Total alkali *versus* silica (A) K/Na *versus* SiO<sub>2</sub> (B), and K<sub>2</sub>O *versus* SiO<sub>2</sub> (C) for experimental melts (coloured squares: brown, sediment bulk; green, basanite bulk). Coloured circles: blue 1 GPa/900 °C; lime 2 GPa/900 °C; yellow 3 GPa/800 °C; grey 3 GPa/1000 °C; brown 4 GPa/1000 °C; purple 2 GPa/1200 °C; green 3 GPa/1200 °C). Compositions are compared to post-collisional lavas with K/Na > 2 (faint yellow diamonds) and < 2 (faint blue diamonds). Generally, melts of sediment and basanite increase in K/Na as reaction proceeds. Sediment/dunite reaction melts are generally high in SiO<sub>2</sub> and total alkalis (A) and only show similarities to post-collisional lavas at T > 900 °C, while melts of phlogopite-enriched dunite, which formed by sediment/dunite reaction (termed 2<sup>nd</sup>-stage melt, \*Chapter 3), are comparable to post-collisional lavas. The basanite/dunite reaction melts (green circles) attain K<sub>2</sub>O contents of 3 wt% and K/Na of 0.5-1.2 (B, C).

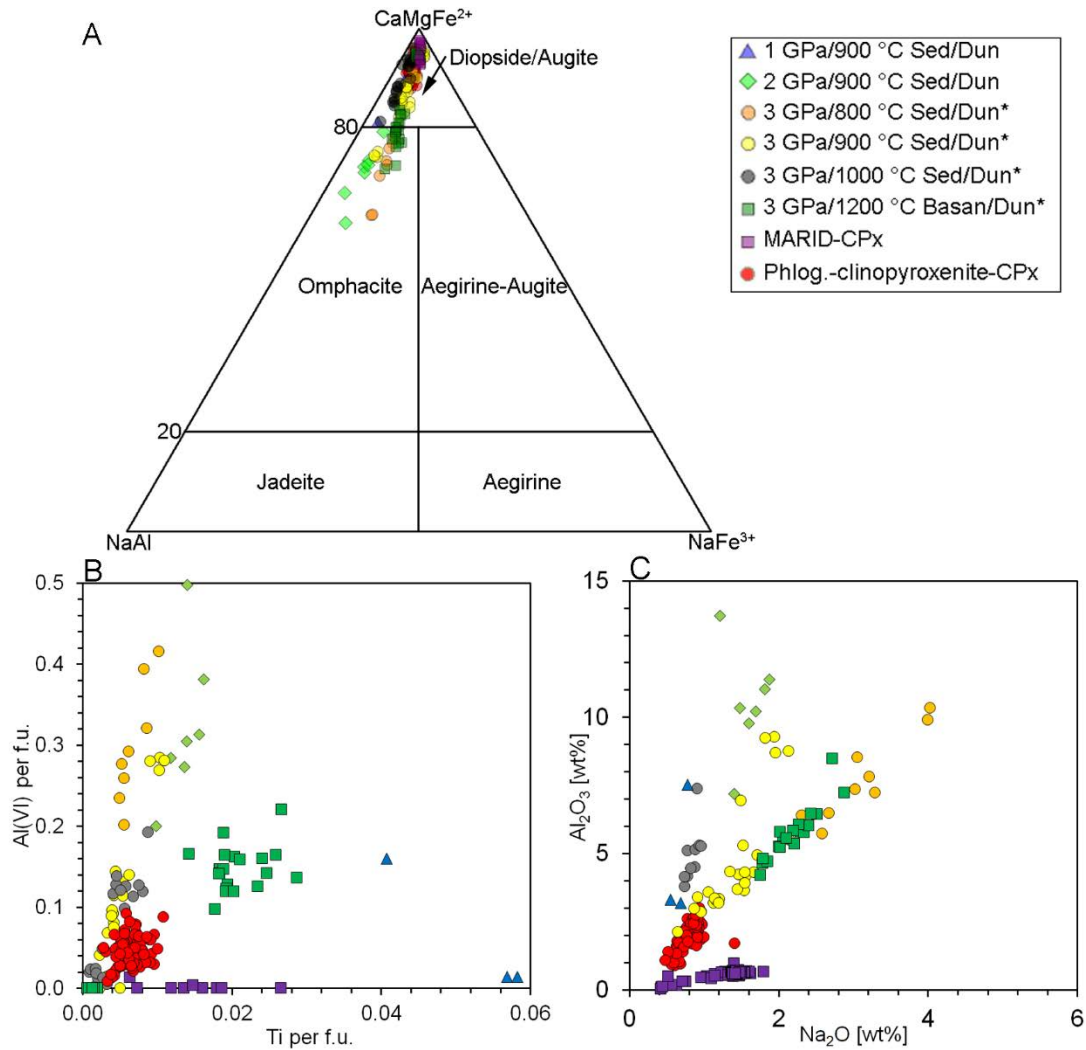


**Fig. 4.3:** Compositions of pyroxenes from reaction experiments (blue triangles 1 GPa/900 °C; lime diamonds 2 GPa/900 °C; orange circles 3 GPa/800 °C; yellow circles 3 GPa/900 °C; grey circles 3 GPa/1000 °C; green squares 3 GPa/1200 °C) compared to MARID-type clinopyroxenes (purple squares) and phlogopite clinopyroxenite xenoliths from post-collisional settings (red circles). (A) The  $\text{CaMgFe}^{2+}$ - $\text{NaAl}$ - $\text{NaFe}^{3+}$  diagram (Morimoto, 1988) shows that clinopyroxenes compositionally vary from the diopside/augite field towards omphacitic composition. The Al (VI) *versus* Ti (a.f.u.) plot (B) show that clinopyroxenes associated with melts of sediment trend to higher Al(VI) at given Ti compared to those from basanite melts. While clinopyroxenes from phlogopite clinopyroxenite xenoliths plot with experimental samples, MARID clinopyroxenes are devoid of Al(VI) and plot at very low  $\text{Al}_2\text{O}_3$  at given  $\text{Na}_2\text{O}$  (C).

Phlogopites formed by sediment/dunite reaction show >8 wt%  $\text{K}_2\text{O}$  and 0.1-0.5 wt%  $\text{Na}_2\text{O}$  as well as 10-17 wt%  $\text{Al}_2\text{O}_3$  and 0.1-1.4 wt%  $\text{TiO}_2$ , while those from basanite/dunite reaction have higher  $\text{Na}_2\text{O}$  of 0.8-1.7 wt% and 2.2-2.6 wt%  $\text{TiO}_2$  (Fig. 4.4 A,B). Experimental phlogopites have compositions similar to those from post-collisional lavas but show generally higher contents of  $\text{Al}_2\text{O}_3$  similar to those in phlogopite of phl-clinopyroxenites xenoliths (Fig. 4.4 B). Garnet from sediment/dunite reaction are lower in  $\text{MgO}$  (<13 wt%) and high in  $\text{MnO}$  (>3 wt%), compared to those from basanite/dunite reaction which attain >21 wt%  $\text{MgO}$  (Table 4.3).



**Table 4.3:** Average analyses for silicate phases in the experiments (oxides in wt%).

Olivine	Na <sub>2</sub> O	K <sub>2</sub> O	MnO	SiO <sub>2</sub>	MgO	FeO	Al <sub>2</sub> O <sub>3</sub>	Cr <sub>2</sub> O <sub>3</sub>	CaO	TiO <sub>2</sub>	Total
1 GPa/900 °C Sediment/Dunite reaction	0.01(1)	0.01(1)	0.17(2)	40.3(1)	50.5(2)	8.6(1)	0.01(1)	0.03(2)	0.06(1)	0.01(1)	99.7(2)
2 GPa/900 °C Sediment/Dunite reaction	0.02(2)	0.01(1)	0.13(2)	40.5(1)	50.5(1)	8.61(4)	0.02(1)	0.03(2)	0.04(1)	0.01(1)	99.8(3)
3 GPa/1200 °C Basanite/Dunite reaction	0.01(1)	0.01(1)	0.35(9)	41.4(6)	55(1)	5(2)	0.03(2)	0.05(3)	0.06(4)	0.02(1)	102(1)
Phlogopite	Na <sub>2</sub> O	K <sub>2</sub> O	MnO	SiO <sub>2</sub>	MgO	FeO	Al <sub>2</sub> O <sub>3</sub>	Cr <sub>2</sub> O <sub>3</sub>	CaO	TiO <sub>2</sub>	Total
2 GPa/900 °C Sediment/Dunite reaction	0.25(5)	9.6(4)	0.06(6)	41(1)	25(2)	3.2(5)	13(1)	0.5(4)	0.2(4)	0.5(4)	94(1)
3 GPa/1200 °C Basanite/Dunite reaction	1.1(3)	8.8(6)	0.03(3)	39.6(9)	23.7(8)	4.4(4)	15.1(3)	0.2(2)	0.09(5)	2.2(5)	96(1)
Clinopyroxene	Na <sub>2</sub> O	K <sub>2</sub> O	MnO	SiO <sub>2</sub>	MgO	FeO	Al <sub>2</sub> O <sub>3</sub>	Cr <sub>2</sub> O <sub>3</sub>	CaO	TiO <sub>2</sub>	Total
1 GPa/900 °C Sediment/Dunite reaction	0.7(1)	0.12(6)	0.6(4)	49.0(7)	11(1)	9.7(1)	5(2)	0.04(2)	21.2(6)	1.8(3)	99.24(6)
2 GPa/900 °C Sediment/Dunite reaction	1.6(2)	0.4(7)	0.9(4)	50(2)	11(2)	4(1)	11(2)	0.04(2)	18(2)	0.48(7)	97(1)
3 GPa/1200 °C Basanite/Dunite reaction	2.2(3)	0.01(1)	0.10(3)	53.3(6)	15.9(8)	4.5(5)	6(1)	0.13(9)	18.2(5)	0.8(1)	100.9(6)
Orthopyroxene	Na <sub>2</sub> O	K <sub>2</sub> O	MnO	SiO <sub>2</sub>	MgO	FeO	Al <sub>2</sub> O <sub>3</sub>	Cr <sub>2</sub> O <sub>3</sub>	CaO	TiO <sub>2</sub>	Total
3 GPa/1200 °C Basanite/Dunite reaction	0.07(3)	0.01(2)	0.48(3)	58.2(4)	38.8(6)	2.1(8)	1.4(1)	0.12(4)	0.59(5)	0.05(1)	101.9(4)
Garnet	Na <sub>2</sub> O	K <sub>2</sub> O	MnO	SiO <sub>2</sub>	MgO	FeO	Al <sub>2</sub> O <sub>3</sub>	Cr <sub>2</sub> O <sub>3</sub>	CaO	TiO <sub>2</sub>	Total
2 GPa/900 °C Sediment/Dunite reaction	0.3(2)	0.2(1)	6(2)	40(1)	7.3(5)	10.4(4)	20(1)	0.06(4)	13.7(6)	1.4(4)	99(1)
4 GPa/1000 °C Sediment melting	0.14(2)	0.01(1)	3(2)	42.0(7)	13(5)	8(3)	21.9(4)	-	12(3)	0.8(2)	101(2)
3 GPa/1200 °C Basanite/Dunite reaction	0.08(8)	0.01(2)	0.8(4)	42(1)	21(4)	8(4)	22(2)	2(3)	5(2)	0.7(6)	101.6(5)

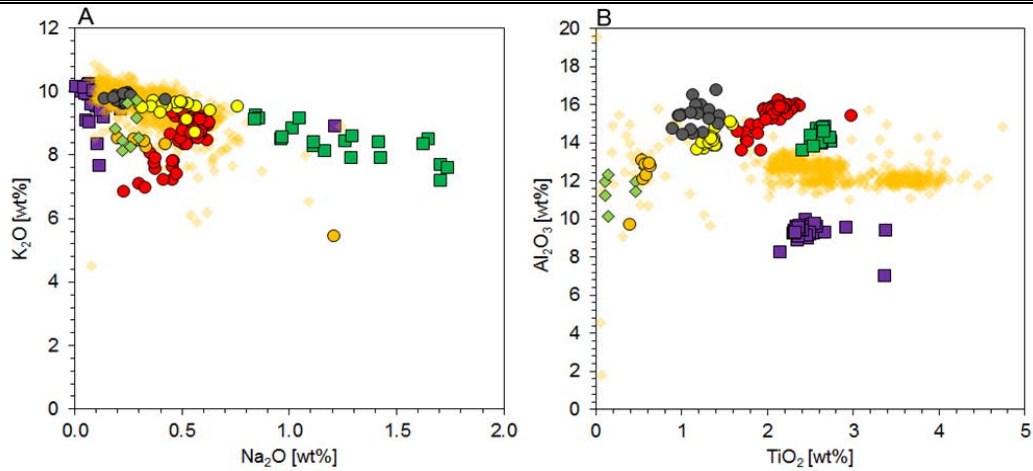


**Fig. 4.4:** Compositions of phlogopites from experiments (lime diamonds 2 GPa/900 °C; orange circles 3 GPa/800 °C; yellow circles 3 GPa/900 °C; grey circles 3 GPa/1000 °C; green squares 3 GPa/1200 °C) compared to phlogopites in post-collisional lavas (yellow diamonds, Fritschle et al., 2013), phlogopite clinopyroxenite xenoliths (red circles), and MARID phlogopites (purple squares, Förster et al., 2017; 2018). (A) K<sub>2</sub>O *versus* Na<sub>2</sub>O shows that experimental phlogopites from sediment/dunite reaction (circles) plot at Na<sub>2</sub>O <0.5 wt%, while those from basanite/dunite reaction (green squares) attain 0.8-1.7 wt% Na<sub>2</sub>O. (B) Al<sub>2</sub>O<sub>3</sub> *versus* TiO<sub>2</sub> shows that experimental phlogopites attain 10-17 wt% Al<sub>2</sub>O<sub>3</sub> and 0.2-1.5 wt% TiO<sub>2</sub> for sediment/dunite reaction and 2-2.5 wt% for basanite/dunite reaction. Phlogopites from post-collisional lavas show a wide range with most data points at 12-14 wt% Al<sub>2</sub>O<sub>3</sub> and 2-4 wt% TiO<sub>2</sub>, while phlogopites from phlogopite clinopyroxenite xenoliths attain higher Al<sub>2</sub>O<sub>3</sub> of 13-16 wt% at 1.5-2.2 wt% TiO<sub>2</sub>. MARID-phlogopites show overall lower Al<sub>2</sub>O<sub>3</sub> values at similar TiO<sub>2</sub>.

#### 4.3.3 Trace element composition

N-MORB normalized trace element pattern of sediment/dunite reaction melts are high in large ion lithophile elements (LILE), high field strength elements (HFSE), and show pronounced negative anomalies at Nb, P, and Ti (Fig. 4.5 A). The pattern overall follows that of post-collisional lavas with K/Na >2 (Prelević et al., 2008b; 2013), while the starting bulk sediment composition shows higher heavy rare earth elements (REE) and lower LILE. The N-MORB normalized trace element patterns of basanite/dunite reaction melts (Fig. 4.5 B) show lower mass fractions for LILE and a slight negative anomaly for Ti. The reaction melts fall broadly within the array found for post-collisional lavas showing low K/Na of 0.5-1 (Prelević et al., 2008b; 2013). K-rich lavas with K/Na of 1-2 show both geochemical signatures as present in rocks with K/Na of 0.5-1 and K/Na >2 (Fig. 4.5) and thus form a transient group where rocks can be formed by 'orogenic' and 'anorogenic' processes. CI-Chondrite normalized REE of clinopyroxene are steeper for sediment/dunite reaction experiments compared to basanite/dunite reaction (Fig. 4.6 A), while CI-Chondrite normalized garnet of both reaction experiments are nearly identical in composition (Fig. 4.6 B). Garnet which crystallized from the sediment melting experiment, however, has lower mass fractions of light REE (Fig. 4.6 B). The mass fractions of compatible trace elements within phlogopite (Fig. 4.7) of both experiments from sediment/dunite and basanite/dunite reaction fall within the broad range reported for phlogopites in post-collisional lavas (Fritschle et al., 2013). Partitioning coefficients for clinopyroxene/melt, garnet/melt, and phlogopite/melt for both sediment/dunite and basanite/dunite reaction are generally <1 except the heavy REE in garnet and LILE in phlogopite (Fig. 4.8 A-C). Partitioning of trace elements between clinopyroxene and garnet is largely controlled by the strong differences in trace element partitioning in clinopyroxene/melt which reaches higher values for sediment/dunite reaction (Fig. 4.8 D). Ratios of Th/La *versus* Sm/La, Th/Yb *versus* Nb/Yb, and Sm/Nd *versus* Rb/Sr show that sediment/dunite reaction melts plot with post-collisional lavas (Prelević et al., 2008b) (Fig. 4.9 A-C). Those from basanite/dunite reaction attain the lowermost ratios of Th/La, Rb/Sr, and high Nb/Yb at the end of the spectrum found within post-collisional lavas. Lithium is generally enriched in sediments as well as melts of sediment and phlogopites forming from sediment-melt/dunite reaction attain high Li concentrations (Fig. 4.9 D). In contrast, basanite/dunite reaction melts and phlogopites are very low in Li.

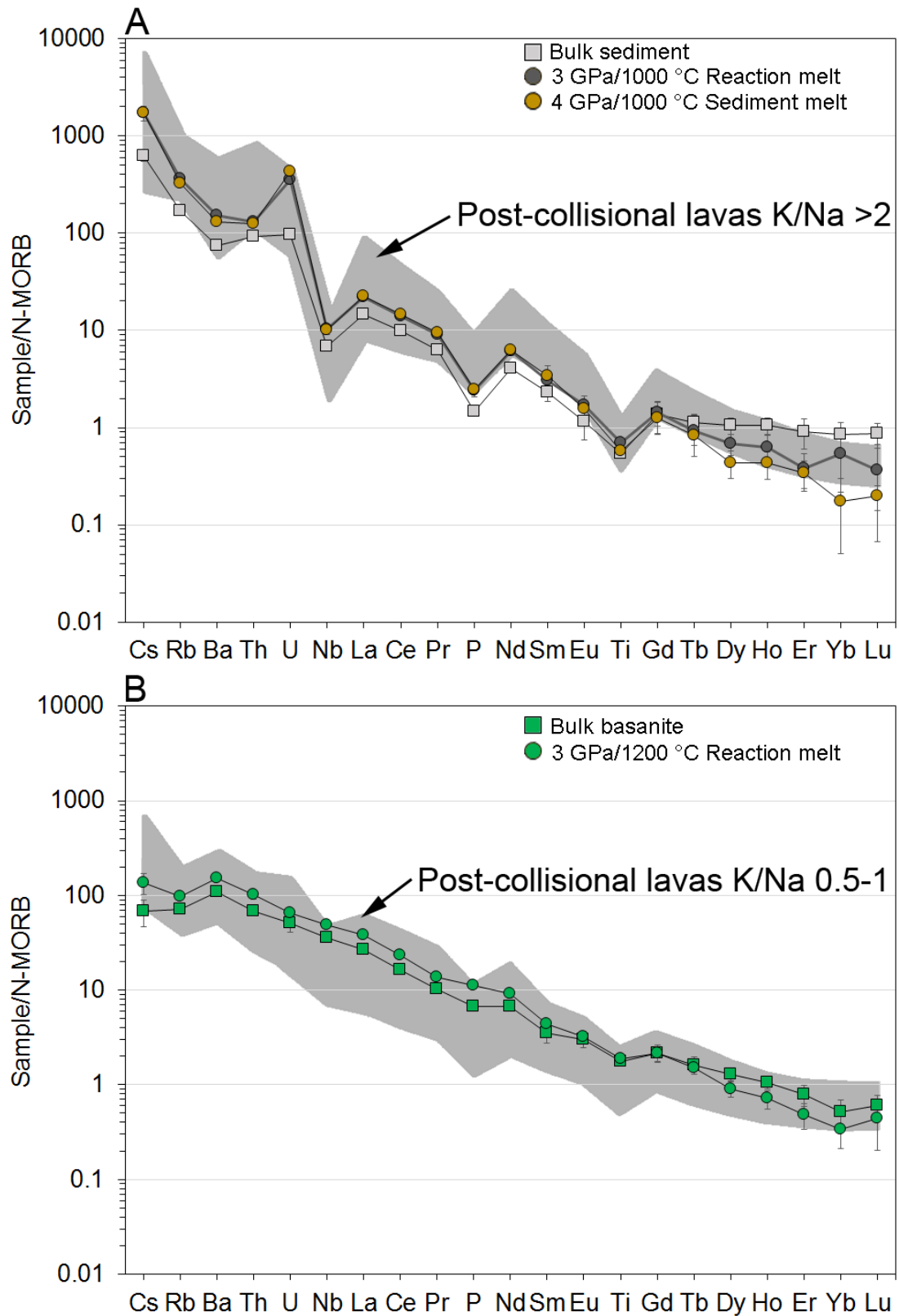


**Fig. 4.5:** Trace element compositions of starting materials (grey squares, sediment; green squares, basanite) compared to experimental melts (grey circles 3 GPa/1000 °C; brown circles 4 GPa/1000 °C; green circles 3 GPa/1200 °C) and post-collisional lavas (shaded area, Prelević et al., 2008b). The sediment/dunite reaction melts (A) are rich in Cs, Rb, Ba, and show negative anomalies at Nb, P, and Ti, similar to post-collisional lavas with K/Na >2. The basanite/dunite reaction melt (B) shows lower Cs, Rb, Ba, and is devoid of any pronounced anomaly. The observed pattern plots within post-collisional lavas that overall show lower K/Na of 0.5-1.0. Normalized to N-MORB (Sun and McDonough, 1989).

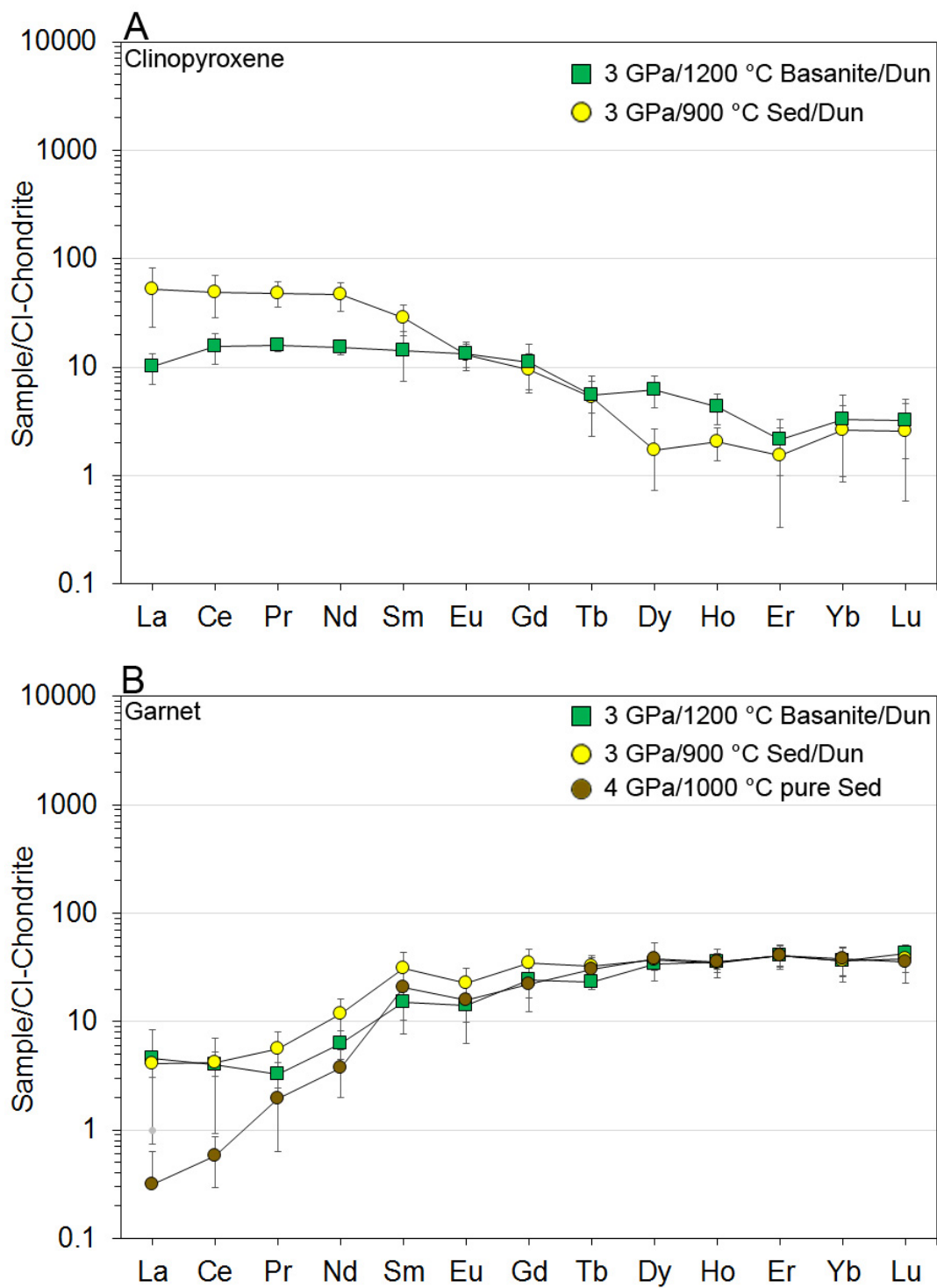


**Fig. 4.6:** C1-Chondrite normalized REE patterns of clinopyroxene (A) and garnet (B) of samples from basanite/dunite (green squares), sediment/dunite reaction (yellow circles), and pure sediment melting (brown circles). Clinopyroxene samples from sediment/dunite reaction show higher light REE to heavy REE fractionation than those from basanite/dunite reaction (A). Garnet samples from sediment/dunite and basanite/dunite reaction experiments are similar in composition and attain higher light REE than those from pure sediment melting experiments (B), while their heavy REE signatures are nearly identical.

## 4.4 Discussion

### 4.4.1 Sediment/dunite reaction

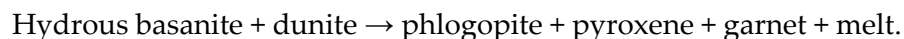
The reaction of melts of sediment with depleted mantle (dunite) generally lead to the formation of a strongly layered reaction zone and the reorganization of elements from both domains into metasomatic phases (Fig. 4.1 B). Silica is the most mobile element as evident from orthopyroxene veins on olivine grain boundaries, followed by K and Al in phlogopite, and Ca in clinopyroxene. The infiltrating reaction melts show a general trend of decrease in SiO<sub>2</sub> with increasing temperature and melt fraction, thus diluting SiO<sub>2</sub> within the liquid (Fig. 4.2, Table 4.1). Generally, K<sub>2</sub>O is enriched and K/Na ratios are higher in melts compared to the starting sediment composition (Fig. 4.2 B,C). The trace element concentrations of experimental glasses show a steepened pattern from LILE, HFSE, and light REE to heavy REE when compared to the starting sediment composition (Fig. 4.5 A). Bulk sediment trace element contents are too low in LILE and too high in heavy REE to satisfy the values observed for post-collisional lavas, while experimental melt compositions fall within the range of natural rocks with K/Na >2 (Prelević et al., 2008b). The mass fraction of K in the melt is controlled by the composition of the phases in the residue of the melted, which are clinopyroxene and garnet, and thus devoid of K (Fig. 4.3, Table 4.1). Clinopyroxenes show a strong zonation across the reaction zone from a diopsidic end-member within the dunite towards an omphacitic composition within the former sediment (Fig. 4.3 A), thus transforming the residual sediment to an eclogite-like assemblage. The K-rich, rhyolitic melt formed from the sediment infiltrates and reacts with olivine following the reaction:



This reaction takes place in all sediment/dunite reaction experiments. Since the solidus increases from 800 °C for the sediment to ~1150 °C for phlogopite-pyroxenite (Förster et al., 2017), the melt is gradually consumed. Phlogopite formed during this reaction shares strong similarities to that occurring in metasomatic phlogopite clinopyroxenite mantle xenoliths (Fig. 4.4), while they possess slightly higher Al<sub>2</sub>O<sub>3</sub> than those in post-collisional lavas (Fritschle et al., 2013). However, compatible trace elements are within the range reported for post-collisional lavas (Fritschle et al., 2013) (Fig. 4.7). Re-melting of the metasomatized dunite in a 2<sup>nd</sup>-stage capsule experiment produced melts with K<sub>2</sub>O mass fractions of 8-9 wt% (Fig. 4.2) and demonstrated that high-K lavas can form in a multi-stage metasomatism and melting process (Chapter 3).

#### 4.4.2 Hydrous-basanite/dunite reaction

The reaction of melt of hydrous basanite with dunite also leads to strong layering and reorganization of elements from both domains into metasomatic phases. Silica, K, Al, and Ca are the most mobile elements and caused the crystallisation of a phlogopite-bearing pyroxenite in place of dunite (Fig. 4.1 A). Between melt and dunite, an eclogite layer formed, solely composed of garnet and clinopyroxene. Clinopyroxenes show a trend from diopside composition within the dunite to omphacite within the garnet-clinopyroxene layer (Fig. 4.3 A). Analogous to the sediment/dunite reaction, melts in the basanite/dunite reaction show higher K<sub>2</sub>O and K/Na than the starting composition (Fig. 4.2). Trace element compositions of both the basanite starting composition and melts formed in the reaction zone fall within the range for post-collisional lavas with K/Na 0.5-1 (Prelević et al., 2008b). In contrast to the sediment/dunite reaction, the melt in the basanite/dunite reaction experiments is SiO<sub>2</sub>-undersaturated, yet the reaction leads to the formation of phlogopite pyroxenites. Since the experiment is conducted above the solidus of phlogopite pyroxenite and phlogopite peridotite (Condamine et al., 2016; Förster et al., 2017), the melt present in the capsule is not consumed by the reaction, thus:



While the melt on the product side still corresponds to basanite according to the total alkali *versus* silica diagram (Fig. 4.1 A), it is more foiditic in composition and contains higher alkalis than the starting basanite which lies at the border to trachybasalt. Phlogopites are higher in Na<sub>2</sub>O and TiO<sub>2</sub> compared to those from melts of sediment/dunite reaction (Fig. 4.4) and reflect higher Na<sub>2</sub>O partitioning and content of the basanitic melt. However, compatible trace elements of phlogopites (Fig. 4.7) are similar to those within post-collisional lavas and show lower Cs, and higher Ni compared to those from melts of sediment/dunite reaction (Fritschle et al., 2013).

#### 4.4.3 Trace element partitioning

For both starting materials, sediment and basanite, trace element contents of reaction melts were enriched in LILE, HFSE, and light REE, while heavy REE were found to be depleted (Fig. 4.5). Partitioning is controlled by the two main minerals of the residue, clinopyroxene and garnet, which incorporate mainly light REE and heavy REE, respectively (Fig. 4.6).

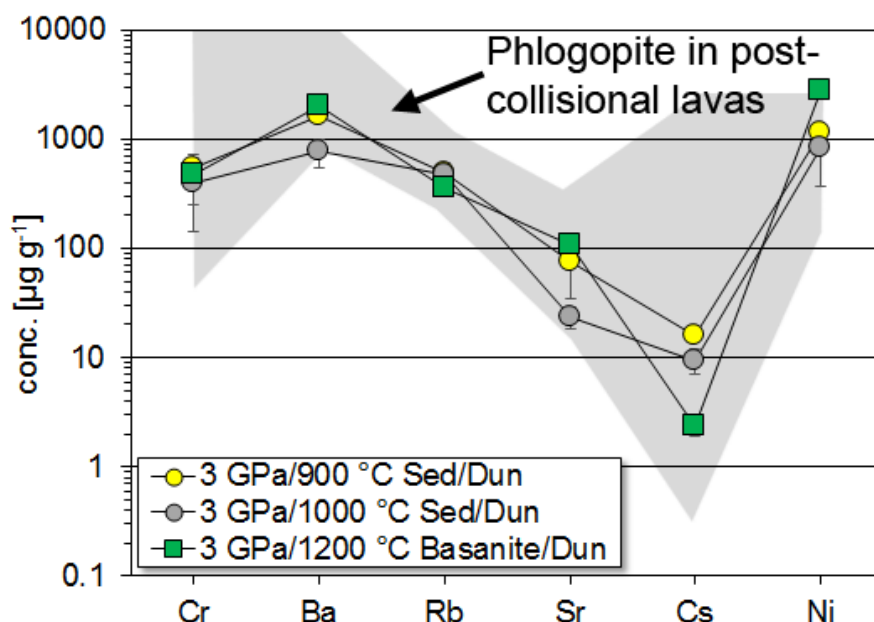


**Fig. 4.7:** Concentration of compatible trace elements in phlogopite from experiments (yellow circles 3 GPa/900 °C; grey circles 3 GPa/1000 °C; green squares 3 GPa/1200 °C) compared to samples from post-collisional lavas (Fritschle et al., 2013). All experimental samples from basanite/dunite and sediment/dunite reaction fall within the range observed for phlogopites in post-collisional lavas regardless of starting material.

Partition coefficients for clinopyroxene/melt are generally below unity except for Nd-Eu and slightly prefers light REE over heavy REE for the sediment/dunite reaction melts (Fig. 4.8 A), while those from the basanite/dunite reaction melt show a preference of heavy REE over light REE, which is in agreement with previous studies (Foley et al., 1996; Hauri et al., 1994; Johnston and Schwab, 2004; Wang and Foley, 2018). Partition coefficients are higher for sediment/dunite reaction melts than basanite/dunite reaction melts as a result of their more polymerized Si-rich compositions (Nash and Crecraft, 1985), and are even higher for Si-rich phyllite melts from Wang and Foley (2018). Garnet/melt partitioning is strongly dependant on the garnet composition, which is almandine-rich (Fe-rich) for the sediment/dunite and pyrope-rich (Mg-rich) for the basanite/dunite reaction experiments (Table 4.3). Heavy REE are strongly compatible in both garnet types (Fig. 4.6 B), while garnet/melt partition coefficients are slightly higher for light REE for the almandine-rich garnet in the sediment/dunite reaction experiments (Fig. 4.8 B). For both garnet types, the slope is clearly positive, denoting their strong preference for heavy REE over light REE (Johnson, 1998; Pertermann et al., 2004; Shimizu and Kushiro, 1975; van Westrenen et al., 2001; Wang and Foley, 2018). For sediment/dunite garnets, partitioning is above unity for elements to the right of Nd, while for basanite/dunite garnets, they are above unity from Dy (Fig. 4.8 B). Partitioning between phlogopite/melt is above unity for Cs-Ba and Ti in the



sediment/dunite reaction melts and for Rb, Ba, and Ti for the basanite/dunite reaction melts (Fig. 4.8 C) similar to natural phlogopites in lamprophyre and basanite (Foley et al., 1996; LaTourrette et al., 1995). Partitioning between clinopyroxene and garnet shows that within the residue of both sediment/dunite and basanite/dunite reaction pairs, light REE are enriched into clinopyroxene and heavy REE into garnet (Fig. 4.8 D).

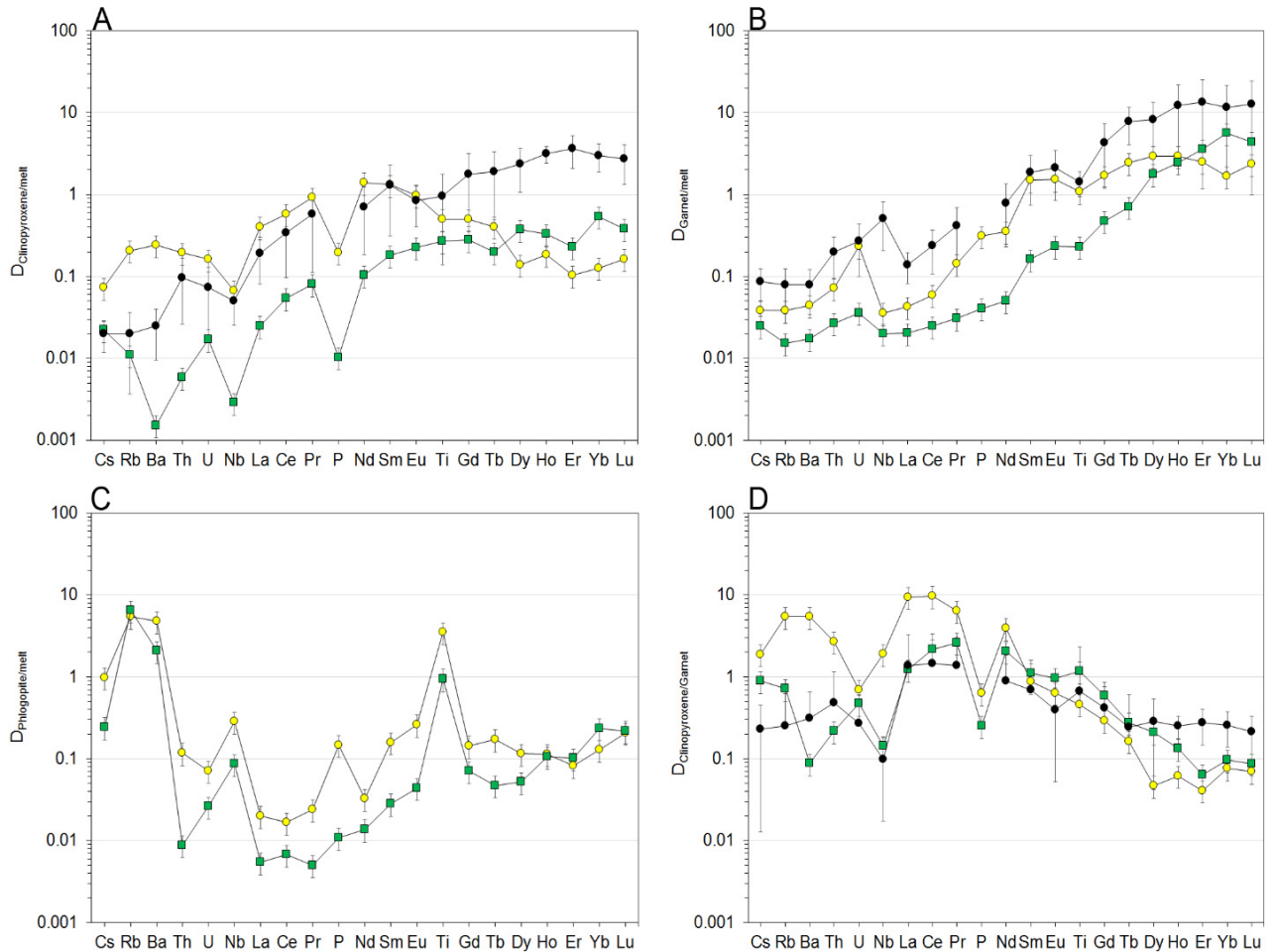


**Fig. 4.8:** Partition coefficients for trace elements of (A) clinopyroxene/melt (B) garnet/melt (C) phlogopite/melt pairs, and (D) clinopyroxene/garnet from sediment/dunite experiment at 3 GPa/900 °C (yellow circles) and basanite/dunite reaction at 3 GPa/1200 °C (green circles) compared to values from Wang and Foley (2018) (black circles). Generally, partition coefficients are higher for the sediment/dunite experiment than basanite/dunite with the exception of heavy REE. Partition coefficients are generally <1 for mineral/melt (A-C) except for heavy REE in garnet (B) and Cs, Rb, Ba, and Ti in phlogopite (C). Partitioning of trace elements between clinopyroxene and garnet (D) is mainly influenced by partitioning of clinopyroxene and melt (A).

#### 4.4.4 Trace elements as indicators for recycling- and mantle melting processes

Trace element distribution patterns in melts produced by sediment/dunite reaction and basanite/dunite reaction show that both produce distinct signatures that can be found within post-collisional lavas (Fig. 4.5). While lavas with  $K/Na > 2$  are extremely enriched in LILE and HFSE with pronounced negative anomalies at Nb, P, and Ti, those with  $K/Na$  0.5-1 are less

enriched and show a negative Rb, P, and Ti-anomaly. Due to enrichment of LILE, HFSE, and light REE over heavy REE during sediment melting and reaction, the negative anomalies at Nb, P, and Ti of the bulk sediment composition are pronounced within the sediment/dunite reaction melts. This strongly suggests that Nb, P, and Ti anomalies within K/Na >2 post-collisional lavas are inherited from a source mantle that had been metasomatized by a sediment-derived melt (Prelević et al., 2008b; 2013). The basanite/dunite reaction melt behaves in a similar way to the sediment/dunite reaction melts and LILE, HFSE, and light REE are enriched over heavy REE. However, the basanite/dunite reaction melts show a negative Rb anomaly (Fig. 4.5 B), which results from Rb/Cs fractionation during the formation of phlogopite which has contrasting  $D_{Rb}$  of  $\sim 6.5$  and  $D_{Cs}$  of  $\sim 0.25$ , thus slightly enriching Cs in the melt (Fig. 4.8 C). The strong enrichment of Th over REE within K/Na >2 post-collisional lavas is evident in the Th/La *versus* Sm/La plot and Th/Yb *versus* Nb/Yb where post-collisional lavas attain high Th/La and Th/Yb (Fig. 4.9 A,B). The grouping of sediment/dunite and basanite/dunite reaction melts around their starting composition at Th/La  $\sim 0.3$ , Sm/Nd 0.1-0.2 and at Th/La  $\sim 0.1$ , Sm/La 0.5-2.0 suggests that variations within post-collisional lavas reflect heterogeneities in recycled components (Fig. 4.9 A). In both experimental samples and post-collisional lavas, Th/Yb *versus* Nb/Yb are positively correlated (Fig. 4.9 B). Mantle melts attain lowest Th/Yb and high Nb/Yb as evident from the basanite/dunite reaction experiments and MARID compositions (Förster et al., 2018), while those from sediment/dunite reaction attain highest Th/Yb and low Nb/Yb. Since sediment/dunite and basanite/dunite reaction melts form parallel trending lines and overlap with the bulk starting material compositions, differences in Th/Yb *versus* Nb/Yb are inherited from the composition of the source material. Basanite/dunite reaction melts also attain lowest Rb/Sr, identical with the bulk starting material composition at similar Sm/Nd to the sediment/dunite reaction melts which attain higher Rb/Sr than their starting composition and thus show higher  $D_{Rb}$  than  $D_{Sr}$  during melting and reaction (Fig. 4.9 C). While a small proportion of samples from post-collisional lavas show high Rb/Sr >0.2 similar to the sediment/dunite reaction melts, most analysed samples plot at Rb/Sr of  $\sim 0.1$ , thus between sediment/dunite and basanite/dunite reaction melts. In the Rb *versus* Li plot, phlogopites attain highest Rb concentrations in accordance with  $D_{Rb(\text{phlogopite/melt})}$  of  $\sim 6.5$  for basanite/dunite and  $\sim 5$  for sediment/dunite reaction experiments (Fig. 4.9 D). Lithium, a generally incompatible element attains  $D_{Li(\text{phlogopite/melt})}$  of  $\sim 0.7$  for both basanite/dunite and sediment/dunite reaction melts. Lithium concentrations of generally  $10\text{--}60\ \mu\text{g}\cdot\text{g}^{-1}$  to  $220\ \mu\text{g}\cdot\text{g}^{-1}$  are common within post-collisional lavas (Foley et al., 2013) and can be explained by concentrations of  $15\text{--}85\ \mu\text{g}\cdot\text{g}^{-1}$  to up to  $310\ \mu\text{g}\cdot\text{g}^{-1}$  within recycled sediments.

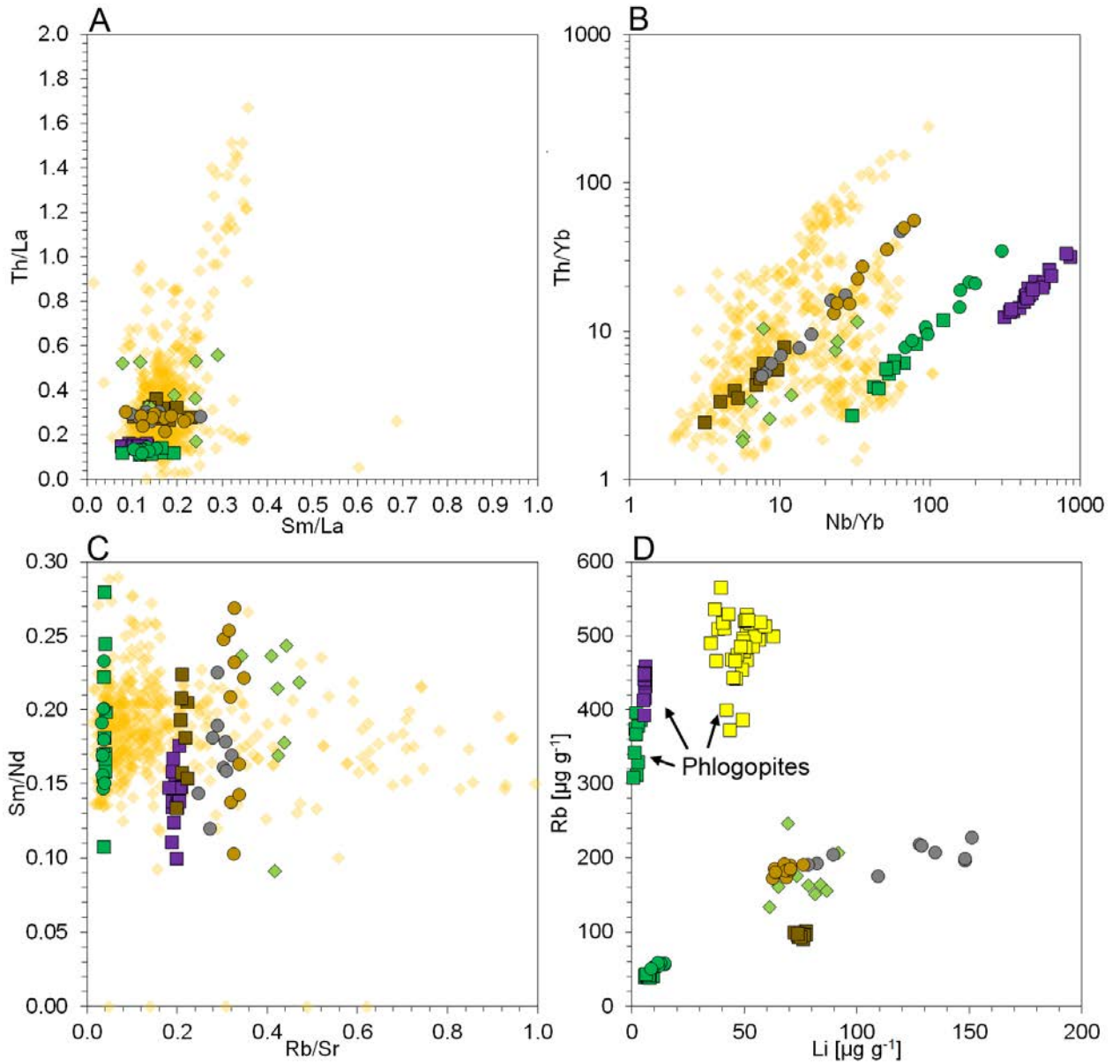


**Fig. 4.9:** Trace element compositions of experimental melts (lime diamonds 2 GPa/900 °C; grey circles 3 GPa/1000 °C; brown circles 4 GPa/1000 °C; green squares 3 GPa/1200 °C) compared to post-collisional lavas (yellow diamonds) and MARID xenoliths (purple squares, Förster et al., 2018). (A) Th/La *versus* Sm/La shows experimental sediment/dunite reaction melts at Th/La 0.2-0.6, plotting with the bulk of post-collisional lavas, while basanite/dunite reaction melts plot at Th/La <0.2 with MARID xenoliths. (B) Th/Yb *versus* Nb/Yb of sediment/dunite reaction melts plot with post-collisional lavas, while basanite/dunite reaction melts and MARID xenoliths attain higher Nb/Yb ratios and plot largely outside the field of post-collisional lavas. (C) Sm/Nd *versus* Rb/Sr shows that sediment/dunite reaction melts largely at Rb/Sr >0.2 while most post collisional lavas plot around Rb/Sr of 0.1. Samples from basanite/dunite reaction are very low in Rb/Sr and attain ratios of 0.04. (D) In the Rb *versus* Li plot, sediment/dunite reaction melts attain high Li mass fractions of 50-150  $\mu\text{g}\cdot\text{g}^{-1}$ , while corresponding phlogopites (yellow squares) attain similar mass fractions of Li (50  $\mu\text{g}\cdot\text{g}^{-1}$ ). Basanite/dunite reaction melts and corresponding phlogopites (green squares) attain low Li mass fractions of <20  $\mu\text{g}\cdot\text{g}^{-1}$  similar to MARID phlogopites (purple squares).

#### 4.4.5 Melts of sediment- *versus* mantle melt-metasomatism

Irrespective of starting composition, the reaction of hydrous melt with depleted peridotite leads to metasomatic overprinting of the peridotite and enrichment in K, Al, Si, LILE, HFSE, and light REE. However, metasomes formed by reaction between melts of sediment/dunite and basanite/dunite pairs show significant differences in major and trace element concentrations. Metasomes formed by melts of sediment are generally more strongly enriched in LILE (especially Cs) with higher Li, Th/La, Th/Yb, and Rb/Sr compared to those formed by mantle melts (Fig. 4.5, 4.9), and likely represent the source for post-collisional lavas with high K/Na of >2 of 'orogenic' origin such as shoshonites, Roman-type lavas, and lamproites (Prelević et al., 2008b). Phlogopites formed by melts of sediment/dunite reaction are also lower in Na<sub>2</sub>O and TiO<sub>2</sub> than those from basanite/dunite reaction and reflect the low Ti, Na composition of recycled sediments (Fig. 4.4). Additionally, phlogopites formed by hydrous basanite/dunite reaction show lowest Cs concentrations, which reflect its low concentrations in the basanite starting composition (Fig. 4.7). While subduction and melts of sediment/dunite reaction generally occurs at temperatures <1000 °C, below the solidus of phlogopite pyroxenites (~1150 °C), the metasome formation in this scenario consumes all melt and requires a secondary activation of the metasome by later heat input from the asthenosphere which is enabled by e.g. slab rollback as evident from Turkey and Mexico (Gülmez et al., 2016; Vigouroux et al., 2008). The hydrous basanite/dunite reaction shows a different story since the reaction takes place above the solidus of phlogopite pyroxenites and phlogopite peridotite (Condamine et al., 2016; Förster et al., 2017), and thus the melt is not completely consumed during the reaction. Instead, the percolating and reacting melt attains a K-rich composition by crystallizing an eclogite-like layer, bearing omphacitic, Na-rich, clinopyroxene in contact with the dunite (Fig. 4.3 A). Thus, the melt dynamically increases its K/Na by leaving behind a low K/Na eclogite, while the dunite next to it is strongly enriched in phlogopite and orthopyroxene (Fig. 4.1 A). Since hydrous melting of eclogite leads to the formation of low K/Na tonalitic melt which would dilute high K/Na melt from the phlogopite pyroxenites of the metasomatized dunite, maximum K/Na is limited by equilibrium with eclogite (Lambert and Wyllie, 1970; Xiong, 2006). Thus, the basanite/dunite reaction melts might represent post-collisional lavas with lower K/Na of 0.5-1 of extension-related 'anorogenic' origin such as K-rich foidites/basanites and kamafugites (Foley et al., 1987; Prelević et al., 2008a), which is in accordance with the lower content of LILE, HFSE and low Th/La and Th/Nb (Fig. 4.5, 4.9).

However, if eclogite delaminates as a result of its higher density (Elkins-Tanton and Foulger, 2005), the low K/Na part will be separated from the phlogopite pyroxenites and lavas of 'anorogenic' origin can reach K/Na >1 which might explain the mixed appearance of 'orogenic' and 'anorogenic' rocks at K/Na of 1-2.

#### 4.5 Conclusion

In this study we reacted layered sediment/dunite and hydrous basanite/dunite experiments at thermobaric conditions of 1-4 GPa/800-1200 °C that represent a subduction environment (Fig. 4.10 A) for the sediment/dunite, and a non-cratonic lithospheric mantle environment (Fig. 4.10 B) for the hydrous basanite/dunite reaction experiments. All experiments show the growth of a reaction zone between both starting materials, which is strongly enriched in K, Al, and Si as evident from metasomatically grown phases such as pyroxene and phlogopite (Fig. 4.1). In the sediment/dunite reaction experiments, the melt of sediment is highly enriched in LILE, HFSE, and light REE similar to post collisional lavas with K/Na >2 (Fig. 4.5 A) and shows high Th/La, Th/Yb, and Rb/Sr (Fig. 4.9). Since the products of the reaction of melts of sediment with dunite are below their hydrous solidus, all melt is consumed as it reacts with the depleted peridotite. In a subduction zone scenario this leads to progressive growth of metasomatic phlogopite pyroxenite within the fore-arc (Fig. 4.10 A), which is only activated after the cessation of subduction during asthenospheric upwelling by slab rollback, tear, or break-off. Melts of the hydrous basanite/dunite reaction experiments show LILE, HFSE, and REE patterns similar to lavas in post-collisional settings with K/Na of 0.5-1 (Fig. 4.5 B). In contrast to sediment/dunite reaction melts, the hydrous basanite/dunite reaction melts are low in Th/La, Th/Yb, and Rb/Sr and high in Nb/Yb (Fig. 4.9). Since the basanite/dunite reaction occurs above the solidus of phlogopite pyroxenite, the melt is not totally consumed and instead, dynamically increases in K/Na as it percolates through the dunite by reacting to form a low K/Na eclogitic residue containing omphacitic clinopyroxene (Fig. 4.3 A). Accordingly, upwelling of asthenospheric mantle due to e.g. stretching and rifting of the lithosphere (Fig. 4.10 B) leads to incipient melting of the asthenosphere and metasomatic growth of phlogopite pyroxenites within the lithospheric mantle. The enrichment of K within the lithospheric mantle is thus not dependent on the migration of liquids that are originally ultrapotassic.

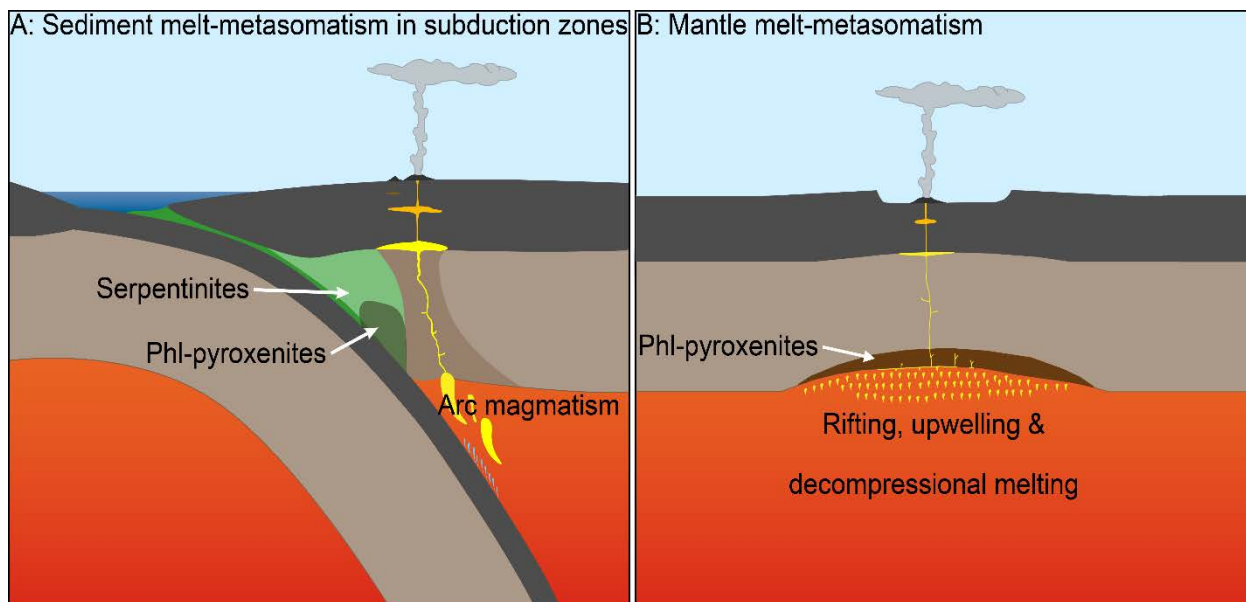


**Fig. 4.10:** Melts of sediment- metasomatism in a subduction zone (A) and mantle melt-metasomatism in a rifting & upwelling scenario (B). In both cases metasomatism leads to the formation of phlogopite pyroxenites and enrichment of the lithospheric mantle in K.

### Author contributions

MF performed all experiments and processed and interpreted the data. MF wrote the manuscript. SB and RMK assisted in analysis and evaluation of the datasets. SF and DP helped in data interpretation and manuscript evaluation. MF handles the correspondence of the submitted manuscript version of this chapter.

### Acknowledgements

We gratefully acknowledge Qing Xiong for providing the dunite sample ZD11-53 used in the experiments. The International Ocean Discovery Project (IODP) supported this study in providing the Mediterranean marine sediment sample from sampling site 161-976. This work is part of the lead author's PhD thesis supported by an Australian Government International Postgraduate Research Scholarship (IPRS) and Postgraduate Research Fund (PGRF). Thomas Kautz of the Goethe University, Frankfurt assisted with the belt apparatus experiments. DP was supported through the Deutsche Forschungsgemeinschaft (DFG) project PR 1072/9-1.



## Chapter 5:

# Melting Phlogopite-rich MARID: Lamproites and the Role of Alkalis in Olivine-Liquid Ni-partitioning

Michael W. Förster<sup>1</sup>, Dejan Prelević<sup>2,3</sup>, Harald R. Schmück<sup>2</sup>, Stephan Buhre<sup>2</sup>, Horst R. Marschall<sup>4</sup>,  
Regina Mertz-Kraus<sup>2</sup>, Dorrit E. Jacob<sup>1</sup>

<sup>1</sup>Australian Research Council Centre of Excellence for Core to Crust Fluid Systems (CCFS) and  
GEMOC, Macquarie University, NSW 2109, Sydney, Australia

<sup>2</sup>Institute for Geosciences, Johannes Gutenberg University, 55099 Mainz, Germany

<sup>3</sup>Faculty of Mining and Geology, University Belgrade, 11000 Belgrade, Serbia

<sup>4</sup>Institute for Geosciences, Goethe University, 60438 Frankfurt am Main, Germany

This chapter is published as an article in *Chemical Geology*.

## Abstract

In this study, we show how veined lithospheric mantle is involved in the genesis of ultrapotassic magmatism in cratonic settings. We conducted high pressure experiments to simulate vein + wall rock melting within the Earth's lithospheric mantle by reacting assemblages of harzburgite and phlogopite-rich hydrous mantle xenoliths. These comprised a mica-, amphibole-, rutile-, ilmenite-, diopside (MARID) assemblage at 3–5 GPa and 1325–1450 °C. Melting of the MARID assemblages results in infiltration of melt through the harzburgite, leading to its chemical alteration. At 3 and 4 GPa, melts are high in K<sub>2</sub>O (> 9 wt%) with K<sub>2</sub>O/Na<sub>2</sub>O >> 2 comparable to anorogenic lamproites. Higher pressures and temperatures (5 GPa/1450 °C) lead to increasing MgO contents of the melt and to some extent lower K<sub>2</sub>O contents (5–7 wt%) at equally high K<sub>2</sub>O/Na<sub>2</sub>O ratios. Our experiments provide insights into the role of alkalis in nickel-partitioning ( $D_{Ni}$ ) between olivine and ultrapotassic melt. We observe that the high contents of Na, K, and Al are indicative of high  $D_{Ni}$  values, implying that the melt polymerization is the dominant factor influencing the olivine/melt nickel partitioning. The change of  $D_{Ni}$  as a function of melt composition results in a pressure independent, empirical geothermometer:

$$T (^{\circ}\text{C}) = -88.14 \cdot \ln\left( \frac{[\text{liq}(\text{Na}_2\text{O}+\text{K}_2\text{O})] \cdot [\text{liq}\left(1+\frac{\text{SiO}_2}{\text{TiO}_2}\right)] \cdot [\text{liq}(\text{Al}_2\text{O}_3)]}{[\text{liq}(\text{MgO}+\text{FeO})]} \cdot D_{Ni} \right) + 1906.2$$



Element oxides represent the composition of the glass (in wt%), and  $D_{Ni}$  is the liquid/olivine Ni-partitioning coefficient. We propose that this geothermometer is applicable to all natural silicate melts that crystallized olivine in a temperature interval between 1000 and 1600 °C. Application to glass-olivine pairs from calc-alkaline settings (Mexico), MORB (East Pacific Rise), and OIB (Hawaii) yielded reasonable values of 996–1199 °C, 1265 °C, and 1330 °C, respectively.

## 5.1 Introduction

Basaltic magmas are traditionally viewed to be generated in a homogeneous peridotitic upper mantle (Jaques and Green, 1980). An increasing number of petrological studies challenge this view, as they suggest that melting in the upper mantle in many cases begins with melting of mixed source regions that consist of fertile olivine-free ultramafic lithologies within peridotite (Foley, 1992b; Hirschmann and Stolper, 1996; Lassiter et al., 2000; Meen, 1987; Prelević et al., 2008b; Sobolev et al., 2005). This scenario is particularly applicable for K-alkaline and ultrapotassic melt compositions like lamproites (Foley, 1992a), which cannot be explained by the low extent of partial melting of a homogeneously metasomatized peridotite (Green et al., 2014; Green and Falloon, 2005; Novella et al., 2014; Novella and Frost, 2014) because the experimental studies of low degrees (<1 %) of partial melting of phl-bearing peridotite never yielded sufficiently high K contents (>5 wt%) and  $K_2O/Na_2O$  ratios (>2) to explain ultrapotassic magmatism (Novella and Frost, 2014 and references therein).

The inability of low-degree melting experiments to produce melts with high contents of K and the fact that liquidus experiments failed to produce multiple saturation points that include olivine, orthopyroxene, clinopyroxene and garnet/spinel (Edgar and Mitchell, 1997; Foley, 1992b; Foley et al., 2012; Foley and Peccerillo, 1992; Mitchell and Edgar, 2002; Sato, 1997) led to an alternative model explaining lamproitic magmatism as being sourced from mantle veined by fertile phlogopite-rich clinopyroxenites, so-called metasomes (Foley, 1992b). The wall-rock peridotite is usually of harzburgitic composition as it underwent previous melt extraction and contains high-Fo olivine and Cr-rich spinel (Prelević and Foley, 2007). Vein wall-rock reactions in this system are thought to produce melts of lamproitic compositions with a characteristically high  $K_2O$ , and low CaO and  $Al_2O_3$ .

Recent experimental studies found that hybridization of depleted mantle with K-rich metasomes is a robust process to explain the source rock of ultrapotassic magmatism (Förster et al., 2017; Mallik et al., 2015; Mallik et al., 2016; Wang et al., 2017b; Wang et al., 2017a; Wang and

Foley, 2018). Furthermore, phlogopite-rich mantle xenoliths and abundant phlogopite-xenocrysts are associated with the ultrapotassic volcanics (Downes et al., 2002; Fritschle et al., 2013; Prelević et al., 2010; Zhang et al., 2011) and suggest a genetic link.

Mica-amphibole-rutile-ilmenite-diopside (MARID)-type mantle xenoliths from the Kaapvaal craton (RSA) are phlogopite-rich xenoliths typical for cratonic settings (Harte, 1987). Their phlogopite-rich endmember is also referred to as glimmerite. MARID-type xenoliths are either mantle metasomatic assemblages or represent cumulates from ultrapotassic rocks that crystallized from hydrous melts similar to lamproites or kimberlites (Dawson and Smith, 1977; Erlank et al., 1982; Sweeney et al., 1993; Waters, 1987). MARID assemblages are stable over a wide range of pressure and temperatures, including those of the cratonic lithosphere of 3–8 GPa/900–1300 °C (Konzett et al., 1997), thus it is conceivable that they take part in partial melting of the lithospheric mantle.

Numerous recent studies established source–melt kinship between heterogeneously metasomatized lithospheric mantle and ultrapotassic lavas through a complex vein-wall rock melting relationship (Foley, 1992b; Giuliani et al., 2015; Rosenthal et al., 2009; Tappe et al., 2008). The vein component in this setting is thought to consist of metasomes similar to MARID xenoliths that explain the extreme variations in isotopic and chemical compositions of the hybrid melts. However, the application of these models faces a significant obstacle due to the lack of comprehensive experimental studies that constrain melting and dynamic metasomatism of a source consisting of mixed peridotite and MARID assemblages.

In this study we discuss the melting of a mixed MARID-glimmerite plus harzburgite source rock at 3–5 GPa, which corresponds to cratonic lithospheric depths of 90 to 150 km. It is a follow up study to Förster et al. (2017) which presented results for similar compositions and melting of metasomatized mantle at low pressures of <2 GPa corresponding to post-collisional geodynamic settings.

Our study follows a twofold approach: firstly, we use high-pressure experiments to determine the melting reactions of MARID-glimmerites with wall-rock harzburgite and investigate the composition of the produced glass and mineral assemblages. The experiments are carried out in order to provide new insights into the role of veined-peridotites in the generation of ultrapotassic magmas. Secondly, we determine the Ni-partitioning between olivine and melt over a range of 1–5 GPa and 1150–1450 °C. Partitioning of nickel in olivine/melt ( $D_{Ni}$ ) pairs is known to vary from 2 to 20 in basaltic melts (Beattie, 1994; Dunn and Sen, 1994; Hart and Brooks,

1974; Kennedy et al., 1993; Matzen et al., 2013; 2017; Snyder and Carmichael, 1992; Ulmer, 1989; Wang and Gaetani, 2008), to values of up to 80 in highly alkaline melts (Foley et al., 2011; 2013).  $D_{\text{Ni}}$  shows significant exponential correlations with MgO, whereas pressure and temperature could primarily influence the melt composition (Foley et al., 2011; 2013; Li and Ripley, 2010; Wang and Gaetani, 2008). However, recent studies on experimental compositions with constant melt compositions at changing thermobaric conditions show a significant influence of temperature on  $D_{\text{Ni}}$  (Matzen et al., 2013; 2017). The high variability of our melt compositions also enables the definition of a new empirical pressure-independent geothermometer applicable to basaltic, alkaline, and ultrapotassic melts, which correctly reproduced temperatures in the range of 1000–1600 °C.

## 5.2 Materials and Methods

### 5.2.1 Starting materials

MARID samples were collected from the Boshof Road Dump at the De Beers diamond mine in Kimberley, South Africa. The samples are coarse-grained sub-rounded xenoliths of about 10 cm in diameter. The mineral assemblage is dominated by ca. 90 vol% mm-sized phlogopites. Other phases in descending order of abundance are: diopside, K-richterite, rutile, and ilmenite. Calcite and barite occur as accessories. Two samples (DJ0227, DJ0228A) were used to produce thin sections (100  $\mu\text{m}$  thickness) and agate milled powders. The full dataset of mineral composition data, including major and trace element data, as well as details on the electron-probe micro analyser (EPMA)-routine is provided in [Supplementary Tables 5.1–5.11](#).

Synthetic harzburgite and MARID compositions were synthesized to provide mantle wall-rock clean of trace elements for the layered reaction experiments, as well as MARID melt clean of trace elements for one Ni-partitioning experiment. They were produced from metal-oxides and carbonates (SIGMA-ALDRICH®) to match the composition of AVX-51 (Rapp et al., 1999) and the bulk analysis of the natural MARID samples, respectively. After grinding and mixing in an agate mortar using acetone, the mixtures were oven-dried and decarbonized. The AVX-51 mix was transformed to harzburgite at 1200 °C, 1 GPa over 10 days.

### 5.2.2 Experimental techniques

Experiments were carried out at 1 and 3 GPa using a Piston Cylinder Apparatus at the University of Mainz, and at 4–5 GPa using a Belt Apparatus at the University of Frankfurt. Natural MARID

and synthetic harzburgite powders were placed in a capsule as a two-layer charge (Table 5.1). The experimental charge was filled into a carbon capsule to control  $fO_2$  via the  $C + CO$  equilibrium which, in turn, was placed into a platinum capsule. The synthetic MARID powder was placed into a capsule made of a San Carlos olivine encased in platinum capsule. The capsules were fitted into a pressure cell consisting of  $Al_2O_3$  spacers, a graphite furnace, b-type thermocouple, and a  $CaF_2$  spacer on the outside of the assemblage for the piston cylinder experiments. For the experiments using the Belt apparatus, the spacer and capsule holder consisted of natural calcium-fluoride, while other materials were identical to those used in the piston-cylinder experiments. The cell assemblies were first pressurized and subsequently heated at a rate of 50 °C/min. Both the Piston cylinder- and Belt apparatus were continuously water-cooled (water temperature ca. 13 °C) and pressure and temperature were kept constant for 24–48 h. All charges were quenched to temperatures below 500 °C within 8 s in the Piston-cylinder runs, and within 10 s in the Belt runs. The position of the cooling plates in the Belt apparatus, which are further away from the high-pressure cell, result in lower quench rates compared to the Piston cylinder-apparatus.

**Table 5.1:** Composition, temperature, pressure, and duration of each experiment.

#	Composition	T [°C]	P [GPa]	% Melt	Phases	Duration [h]
1	MARID/Harzb. Reaction	1325	3	~50	Ol + Opx + Cpx + melt	24
2	MARID/Harzb. Reaction	1360	4	~20	Ol + Opx + Cpx + Phlog + melt	48
3	MARID/Harzb. Reaction	1400	5	~30	Ol + Opx + Cpx + Garnet + Phlog + melt	48
4	MARID/Harzb. Reaction	1450	5	~50	Ol + Opx + Cpx + Phlog + melt	48
5	Synthetic MARID	1300	1	~90	Ol + melt	24

### 5.2.3 Analytical techniques

Major element contents in the experimental run products were measured using a JEOL JXA 8200 Superprobe electron-probe microanalyzer (EPMA) equipped with 5 wavelength dispersive spectrometers at the University of Mainz, Germany. Micas, silicates, and glasses were analyzed with 15 kV accelerating voltage and a beam current of 12 nA, except for the olivines which were analyzed at 20 kV and 30 nA. Peak counting times were 20–30 s for melts, silicates, and micas, and 150 s for olivines. The beam diameter was set to 2 µm in the 3 and 4 GPa experiments, and to 20 µm in the experiments at 5 GPa, to average quench phases. A range of synthetic materials were used as reference materials (Supplementary Table 5.1). Trace element analyses were carried out by laser ablation-inductively coupled plasma mass spectrometry (LA-ICP-MS) at the University

of Mainz. An ESI NWR193 ArF Excimer laser ablation system (193 nm wavelength) equipped with a TwoVol2 ablation cell was used for the formation of a dry aerosol from the samples. After ablation with a repetition rate of 10 Hz at 3 J/cm<sup>2</sup>, the dry aerosol was transferred to an Agilent 7500ce mass spectrometer by a He-Ar mixed gas flow. Synthetic NIST SRM 612 was used as calibration material with values from Jochum et al. (2011) and <sup>29</sup>Si was selected as internal standard using the SiO<sub>2</sub> data determined by electron-microprobe. For quality control, basaltic USGS BCR-2G was measured as an unknown in each run ([Supplementary Table 5.3](#)). Results for USGS BCR-2G were within 10% of the data tabulated in the GeoReM database (<http://georem.mpch-mainz.gwdg.de/>, Jochum et al., 2005). For each analysis, background signals were acquired for 20 s, followed by a dwell time of 30 s with spot sizes of 20 or 50 µm. Where possible, laser ablation spots were co-located with the electron-microprobe analyses. Data processing was carried out using the commercial software GLITTER 4.4.1 (Griffin, 2008).

## 5.3 Results

### 5.3.1 Textural observations

The experiments using synthetic MARID powder consisted of glass, free-floating olivines, and capsule-wall olivine ([Supplementary Fig. 5.1](#)). All reaction experiments comprised two layers with a melted vein that infiltrated the harzburgite and originated from the former MARID layer of the sample charge. The experiment at 3 GPa contained glass as well as an accumulation of clinopyroxene and olivine crystals at the bottom of the capsule ([Fig. 5.1 A](#)). We observed the clinopyroxenes to occur both as euhedral grains and as inclusions in olivine, emphasizing that clinopyroxene crystallized prior to olivine. The harzburgite showed patches of glass, as well as phlogopite and clinopyroxene. We observed less glass in the MARID part at 4 GPa, however, this layer had completely recrystallized to contain 50 vol% rounded olivine and idiomorphic clinopyroxene. No glass was observable in the harzburgite part, while phlogopite and clinopyroxene were found in patchy occurrences. At 5 GPa, the MARID part contained an accumulation of garnet and orthopyroxene, whereas the harzburgite contained phlogopite- and clinopyroxene-bearing veins ([Fig. 5.1 B](#)). No glass could be observed in the MARID part of the capsule, but 2 µm quench-lamellae of clinopyroxene and phlogopite were evident ([Fig. 5.1](#)). In the harzburgite part of the sample, an interconnected network of clinopyroxene and phlogopite covered the lower half.

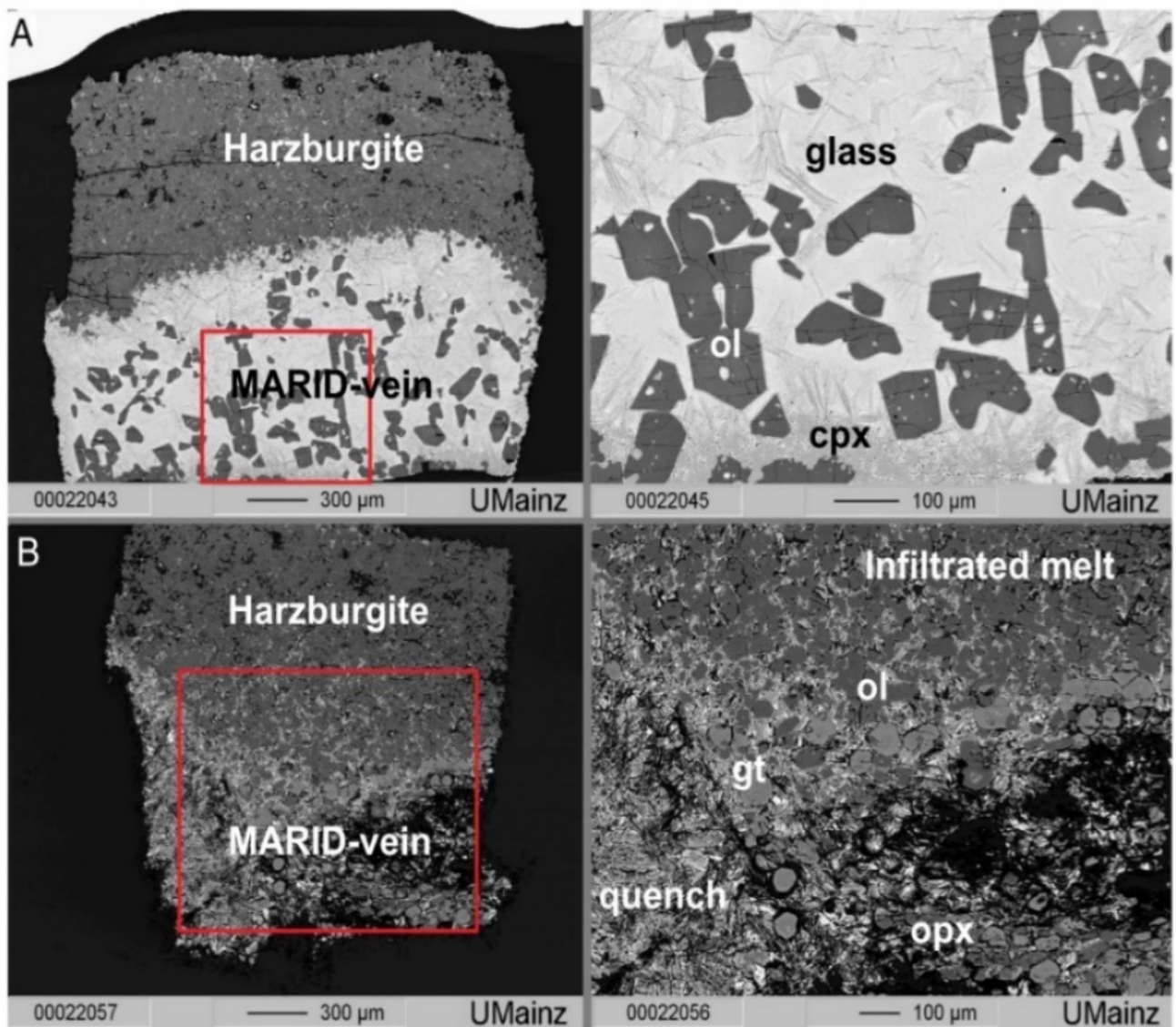


**Fig. 5.1:** Composition (Backscattered electron - BSE) images of polished sectioned capsules showing typical textures of the experimental charges. Labels are laid on top of phases: ol - olivine, cpx - clinopyroxene, gt - garnet, glass – quenched melt, quench - quench phases of former melt. A) Experiment at 3 GPa/1325 °C. B) at 5 GPa/1400 °C.

### 5.3.2 Melt compositions in the reaction experiments

The 3 GPa experiment comprised three different melt-types ([Table 5.2](#)): (1) Incongruent melting of the MARID domain produced a melt by crystallizing clinopyroxene and olivine ([Fig. 5.2](#)). The glass reached < 45 wt% SiO<sub>2</sub>, 12 wt% MgO, Mg# of 75–80, and 9 wt% K<sub>2</sub>O ([Fig. 5.2 B,C,E](#)). (2) Melt-inclusions in olivine comprised 11 wt% K<sub>2</sub>O, 13 wt% Al<sub>2</sub>O<sub>3</sub>, 8 wt% CaO, <5 wt% MgO, and Mg# of 65–70 ([Fig. 5.2 D,E](#)). (3) A heterogeneous melt with 45–50 wt% SiO<sub>2</sub> ([Table 5.2](#)) that infiltrated the harzburgite with domains showing > 10 wt% CaO and <6 wt% K<sub>2</sub>O, as well as domains <5 wt% CaO and >8 wt% K<sub>2</sub>O ([Fig. 5.2 B,D](#)). The glass of the 4 GPa experiment exhibited K<sub>2</sub>O values



between 14 and 18 wt% and total alkalis of about 20 wt% plotting mostly above the foidite-field in the total alkali *versus* silica diagram (Fig. 5.2 A). The high K<sub>2</sub>O-content is accompanied by MgO values of 0.5–4.0 wt% and Mg# of 30–60 at 43–45 wt% SiO<sub>2</sub> and Al<sub>2</sub>O<sub>3</sub> of 10–13 wt% (Fig. 5.2 B-E). The melts in the 5 GPa experiments consisted of <2 µm phlogopite clinopyroxene quench lamellae, but no glass was observed. EPMA analyses were therefore carried out with a large beam diameter of 20 µm to average across the quench phases and to yield approximate melt compositions. The melts in these experiments comprise 5–7 wt% K<sub>2</sub>O at >15 wt% MgO and Mg# of 75–85, while Al<sub>2</sub>O<sub>3</sub> and CaO reach 5–8 wt% and 5–10 wt%, respectively (Fig. 5.2 B-E, Table 5.2).

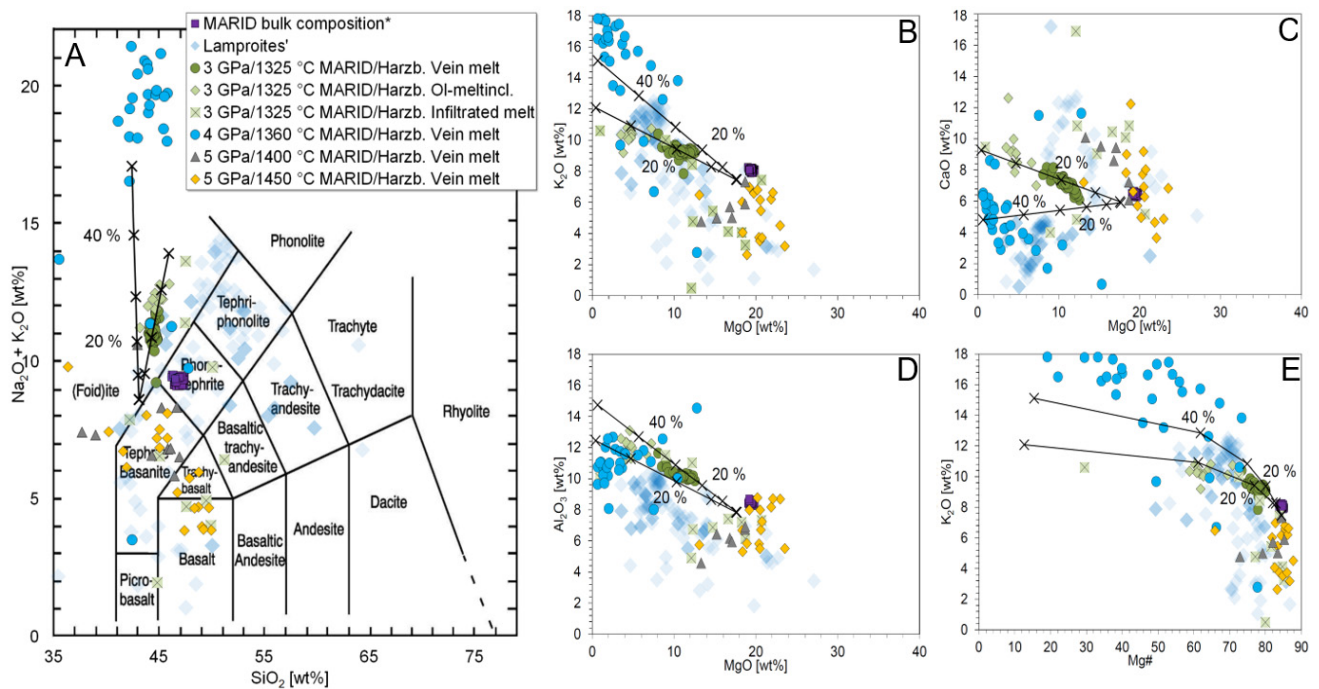


**Fig. 5.2:** Major element composition of melts in the experimental charges (3 GPa/1325 °C – green circles/diamonds/squares, 4 GPa/1360 °C – blue circles, 5 GPa/1400 °C – grey triangles, 5 GPa/1450 °C – orange diamonds) compared to lamproites (blue diamonds). A) shows total alkali *versus* silica, B) K<sub>2</sub>O *versus* MgO, C) CaO *versus* MgO, D) Al<sub>2</sub>O<sub>3</sub> *versus* MgO, and E) K<sub>2</sub>O *versus* Mg#. Melts from the reaction of MARID with harzburgite comprise a wide range of composition depending on the PT-conditions of the experiment. Fractionation pathways with 10% increments were modelled for vein melts of the 3 and 4 GPa experiments starting from the bulk MARID composition normalized to 95 wt%, accounting for 5 wt% volatiles. Residues were calculated by mass balance and comprise 21 wt% olivine and 2 wt% clinopyroxene at 3 GPa as well as 28 wt% olivine and 19 wt% clinopyroxene at 4 GPa. The experimental melts broadly overlap with natural lamproite compositions except the experiment at 4 GPa/1360 °C (blue circles) which shows strong olivine and clinopyroxene fractionation. (Lamproite data: Davies et al., 2006; Fraser et al., 1985; Jaques, 1986; Mirnejad and Bell, 2006; Murphy et al., 2002) (Bulk rock data: Förster et al., 2017).



**Table 5.2:** Representative analysis for bulk MARID composition and high-pressure experiment melts (oxides in wt%).

Melt	SiO <sub>2</sub>	TiO <sub>2</sub>	Al <sub>2</sub> O <sub>3</sub>	FeO	MnO	MgO	CaO	Na <sub>2</sub> O	K <sub>2</sub> O	P <sub>2</sub> O <sub>5</sub>	SO <sub>3</sub>	Total	Mg#
MARID bulk composition*	47.37	3.17	8.56	6.29	0.05	19.41	6.47	1.30	8.03	0.11	0	101.0	85
Synthetic MARID melt													
1 GPa/1300 °C	47.06	4.12	11.18	4.36	0.05	10.98	5.87	1.62	9.50	-	-	94.82	82
3 GPa 1325 °C	44.65	3.62	10.11	5.39	0.14	12.08	6.53	1.61	9.16	0.10	0.14	93.91	80
MARID/Harzb. Vein melt													
3 GPa/1325 °C	43.01	4.63	10.18	6.23	0.09	15.82	2.63	0.72	10.12	0.08	0.13	94.37	82
MARID/Harzb. Infiltrated melt													
3 GPa/1325 °C	46.02	4.22	13.09	4.45	0.09	4.58	7.86	2.03	10.80	0.12	0.16	93.97	65
MARID/Harzb. Ol-Melt inclusions													
4 GPa/1360 °C	44.72	4.97	11.89	5.10	0.09	2.82	2.91	2.38	17.33	0.24	0.18	93.05	50
MARID/Harzb. Vein melt													
5 GPa/1400 °C	45.28	3.47	6.92	6.15	0.08	18.70	6.08	1.00	7.33	-	-	95.35	84
MARID/Harzb. Vein melt													
5 GPa/1450 °C	43.84	2.56	7.99	7.13	0.06	19.21	6.61	1.08	6.97	0.54	0.08	96.16	83

\*Data from Förster et al. (2017)

### 5.3.3 Trace element composition of melts and olivine

Trace elements were measured for the 3 and 5 GPa experiments (Fig. 5.3, Supplementary Tables 5.3–5.11). All melts are enriched in LILE, HFSE, and LREE (La to Eu), with a positive Ti anomaly (Fig. 5.3). For determining Ni partitioning between olivine and liquid ( $D_{Ni}$ ), the Ni content of adjacent olivine-melt pairs of 8 experiments with natural MARID-composition at 1–5 GPa/1150–1450 °C and one synthetic MARID composition at 1 GPa/1300 °C yielded 37–2550  $\mu\text{g}\cdot\text{g}^{-1}$  for olivine and 4.4–127  $\mu\text{g}\cdot\text{g}^{-1}$  for adjacent glass (Table 5.3).

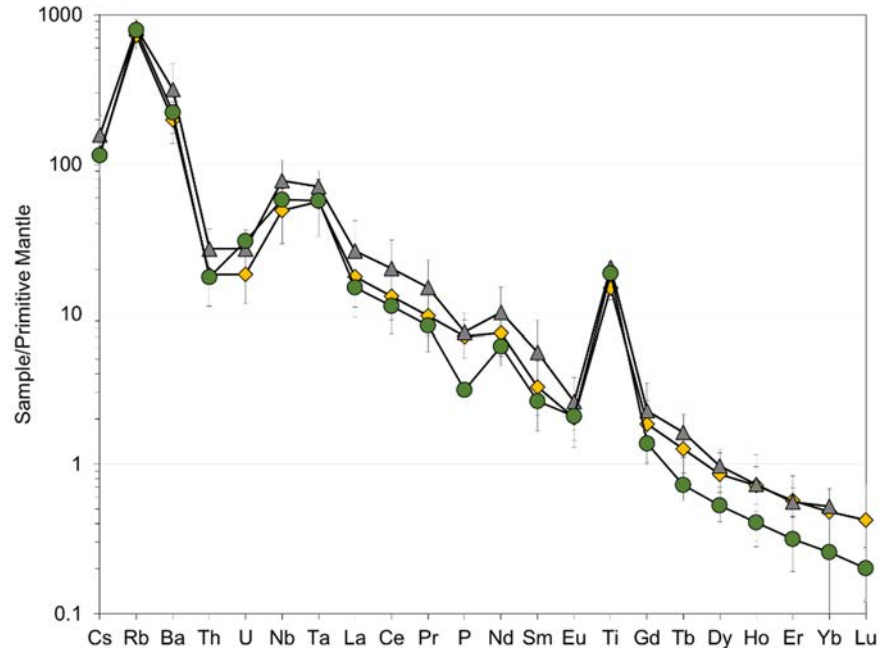


**Fig. 5.3:** Trace element composition of melts 3 GPa/1325 °C – green circles, 5 GPa/1400 °C – grey triangles, 5 GPa/1450 °C – orange diamonds) normalized to primitive mantle composition. All experimental charges show a steep trace element pattern containing positive Rb and Ti anomalies due to the high content of phlogopite in the MARID starting material.

**Table 5.3:** Ni-contents of melt and olivine and  $D_{Ni}$  of experimental charges.

Experiment	Average Ni contents [ $\mu\text{g}\cdot\text{g}^{-1}$ ]		$D_{Ni}$
	Olivine	Glass	
1 GPa/1225 °C MARID*	1104	37.5	<b>29.5</b>
1 GPa/1300 °C Synthetic MARID	989	68.3	<b>14.5</b>
1 GPa/1225 °C MARID/Harzb. experiment*	848	44.9	<b>18.9</b>
2 GPa/1150 °C MARID/Harzb. experiment*	255	102	<b>25.0</b>
2 GPa/1250 °C MARID/Harzb. experiment*	141	81.8	<b>17.2</b>
2 GPa/1300 °C MARID/Harzb. experiment*	177	14.8	<b>11.9</b>
3 GPa/1325 °C MARID/Harzb. experiment	1962	127	<b>15.4</b>
5 GPa/1400 °C MARID/Harzb. experiment	103	11.4	<b>9.1</b>
5 GPa/1450 °C MARID/Harzb. experiment	36.7	4.4	<b>8.4</b>

\*Data from Förster et al. (2017)

### 5.3.4 Composition of the mineral phases

All experimental melts were found to have crystallized mineral phases that were either not present in the starting material (olivine, orthopyroxene, and pyrope-rich garnet) or that had a distinctly different major and trace element composition (clinopyroxene and phlogopite).

Major elements in olivines were analyzed from the experiments at 3 and 5 GPa. The experiments contain two sources for olivine, the harzburgite and the MARID vein. The 3 GPa experiment shows groups from both sources: The first group consists of olivine crystallized after the incongruent breakdown of phlogopite in the MARID part and shows Fo contents of 92 and [NiO] of 0.1–0.2 wt% (Table 5.4). The reaction olivine in the infiltrated harzburgitic part of the charge contains 0.25–0.35 wt% NiO at similar Fo contents of approximately 92 (Table 5.4). The 5 GPa experiments contain reaction olivine that must have settled from the harzburgite, since the MARID vein crystallized orthopyroxene instead of olivine. This reaction olivine shows [NiO] of 0.05 wt% at Fo contents of 92, and [MgO] of 51–52 wt% (Table 5.4).

Clinopyroxene separate into two groups based on their  $\text{Cr}_2\text{O}_3$  content (Table 5.4). The harzburgite contains clinopyroxene with a  $\text{Cr}_2\text{O}_3$ -rich composition (1.2–2.3 wt%), while the MARID vein part comprises those of  $\text{Cr}_2\text{O}_3$ -poor compositions (<0.8 wt%) (Table 5.4). Both compositions are abundant in the experiment at 3 GPa, whereby the  $\text{Cr}_2\text{O}_3$ -poor clinopyroxenes are found in the cumulate part (Fig. 5.1 A). This clinopyroxene is higher in MgO (20 wt%),  $\text{Al}_2\text{O}_3$  (2–3 wt%), and lower in CaO (15–17 wt%) and Na<sub>2</sub>O (<1 wt%) compared to the diopside of the MARID starting material, which presents an MgO content of approximately 15 wt% and [CaO] of approximately 20 wt% (Table 5.4). The reaction clinopyroxene in the harzburgite is similar to the diopside in the harzburgite starting material, however, it shows lower contents for  $\text{Cr}_2\text{O}_3$  (1.2–2.3 wt%). The 5 GPa experiment only contains reaction clinopyroxene with high contents of  $\text{Cr}_2\text{O}_3$  (1.0–1.6 wt%) and  $\text{Al}_2\text{O}_3$  (2.2–4.0 wt%).

Phlogopite is abundant in all experiments. It shows a gradual increase in TiO<sub>2</sub> (2–8 wt%) and decrease in SiO<sub>2</sub> (43–35 wt%) as well as Al<sub>2</sub>O<sub>3</sub> (10–4 wt%), with rising pressure and temperature (Fig. 5.4 A,B). Remarkably, all Ti-rich and Al-poor phlogopite is higher in FeO (15–20 wt%) compared to the phlogopite in the MARID starting material (6–7 wt% FeO) (Table 5.4).

**Table 5.4:** Representative analyses for silicate phases in the experiments (oxides in wt%).

Olivine	SiO <sub>2</sub>	TiO <sub>2</sub>	Al <sub>2</sub> O <sub>3</sub>	FeO	MnO	MgO	CaO	Cr <sub>2</sub> O <sub>3</sub>	NiO	P <sub>2</sub> O <sub>5</sub>	SO <sub>3</sub>	Total	Mg#
Synthetic Harzburgite-olivine*	40.33	0	0.06	8.81	0.15	50.72	0.18	0.13	0.46	-	-	100.84	91
3 GPa/1325 °C Vein olivine	41.85	0.16	0.04	7.50	0.07	50.67	0.16	0.15	0.20	-	-	100.73	92
3 GPa/1325 °C Reaction olivine	41.75	0.03	0.04	7.53	0.08	50.76	0.15	0.18	0.32	-	-	100.83	92
5 GPa/1400 °C Reaction olivine	40.93	0.04	0.07	7.83	0.12	51.22	0.13	0.09	0.05	-	-	100.54	92
Phlogopite	SiO <sub>2</sub>	TiO <sub>2</sub>	Al <sub>2</sub> O <sub>3</sub>	FeO	MnO	MgO	CaO	Na <sub>2</sub> O	K <sub>2</sub> O	Cr <sub>2</sub> O <sub>3</sub>	NiO	Total	Mg#
MARID phlogopite*	42.07	2.58	9.59	6.58	0.06	22.05	0	0.15	10.01	0.29	-	93.89	86
3 GPa/1325 °C Reaction phlogopite	42.30	4.98	11.24	5.17	0.04	20.59	0.16	0.11	10.11	-	-	95.51	88
5 GPa/1400 °C Vein phlogopite	41.35	3.78	11.42	7.46	0.06	19.59	0.15	0.20	10.40	-	-	95.25	82
5 GPa/1400 °C Vein Fe-phlogopite	38.26	6.84	6.05	20.59	0.20	6.41	1.41	0.86	9.11	-	-	90.76	36
5 GPa/1450 °C Vein phlogopite	41.31	3.39	10.87	5.03	0.05	22.35	1.27	0.19	9.65	-	-	94.72	89
5 GPa/1450 °C Vein Fe-phlogopite	42.03	6.14	4.44	17.00	0.11	11.20	0.46	0.19	9.65	-	-	91.78	54
Clinopyroxene	SiO <sub>2</sub>	TiO <sub>2</sub>	Al <sub>2</sub> O <sub>3</sub>	FeO	MnO	MgO	CaO	Na <sub>2</sub> O	K <sub>2</sub> O	Cr <sub>2</sub> O <sub>3</sub>	NiO	Total	Mg#
MARID clinopyroxene*	55.31	0.10	0.65	5.38	0.18	15.88	20.49	1.40	0.02	0.48	-	99.89	75
Synthetic Harzburgite- clinopyroxene*	55.71	0.02	1.23	3.45	0.12	19.75	16.35	1.46	0.02	2.24	0.09	100.44	91
3 GPa/1325 °C Vein-clinopyroxene	54.79	0.40	2.07	3.35	0.04	21.01	16.08	0.77	0.08	0.60	0.02	99.21	92
3 GPa/1325 °C Reaction- clinopyroxene	55.14	0.21	1.70	3.64	0.13	21.49	14.65	0.95	0.06	2.06	0.06	100.09	91
5 GPa/1400 °C Reaction- clinopyroxene	54.99	0.22	2.47	3.50	0.07	22.10	13.64	1.18	0.14	1.36	0	99.66	92
Orthopyroxene	SiO <sub>2</sub>	TiO <sub>2</sub>	Al <sub>2</sub> O <sub>3</sub>	FeO	MnO	MgO	CaO	Na <sub>2</sub> O	K <sub>2</sub> O	Cr <sub>2</sub> O <sub>3</sub>	NiO	Total	Mg#
Synthetic Harzburgite-opx*	58.58	0.01	0.49	3.12	0.12	36.68	1.18	0.01	0.01	0.16	0.14	100.51	95
3 GPa/1325 °C Reaction-orthopyroxene	58.16	0.03	0.28	3.03	0.14	36.33	1.75	0.16	0.02	0.23	0.12	100.25	96
5 GPa/1400 °C Reaction- orthopyroxene	56.35	0.15	1.97	4.39	0.09	34.21	1.74	0.21	0.03	0.35	0.05	99.54	93
Garnet	SiO <sub>2</sub>	TiO <sub>2</sub>	Al <sub>2</sub> O <sub>3</sub>	FeO	MnO	MgO	CaO	Na <sub>2</sub> O	K <sub>2</sub> O	Cr <sub>2</sub> O <sub>3</sub>	NiO	Total	Mg#
5 GPa/1400 °C Vein-garnet	42.53	0.68	20.86	5.11	0.14	22.87	4.83	0.03	0.02	2.78	0	99.85	89

\*Data from Förster et al. (2017)

## 5.4 Discussion

### 5.4.1 Constraints on the formation of cratonic ultrapotassic magmas

Our experimental charges contain melts of contrasting composition, which are the consequence of an intended disequilibrium between the two parts of the layered sample. The MARID-part in the 3 GPa experiment melted incongruently and comprises a melt with high K<sub>2</sub>O and moderate MgO contents with values of 9 and 12 wt%, respectively (Fig. 5.2 B). Fractionation curves, calculated from mass balance calculations (Supplementary Table 5.2), show that the melt evolved from the bulk MARID composition by fractionating 21 wt% olivine and 2 wt% clinopyroxene. Small amounts of melt penetrated the harzburgitic part of the sample charge and reacted upon infiltration (Fig. 5.1 A). This infiltrated melt shows a higher variability of K<sub>2</sub>O compared to the vein melt due to the small size of individual melt pockets and is generally lower in Al<sub>2</sub>O<sub>3</sub> (Fig. 5.1 D) The vein melt in the 4 GPa experiment is similar to the vein melt in the 3 GPa experiment but is of a more evolved composition (Fig. 5.2). The melt of the 4 GPa experiments shows fractionation

of 28 wt% olivine and 19 wt% clinopyroxene as evident from mass balance ([Supplementary Table 5.2](#)). Melts in the 5 GPa experiments are lower in K<sub>2</sub>O (3–6 wt%) since higher temperatures led to intense harzburgite melting and consequently decreasing K, Al, and Ca, and increased Mg# in the melt ([Fig. 5.2](#), [Table 5.2](#)). Their quench textures are likely a result of the Mg-rich melt composition that provides all constituents for the rapid growth of phlogopite and clinopyroxene.

Melt compositions of the reaction experiments from 3 to 5 GPa are similar to anorogenic lamproites ([Fig. 5.2](#)). Anorogenic lamproites are primitive, ultrapotassic, mantle-derived lavas that are common to cratons and stabilized terranes. Their petrogenesis is highly complex since their mantle source is enriched in high LILE and REE, while simultaneously depleted in CaO, Al<sub>2</sub>O<sub>3</sub> (Mitchell and Bergman, 1991). The composition of anorogenic lamproites comprises K<sub>2</sub>O >8 wt% and K<sub>2</sub>O/Na<sub>2</sub>O >2 at MgO of 10 to 20–25 wt% (olivine-lamproites) and SiO<sub>2</sub> of generally <50 wt% (Davies et al., 2006; Fraser et al., 1985; Jaques, 1986; Mirnejad and Bell, 2006; Murphy et al., 2002). Lower contents of SiO<sub>2</sub> (41–45 wt% in primary melts) and higher contents of MgO separate them from orogenic lamproites that show overall lower MgO (<10 wt%) and higher contents of SiO<sub>2</sub>, ranging from 46 to 60 wt% (Förster et al., 2017 and references therein). Lamproites are also very low in Na<sub>2</sub>O, CaO and Al<sub>2</sub>O<sub>3</sub>, which favors a depleted, harzburgitic source over a lherzolitic one (Mitchell and Bergman, 1991 and references therein). Nevertheless, high K-contents in lamproites demands enrichment in phlogopite of this source.

When compared with bulk rock analyses of lamproites (Davies et al., 2006; Fraser et al., 1985; Jaques, 1986; Mirnejad and Bell, 2006; Murphy et al., 2002), vein melts in the 3 GPa experiment plot near the anorogenic lamproite composition in [Fig. 5.2](#). However, at similar MgO contents, they reach about 2 wt% higher Al<sub>2</sub>O<sub>3</sub> contents. The infiltrated melts at 3 GPa, in turn, are lower in Al<sub>2</sub>O<sub>3</sub> and CaO due to their reaction with the harzburgite ([Table 5.2](#)) and thus resemble anorogenic lamproites more closely. Their lower contents of K<sub>2</sub>O and Al<sub>2</sub>O<sub>3</sub> can be explained by crystallization of phlogopite. These phlogopites comprise higher Al<sub>2</sub>O<sub>3</sub>-contents (12 wt%) compared to MARID phlogopites (10 wt%, [Fig. 5.4 B](#)) and lie within the range of compositions observed in lamproites ([Fig. 5.4 A,B](#)).

Crystallization of garnet and orthopyroxene ([Fig. 5.1 B](#)) at 5 GPa/ 1400 °C led to lower Al and Si compared to the experiment at 1450 °C ([Table 5.2](#)). The overall major element chemistry of the infiltrated melts plot at the MgO-rich end of the lamproite array ([Fig. 5.2](#)), and thus, is comparable to olivine lamproites. The experimental melts are low in SiO<sub>2</sub> (< 45 wt%) due to the crystallization of clinopyroxene in addition to olivine. This complements the findings of (Förster et al., 2017) where experimental conditions of 1–2 GPa resulted in melts high in SiO<sub>2</sub> (up to 60

wt%). At low pressures, only olivine fractionates, which leads to a strong SiO<sub>2</sub> increase of the reaction melts, and thus, silica-rich orogenic lamproites (Prelević et al., 2008b).

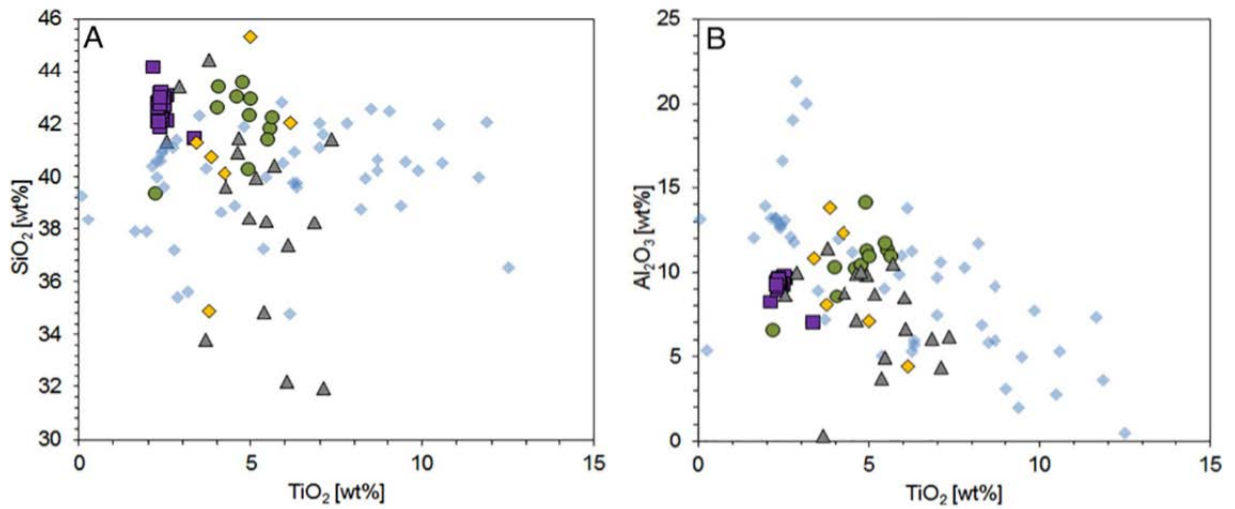


**Fig. 5.4:** Major element composition of phlogopites from start materials (MARID phlogopites – purple squares) and experiments (3 GPa/1325 °C – green circles, 5 GPa/1400 °C – grey triangles, 5 GPa/1450 °C – orange diamonds) compared to lamproites phlogopites (blue diamonds). A) SiO<sub>2</sub> *versus* TiO<sub>2</sub>, B) Al<sub>2</sub>O<sub>3</sub> *versus* TiO<sub>2</sub>. \*(MARID phlogopite data: Förster et al., 2017) †(Lamproite phlogopite: Carmichael, 1967; Barton and van Bergen, 1981; Jaques et al., 1986 and Hwang et al., 1994).

#### 5.4.2 Ni-partitioning in olivine and ultrapotassic melts

The reaction experiments of MARID and depleted peridotite comprised  $D_{Ni}$  of 8.4–29.5 at 6–12 wt% Na<sub>2</sub>O+K<sub>2</sub>O. We propose that this “wide” range in total alkali content can be used to probe the influence of Na and K variations on  $D_{Ni}$ . Experimental durations of 24–48 h ensured Ni to equilibrate between olivine and liquid. Additionally, one inverse experiment was conducted consisting of synthetic MARID melt in an inner capsule made of San Carlos olivine with  $D_{Ni}$  of 14.5 at 11 wt % Na<sub>2</sub>O+K<sub>2</sub>O (Supplementary Fig. 5.1). The observed range in total alkali content underlines the earlier findings of Foley et al. (2013), who demonstrated that alkaline melts show  $D_{Ni(olivine/melt)}$  twice as high compared to basaltic compositions. A plot of  $D_{Ni}$  *versus* K<sub>2</sub>O and total alkalis of the melts from the experimental charges shows positive exponential correlations ( $R^2 = 0.70$  for K<sub>2</sub>O and  $R^2 = 0.83$  for Na<sub>2</sub>O+K<sub>2</sub>O) (Fig. 5.5). The well-known exponential correlation of  $D_{Ni}$  *versus* MgO achieves an  $R^2$  of only 0.57 in our experiments (Supplementary Fig. 5.2), whereas low alkaline compositions with similar contents of MgO achieve a high  $R^2$  of 0.9 (Li and Ripley, 2010; Wang and Gaetani, 2008). This means that the influences of MgO and total alkalis in the partitioning between Ni and the alkaline melt are superimposed. Accordingly, the coefficient of determination ( $R^2$ ) is highest for  $D_{Ni}$  *versus* a constituent that dominates the partitioning process for each melt composition (Table 5.5).

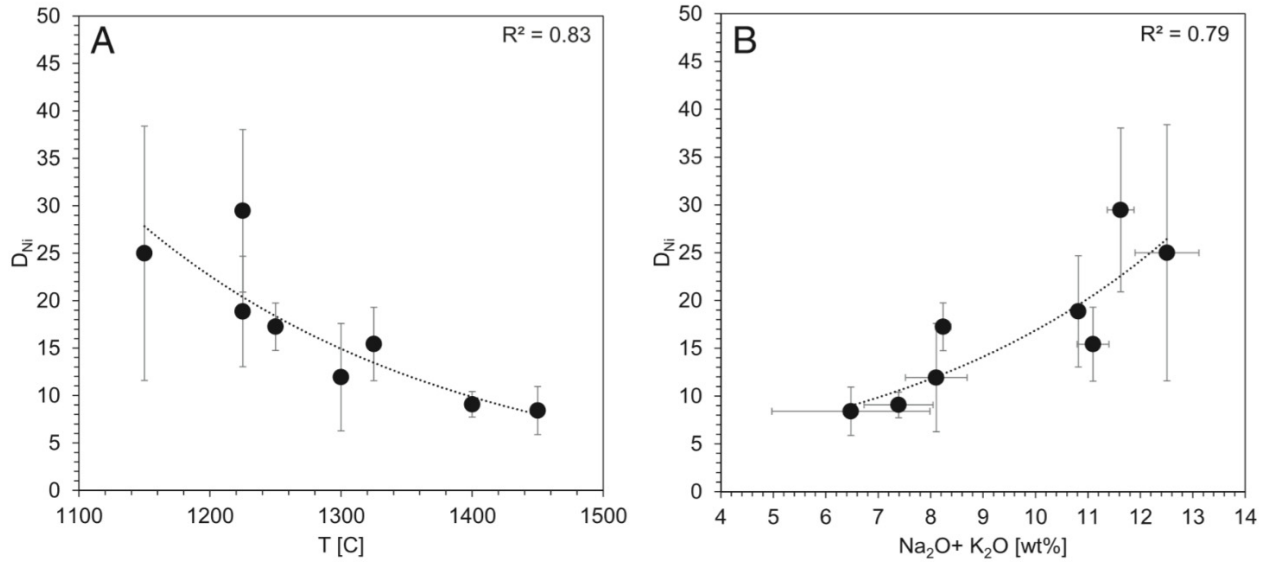


**Fig. 5.5:** Ni-partitioning of melt/olivine ( $D_{Ni}$ ) of experiments from this study (1325–1450 °C) and data from Förster et al. (2017) for experiments from 1150 to 1300 °C. A) shows  $D_{Ni}$  versus temperature, B)  $D_{Ni}$  versus total alkalis.

**Table 5.5:** Correlation coefficients of various combinations of constituents versus  $D_{Ni}$  and  $T$ .

Combination of constituents:		Coefficient of determination, $R^2$ :
$D_{Ni}$ versus	$\frac{(Na_2O + K_2O) \cdot (SiO_2 + TiO_2) \cdot Al_2O_3}{(MgO + FeO) \cdot CaO}$	0.94
$T$ versus	$\frac{(Na_2O + K_2O) \cdot (SiO_2 + TiO_2) \cdot Al_2O_3}{(MgO + FeO) \cdot CaO}$	0.84
$D_{Ni}$ versus	$Na_2O + K_2O$	0.83
$D_{Ni}$ versus	$T$	0.83
$D_{Ni}$ versus	$FeO$	0.82
$D_{Ni}$ versus	$P$	0.73
$D_{Ni}$ versus	$K_2O$	0.70
$D_{Ni}$ versus	$MgO$	0.57
$D_{Ni}$ versus	$CaO$	0.53
$D_{Ni}$ versus	$Al_2O_3$	0.29
$D_{Ni}$ versus	$Na_2O$	0.28
$D_{Ni}$ versus	$TiO_2$	0.18
$D_{Ni}$ versus	$SiO_2$	0.10

The dependence of  $D_{Ni}$  on the total alkali content suggests that the change in melt structure affects the solubility of Ni. This structural change also affects the melt-viscosity, since Na and K are large cations, and thus, strong modifiers of the melts' silicate network. The melts' viscosity therefore may be indicative for structural changes of the melts' network. Giordano et al. (2008) presented an empirical melt-viscosity model that is based on an optimized version of the equation of Fulcher (1925). It can predict the viscosity of silicate melts based on the melts' composition and temperature:

$$\log \eta = A + \frac{B}{T[K] - C}$$



Parameter A is defined by the viscosity of a silicate melt at infinite temperature and independent of the composition. B and C are compositional parameters that account for the influence of silicate network formers (e.g. Si, Fe) and network modifiers (Ca, Mg, Na, K, Al). Aluminum is known to act as a network former when present as Al[4], however, high temperature, as present in mantle-derived melts, increases the abundance of Al[5], which reduces melt viscosity (Le Losq et al., 2014). Since this study is confined to primitive mantle derived melts, Al is treated as network modifier, while it likely could be a transient species, aiding in melt-network formation at temperatures close to 1000 °C. Volatiles act as network modifiers, and strongly influence the parameter C and  $\log \eta$  in the melt-viscosity model, while parameter B is less influenced (Giordano et al., 2008). Since our experimental melts contain volatiles, they were included as difference of EPMA totals from 100 wt%, while the literature data sets resemble dry melts with totals close to 100 wt%.

We applied this model to melts from experimental charges of this study and literature datasets (Supplementary Fig 5.3), which resulted in a positive exponential correlation of  $D_{Ni}$  versus melt viscosity (Fig. 5.6 A).

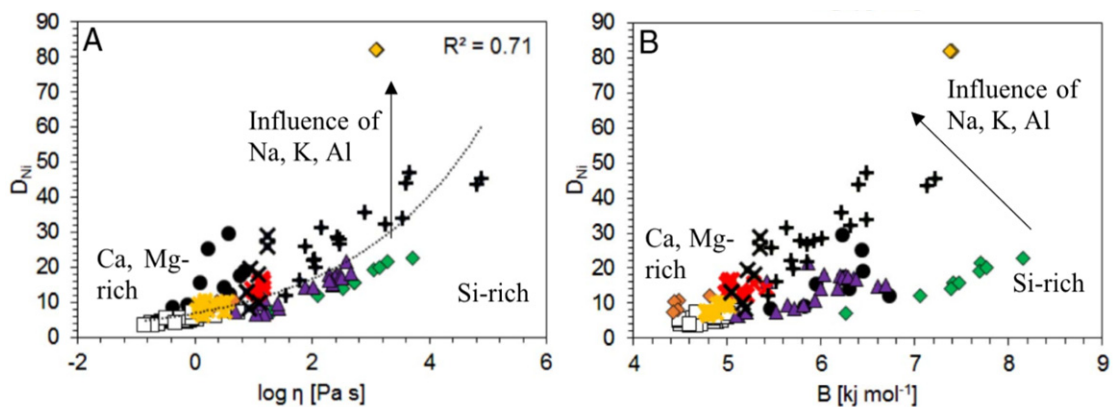


**Fig. 5.6:**  $D_{Ni}$  of olivine/melt versus melt-viscosity calculated with model from Giordano et al. (2008) applied to ultrapotassic melts from this study (black circles) and literature data: red crosses – East Pacific Rise/MORB (Allan et al., 1989); black pluses – Mexico/calc-alkaline basaltic andesite (Luhr and Carmichael, 1985); black crosses – basaltic-melt (Ford et al., 1983); purple triangles – alkaline-basaltic melt (Snyder and Carmichael, 1992); yellow diamond – Gaussberg/leucitite (Foley and Jenner, 2004); orange diamonds – basaltic, and green diamonds – eclogite melt (Wang and Gaetani, 2008); yellow crosses – Fe-rich basaltic melt (Filiberto et al., 2009); white and grey squares – basaltic melt (Matzen et al., 2013; Matzen et al., 2017).  $D_{Ni}$  shows a positive exponential correlation with the melts viscosity ( $\log \eta$ ). Alkali-rich melt compositions are vertically offset (arrow), showing that the melt modifier Na and K strongly influence the partitioning process. B) shows  $D_{Ni}$  of olivine/melt versus the compositional value B of the melt-viscosity model. Primitive, magnesian melts plot at low  $D_{Ni}$  olivine/melt and comprise low B-values due to high contents of the network modifier-cations Ca, Mg, and Fe. With increase of B, the  $D_{Ni}$  of olivine/melt branches into two pathways depending on the content of the volatiles (and network modifiers) Na and K over the network formers Al and Si.



This correlation is strongly influenced by temperature in two ways: First, low temperature leads to increased cohesive forces between molecules, and therefore, viscosity increase. Second, fractionation results in loss of the melt modifiers Ca and Mg, which relatively increases the abundance of the network former Si. Nevertheless, fractionation also increases the concentration of the network modifiers Na, K, and volatiles, which delays increase in viscosity (Giordano et al., 2008).

Melts rich in Na, K, and Al are vertically offset towards higher  $D_{Ni}$ , when compared to basaltic compositions at similar temperature and viscosity (Fig. 5.6 A). This finding is enhanced in a plot of  $D_{Ni}$  versus the compositional parameter B, since it excludes the effect of temperature and volatiles on the viscosity (Fig. 5.6 B). However, Na, K, and Al-rich melts are also Si-rich, indicating that melt polymerization is crucial for the partitioning process. At similar temperature, eclogite melts (Wang and Gaetani, 2008) show higher  $D_{Ni}$  (12–23) when compared to basaltic melts of the same study (7–12), since the latter reach ~10 wt% higher contents of SiO<sub>2</sub>. Eclogite melts have similar SiO<sub>2</sub> contents as andesites (Luhr and Carmichael, 1985), which explains their similar range in melt viscosity (Fig. 5.6 A). However, the andesites achieve twice as high  $D_{Ni}$  values as the eclogite melts (20–47 versus 12–23). We assume this difference to arise from their ~150 °C lower temperature and significantly higher fraction of Al<sub>2</sub>O<sub>3</sub> (16.3 versus 13.4 wt%). At low temperatures of ~1000 °C, as achieved by the andesites, Al increases melt viscosity (Le Losq et al., 2014). This implies, that the andesites might have a higher degree of melt polymerization than the eclogite melts. Therefore, we conclude that high fractions of Na, K, and Al are characteristic for high-grade polymerized melts and, therefore, imply also high  $D_{Ni}$ .

We interpret the Ni-partitioning between olivine and liquid to be dominated by the melt polymerization. Their influence on  $D_{Ni}$  is stronger than the temperature-influence, since highest  $D_{Ni}$  are not achieved by the coolest melts, but those with greatest polymerization as evident by high contents of Na, K, and Al (Supplementary Fig 5.4). Nevertheless, since (Matzen et al., 2013; 2017) reported significant influence of temperature on the partitioning process, the combination of  $D_{Ni}$  and change of melt composition should result in a sensitive geothermometer (4.3).

#### 5.4.3 Ni-partitioning in olivine/liquid as a geothermometer

To investigate the correlation of  $D_{Ni(olivine/melt)}$  versus all major constituents, their oxide-wt% were combined in groups of similar charges and ionic-radii ratios and coordination environments. Furthermore, oxides that correlate with  $D_{Ni}$  positively (Na<sub>2</sub>O, K<sub>2</sub>O, SiO<sub>2</sub>, TiO<sub>2</sub>, Al<sub>2</sub>O<sub>3</sub>) were

positioned at the numerator, while those groups that correlate negatively (MgO, FeO, CaO), were positioned at the denominator, resulting in [I] (Fig. 5.7) with  $R^2$  of 0.94:

$$\frac{[liq(Na_2O + K_2O)] \cdot [liq(SiO_2 + TiO_2)] \cdot [liq(Al_2O_3)]}{[liq(MgO + FeO)] \cdot [liq(CaO)]} \quad [I]$$

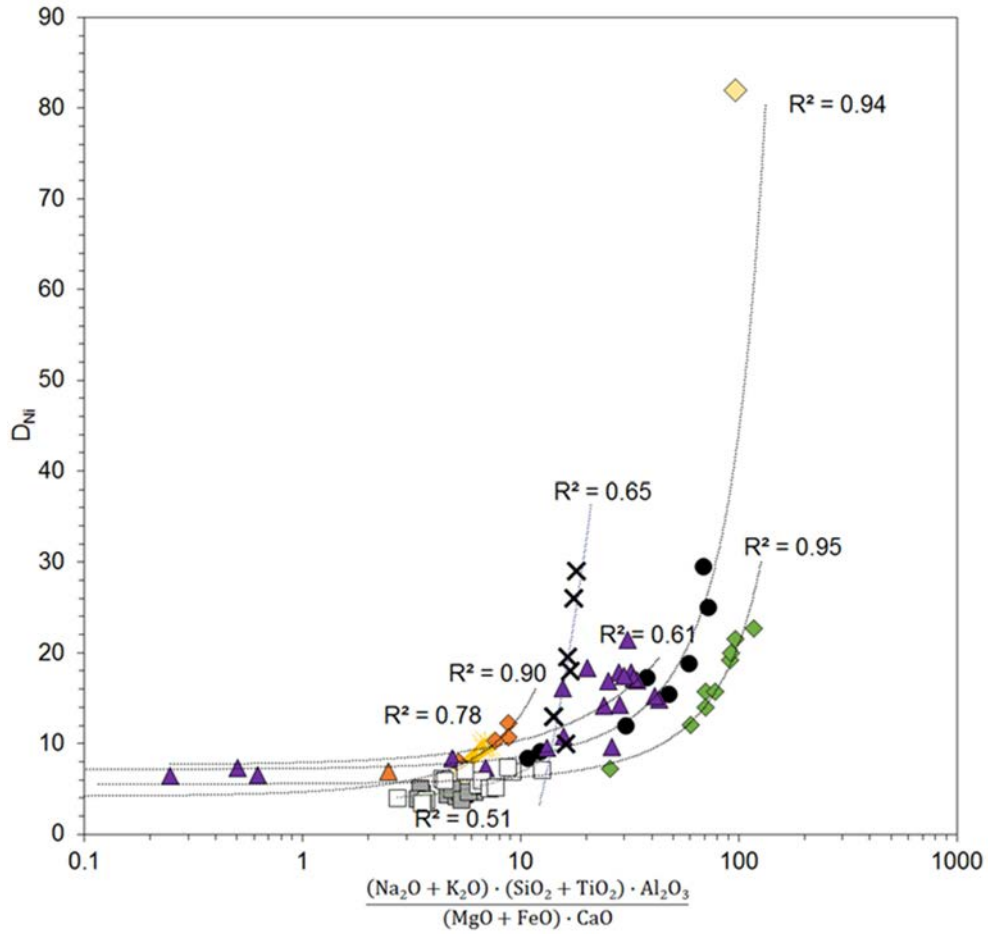


**Fig. 5.7:**  $D_{Ni}$  dependencies of our melts (black circles) and test datasets (symbols are the same as in Fig. 5.6). The large yellow diamond is the Gaussberg datapoint from Foley and Jenner (2004), a leucitite from Antarctica with total alkalis of ~14 wt% which is not included into any regression. It closely plots to the extrapolation of the exponential fit of our dataset and shows that ultrapotassic compositions are able to reach exceptionally high  $D_{Ni}$  for olivine/melt.

We applied this term to datasets of contrasting compositions ranging from basaltic-, Fe-rich basaltic, and alkaline-, to eclogite melts (Filiberto et al., 2009; Ford et al., 1983; Matzen et al., 2013; 2017; Snyder and Carmichael, 1992; Wang and Gaetani, 2008). All datasets show positive exponential fits with  $D_{Ni}$  (Fig. 5.7). The  $D_{Ni}$  of ~80 found in a leucitite from Antarctica (Foley and Jenner, 2004) is close to the extrapolation of the exponential curve fit of our dataset, showing that ultrapotassic melts can reach exceptionally high  $D_{Ni}$  values.

The relationship of melt composition and nickel partitioning between olivine and liquid is established here as a new geothermometer. The temperature-dependent variation of the melt

compositions were used previously to calibrate geothermometers based on glass composition (Helz and Thornber, 1987; Putirka, 2008; Thornber et al., 2003) and olivine/liquid Ni-partitioning (Arndt et al., 1977; Håkli and Wright, 1967). The new thermometer is derived from [I], whereby CaO is replaced by TiO<sub>2</sub> [II]. The replacement of CaO was necessary since it shows opposed sloping correlations with D<sub>Ni</sub> upon test data sets (Supplementary Fig. 5.5). The differences in sloping of CaO *versus* D<sub>Ni</sub> lead to the spread of the literature datasets along the X-axis when [I] is plotted *versus* D<sub>Ni</sub> (Fig. 5.7). This difference in correlation is only present for CaO and is connected to fractionation: simple olivine fractionation leads to an increase with D<sub>Ni</sub>, whereas fractionation of olivine + clinopyroxene (+plagioclase) removes CaO and leads to a decrease with D<sub>Ni</sub>. However, datasets plot in the same range when CaO is replaced by TiO<sub>2</sub>. Rearrangement of the term moves TiO<sub>2</sub> as a denominator to SiO<sub>2</sub>. This term then shows a similar correlation of all test data sets *versus* D<sub>Ni</sub>:

$$\frac{[liq(Na_2O+K_2O)] \cdot [liq(1+\frac{SiO_2}{TiO_2})] \cdot [liq(Al_2O_3)]}{[liq(MgO+FeO)]} \quad II$$

For temperature calibration, D<sub>Ni</sub> was added to the term and plotted against the experimental run temperature. This yielded a logarithmic dependency, which results in [III]:

$$T (^{\circ}C) = -88.14 \cdot \ln\left( \frac{[(liq(Na_2O+K_2O)] \cdot [liq(1+\frac{SiO_2}{TiO_2})] \cdot [liq(Al_2O_3)]}{[liq(MgO+FeO)]} \cdot D_{Ni} \right) + 1906.2 \quad III$$

This thermometer is closely aligned to the bisectrix of a 1:1 fit between measured and calculated temperature and shows an R<sup>2</sup> of 0.87 for the calibration dataset of our study (Supplementary Fig. 5.6). It is applicable to temperature ranges of 1000–1600 °C for natural melt compositions over the range of olivine crystallization (Fig. 5.8 A). The calculated temperatures agree well with the measured temperatures of the test datasets. Average temperature deviations between calculated and measured values range from 17 to 33 °C, compared to 10–87 °C for thermometers that solely use Ni-partitioning (Hart and Davis, 1978) (Fig. 5.8 B), as well as 29–67 °C and 38–122 °C for thermometers using glass composition only (Fig. 5.8 C,D) (Helz and Thornber, 1987; Putirka, 2008; Thornber et al., 2003).

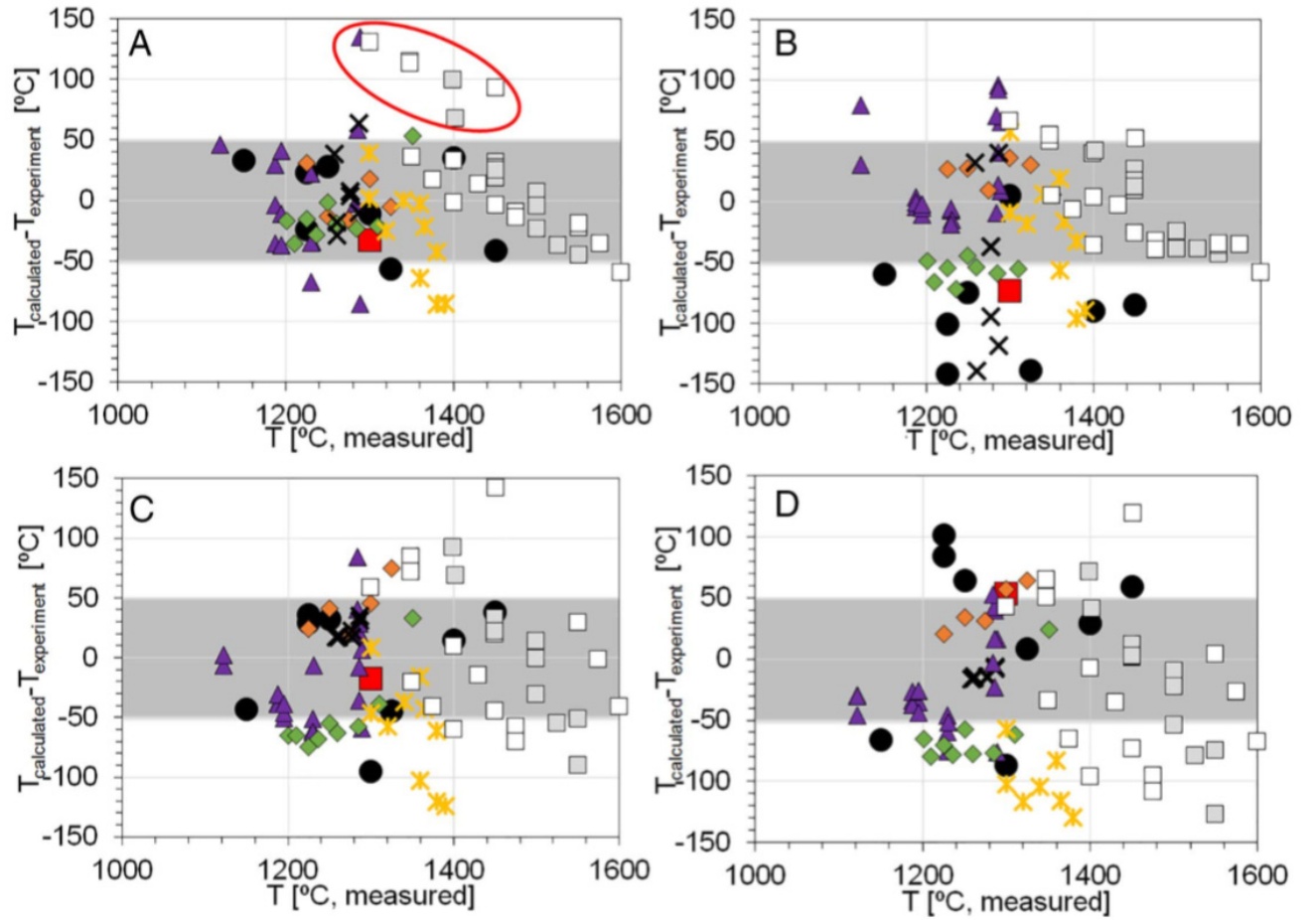


**Fig. 5.8:** Glass-based geothermometers showing deviations of calculated- from measured temperatures of ultrapotassic melts from our study (black circles and red square) and literature data: the symbols are the same as in Fig. 5.6. Grey inlay corresponds to a deviation of  $\pm 50$  °C from the measured temperature. Encircled data points are not included in deviations since they are derived from experiments with significant loss of alkalis and iron. A) shows our new thermometer, comprising average deviations of the test data sets ranging from  $\pm 17$ – $33$  °C. B) is a pure Ni-partitioning based geothermometer from Hart and Davis (1978), which gives deviations from measured values ranging from  $\pm 10$ – $87$  °C. C) and D) are thermometers from Putirka (2008), based on the glass composition with average deviations of  $\pm 29$ – $67$  °C and  $\pm 38$ – $122$  °C, respectively.

While Matzen et al. (2013; 2017) reports an influence of pressure on  $D_{\text{Ni}}$  between 2 and 3 GPa, our thermometer reproduces temperatures independent of the experimental pressures (0.0001–5 GPa), suggesting that any influence is a secondary effect of changing melt compositions. Some data points from Snyder and Carmichael (1992) and Matzen et al. (2013; 2017) show overestimations of  $>100$  °C for calculated temperatures of experiments conducted at 0.1 MPa, (Fig. 5.8 A, Supplementary Fig. 5.6). However, the authors report loss of Na, K, and Fe in these experiments, which likely explains the overestimation of the calculated temperatures as the composition of the liquid changed. Similar experiments, conducted at 0.1 MPa pressure (Wang

and Gaetani, 2008), report no element loss and do indeed yield correctly reproducible temperatures.

Recently, Pu et al. (2017) provided a new Ni-partitioning thermometer that calculates temperature based on  $D_{Ni}$  and the molar abundances of major and minor constituents (FeO, MnO, MgO, CaO, CoO, NiO,  $TiO_2$ ,  $Al_2O_3$ ) in melt and olivine and is calibrated on 123 different 1-atm pressure experiments. This thermometer reproduces melt temperatures of experiments at ambient pressures well, however, melt temperatures of high-pressure experiments are underestimated by  $>50\text{ }^{\circ}\text{C}$  (Supplementary Fig. 5.7).

Nickel partitioning between olivine and melt and the change of melt composition complement each other well, since both monitor the temperature of the host magma. We encourage researchers to examine this thermometer in further studies to unravel the exact connection between  $D_{Ni}$  and melt composition.

#### 5.4.4 Geothermometry on natural glass-olivine pairs

Fig. 5.9 gives an application of our thermometer with calculated temperatures *versus*  $D_{Ni}$  to datasets of various composition ranging from calc-alkaline to ultrapotassic to MORB to OIB (Hawaii) compositions. Our aim here is to test if the thermometer is applicable to natural olivine/liquid pairs.

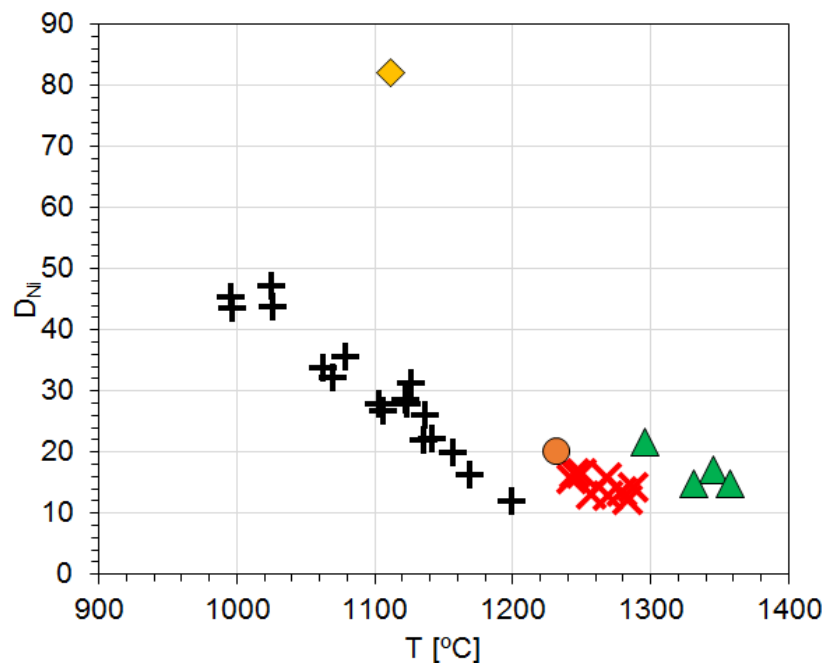


**Fig. 5.9:** Application of the thermometer to olivine-glass pairs from lavas of different geologic settings: orange diamond – Gaussberg (Antarctica)/leucitite (Foley and Jenner, 2004), black pluses – Mexico/calc-alkaline basaltic-andesite (Luhr and Carmichael, 1985), red crosses – East Pacific Rise/MORB (Allan et al., 1989), orange circle – Gakkel Ridge/MORB (Mühe et al., 1997), green triangles – Hawaii/olivine-tholeiite (Leeman and Scheidegger, 1977).

The reproducibility of temperatures from melts in high- and ambient pressure experiments (Fig. 5.8) suggests considerable agreement with our calculations for the majority of the melt compositions. Calculated temperatures (996–1199 °C) for calc-alkaline basalts and andesites from Mexico (Luhr and Carmichael, 1985) agree well with calculated temperatures (1020–1177 °C) from Pu et al. (2017). However, the calculated temperature for MORB compositions (~1265 °C) from the East Pacific Rise (Allan et al., 1989) exceeds that calculated by Pu et al. (2017) (~1177 °C). Nevertheless, the average for East Pacific Rise-MORB and the temperature of 1232 °C calculated for Gakkel-ridge MORB (Mühe et al., 1997) are within the range of temperatures (1218–1336 °C) that were experimentally determined for dry crystallizing MORB-magma (Almeev et al., 2007; Falloon et al., 2007a). An average calculated temperature of 1330 °C for glasses from Hawaii (Leeman and Scheidegger, 1977) is also close to the temperature (1365 °C) of Hawaiian primary magmas (Green et al., 2001), however, highest observed eruption temperatures of Hawaiian lavas are lower at about 1190 °C (Ault et al., 1961). Erupted Hawaiian glass also contains 0.93 wt% H<sub>2</sub>O (Falloon et al., 2007b), which is 3-times higher than basalt intruding into the summit magma-chambers (0.32 wt%: Greenland et al., 1985). In addition, the Kilauea glass has a K<sub>2</sub>O/H<sub>2</sub>O ratio of 2, while olivine fractionation should increase both species on a 1:1 line (Falloon et al., 2007b). Small amounts of H<sub>2</sub>O (<1 wt%) significantly depress the liquidus of basalt by <100 °C, an effect that is less-pronounced in silicic magmas (Médard and Grove, 2008). The enrichment of H<sub>2</sub>O takes place at the roof of the magma-chamber prior to the eruption (Jaupart and Vergnolle, 1989), thereby reducing the liquidus of the basalt and enabling the overheated magma to cool to the measured eruption temperature.

Accordingly, this thermometer [III] calculates magma-chamber temperatures of the last equilibration of olivine with melt, rather than eruption temperatures that are lower due to cooling prior to eruption.

## 5.5 Conclusion

1. Incongruent melting of MARID glimmerites produces melts with K<sub>2</sub>O of 8–10 wt%, 11–12 wt% Al<sub>2</sub>O<sub>3</sub> at MgO values of 10–15 wt% and SiO<sub>2</sub> of < 45 wt%. Upon reaction with harzburgite, these melts crystallize clinopyroxene and phlogopite, lowering Al<sub>2</sub>O<sub>3</sub> and K<sub>2</sub>O of the melt. Thus, incongruent and reaction melts of MARID glimmerites are capable of explaining the composition of various ultrapotassic magmas.

2. The ultrapotassic melt compositions show that olivine/liquid Ni-partitioning is dominated by the melts polymerization as expressed by high contents Na, K, and Al.

3. The change in melt composition and influence of temperature on nickel-partitioning complements to a new pressure-independent geothermometer. It yields precise melt temperatures in the range of 1000–1600 °C and is applicable for basaltic, alkaline, and ultrapotassic melts.

4. Geothermometry on natural olivine-liquid pairs shows that calculated temperatures likely represent magma-chamber temperatures of the last olivine-liquid equilibration. We estimate temperatures of 997–1199 °C for calc-alkaline magmas (Mexico), 1265 °C for MORB (East Pacific Rise), and 1330 °C for Hawaiian magma (Kilauea).

### **Author contributions**

MF performed all experiments and processed and interpreted the data. MF wrote the manuscript. SB and RMK assisted in analysis and evaluation of the datasets. DJ, HRM, HRS and DP helped in data interpretation and manuscript evaluation. MF handles the correspondence of the submitted manuscript version of this chapter.

### **Acknowledgements**

This work is part of the lead authors PhD thesis and is supported by an Australian Government International Postgraduate Research Scholarship (IPRS). This project was also financed by the “Internal University Research Funding” program of the Johannes-Gutenberg University, Mainz. DP was supported through the Deutsche Forschungsgemeinschaft (DFG) within the project PR 1072/9-1. Thomas Kautz and Fabian Schroeder-Frerkes of the Goethe University, Frankfurt are thanked for assistance with the Belt-apparatus. Jennifer Rowland is gratefully acknowledged for proof-reading the manuscript and language improvement. Ananya Mallik and Cliff Shaw are gratefully acknowledged for providing reviews that significantly improved this manuscript.



## Chapter 6:

# Partitioning of Nitrogen during Slab-melting and Recycling in Subduction Zones

Michael W. Förster<sup>1</sup>, Stephen F. Foley<sup>1</sup>, Olivier Alard<sup>1</sup>, Stephan Buhre<sup>2</sup>

<sup>1</sup>Australian Research Council Centre of Excellence for Core to Crust Fluid Systems (CCFS) and GEMOC, Macquarie University, NSW 2109, Sydney, Australia

<sup>2</sup>Institute for Geosciences, Johannes Gutenberg University, 55099 Mainz, Germany

This chapter is prepared for submission to *Chemical Geology*.

### Abstract

The subduction of sediment connects the surficial nitrogen cycle to that of the deep Earth. To understand the evolution of nitrogen within Earth's atmosphere, the behavior of nitrogen during subduction and the melting of subducted sediments has to be estimated. This study follows a high-pressure experimental approach to measure the partitioning of nitrogen in melting sediments at sub-arc depths. For quantitative analysis of nitrogen in minerals and glasses, we calibrated the electron probe micro-analyzer on synthetic ammonium-feldspar to measure nitrogen mass fractions down to 500 µg g<sup>-1</sup>. Nitrogen abundances in melt and mica as well as mass balance calculations are used to determine  $D_{N(\text{Mica/Melt})}$ ,  $D_{N(\text{Fluid/Mica})}$ , and  $D_{N(\text{Fluid/Melt})}$ . Calculated partition coefficients correspond to expected values for NH<sub>4</sub><sup>+</sup>, which behaves similarly to Rb<sup>+</sup> due to its nearly identical size. We found that nitrogen partitioning between fluid and melt ( $D_{N(\text{Fluid/Melt})}$ ) and fluid and bulk residue (melt+mica) ( $D_{N(\text{Fluid/Bulk})}$ ) increases linearly with temperature normalized to pressure. This linear relationship can be used to calculate  $D_{N(\text{Fluid/Melt})}$  and  $D_{N(\text{Fluid/Bulk})}$  for slab melts from 800-1200 °C following:

$$D_{N(\text{Fluid/Melt})} = 0.012 \times \frac{T [^{\circ}\text{C}]}{P [\text{GPa}]} - 2.02 \quad D_{N(\text{Fluid/Bulk})} = 0.04 \times \frac{T [^{\circ}\text{C}]}{P [\text{GPa}]} - 8.48$$

We used these partition coefficients to quantify the amount of N recycled to Earth's mantle as 50 ± 6 % of today's atmospheric N. Depending on the rate of mantle N degassing we calculated 4 different scenarios of pN<sub>2</sub> evolution. All 4 scenarios estimate pN<sub>2</sub> to be 8-12 % higher at the beginning of the Phanerozoic. These estimates diverge towards the past due to uncertainties of N-degassing from Earth's mantle. Assuming degassing of N in the past stayed close to modern

degassing from MORB,  $pN_2$  was up to 40 % higher at the onset of plate tectonics. However, since degassing was likely higher, 10x and 20x times the degassing of N at the onset of plate tectonics leads to  $pN_2$  within 20 % of modern values. If N-degassing from the mantle is increased to 40x the modern MORB,  $pN_2$  in the Archean would have been 50 % lower than today's, which is in accordance with observations from paleo atmospheric studies.

## 6.1 Introduction

Nitrogen is the main element of Earth's atmosphere. It is an essential element for life and takes part in complex biogeochemistry due to numerous oxidation states spanning from +5 to -3. The various reactions of nitrogen, forming reduced and oxidized species take part in a surficial nitrogen cycle (Boyd, 2001; Vitousek et al., 1997). Besides the well-established and relatively rapid cycling of nitrogen at and near the surface, nitrogen takes part in a deep geological cycle and is an important constituent of Earth's mantle (Johnson and Goldblatt, 2015). Recent studies favour the view that the majority of Earth's nitrogen is sequestered in the solid Earth (Barry and Hilton, 2016; Johnson and Goldblatt, 2015; Mallik et al., 2018; Marty, 2012), rather than in the atmosphere as originally proposed (Goldschmidt, 1937). The connection of the surficial to the deep nitrogen cycle takes place in the oceans: atmospheric nitrogen is continuously fixed and deposited in marine sediments and added to the oceanic crust by hydrothermal alteration (Johnson and Goldblatt, 2015). The ongoing recycling of nitrogen to mantle depths is thought to be associated with potassium-bearing silicates in subduction zones, where micas play an integral role, dominated by the substitution of ammonium ( $NH_4^+$ ) for potassium ( $K^+$ ) in silicates (Watenphul et al., 2009; 2010). During melting of sediments and magma formation,  $NH_4^+$  is likely re-oxidized to  $N_2$  and escapes from the mantle via magmatic volatiles in arc settings. Li et al. (2013) showed that nitrogen behaves highly incompatibly during melting of anhydrous mantle rocks and has low abundances in basalts ( $<10 \mu g g^{-1} N$ ). However, ultrapotassic magmas are nitrogen-rich ( $\sim 400 \mu g g^{-1} N$ ), indicating the presence of nitrogen-bearing lithologies that reside within the shallow and metasomatized lithospheric mantle (Jia et al., 2003). The origin of nitrogen within Earth's mantle and atmosphere is an ongoing matter of debate and recent models favour three main scenarios (Johnson and Goldblatt, 2018):

- (1) A thick, N-rich, atmosphere dates from shortly after Earth's formation and is subducted over time, meaning that N within the Earth's mantle is mainly of recycled origin (Barry and Hilton, 2016; Goldblatt et al., 2009; Johnson and Goldblatt, 2015; Mallik et al., 2018).

(2) A thin, N-poor, atmosphere prevailed on the early Earth: N is degassed over time from Earth's mantle (Som et al., 2012; 2016) to form the current atmosphere.

(3) A steady state partial pressure of N<sub>2</sub> over Earth's history with balanced degassing and recycling of N (Berner, 2006; Marty et al., 2013; Zhang and Zindler, 1993).

Scenario (1) is in accordance with mass balance calculations that show a strong imbalance, with N recycling within subduction zones dominating over N degassing from Earth's mantle (Busigny et al., 2011). This scenario promotes a thick atmosphere during the Archean which would also be a solution to the 'faint young sun' paradox due to pressure broadening of the absorption lines of greenhouse gases (Goldblatt et al., 2009; Goldblatt and Zahnle, 2011). A recent model based on N isotopes in oceanic basalts also predicts a 50 % higher atmospheric density in the Archean atmosphere than at present (Barry and Hilton, 2016). Scenario (2), which foresees a thin N-poor atmosphere at Earth's formation, is dependent on gradual degassing of N from Earth's mantle due to ineffective recycling of N at subduction zones (Fischer et al., 2002). This scenario promotes a thin Archean atmosphere, which had a density similar to or lower than today's atmosphere, as estimated from fossilized rain drop imprints (Som et al., 2012). The use of rain drop imprints as an indicator for atmospheric density has been shown to be strongly dependent on the precipitation rate which cannot be estimated for fossilized rain drop imprints (Kavanagh and Goldblatt, 2015). However, vesicle size distribution within Archean basalt (Som et al., 2016) also favour an Archean atmosphere with lower density than today's. Scenario (3) is supported by fluid inclusions in Archean hydrothermal quartz which show density and partial pressure of N similar to today's atmosphere (Marty et al., 2013). Previous models that calculated constant N within Earth's atmosphere were based on the assumption that N behaves like C during subduction (Berner, 2006). However, since N is present as NH<sub>4</sub><sup>+</sup> in silicates, its behavior should certainly be less volatile (Johnson and Goldblatt, 2015).

Venus provides a clue about the amounts of N that might have been cycled during Earth's geological history since it has 3.4x the mass of N compared to Earth's atmosphere when Venus is normalized to Earth's mass (Johnson and Goldblatt, 2015). However, Venus does not possess active plate tectonics and it is unknown whether N within the Venusian atmosphere is of primary origin (1) or degassed over time (2).

The effectiveness of recycling of N at subduction zones dominates the evolution of N in the atmosphere in all three scenarios. Hence, our understanding of the geological cycling of N relies on detailed knowledge on the behavior of N in subduction zones (Johnson and Goldblatt, 2018). The different estimates of recycled versus degassed N in subduction zones range from total

degassing (Fischer et al., 2002) to up to 92 % recycling of N to the deeper mantle (Barry and Hilton, 2016; Busigny et al., 2011). Minerals such as  $\text{NH}_4$ -bearing mica, feldspar, pyroxene, beryl, and olivine are possible hosts for subducted N (Bebout et al., 2016; Watenphul et al., 2009; 2010). Experimental studies determined that  $12 \pm 5$  % to  $17 \pm 8$  % of N within Earth's mantle is of recycled origin as determined by the effectiveness of N recycling at the solubility limit of N in rhyolitic slab melts and  $\text{NH}_4^+$ -partitioning between mica and melt similar to Rb (Mallik et al., 2018). However, partition coefficients for N as  $\text{NH}_4^+$  between mica/melt and melt/fluid remain to be determined.

In this study, we experimentally investigate the partitioning of N during sediment subduction. Partition coefficients are used to calculate the amounts of N that were metasomatized to the shallow- and recycled to the deep mantle since the onset of plate tectonics. The experimental setup includes a 2-layer arrangement of sediment and dunite, representing sediment below depleted mantle within the fore-arc of a subduction zone. During the experiment, the sediment melts and reacts with the dunite, producing a hydrous reaction assemblage. We determine partition coefficients of N for mica/melt by measuring these phases with EPMA and partition coefficients of N for melt/fluid by mass balance calculations.

## 6.2 Materials and Methods

The experimental charges consisted of layered sediment (ODP 161-976 B 18 X3 105-106.5; a carbonate-bearing (<10%) siliciclastic marine sediment) and dunite (sample ZD11-53 from the Zedang ophiolite, south Tibet, China) containing olivine (>97%), spinel (~2%), and clinopyroxene (<1%). Both samples were powdered in an agate mortar.

Experiments at 2 and 3 GPa were conducted in a piston-cylinder apparatus at the University of Mainz and at 4 GPa in a belt apparatus at the University of Frankfurt. Experimental charges were filled into a carbon capsule to control  $f\text{O}_2$  via the C + CO equilibrium and then were placed into platinum outer capsules. These were fitted into  $\text{Al}_2\text{O}_3$  spacers, a graphite furnace, b-type thermocouple, and sintered  $\text{CaF}_2$  spacer on the outside of the assemblage for the piston cylinder experiments. For belt apparatus experiments, the spacer and capsule holder consisted of natural polycrystalline calcium fluoride, while other materials were identical to those used in the piston-cylinder experiments. All assemblies were pressurized first and heated at a rate of 50 °C/min. Both the piston cylinder and belt apparatus experiments were cooled by a water circuit (at approximately 13 °C) and pressure and temperature were kept constant for 2-14 days. All charges

were quenched to temperatures below 500 °C within 8 s in the piston-cylinder runs, and within 10 s in the belt runs. The NH<sub>4</sub>-feldspar (buddingtonite) was synthesized in a Walker-type multi-anvil press at Macquarie University, Sydney, using a 25/17 assemblage. The buddingtonite was synthesized following the method described in Harlov et al. (2001) using a stoichiometric Al<sub>2</sub>O<sub>3</sub> and SiO<sub>2</sub> mix and a 25 % NH<sub>3</sub> solution (all three constituents from SIGMA-ALDRICH®) with an excess of 50 % over that needed for synthesis. The sample mix was placed into a Ni capsule and welded whilst cooled in a water bath. The synthesis run was performed at 0.5 GPa and 600 °C for 1 week.

We have calibrated a new EPMA routine for the analysis of N in silicate minerals using the LDE-B, a synthetic crystal for light element wavelength analysis, of a JEOL JXA 8200 Superprobe at the Johannes Gutenberg-University, Mainz. The acceleration voltage was set to 10 kV with a sample current of 20-40 nA and a defocused beam of 10-20 µm in diameter. As reference materials we used boron nitride (56.4 wt% N) as well as the synthesized NH<sub>4</sub>-feldspar (5.3 wt% N, [Table 6.1](#), [Supplementary Fig. 6.1](#)). Nitrogen counts were found to be stable for peak counting times of 160 s on buddingtonite ([Supplementary Fig. 6.2](#)), which resulted in detection limits of ~500 µg g<sup>-1</sup>. The whole dataset of analyzed phases are given in [Supplementary Data Tables 1-10](#).

Raman spectra of buddingtonite, phlogopite, and glass were collected at room temperature using a Horiba Jobin Yvon LabRAM HR Evolution confocal spectrometer at Macquarie University, Sydney, with 532 nm laser excitation. Spectra were recorded from 150-3900 cm<sup>-1</sup> using a spectral acquisition time of 30 seconds and 2 accumulations. A 1800 grooves/mm grating with a slit width of 100 µm was used which ensured a spectral resolution of ca. 0.8 cm<sup>-1</sup>.

Abundances of the light elements H, C, and N in the sediment were determined using an automated vario EL cube elemental analyzer (Elementar, Langenselbold, Germany). Three aliquots were measured using the method described in Le Huong et al. (2018). Analyses of SDO-1 (USGS reference material - shale) yielded H = 1.57 ±0.14 wt%; C = 9.11 ±0.01 wt% and N = 0.36 ±0.01 wt%, within error of the compiled values in GeoReM (<http://georem.mpch-mainz.gwdg.de/>, Jochum et al., 2005) for H and C (H = 1.34 wt%; C = 9.95 wt%).

**Table 6.1:** Composition of the synthetic buddingtonite (NH<sub>4</sub>AlSi<sub>3</sub>O<sub>8</sub>)•0.5(H<sub>2</sub>O), used as N-reference material for EPMA.

	N [wt%]	Al [wt%]	Si [wt%]	O [wt%]*	H [wt%]
Av. measured buddingtonite [N=15]	5.2 ±0.2	9.1 ±0.2	32.1 ±0.8	51.7 ±0.9	1.9 ±0.1
Calculated composition	5.3	10.1	31.6	51.1	1.9

\*calculated from cation difference to 100 wt%

## 6.3 Results

### 6.3.1 Structural observations

Eight reaction experiments were performed at 2-4 GPa at temperatures ranging from 750 to 1200 °C, which produced a metasomatic reaction zone at the interface between the melted sediment and the depleted peridotite (Table 6.2). In addition, one melting experiment on the sediment without addition of peridotite was performed at 4 GPa/1000 °C. The sedimentary starting material contains 0.35 wt% N, as determined by CHNS elemental analyzer. The reaction experiments show a reaction zone of variable thickness (80-400 µm) sandwiched between the sediment and dunite layers (Fig. 6.1). This reaction zone is mainly composed of 4 minerals, namely orthopyroxene, clinopyroxene, phlogopite, and magnesite (Fig. 6.1 A). Experiments performed at >800 °C also contain veins of orthopyroxene with minor amounts of magnesite extending from the reaction zone further into the peridotite along olivine grain boundaries. The former sediment consists mainly of silicate glass (~20-40 wt%), Mn-rich garnet, and Na-Al-rich clinopyroxene in all experiments >800 °C, while at 850 °C phengite (Fig. 6.1 B), and at 800 °C coesite, were also present.

**Table 6.2:** Thermobaric conditions and phases present in experimental runs.

#	Experiment	P [GPa]	T [°C]	Phases	Duration
1	Sediment/dunite reaction	2	750	Cc + Phe + Cpx + Qz + C	4 d
2	Sediment/dunite reaction	2	900	Ol + Opx + Cpx + Gt + melt	4 d
3	Sediment/dunite reaction	3	800	Ol + Opx + Cpx + Phl + Mgs + Gt + Phe + Coe + Cc + melt	7 d
4	Sediment/dunite reaction	3	850	Ol + Opx + Phl + Cpx + Mgs + Gt + melt	14 d
5	Sediment/dunite reaction	3	900	Ol + Opx + Phl + Cpx + Mgs + Gt + melt	14 d
6	Sediment/dunite reaction	3	1000	Ol + Opx + Cpx + Gt + (Phl) + melt	4 d
7	Sediment melting	4	1000	Ky + Gt + Coe + melt	4 d
8	Sediment/dunite reaction	4	1100	Ol + Opx + Gt + (Phl) + melt	2 d
9	Sediment/dunite reaction	4	1200	Ol + Opx + Gt + melt	2 d



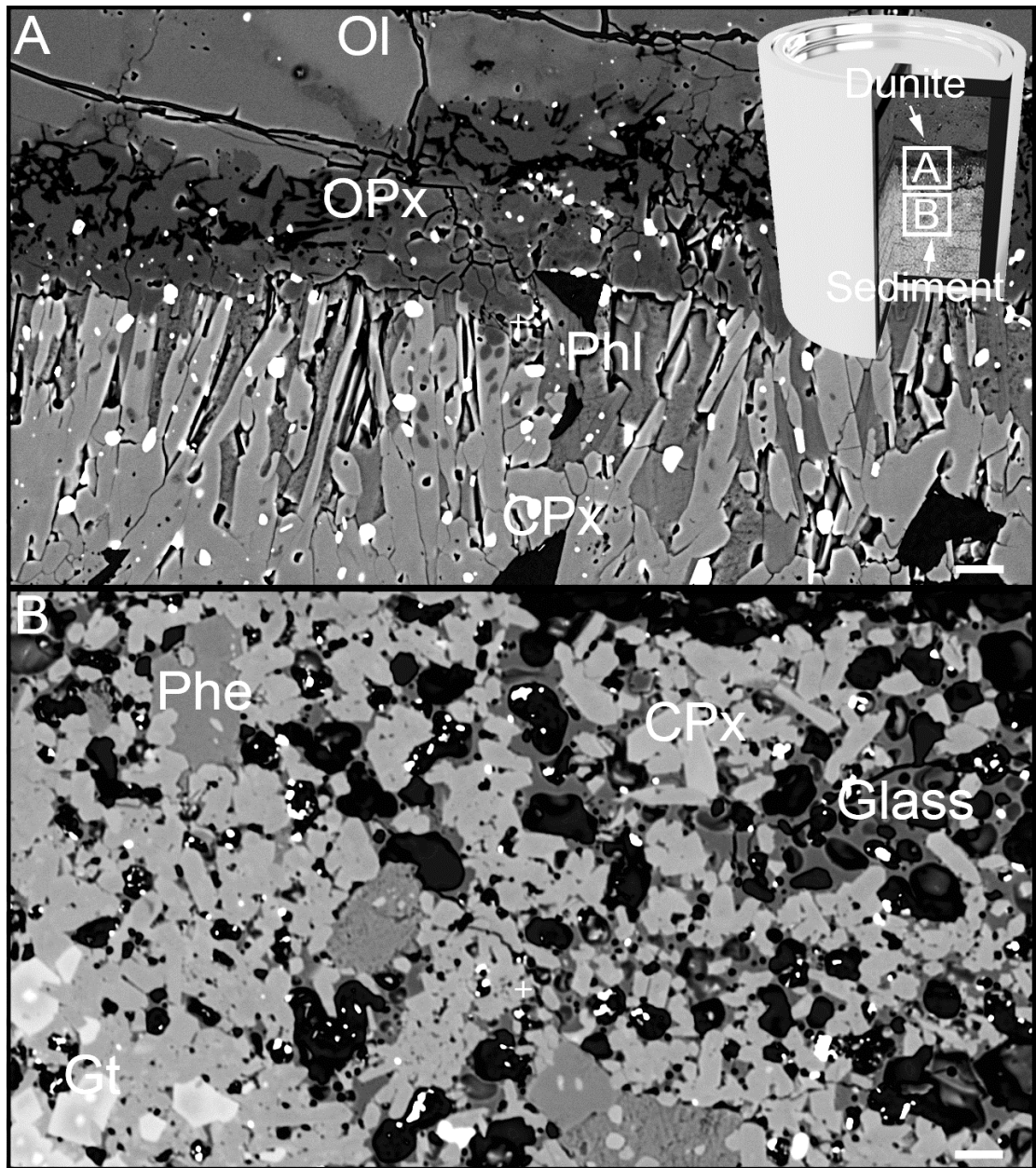


**Fig. 6.1:** Backscattered electron image of the 3 GPa/850 °C experiment. The location of the reaction zone (A) and the melted sediment (B) are highlighted on the capsule image. A) Melts of sediment react with olivine to form metasomatic phases orthopyroxene, clinopyroxene, magnesite, and phlogopite. B) The sediment melted and crystallized phengite, garnet, and clinopyroxene. Scale bar in A) and B) represents 10  $\mu\text{m}$ .

### 6.3.2 Nitrogen concentration and -speciation in experimental phases

We measured N in glass, phengite and phlogopite mica, as well as in the residual former sediment. The breakdown of carbonate, clay, and organic material produced an N-bearing  $\text{H}_2\text{O} \pm \text{H}_2 \pm \text{CO}_2 \pm \text{CO} \pm \text{CH}_4$  fluid, whereby the speciation depends on pressure, temperature, and oxygen fugacity. Since the sediment is saturated in carbon by the graphite inner capsule, the breakdown of organic carbon and carbonate follows the reaction:  $\text{CH}_4 + \text{H}_2\text{O} = 3 \text{H}_2 + \text{CO}$  (Chiodini and Marini, 1998). For the experimental pressure range, equilibrium constants are

undetermined and measured mass fractions of 8.18 wt% C, 1.83 wt% H, and 4.98 wt% O by CHNS elemental analyzer will lead to a range in abundance for each species: 5.92-6.85 wt% CH<sub>4</sub>, 7.05-8.68 wt% CO, 0-1.05 wt% H<sub>2</sub>O, 0-0.35 wt% H<sub>2</sub>. In addition to the fluid species, the N-bearing residual sediment contains C as carbonate, and graphite and is present within the two coolest experiments at 750 °C and 800 °C. All other phases, such as pyroxene, olivine, garnet, and coesite did not yield any counts for N and are thus well below the detection limit; these phases are summarized as containing 0 wt% N in the mass balance of the experiments. The mass fraction of N within each experiment ranges from 0.35 wt% N to 0.21 wt% N depending on the degree of reaction (0 to 40 %) with N-free dunite from 750-1200 °C (Table 6.3). The mass fraction of N in phengite of the 750 °C experiment was determined by a linear correlation of N versus K<sub>2</sub>O from multiple measurements (Supplementary Fig. 6.3) and yielded 0.67 wt% N at 10 wt% K<sub>2</sub>O, while the residual sediment contained 0.19 wt% N. The linear correlation was necessary since individual phengite grains were smaller than the minimum diameter of the beam (10 µm) that is used for the measurement of N. Experiments at 800-1200 °C exhibit grain sizes >>10 µm and N mass fractions were determined for glass (0.06-0.44 wt% N), phlogopite (0.04-0.28 wt% N), phengite (0.09-0.18 wt%), and residual sediment (0.14 wt% N). While phengite shows a small increase, N generally decreases with increasing temperature in phlogopite and glass (Supplementary Fig. 6.4). The Raman spectra of phlogopite and glass show broadening of the H<sub>2</sub>O/OH peak region (Fig. 6.2), which is in accordance with the presence of NH<sub>3</sub>/NH<sub>4</sub> within the crystal lattice (Li et al., 2013). A CH<sub>4</sub> peak within the glass shows the reduced nature of melts from the carbon-rich sediment. Partition coefficients for N ( $D_N$ ) of phengite/melt and phlogopite/melt range from 0.4-1.5 and 0.4-1.2 (Table 6.3, Fig. 6.3), respectively, and are generally smaller than  $D_K$  which reach ~2.5 (phengite) and ~2 (phlogopite), despite N being incorporated as NH<sub>4</sub><sup>+</sup> on the K<sup>+</sup> position in mica (Watenphul et al., 2009). One experiment at 800 °C shows anomalously high  $D_{N(\text{Phlogopite/Melt})}$  of ~4.6 probably because it was near the solidus and only contains a low degree melt. Mass balance calculations give  $D_N$  between fluid and melt of 0.4-3.7 (Table 6.3, Fig. 6.4 A). A plot of  $D_{N(\text{Fluid/Melt})}$  versus temperature gives a linear fit ( $R^2 = 0.76$ ) when normalized to the experimental pressure (Fig. 6.4 B). Partitioning of N between fluid and bulk composition (melt+mica) versus temperature gives excellent linear fits for 3 GPa ( $R^2 = 0.99$ ) and 4 GPa ( $R^2 = 0.92$ ) (Fig. 6.5 A). The plot of  $D_{N(\text{Fluid/Bulk})}$  versus temperature normalized to pressure gives a linear fit ( $R^2 = 0.95$ ) for all experiments at 2-4 GPa (Fig. 6.5 B).

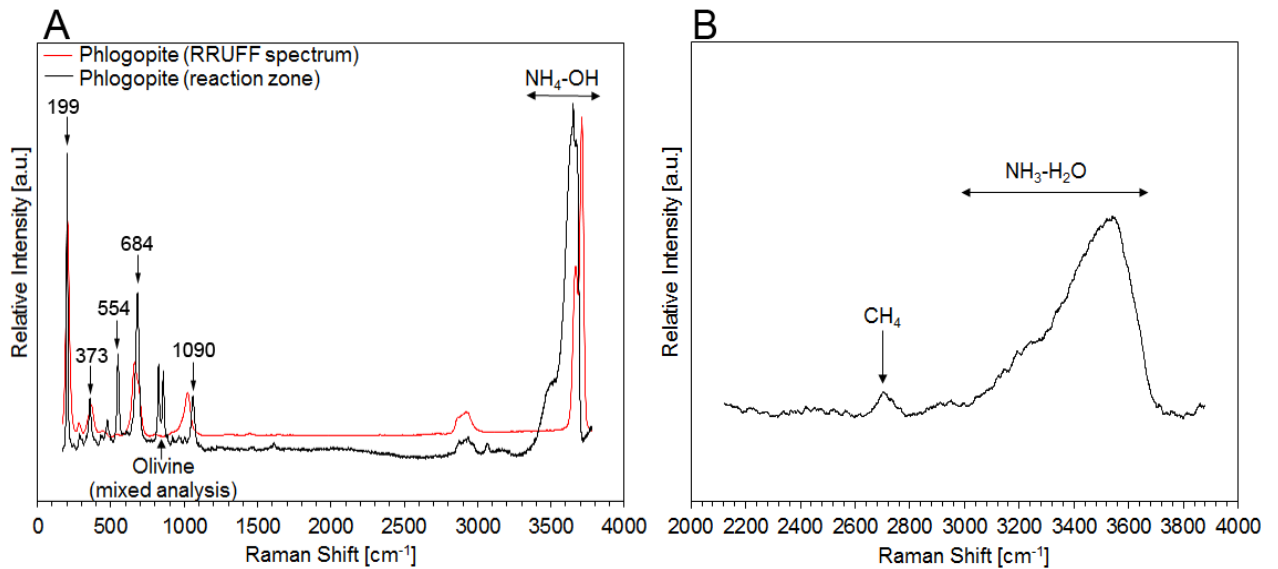


**Fig. 6.2:** Raman spectra of A) phlogopite and B) glass of the 3 GPa/850 °C reaction experiment. A) Phlogopite from the reaction zone is similar to natural phlogopite (spectra from RRUFF database: <http://rruff.info/>, Armbruster and Danisi, 2016) with peak positions from McKeown et al. (1999), while the OH-peak is broadened due to the presence of  $\text{NH}_4^+$  on the  $\text{K}^+$  position. B) The spectra of the hydrous glass within the melted sediment shows a broadened  $\text{H}_2\text{O}$  peak due to the presence of  $\text{NH}_3$  and the existence of a  $\text{CH}_4$  peak, similar to the observations of Li et al. (2013).

**Table 6.3:** Results of nitrogen mass-balance between experimental phases.

Exp #	Total N [wt%]	N [wt%] (%Resid. Sed)	N [wt%] (%Phe)	N [wt%] (%Phl)	N [wt%] (%Glass)	N in Fluid [wt%]	Bulk N [wt%]	$D_N$ Phe/Melt + Phl/Melt	$D_N$ Fluid/Melt	$D_N$ Fluid/Bulk
1	0.35	0.19(6) (91)	0.67(6) (9)	-	-	0.07	0.28	-	-	0.6
2	0.25	-	-	0.07(5) (1)	0.06(2) (38)	0.22	0.02	-1.2	3.7	9.4
3	0.30	0.14(8) (73)	0.09(5) (15)	0.28(5) (1)	0.06(2) (11)	0.17	0.13	1.5/4.7	2.7	1.4
4	0.26	-	0.18(15) (9)	0.27(8) (3)	0.44(10) (15)	0.17	0.09	0.4/0.6	0.4	1.9
5	0.26	-	-	0.17(10) (6)	0.22(12) (24)	0.20	0.06	-0.8	0.9	3.2
6	0.25	-	-	0.04(4) (6)	0.09(4) (43)	0.20	0.04	-0.4	2.2	4.9
7	0.35	-	-	-	0.15(5) (68)	0.25	0.08	-	1.6	2.4
8	0.21	-	-	-	0.23(9) (25)	0.15	0.06	-	0.7	2.7
9	0.21	-	-	-	0.17(9) (27)	0.17	0.06	-	1.0	3.6

## 6.4 Discussion

### 6.4.1 Partitioning of nitrogen in subduction zones

The melting of sediment leads to redistribution of N between crystalline, glass, and fluid phases. Raman spectroscopy of phlogopite and glass both show broadening of peaks in the  $\text{H}_2\text{O}/\text{OH}$  region which is in accordance with the presence of  $\text{NH}_3/\text{NH}_4$  (Li et al., 2013). However, Mallik et

al. (2018) did not observe broadening of the H<sub>2</sub>O peak by NH<sub>3</sub> and demonstrated that at oxygen fugacities of log  $f_{O_2}$  ( $\Delta NNO$ ) -1 to -4, close to the CCO buffer within our experiments, the speciation of N in the glass is N<sub>2</sub>. While Mallik et al. (2018) enriched their experiments with <sup>15</sup>N to visualize the Raman peak of <sup>15</sup>N-<sup>15</sup>N, we cannot estimate the presence of N<sub>2</sub> in our natural samples due to the N<sub>2</sub> peak being at the <sup>14</sup>N-<sup>14</sup>N position and thus overlapped by atmospheric N<sub>2</sub>. However, our experiments are ~300 °C cooler, C-saturated, and CHNS as well as Raman analysis all demonstrate the presence of CH<sub>4</sub>. Hence, log  $f_{O_2}$  is ( $\Delta NNO$ ) -3 to -5 (Foley, 2010; Sokol et al., 2010), below the C + H<sub>2</sub>O water maximum, where N is present as N<sub>2</sub>/NH<sub>3</sub> mixed species within the glass phase.

The exponential decrease of N with temperature in phlogopite ( $R^2 = 0.95$ ) and the overall decrease of N in glass (Supplementary Fig. 6.4), leads to partition coefficients of  $D_{N(\text{Mineral/Melt})}$  that are generally ~0.8 (Fig. 6.3) and thus about half of that of  $D_{K(\text{Mineral/Melt})}$ .

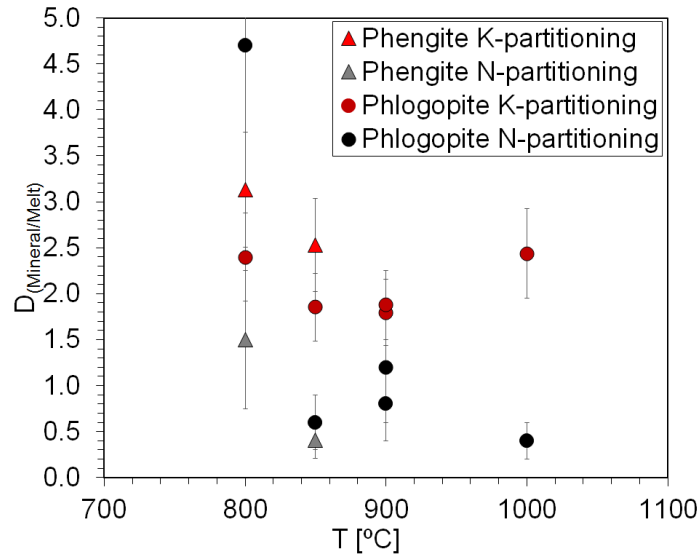


**Fig. 6.3:** Partition coefficients for N and K for phengite/melt and phlogopite/melt.  $D_{N(\text{phlogopite/melt})}$  reach ~0.8 and  $D_{N(\text{phengite/melt})}$  ~0.9, while  $D_{K(\text{phlogopite/melt})}$  attains ~2 and  $D_{K(\text{phengite/melt})}$  ~2.6. The 800 °C experiment reaches very high  $D_{N(\text{phlogopite/melt})}$  of ~4.5, probably as a consequence of loss of N to a fluid-phase at low-degrees of melting. All other experiments show similar  $D_{N(\text{phlogopite/melt})}$  independent of experimental temperature.

It was previously argued that NH<sub>4</sub><sup>+</sup> behaves in a similar way to Rb<sup>+</sup> in terms of fluid/melt and fluid/mica partitioning since the ionic radius of NH<sub>4</sub><sup>+</sup> closely resembles that of Rb<sup>+</sup> (Mallik et al., 2018; Shannon, 1976; Watenphul et al., 2009). Indeed, measured  $D_{N(\text{Fluid/Mica})}$  of 0.1 (subsolidus) and  $D_{N(\text{Fluid/Melt})}$  of 0.4-3.7 are within the range of published  $D_{Rb(\text{Fluid/Mica})}$  of 0.1 (subsolidus) and  $D_{Rb(\text{Fluid/Melt})}$  of 0.3-4.3 (Adam et al., 2014). The  $D_{N(\text{Fluid/Melt})}$  of 0.4-3.7 are lower than  $D_{N(\text{Fluid/Melt})}$  of 2.6-7.5 published by Mallik et al. (2018) (Fig. 6.4 A), but experimental temperatures of the latter study are higher by ~300 °C. The normalization of experimental temperature to pressure (T/P) gives a

linear fit ( $R^2 = 0.76$ ) when plotted versus  $D_{N(\text{Fluid/Melt})}$  (Fig. 6.4 B). However, to attain this fit, the three highest  $D_{N(\text{Fluid/Melt})}$  of Mallik et al. (2018) at 2-4 GPa of 15.5, 6.2, and 12.4 (indicated with red arrows in Fig. 6.4 B) are excluded from calculation of the regression since they are twice as enriched in N (6.2 wt%) compared to their other experiments (1.3-3.0 wt% N). Since N dissolution within the silicate melt is limited by the solubility maximum, excess N within the starting composition leads to overestimation of  $D_{N(\text{Fluid/Melt})}$ . Linear regression of experiments of this study and that of Mallik et al. (2018) gives the N partitioning of fluid/melt in siliceous slab melts:

$$D_{N(\text{Fluid/Melt})} = 0.012 \times \frac{T [^\circ\text{C}]}{P [\text{GPa}]} - 2.02 \quad \text{I}$$

Equation (I) is calibrated for a temperature and pressure ranges of 800-1300 °C and 2-4 GPa.

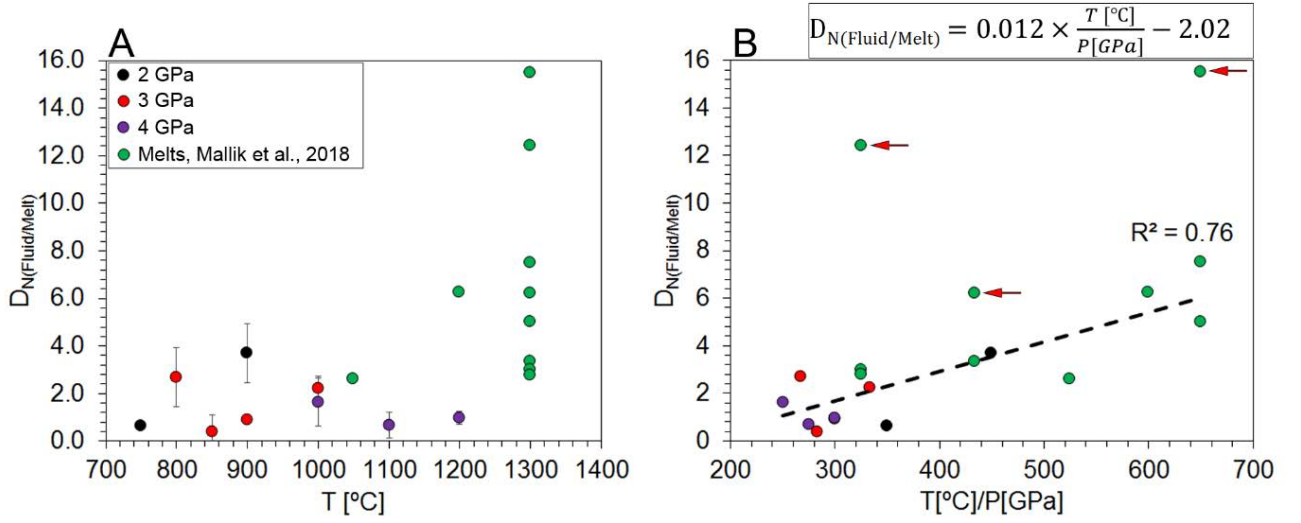


**Fig. 6.4:** Partition coefficients for N between fluid and melt *versus* experimental run temperature (A) and experimental run temperature normalized to pressure (B). A) Partition coefficients of N between fluid and melt compared to values from Mallik et al. (2018) (green circles). B) Normalization of temperature to pressure leads to a linear dependency ( $R^2 = 0.76$ ) of  $D_{N(\text{Fluid/Melt})}$  versus  $T/P$ . Data points highlighted with a red arrow resemble experiments twice as enriched in N (6.2 wt%) over other experiments (1.3-3 wt% N) of Mallik et al. (2018) and are not included in the regression.

Compared to  $D_{N(\text{Fluid/Melt})}$ , which does not show a fit versus temperature,  $D_{N(\text{Fluid/Bulk})}$ , the partitioning of fluid against all N-bearing phases combined (bulk = residual sediment, mica, and melt) shows an excellent linear dependency versus temperature for experiments at 3 GPa ( $R^2 = 0.99$ ) and 4 GPa ( $R^2 = 0.92$ ) (Fig. 6.5 A). When  $D_{N(\text{Fluid/Bulk})}$  is plotted against  $T/P$ , all melt-bearing experiments follow an excellent linear dependency with  $R^2 = 0.95$  (Fig. 6.5 B). Accordingly, N partitioning between fluid and bulk residue in siliceous slab melts can be calculated as follows:

$$D_{N(\text{Fluid/Bulk})} = 0.04 \times \frac{T [^\circ\text{C}]}{P [\text{GPa}]} - 8.48 \quad \text{II}$$

Equation (II) is calibrated for temperature and pressure ranges of 800-1200 °C and 2-4 GPa.

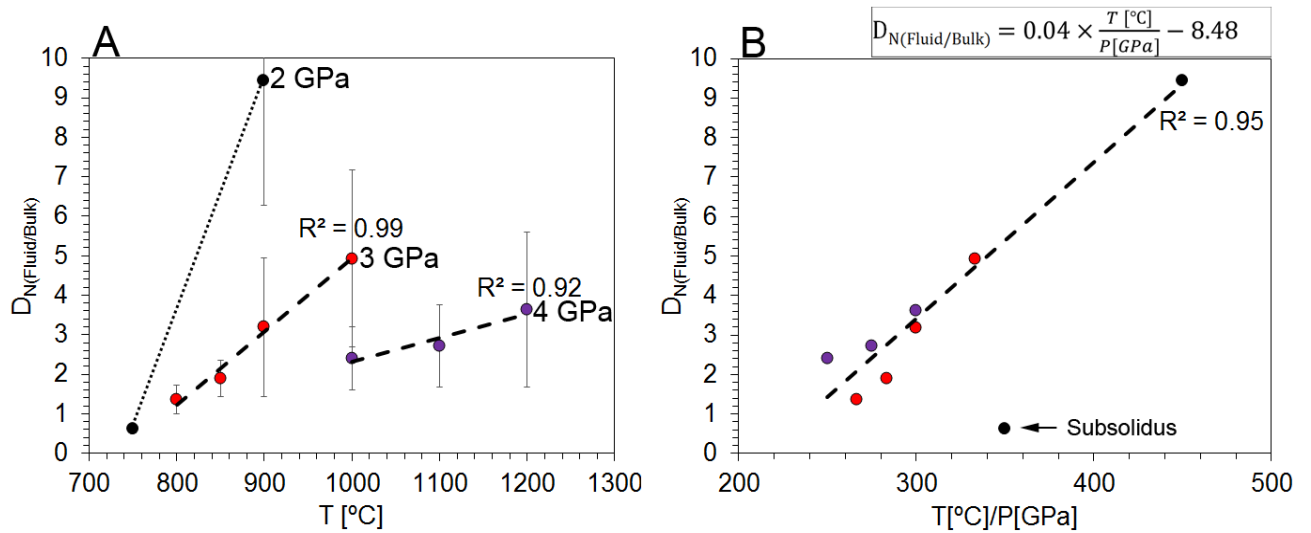


**Fig. 6.5:** Partition coefficients for N between fluid and bulk (melt+mica) *versus* experimental run temperature (A) and experimental run temperature normalized to pressure (B). A) The runs performed at 3 GPa and 4 GPa show an excellent linear dependency ( $R^2 = 0.99$ ,  $R^2 = 0.92$ ) of  $D_{N(\text{Fluid/Bulk})}$  on temperature. Increasing  $P$  from 3 to 4 GPa moves the linear trend to lower values of  $D_N$ . B) Normalization of the temperature on pressure leads to a linear dependency ( $R^2 = 0.95$ ) of  $D_{N(\text{Fluid/Bulk})}$  *versus*  $T/P$ .

Since  $D_{N(\text{Fluid/Mica})} \ll D_{N(\text{Fluid/Melt})}$ , the subsolidus experiment does not follow the trend and shows low  $D_N$  at high  $T/P$  (Fig. 6.5 B). Thus, retention of N within the slab is high as long as melting does not occur and N is carried away by dehydration only (Mallik et al., 2018).

#### 6.4.2 Subduction zone N budgets

To quantify the amount of N recycled at subduction zones, we calculated the average N mass fraction in the uppermost 17.5 km of the subducting slab to be  $21 \mu\text{g g}^{-1}$  N (Table 6.4), using published layer thicknesses (Hacker, 2008; Halama et al., 2014; Jarrard et al., 2003; Syracuse et al., 2010) as well as corresponding average N mass fractions (Johnson and Goldblatt, 2015). We calculated average quantities of subducted N to amount to  $2.57 \cdot 10^9$  kg/a by using published arc lengths with average plate tectonic speeds (Allegre et al., 1984) together with the calculated average N mass fraction in the subducting slab (Table 6.5). Mass-balance calculations give the distribution of N between residual sediment, mica, and melt from 2-4 GPa and 750-1200 °C (Fig. 6.6).



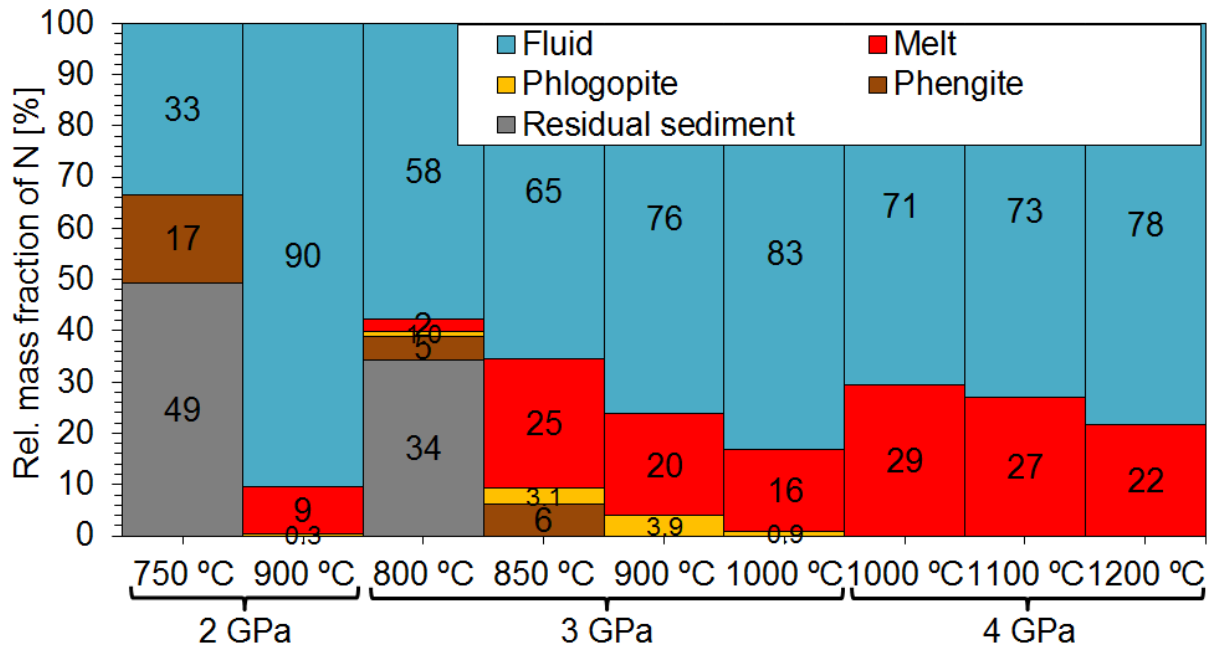


**Fig. 6.6:** Mass-balance calculations show the distribution of nitrogen between the different N-bearing experimental phases. The 750 °C experiment is sub-solidus and 2/3 of the nitrogen is retained within phengite and residual sediment (graphite and carbonaceous material). With the onset of partial melting (800 °C), nitrogen is lost to a fluid phase. At 850-1200 °C, melt forms the main nitrogen phase besides the fluid. The amount of nitrogen lost to the fluid phase increases with temperature, while pressure increase retains more nitrogen in the melt phase.

The quantity of N lost to a fluid phase increases with increasing temperature and decreases with increasing pressure, culminating in strong incompatibility of N in the magmatic systems of volcanoes at  $P < 1$  GPa (Li et al., 2015). Nitrogen that is found in the melt phase at  $T < 1000$  °C will be trapped in mica following the reaction  $\text{Melt} + \text{Olivine} \rightarrow \text{Phlogopite} + \text{Pyroxene}$ . Since  $D_{\text{N}}(\text{Fluid/Mica}) = 0.1$ , the loss of N during freezing of the melt and phlogopite crystallization is minimal and ~90 % of N in the melt at  $T < 1000$  °C will be transferred to mica. Using the distribution of N between fluid, melt, mica, and residual sediment (Fig. 6.6) the quantities of N subducted past the arc and that may therefore metasomatize the lithospheric mantle are calculated and normalized to present-day atmospheric nitrogen (PAN) in Supplementary Fig. 6.5 A,B. The sum of N subducted and sequestered in metasomatic assemblages gives the total quantity of N retained in Earth's mantle (Fig. 6.7). Hence, the quantity of N recycled to Earth's mantle varies from 1.3-1.7 PAN at 750 °C to as low as 0.3-0.4 PAN at 1000 °C, depending on the timing of the onset of subduction. Intriguingly, the maximum amount of recycled N, as provided by the path of the subsolidus experiment at 750 °C gives an atmosphere of ~2.7 PAN at the onset of subduction, which is close to the Venusian atmosphere that contains 3.4 PAN when Venus is normalized to the Earth's mass (Johnson and Goldblatt, 2015). However, a constant linear recycling of N is an



unlikely scenario, because modern, cold subduction has only been operative on Earth for the last 0.6 Ga and subduction temperatures were higher in the Archean (Condie and Kröner, 2008).

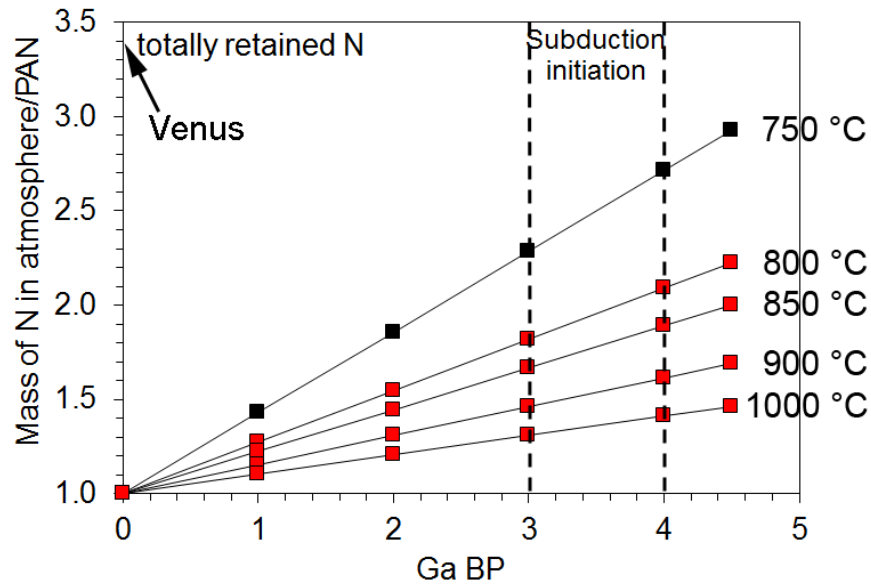


**Fig. 6.7:** Total mass fraction of atmospheric nitrogen recycled to combined shallow and deep mantle (metasomatized and subducted past the arc) normalized to present-day atmospheric nitrogen (PAN). The amount of recycled nitrogen decreases with temperature while at >1000 °C nitrogen is still recycled to the shallow (lithospheric) mantle.

**Table 6.4:** Mass fraction of N in the oceanic lithosphere.

Lithology	N* [ $\mu\text{g g}^{-1}$ ]	Thickness [km]	Relative N (%)	References for thickness
Oceanic Sediments	560	0.5	76	(Syracuse et al., 2010)
Extrusives and dikes	6.5	0.6+1.4	4	(Hacker, 2008; Jarrard et al., 2003)
Gabbros	5.9	5	8	
Serpentinized mantle	4.5	10	12	(Halama et al., 2014)
<b>Average</b>	<b>21</b>	<b>17.5</b>	-	-

**Table 6.5:** Parameters for N recycling budgets.

Average convergence rate	5 cm/a*
Average thickness of altered lithosphere+sediments	17.5 km
Average N mass fraction of altered lithosphere	21 [ $\mu\text{g g}^{-1}$ ]
Global arc lengths	40000 km*
Subducted volume of altered lithosphere+sediments	35 km <sup>3</sup> /a
Subducted mass of altered lithosphere+sediments	1.225·10 <sup>14</sup> kg/a
Subducted mass of N	2.57·10 <sup>9</sup> kg/a

\*(Allegre et al., 1984)

#### 6.4.3 Evolution of $pN_2$ in Earth's atmosphere

The evolution of  $pN_2$  in the Earth's atmosphere depends on the proportions of N recycling versus degassing from the mantle. Since subducted sediments account for about  $\frac{3}{4}$  of recycled N (Table 6.4), and N is mainly of marine biogenic and clastic origin (Johnson and Goldblatt, 2015), the quantities of recycled N are more dependent on biological than geological factors. As a consequence, any increase in subduction speed will not significantly change the rate of subduction of N since the young subducting seafloor will have a thinner cover of sediment. Contrarily, young, hot subduction will lead to less effective N recycling (lower curves in Fig. 6.7). As such, higher plate tectonic activity will increase the ratio of N degassing to N recycling, since increased sea-floor spreading induced by higher mantle potential temperature (Korenaga, 2011) will also lead to increased length of ridges, and thus, younger plate age at subduction zones (Hargraves, 1986).

Using the partitioning of N between fluid and bulk residue from the subsolidus experiment (750 °C) and for melt bearing experiments (Eq. II), we calculated four scenarios for average N recycling at subduction zones over the last 3-4 Ga (Fig. 6.8). All scenarios contain minimum (MIN) and maximum (MAX) estimates of N subduction (Supplementary Fig. 6.6). The MAX estimate includes N recycling within the Phanerozoic by cold subduction zones (dehydration only), as well as hot subduction zones with apparent slab melting and cold subduction/hot subduction ratio changing from 60/40 to 0/100 from 0 to 0.6 Ga, respectively. The ratio of cold/hot subduction is estimated from the increasing abundance of blueschist facies rocks over the last 0.6 Ga (Condie and Kröner, 2008). At 4 to 0.6 Ga, no blueschist facies rocks are found and  $D_{N(\text{Fluid/Bulk})}$  is calculated (Eq. II) with a 50 °C decrease in mantle potential temperature every 0.5 Ga (Korenaga, 2011). The MIN estimate does not include cold subduction (dehydration only) and calculates  $D_{N(\text{Fluid/Bulk})}$  with a 100 °C higher starting temperature and a 50 °C T increase every 0.5 Ga. Between the 4 scenarios, N degassing from the mantle increases from constant (1x) MORB degassing to 10x, 20x, and 40x the current rate of N-degassing from MORB for a time interval from 0-4.5 Ga (Fig. 6.8, Supplementary Fig. 6.6).

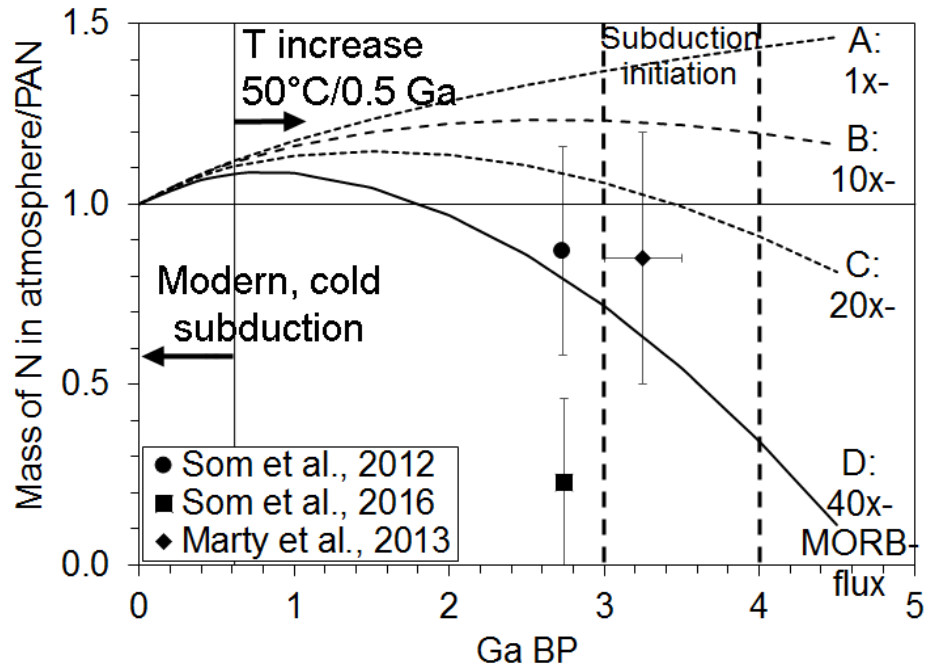


**Fig. 6.8:** Nitrogen retention within global subduction zones plotted according to a dynamic decrease of subduction temperature with time from 0-4 Ga BP. Pathways of N evolution within Earth's atmosphere represent averages from calculated MIN and MAX values (Supplementary Fig. 6.6). From 0-0.6 Ga, modern, cold subduction zones with blueschist-facies metamorphism are apparent (Condie and Kröner, 2008). The outgassing of nitrogen by decompression melting of asthenospheric mantle (MORB-flux: Catling and Kasting, 2017) is subtracted from all four pathways with an increase from constant (1x) to up to 10x, 20x, and 40x of the modern MORB flux. All models show an 8-11 % higher  $pN_2$  at the beginning of the Phanerozoic (0.6 Ga). The pathways of 20x & 40x end up with atmospheric pressures lower than today's in the Archean which were proposed previously (Marty et al., 2013; Som et al., 2012; 2016).

All 4 scenarios (A-D) calculate that  $50 \pm 6$  % of atmospheric N has been recycled to the mantle over 3-4 Ga, but diverge due to the amount of N degassing from the mantle. Using the estimate for N in the mantle of 6 PAN (Johnson and Goldblatt, 2015), we calculate that  $8 \pm 1$  % of N is recycled back to the mantle, which is lower than previous estimates of  $12 \pm 5$  % to  $17 \pm 8$  % (Mallik et al., 2018). Hence, before the onset of subduction (assumed to be 3-4 Ga), we estimate  $\delta^{15}N$  of Earth's mantle to be ca.  $-6 \pm 0.5$  ‰, using modern day mantle  $\delta^{15}N$  of  $-5$  ‰ and of  $\delta^{15}N$  of subducted crust of  $+6$  ‰ (Cartigny and Marty, 2013).

In all scenarios, calculated  $pN_2$  are 8-11 % higher at the beginning of the Phanerozoic (Fig. 6.8). Scenario A assumes that degassing of N from the mantle remained constant over the last 4.5 Ga at a level resembling modern values measured at MORB (Catling and Kasting, 2017). This reaches the highest  $pN_2$  of all scenarios with ~40 % higher levels at the onset of plate tectonics and is in accordance with the lower estimate of previous experimental studies (Mallik et al., 2018) (Supplementary Fig. 6.6 A). This scenario is also in accordance with calculated  $pN_2$  that are 50 %

higher in the Archean based on N–He–Ne–Ar in oceanic basalts (Barry and Hilton, 2016). The higher  $pN_2$  during the Archean could be a solution to the ‘faint young sun’ paradox, because of the higher atmospheric pressure causing broadening of the absorption lines of greenhouse gases (Goldblatt et al., 2009).

However, it is likely that N degassing from the Earth’s mantle was higher in the past due to higher rates of magma extrusion and sea floor spreading as a consequence of higher mantle potential temperature (Korenaga, 2011) and to the increase of  $D_{N(\text{Fluid/Melt})}$  with temperature (Eq. I). While scenario B (10x N degassing) still reaches  $pN_2$  20 % higher than today, scenarios C (20x N degassing) and D (40x N degassing) reach similar to 50 % lower  $pN_2$  at the onset of subduction. The latter case with highest N degassing (40x) attains ~10 % (MIN: 0 %, MAX: 20 %) of today’s  $pN_2$  at the time of formation of Earth and is in accordance with paleoatmospheric pressure estimates from three independent studies (Marty et al., 2013; Som et al., 2012; 2016) (Fig. 6.8). Nevertheless, the ‘faint young sun’ paradox requires greenhouse effect in the Archean stronger than today to account for the distinct lack of glaciation and the presence of warm oceans (Tartèse et al., 2017). Besides pressure broadening of absorption lines, different atmospheric chemistries that may have been methane- (Haqq-Misra et al., 2008), carbonyl sulfide- (Ueno et al., 2009), or carbon dioxide-enriched (Marty et al., 2013) have been put forward to account for stronger greenhouse effects. If N recycling is omitted from scenario D, mantle degassing of N would lead to a today’s atmosphere of N-rich composition of ~1.5 PAN (Supplementary Fig. 6.6 D), ~55 % less than the ~3.4 PAN observed for Venus which, however, has a much denser atmosphere and, unlike Earth, did not lose N as a consequence of collision with Theia.

## 6.5 Conclusion

Marine sediments host  $\frac{3}{4}$  of N recycled at subduction zones while the other  $\frac{1}{4}$  are contained within the altered seafloor and serpentinized mantle lithosphere. In this study we show that N partitioning between fluid and melt ( $D_{N(\text{Fluid/Melt})}$ ) and fluid and bulk residue ( $D_{N(\text{Fluid/Bulk})}$ ) increases linearly with temperature normalized to pressure (T/P). Measured  $D_{N(\text{Fluid/Mica})}$  of 0.1 and  $D_{N(\text{Fluid/Melt})}$  of 0.4-3.7 match the values of  $D_{Rb(\text{Fluid/Mica})}$  and  $D_{Rb(\text{Fluid/Melt})}$  and show that  $NH_4^+$  behaves in a similar manner to the similarly sized  $Rb^+$  ion. This behaviour has consequences on N recycling within subduction zones:

1. Using the linear dependency of  $D_{N(\text{Fluid/Bulk})}$  with  $T$ , we calculated the average quantity of  $N$  recycled at subduction zones since the onset of plate tectonics. Due to increase of mantle potential temperature, and consequent increase of subduction temperature, the efficiency of  $N$  recycling decreases backwards in time.

2. Mass balance calculations show that even at high  $T$ , 10-20 % of recycled  $N$  is retained within the mantle. Since  $D_{N(\text{Fluid/Melt})}$  increases with  $T$  and  $D_{N(\text{Fluid/Mica})} \ll D_{N(\text{Fluid/Melt})}$ , cold subduction (dehydration only) leads to highly effective (~70 %) recycling of  $N$  to Earth's mantle, in contrast with hot subduction in which melting is involved

3. The evolution of atmospheric  $pN_2$  is controlled by both  $N$  degassing from the mantle and  $N$  recycling at subduction zones. An increase from 1x  $N$  degassing (modern MORB degassing) to 40x corresponds to 50 % decreased  $pN_2$  in the Archean where the highest degassing (40x) is in accordance with measured estimates for paleo atmospheric pressures. However, all models for  $pN_2$  are 8-11 % higher than today's at the start of the Phanerozoic.

4. Without subduction and recycling of  $N$ , degassing of Earth's mantle would have resulted in a  $pN_2$  of 1.5 PAN, ~55 % below the ~3.4 PAN of Venus. The difference may be related to the collision of Earth with Theia.

## **Author contributions**

MF performed all experiments and processed and interpreted the data. MF wrote the manuscript. SB and OA assisted in analysis and evaluation of the datasets. SF helped in data interpretation and manuscript evaluation. MF handles the correspondence of the submitted manuscript version of this chapter.

## **Acknowledgements**

We gratefully acknowledge Qing Xiong for providing the dunite sample ZD11-53 used in the experiments. The International Ocean Discovery Project (IODP) supported this study in providing the Mediterranean marine sediment sample from sampling site 161-976. This work is part of the lead author's PhD thesis supported by an Australian Government International Postgraduate Research Scholarship (IPRS) and Postgraduate Research Fund (PGRF). Thomas Kautz of the Goethe University, Frankfurt assisted with the belt apparatus experiments.

## II. Thesis Conclusion

Diamonds and potassium-rich lavas are the most nitrogen-enriched products of Earth's mantle. Previous studies of both diamonds and potassium-rich lavas suggested that subducted sediments are involved in their formation. In this thesis, an experimental petrological approach was used to examine the behavior of potassium and nitrogen within subducted sediments and their reaction with mantle peridotites. The reaction of sediments with depleted peridotites leads to metasomatism within the shallow and deep (cratonic) lithospheric mantle and produces solid and liquid phases enriched in potassium and nitrogen.

### **i. Metasomatism of the shallow lithosphere and the formation of ultrapotassic lavas**

The ongoing recycling of sediments is associated with large scale subduction-related metasomatism of the overlying mantle wedge that occurs along a total of 40,000 km trench length worldwide. This global phenomenon is simulated by using an experimental capsule setup reacting hydrous sediments with depleted peridotite in a 2-layer arrangement at pressure and temperature conditions of 1-3 GPa and <1000 °C. The low solidus of hydrous sediments (~675 °C) compared to significantly higher values characteristic for depleted peridotites leads to melt production in the sediment alone and infiltration of the melt into the peridotite and reaction long before the hydrous solidus of peridotite is reached. The difference in solidus temperatures induces metasomatism by reaction and freezing, forming phlogopite pyroxenites and trapping all products of the infiltrating melt within the fore-arc of subduction zones (Fig. II). All reaction experiments support this process by showing a multiply layered reaction zone where distinct sets of elements are separated from each other in distinct mineral assemblages. Overall, the metasome produced shows enrichment in K, Al, Si, LILE, HFSE, and light REE with high Th/La, Th/Yb, and Rb/Sr while no enrichment is observed for HREE. During metasomatism, the residue from the former sediment was observed to transform to a low K/Na eclogite-like composition, comprising mainly garnet and Na-Al-rich clinopyroxene. Besides the formation of K-rich metasomes, these reactions in the fore-arc lead to depletion of the subducting sediment in HFSE which melts for a second time at later stages beneath the volcanic front and produces characteristic low HFSE signatures of arc lavas. Re-melting of the metasomatized high K/Na mantle occurs during late stages of continental collision and is modelled by our two-stage experimental setup, which

produced melts with ~8.5 wt% K<sub>2</sub>O. This is significant as it is well above the 6 wt% K<sub>2</sub>O threshold that is otherwise the upper limit of single stage sediment/peridotite layered experimental setups. This two-stage formation of potassium-enriched igneous rocks has been described from Mexico and Turkey, where in both cases slab rollback leads to potassic magmatism within the fore-arc of a subduction zone.

Slow, post-collisional upwelling of the asthenospheric mantle sometimes fails to trigger melting of the metasomes because of the cool environment in ongoing subduction. As a consequence, metasomes may reside within the lithospheric mantle until they are activated at a much later stage. Between their formation in subduction settings and their later activation, e.g. in intra-plate rift settings, these metasomes can be considered dormant i.e. not taking part in any geochemical and geological processes (Fig. II). Later activation of the metasomes likely explains K-rich lavas with crustal geochemical and isotopic signatures at locations remote from young orogens or extant subduction zones in places such as Gaussberg, Antarctica. The results in this thesis show that incongruent melting of the metasomes produces high-degree melts with K<sub>2</sub>O of 8–10 wt%, 11–12 wt% Al<sub>2</sub>O<sub>3</sub> at MgO values of 10–15 wt% and SiO<sub>2</sub> of <45 wt%. Subsequent reaction with depleted peridotite crystallizes clinopyroxene and phlogopite and thus generates a variety of ultrapotassic compositions.

Compared to the melts produced from sediment-induced metasomatism, the reaction of hydrous basanite, formed by upwelling and melting of asthenospheric mantle, with dunite at ~1200 °C produces melts with LILE, HFSE, and REE patterns similar to lavas in post-collisional settings with K/Na of 0.5–1. While the relative enrichment of elements is similar to melts of sediment/dunite reaction, the hydrous melts resulting from basanite/dunite reaction have lower Th/La, Th/Yb, and Rb/Sr and higher Nb/Yb. Percolation of the hydrous basanite melt through the dunite dynamically increases its K/Na since reaction occurs above the solidus of phlogopite pyroxenite and thus does not lead to total consumption of the melt. Set into geodynamic context, these results imply that reaction of initially sodic melts leads to metasomatism and the formation of high-K/Na magmas within the lithospheric mantle. Since K-enrichment occurs dynamically via crystallization of a low K/Na residuum, the starting melt composition does not initially have to be potassic. The Eifel volcanic fields in Germany are a recent example of this process where sodic magmatism in the Eocene was followed by potassic magmatism in the Pleistocene. Enrichment



of potassium in the lithospheric mantle was thereby facilitated by the reaction of sodic melts late in the Eocene or just before the onset of potassium enriched magmatism in the Pleistocene.

## **ii. Metasomatism of the cratonic lithosphere and its relation to kimberlite magmatism**

The experiments conducted at 4-6 GPa simulated deep subduction of clastic marine sediments and leads to the crystallization of alkali chlorides from saline fluids at pressures that correspond to depths >120 km (Fig. II). These alkali chlorides form by the reaction of melts of sediment with depleted peridotite and show identical K/Na ratios to saline fluid inclusions in diamonds. Since the reaction of melts derived from sediments with depleted peridotite leads to the crystallization of an eclogitic residue, the escaping saline fluid is likely to be depleted in Sr and Eu and is expected to evolve towards lower  $^{87}\text{Sr}/^{86}\text{Sr}$  ratios due to reaction with the depleted peridotite which generally has low  $^{87}\text{Sr}/^{86}\text{Sr}$ . In addition, the reaction of melts of sediment with peridotite produces magnesite. Both magnesite and alkali chlorides are known to occur as fluid inclusions in diamonds and are essential ingredients for chlorine-enriched kimberlite magmas. The change of metasomatic style from alkali chloride formation to phlogopite crystallization at <120 km has further consequences for the cratonic mantle: Na-K rich fluids that rise from deep within the lithosphere will stall to form mica. This depth coincides with the seismic mid-lithosphere discontinuity, a zone of low seismic velocities that has been associated with hydrous minerals and is found intermittently beneath all continents at a depth of 80–100 km (Fig. II).

## **iii. Nitrogen enrichment of the lithospheric mantle**

The subduction of marine sediment is the main contributor to nitrogen recycling from the surface to the mantle. The partitioning of nitrogen into melt, mica, and residual sediment with respect to a fluid phase increases with temperature. Since mantle potential temperature, and thus subduction temperature, is assumed to have been higher in the past, the efficiency of nitrogen subduction will have changed as a function of time. Nevertheless, 10-20 % of nitrogen is retained within the metasomatized lithospheric mantle at high temperatures of ~1000 °C in the hottest subduction zones, while cold subduction without the presence of slab melting effectively recycles ~70 % of nitrogen down into the deeper mantle. This implies that ~50 % of atmospheric nitrogen has been recycled into the mantle since the initiation of subduction on Earth. Nitrogen recycling

drastically increased during the last 0.6 Ga, at which time the beginning of modern cold subduction was marked by the first appearances of blueschists. The atmosphere is estimated to have contained about 8-11 % more nitrogen at the beginning of the Phanerozoic. Since degassing of nitrogen was likely higher in the Archean as a consequence of higher mantle potential temperatures, the  $pN_2$  of Earth's atmosphere increased and peaked in the late Proterozoic when nitrogen degassing equalled the amount of recycling. As such,  $pN_2$  of the Archean was probably lower than today discounting pressure broadening of the absorption lines of greenhouse gases as an explanation of the 'faint young sun' paradox. If recycling of nitrogen within subduction zones had not occurred,  $pN_2$  of today's atmosphere would be 1.5x higher.

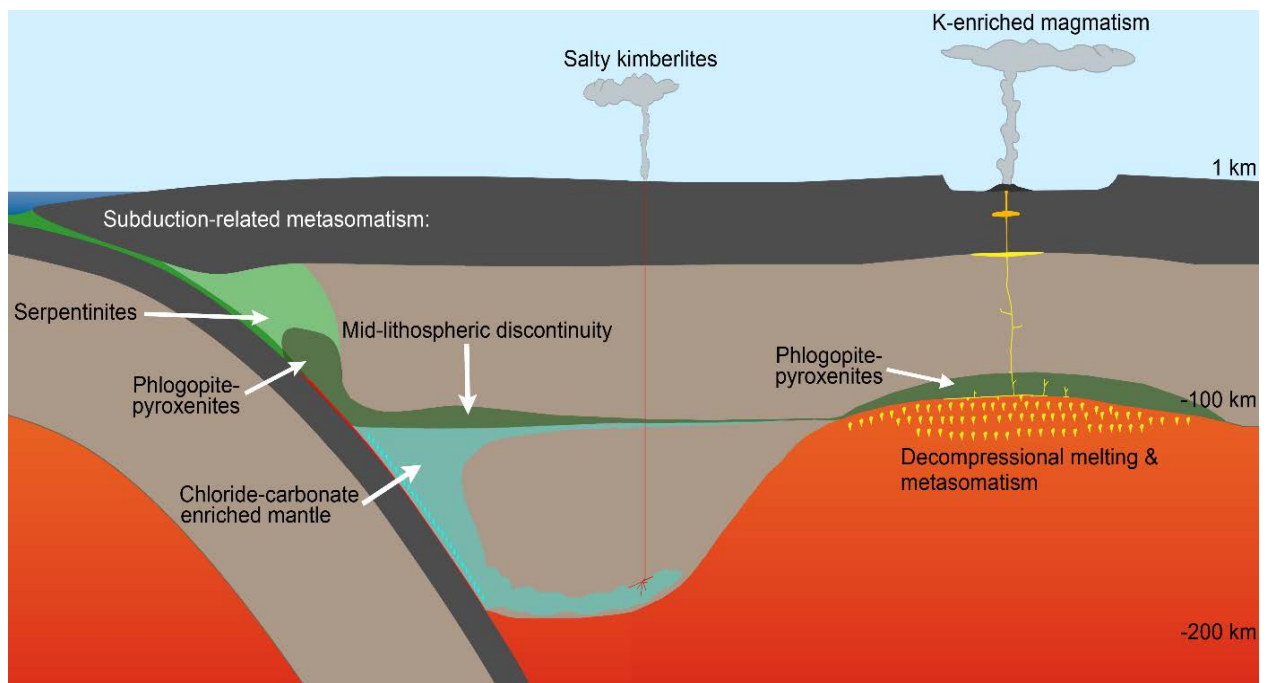


**Fig. III:** Schematic section through subduction, craton-, and continental rift. The subduction of sediment leads to fore-arc serpentinitization at low temperature. At  $T > 675^\circ\text{C}$ , hydrous silicate melts rise from the sediment and react with depleted fore-arc peridotites to form metasomatic phlogopite-pyroxenites. If sediments are subducted to the deep lithospheric mantle beneath cratons, the reaction of sediment melt with depleted peridotite leads to the formation of magnesite and highly saline fluids which precipitate to Na-K chlorides under reduced conditions. The chloride-carbonate enriched mantle is a vital reservoir for the formation of salty kimberlites such as Udachnaya-East. The stalling of saline fluids at 80-100 km depth leads to the crystallization of mica and the formation of the mid-lithospheric seismic discontinuity. Metasomatic phlogopite-pyroxenite also form by infiltration of hydrous sodic melts from the asthenosphere whereby K-enrichment is facilitated by dynamic melt-wall rock reactions.

## References

- Adam, J., Locmelis, M., Afonso, J.C., Rushmer, T., Fiorentini, M.L., 2014. The capacity of hydrous fluids to transport and fractionate incompatible elements and metals within the Earth's mantle. *Geochemistry, Geophysics, Geosystems* 15 (6), 2241–2253.
- Adler, J.F., Williams, Q., 2005. A high-pressure X-ray diffraction study of iron nitrides: Implications for Earth's core. *Journal of Geophysical Research: Solid Earth* 110 (B1), 1–11.
- Aharonov, E., Whitehead, J.A., Kelemen, P.B., Spiegelman, M., 1995. Channeling instability of upwelling melt in the mantle. *Journal of Geophysical Research: Solid Earth* 100 (B10), 20433–20450.
- Akal, C. (2004). Mineralogy and geochemistry of melilite leucites, Balçıkhisar, Afyon (Turkey). *Turkish Journal of Earth Sciences*, 12(3), 215-239.
- Allan, J.F., Batiza, R., Perfit, M.R., Fornari, D.J., Sack, R.O., 1989. Petrology of Lavas from the Lamont Seamount Chain and Adjacent East Pacific Rise, 10° N. *Journal of Petrology* 30 (5), 1245–1298.
- Allegre, C.o., Courtillot, V., Tapponnier, P., Hirn, A., Mattauer, M., Coulon, C., Jaeger, J.J., Achache, J., Schaerer, U., Marcoux, J., 1984. Structure and evolution of the Himalaya–Tibet orogenic belt. *Nature* 307 (5946), 17–22.
- Almeev, R.R., Holtz, F., Koepke, J., Parat, F., Botcharnikov, R.E., 2007. The effect of H<sub>2</sub>O on olivine crystallization in MORB: Experimental calibration at 200 MPa. *American Mineralogist* 92 (4), 670–674.
- Armbruster, T., Danisi, R.M., 2016. Highlights in mineralogical crystallography. Walter de Gruyter GmbH, Berlin, Boston.
- Arndt, N.T., Naldrett, A.J., Pyke, D.R., 1977. Komatiitic and Iron-rich Tholeiitic Lavas of Munro Township, Northeast Ontario. *Journal of Petrology* 18 (2), 319–369.
- Ault, W.U., Eaton, J.P., Richter, D.H., 1961. Lava temperatures in the 1959 Kilauea eruption and cooling lake. *Geological Society of America Bulletin* 72 (5), 791–794.
- Avanzinelli, R., Elliott, T., Tommasini, S., Conticelli, S., 2007. Constraints on the genesis of potassium-rich Italian volcanic rocks from U/Th disequilibrium. *Journal of Petrology* 49 (2), 195–223.
- Avanzinelli, R., Lustrino, M., Mattei, M., Melluso, L., Conticelli, S., 2009. Potassic and ultrapotassic magmatism in the circum-Tyrrhenian region: Significance of carbonated pelitic vs. pelitic sediment recycling at destructive plate margins. *Lithos* 113 (1-2), 213–227.

- Bailey, D.K., 1982. Mantle metasomatism—continuing chemical change within the Earth. *Nature* 296 (5857), 525–530.
- Barry, P.H., Hilton, 2016. Release of subducted sedimentary nitrogen throughout Earth's mantle. *Geochemical Perspectives Letters* 2 (2), 148–159.
- Beattie, P., 1994. Systematics and energetics of trace-element partitioning between olivine and silicate melts: Implications for the nature of mineral/melt partitioning. *Chemical Geology* 117 (1-4), 57–71.
- Bebout, G.E., 2013. Metasomatism in subduction zones of subducted oceanic slabs, mantle wedges, and the slab-mantle interface. In: *Metasomatism and the Chemical Transformation of Rock*. Springer, pp. 289–349.
- Bebout, G.E., Barton, M.D., 2002. Tectonic and metasomatic mixing in a high-T, subduction-zone mélange—insights into the geochemical evolution of the slab–mantle interface. *Chemical Geology* 187 (1-2), 79–106.
- Bebout, G.E., Lazzeri, K.E., Geiger, C.A., 2016. Pathways for nitrogen cycling in Earth's crust and upper mantle: A review and new results for microporous beryl and cordierite. *American Mineralogist* 101 (1), 7–24.
- Bergman, S.C., 1987. Lamproites and other potassium-rich igneous rocks: A review of their occurrence, mineralogy and geochemistry. Geological Society, London, Special Publications 30 (1), 103–190.
- Berner, R.A., 2006. Geological nitrogen cycle and atmospheric N<sub>2</sub> over Phanerozoic time. *Geology* 34 (5), 413–415.
- Bogatikov, V.A., Machotkin, I.L., Kononova, V.A., 1985. Lamproites and their place in the systematics of high-magnesium potassic rocks. *Proceedings of the Russian Academy of Sciences* 12, 3–10.
- Bostock, M.G., Hyndman, R.D., Rondenay, S., Peacock, S.M., 2002. An inverted continental Moho and serpentinization of the forearc mantle. *Nature* 417 (6888), 536–538.
- Boyd, S.R., 2001. Nitrogen in future biosphere studies. *Chemical Geology* 176 (1-4), 1–30.
- Brocher, T.M., Parsons, T., Tréhu, A.M., Snelson, C.M., Fisher, M.A., 2003. Seismic evidence for widespread serpentinized forearc upper mantle along the Cascadia margin. *Geology* 31 (3), 267–270.
- Bulatov, V.K., Brey, G.P., Girnis, A.V., Gerdes, A., Höfer, H.E., 2014. Carbonated sediment–peridotite interaction and melting at 7.5–12 GPa. *Lithos* 200, 368–385.

- Busigny, V., Cartigny, P., Philippot, P., 2011. Nitrogen isotopes in ophiolitic metagabbros: A re-evaluation of modern nitrogen fluxes in subduction zones and implication for the early Earth atmosphere. *Geochimica et Cosmochimica Acta* 75 (23), 7502–7521.
- Bussweiler, Y., Borovinskaya, O., Tanner, M., 2017. Laser Ablation and inductively coupled plasma-time-of-flight mass spectrometry-A powerful combination for high-speed multielemental imaging on the micrometer scale. *Spectroscopy* 32 (5), 14–20.
- Campbell, I.H., Stepanov, A.S., Liang, H.-Y., Allen, C.M., Norman, M.D., Zhang, Y.-Q., Xie, Y.-W., 2014. The origin of shoshonites: New insights from the Tertiary high-potassium intrusions of eastern Tibet. *Contributions to Mineralogy and Petrology* 167 (983), 1–22.
- Carmichael, I.S.E., Turner, F.J., Verhoogen, J., 1974. *Igneous petrology*. McGraw-Hill Companies.
- Cartigny, P., Marty, B., 2013. Nitrogen isotopes and mantle geodynamics: The emergence of life and the atmosphere–crust–mantle connection. *Elements* 9 (5), 359–366.
- Catling, D.C., Kasting, J.F., 2017. *Atmospheric evolution on inhabited and lifeless worlds*. Cambridge University Press.
- Chiodini, G., Marini, L., 1998. Hydrothermal gas equilibria: The H<sub>2</sub>O-H<sub>2</sub>-CO<sub>2</sub>-CO-CH<sub>4</sub> system. *Geochimica et Cosmochimica Acta* 62 (15), 2673–2687.
- Condamine, P., Médard, E., 2014. Experimental melting of phlogopite-bearing mantle at 1 GPa: Implications for potassic magmatism. *Earth and Planetary Science Letters* 397, 80–92.
- Condamine, P., Médard, E., Devidal, J.-L., 2016. Experimental melting of phlogopite-peridotite in the garnet stability field. *Contributions to Mineralogy and Petrology* 171 (95), 1–26.
- Condie, K.C., Kröner, A., 2008. When did plate tectonics begin? Evidence from the geologic record. In: *When did plate tectonics begin on planet Earth*, vol. 440. Geological Society of America Special Papers, pp. 281–294.
- Connolly, J.A.D., Schmidt, M.W., Solferino, G., Bagdassarov, N., 2009. Permeability of asthenospheric mantle and melt extraction rates at mid-ocean ridges. *Nature* 462 (7270), 209–213.
- Conticelli, S., Avanzinelli, R., Ammannati, E., Casalini, M., 2015. The role of carbon from recycled sediments in the origin of ultrapotassic igneous rocks in the Central Mediterranean. *Lithos* 232, 174–196.
- Conticelli, S., Avanzinelli, R., Poli, G., Braschi, E., Giordano, G., 2013. Shift from lamproite-like to leucititic rocks: Sr–Nd–Pb isotope data from the Monte Cimino volcanic complex vs. the Vico stratovolcano, Central Italy. *Chemical Geology* 353, 246–266.

- Conticelli, S., Carlson, R.W., Widom, E., Serri, G., 2007. Chemical and isotopic composition (Os, Pb, Nd, and Sr) of Neogene to Quaternary calc-alkalic, shoshonitic, and ultrapotassic mafic rocks from the Italian peninsula: Inferences on the nature of their mantle sources. *Cenozoic volcanism in the Mediterranean area* 418, 171–191.
- Conticelli, S., Guarnieri, L., Farinelli, A., Mattei, M., Avanzinelli, R., Bianchini, G., Boari, E., Tommasini, S., Tiepolo, M., Prelević, D., 2009. Trace elements and Sr–Nd–Pb isotopes of K-rich, shoshonitic, and calc-alkaline magmatism of the Western Mediterranean Region: Genesis of ultrapotassic to calc-alkaline magmatic associations in a post-collisional geodynamic setting. *Lithos* 107 (1), 68–92.
- Conticelli, S., Peccerillo, A., 1992. Petrology and geochemistry of potassic and ultrapotassic volcanism in central Italy: Petrogenesis and inferences on the evolution of the mantle sources. *Lithos* 28 (3-6), 221–240.
- Cruz-Urbe, A.M., Marschall, H.R., Gaetani, G.A., Le Roux, V., 2018. Generation of alkaline magmas in subduction zones by partial melting of mélange diapirs—An experimental study. *Geology* 46 (4), 343–346.
- Davies, G.R., Stolz, A.J., Mahotkin, I.L., Nowell, G.M., Pearson, D.G., 2006. Trace Element and Sr–Pb–Nd–Hf Isotope Evidence for Ancient, Fluid-Dominated Enrichment of the Source of Aldan Shield Lamproites. *Journal of Petrology* 47 (6), 1119–1146.
- Dawson, J.B., 1984. Contrasting types of upper-mantle metasomatism? In: *Developments in Petrology*, vol. 11. Elsevier, pp. 289–294.
- Dawson, J.B., Smith, J.V., 1977. The MARID (mica-amphibole-rutile-ilmenite-diopside) suite of xenoliths in kimberlite. *Geochimica et Cosmochimica Acta* 41 (2), 309–323.
- Downes, H., 2001. Formation and modification of the shallow sub-continental lithospheric mantle: A review of geochemical evidence from ultramafic xenolith suites and tectonically emplaced ultramafic massifs of western and central Europe. *Journal of Petrology* 42 (1), 233–250.
- Downes, H., Kostoula, T., Jones, A., Beard, A., Thirlwall, M., Bodinier, J.-L., 2002. Geochemistry and Sr–Nd isotopic compositions of mantle xenoliths from the Monte Vulture carbonatite–melilitite volcano, central southern Italy. *Contributions to Mineralogy and Petrology* 144 (1), 78–92.
- Dunn, T., Sen, C., 1994. Mineral/matrix partition coefficients for orthopyroxene, plagioclase, and olivine in basaltic to andesitic systems: A combined analytical and experimental study. *Geochimica et Cosmochimica Acta* 58 (2), 717–733.

- Edgar, A.D., Mitchell, R.H., 1997. Ultra high pressure–temperature melting experiments on an SiO<sub>2</sub>-rich lamproite from Smoky Butte, Montana: Derivation of siliceous lamproite magmas from enriched sources deep in the continental mantle. *Journal of Petrology* 38 (4), 457–477.
- Eldridge, C.S., Compston, W., Williams, I.S., Harris, J.W., Bristow, J.W., 1991. Isotope evidence for the involvement of recycled sediments in diamond formation. *Nature* 353 (6345), 649–653.
- Elkins, L.J., Fischer, T.P., Hilton, Sharp, Z.D., McKnight, S., Walker, J., 2006. Tracing nitrogen in volcanic and geothermal volatiles from the Nicaraguan volcanic front. *Geochimica et Cosmochimica Acta* 70 (20), 5215–5235.
- Elkins-Tanton, L.T., Foulger, G.R., 2005. Continental magmatism caused by lithospheric delamination. *Special Papers-Geological Society of America* 388, 449–461.
- Elser, J.J., Bracken, M.E.S., Cleland, E.E., Gruner, D.S., Harpole, W.S., Hillebrand, H., Ngai, J.T., Seabloom, E.W., Shurin, J.B., Smith, J.E., 2007. Global analysis of nitrogen and phosphorus limitation of primary producers in freshwater, marine and terrestrial ecosystems. *Ecology letters* 10 (12), 1135–1142.
- Erlank, A.J., 1987. Evidence for mantle metasomatism in peridotite nodules from the Kimberley pipes, South Africa. In: *Mantle metasomatism*, 221–311.
- Erlank, A.J., Allsopp, H.L., Hawkesworth, C.J., Menzies, M.A., 1982. Chemical and isotopic characterisation of upper mantle metasomatism in peridotite nodules from the Bultfontein kimberlite. *International Kimberlite Conference: Extended Abstracts* 3, 261–263.
- Ersoy, E.Y., Helvacı, C., Palmer, M.R., 2010. Mantle source characteristics and melting models for the early-middle Miocene mafic volcanism in Western Anatolia: Implications for enrichment processes of mantle lithosphere and origin of K-rich volcanism in post-collisional settings. *Journal of Volcanology and Geothermal Research* 198 (1), 112–128.
- Falloon, T.J., Danyushevsky, L.V., Ariskin, A., Green, D.H., Ford, C.E., 2007a. The application of olivine geothermometry to infer crystallization temperatures of parental liquids: Implications for the temperature of MORB magmas. *Chemical Geology* 241 (3–4), 207–233.
- Falloon, T.J., Green, D.H., Danyushevsky, L.V., 2007b. Crystallization temperatures of tholeiite parental liquids: Implications for the existence of thermally driven mantle plumes. *Special Papers-Geological Society of America* 430, 235–252.
- Fekiacova, Z., Mertz, D.F., Hofmann, A.W., 2007. Geodynamic setting of the Tertiary Hoheifel volcanism (Germany), part II: Geochemistry and Sr, Nd and Pb isotopic compositions. In: *Mantle Plumes*. Springer, pp. 207–239.



- Filiberto, J., Jackson, C., Le, L., Treiman, A.H., 2009. Partitioning of Ni between olivine and an iron-rich basalt: Experiments, partition models, and planetary implications. *American Mineralogist* 94 (2-3), 256–261.
- Fischer, T.P., Hilton, D.R., Zimmer, M.M., Shaw, A.M., Sharp, Z.D., Walker, J.A., 2002. Subduction and recycling of nitrogen along the Central American margin. *Science* 297 (5584), 1154–1157.
- Foley, S., 1992a. Petrological characterization of the source components of potassic magmas: Geochemical and experimental constraints. *Lithos* 28 (3-6), 187–204.
- Foley, S., 1992b. Vein-plus-wall-rock melting mechanisms in the lithosphere and the origin of potassic alkaline magmas. *Lithos* 28 (3-6), 435–453.
- Foley, S., 1992c. Vein-plus-wall-rock melting mechanisms in the lithosphere and the origin of potassic alkaline magmas. *Lithos* 28 (3-6), 435–453.
- Foley, S., Peccerillo, A., 1992. Potassic and ultrapotassic magmas and their origin. *Lithos* 28 (3-6), 181–185.
- Foley, S.F., 1989. Experimental constraints on phlogopite chemistry in lamproites: 1. The effect of water activity and oxygen fugacity. *European Journal of Mineralogy* 1, 411–426.
- Foley, S.F., 2010. A reappraisal of redox melting in the Earth's mantle as a function of tectonic setting and time. *Journal of Petrology* 52 (7-8), 1363–1391.
- Foley, S.F., Barth, M.G., Jenner, G.A., 2000. Rutile/melt partition coefficients for trace elements and an assessment of the influence of rutile on the trace element characteristics of subduction zone magmas. *Geochimica et Cosmochimica Acta* 64 (5), 933–938.
- Foley, S.F., Fischer, T.P., 2017. An essential role for continental rifts and lithosphere in the deep carbon cycle. *Nature Geoscience* 10 (12), 897–901.
- Foley, S.F., Jackson, S.E., Fryer, B.J., Greenough, J.D., Jenner, G.A., 1996. Trace element partition coefficients for clinopyroxene and phlogopite in an alkaline lamprophyre from Newfoundland by LAM-ICP-MS. *Geochimica et Cosmochimica Acta* 60 (4), 629–638.
- Foley, S.F., Jacob, D.E., St. O'Neill, H.C., 2011. Trace element variations in olivine phenocrysts from Ugandan potassic rocks as clues to the chemical characteristics of parental magmas. *Contributions to Mineralogy and Petrology* 162 (1), 1–20.
- Foley, S.F., Jenner, G.A., 2004. Trace element partitioning in lamproitic magmas—the Gaussberg olivine leucitite. *Lithos* 75 (1-2), 19–38.
- Foley, S.F., Link, K., Tiberindwa, J.V., Barifaijo, E., 2012. Patterns and origin of igneous activity around the Tanzanian craton. *Journal of African Earth Sciences* 62 (1), 1–18.

- Foley, S.F., Musselwhite, D.S., van der Laan, S.R. (Eds.), 1999. Melt compositions from ultramafic vein assemblages in the lithospheric mantle: A comparison of cratonic and non-cratonic settings. *Red Roof Design Cape Town*, 238-246.
- Foley, S.F., Pintér, Z., 2018. Primary Melt Compositions in the Earth's Mantle. In: *Magma Under Pressure*. Elsevier, pp. 3–42.
- Foley, S.F., Prelevic, D., Rehfeldt, T., Jacob, D.E., 2013. Minor and trace elements in olivines as probes into early igneous and mantle melting processes. *Earth and Planetary Science Letters* 363, 181–191.
- Foley, S.F., Venturelli, G., Green, D.H., Toscani, L., 1987. The ultrapotassic rocks: Characteristics, classification, and constraints for petrogenetic models. *Earth-Science Reviews* 24 (2), 81–134.
- Foley, S.F., Yaxley, G.M., Rosenthal, A., Buhre, S., Kiseeva, E.S., Rapp, R.P., Jacob, D.E., 2009. The composition of near-solidus melts of peridotite in the presence of CO<sub>2</sub> and H<sub>2</sub>O between 40 and 60 kbar. *Lithos* 112, 274–283.
- Ford, C.E., Russell, D.G., Craven, J.A., Fisk, M.R., 1983. Olivine-Liquid Equilibria: Temperature, Pressure and Composition Dependence of the Crystal/Liquid Cation Partition Coefficients for Mg, Fe<sup>2+</sup>, Ca and Mn. *Journal of Petrology* 24 (3), 256–266.
- Förster, M.W., Prelević, D., Schmück, H.R., Buhre, S., Marschall, H.R., Mertz-Kraus, R., Jacob, D.E., 2018. Melting phlogopite-rich MARID: Lamproites and the role of alkalis in olivine-liquid Ni-partitioning. *Chemical Geology* 476, 429–440.
- Förster, M.W., Prelević, D., Schmück, H.R., Buhre, S., Veter, M., Mertz-Kraus, R., Foley, S.F., Jacob, D.E., 2017. Melting and dynamic metasomatism of mixed harzburgite+ glimmerite mantle source: Implications for the genesis of orogenic potassic magmas. *Chemical Geology* 455, 182–191.
- Fraser, K.J., Hawkesworth, C.J., Erlank, A.J., Mitchell, R.H., Scott-Smith, B.H., 1985. Sr, Nd and Pb isotope and minor element geochemistry of lamproites and kimberlites. *Earth and Planetary Science Letters* 76 (1-2), 57–70.
- Fritschle, T., Prelević, D., Foley, S.F., Jacob, D.E., 2013. Petrological characterization of the mantle source of Mediterranean lamproites: Indications from major and trace elements of phlogopite. *Chemical Geology* 353, 267–279.
- Frost, B.R., 1991. Introduction to oxygen fugacity and its petrologic importance. *Reviews in Mineralogy and Geochemistry* 25 (1), 1–9.

- Fryer, P., Ambos, E.L., Hussong, D.M., 1985. Origin and emplacement of Mariana forearc seamounts. *Geology* 13 (11), 774–777.
- Fulcher, G.S., 1925. Analysis of recent measurements of the viscosity of glasses. *Journal of the American Ceramic Society* 8 (6), 339–355.
- Gao, Y., Hou, Z., Kamber, B.S., Wei, R., Meng, X., Zhao, R., 2007. Adakite-like porphyries from the southern Tibetan continental collision zones: Evidence for slab melt metasomatism. *Contributions to Mineralogy and Petrology* 153 (1), 105–120.
- Giordano, D., Russell, J.K., Dingwell, D.B., 2008. Viscosity of magmatic liquids: A model. *Earth and Planetary Science Letters* 271 (1-4), 123–134.
- Giuliani, A., Kamenetsky, V.S., Kendrick, M.A., Phillips, D., Wyatt, B.A., Maas, R., 2013. Oxide, sulphide and carbonate minerals in a mantle polymict breccia: Metasomatism by proto-kimberlite magmas, and relationship to the kimberlite megacrystic suite. *Chemical Geology* 353, 4–18.
- Giuliani, A., Kamenetsky, V.S., Phillips, D., Kendrick, M.A., Wyatt, B.A., Goemann, K., 2012. Nature of alkali-carbonate fluids in the sub-continental lithospheric mantle. *Geology* 40 (11), 967–970.
- Giuliani, A., Phillips, D., Woodhead, J.D., Kamenetsky, V.S., Fiorentini, M.L., Maas, R., Soltys, A., Armstrong, R.A., 2015. Did diamond-bearing orangeites originate from MARID-veined peridotites in the lithospheric mantle? *Nature communications* 6 (6837), 1–10.
- Goldblatt, C., Claire, M.W., Lenton, T.M., Matthews, A.J., Watson, A.J., Zahnle, K.J., 2009. Nitrogen-enhanced greenhouse warming on early Earth. *Nature Geoscience* 2 (12), 891–896.
- Goldblatt, C., Zahnle, K.J., 2011. Faint young Sun paradox remains. *Nature* 474 (7349), 1–5.
- Goldschmidt, V.M., 1922. On the metasomatic processes in silicate rocks. *Economic Geology* 17 (2), 105–123.
- Goldschmidt, V.M., 1937. The principles of distribution of chemical elements in minerals and rocks. The seventh Hugo Müller Lecture, delivered before the Chemical Society on March 17th, 1937. *Journal of the Chemical Society (Resumed)*, 655–673.
- Gonzalez, C.M., Gorczyk, W., Gerya, T.V., 2016. Decarbonation of subducting slabs: Insight from petrological–thermomechanical modeling. *Gondwana Research* 36, 314–332.
- Grady, M.M., Wright, I.P., Carr, L.P., Pillinger, C.T., 1986. Compositional differences in enstatite chondrites based on carbon and nitrogen stable isotope measurements. *Geochimica et Cosmochimica Acta* 50 (12), 2799–2813.

- Green, D.H., Falloon, T.J., 2005. Primary magmas at mid-ocean ridges, “hotspots,” and other intraplate settings: Constraints on mantle potential temperature. In: *Plates, plumes, and paradigms*, vol. 388. Geological Society of America, Boulder, Colo., pp. 217–247.
- Green, D.H., Falloon, T.J., Eggins, S.M., Yaxley, G.M., 2001. Primary magmas and mantle temperatures. *European Journal of Mineralogy* 13 (3), 437–451.
- Green, D.H., Hibberson, W.O., Rosenthal, A., Kovács, I., Yaxley, G.M., Falloon, T.J., Brink, F., 2014. Experimental study of the influence of water on melting and phase assemblages in the upper mantle. *Journal of Petrology* 55 (10), 2067–2096.
- Greenland, L.P., Rose, W.I., Stokes, J.B., 1985. An estimate of gas emissions and magmatic gas content from Kilauea volcano. *Geochimica et Cosmochimica Acta* 49 (1), 125–129.
- Griffin, W.L., 2008. GLITTER: Data reduction software for laser ablation ICP-MS. *Laser Ablation ICP-MS in the Earth Sciences: Current practices and outstanding issues*, 308–311.
- Griffin, W.L., O'Reilly, S.Y., Afonso, J.C., Begg, G.C., 2008. The composition and evolution of lithospheric mantle: A re-evaluation and its tectonic implications. *Journal of Petrology* 50 (7), 1185–1204.
- Gülmez, F., Genç, Ş.C., Prelević, D., Tüysüz, O., Karacik, Z., Roden, M.F., Billor, Z., 2016. Ultrapotassic volcanism from the waning stage of the Neotethyan subduction: A key study from the Izmir–Ankara–Erzincan Suture Belt, Central Northern Turkey. *Journal of Petrology* 57 (3), 561–593.
- Guo, Z., Wilson, M., Liu, J., Mao, Q., 2006. Post-collisional, potassic and ultrapotassic magmatism of the northern Tibetan Plateau: Constraints on characteristics of the mantle source, geodynamic setting and uplift mechanisms. *Journal of Petrology* 47 (6), 1177–1220.
- Hacker, B.R., 2008. H<sub>2</sub>O subduction beyond arcs. *Geochemistry, Geophysics, Geosystems* 9 (3), 1–24.
- Haggerty, S.E., 1999. A diamond trilogy: Superplumes, supercontinents, and supernovae. *Science* 285 (5429), 851–860.
- Häkli, T.A., Wright, T.L., 1967. The fractionation of nickel between olivine and augite as a geothermometer. *Geochimica et Cosmochimica Acta* 31 (5), 877–884.
- Halama, R., Bebout, G.E., John, T., Scambelluri, M., 2014. Nitrogen recycling in subducted mantle rocks and implications for the global nitrogen cycle. *International Journal of Earth Sciences* 103 (7), 2081–2099.
- Hall, S.J., Matson, P.A., 1999. Nitrogen oxide emissions after nitrogen additions in tropical forests. *Nature* 400 (6740), 152–155.

- Halliday, A.N., 2013. The origins of volatiles in the terrestrial planets. *Geochimica et Cosmochimica Acta* 105, 146–171.
- Hansen, S.M., Dueker, K., Schmandt, B., 2015. Thermal classification of lithospheric discontinuities beneath USArray. *Earth and Planetary Science Letters* 431, 36–47.
- Haqq-Misra, J.D., Domagal-Goldman, S.D., Kasting, P.J., Kasting, J.F., 2008. A revised, hazy methane greenhouse for the Archean Earth. *Astrobiology* 8 (6), 1127–1137.
- Hargraves, R.B., 1986. Faster spreading or greater ridge length in the Archean? *Geology* 14 (9), 750–752.
- Harris, M., Le Roex, A., Class, C., 2004. Geochemistry of the Uintjesberg kimberlite, South Africa: Petrogenesis of an off-craton, group I, kimberlite. *Lithos* 74 (3-4), 149–165.
- Hart, S.E., Brooks, C., 1974. Clinopyroxene-matrix partitioning of K, Rb, Cs, Sr and Ba. *Geochimica et Cosmochimica Acta* 38 (12), 1799–1806.
- Hart, S.R., Davis, K.E., 1978. Nickel partitioning between olivine and silicate melt. *Earth and Planetary Science Letters* 40 (2), 203–219.
- Harte, B., 1987. Metasomatic events recorded in mantle xenoliths: An overview. *Mantle xenoliths*, 625–640.
- Hauri, E.H., Wagner, T.P., Grove, T.L., 1994. Experimental and natural partitioning of Th, U, Pb and other trace elements between garnet, clinopyroxene and basaltic melts. *Chemical Geology* 117 (1-4), 149–166.
- Helz, R.T., Thornber, C.R., 1987. Geothermometry of Kilauea Iki lava lake, Hawaii. *Bulletin of Volcanology* 49 (5), 651–668.
- Hermann, J., Spandler, C., Hack, A., Korsakov, A.V., 2006. Aqueous fluids and hydrous melts in high-pressure and ultra-high pressure rocks: Implications for element transfer in subduction zones. *Lithos* 92 (3-4), 399–417.
- Hermann, J., Spandler, C.J., 2007. Sediment melts at sub-arc depths: An experimental study. *Journal of Petrology* 49 (4), 717–740.
- Hirschmann, M.M., Stolper, E.M., 1996. A possible role for garnet pyroxenite in the origin of the “garnet signature” in MORB. *Contributions to Mineralogy and Petrology* 124 (2), 185–208.
- Hofmann, A.W., 1988. Chemical differentiation of the Earth: The relationship between mantle, continental crust, and oceanic crust. *Earth and Planetary Science Letters* 90 (3), 297–314.
- Holloway, J.M., Dahlgren, R.A., 2002. Nitrogen in rock: Occurrences and biogeochemical implications. *Global Biogeochemical Cycles* 16 (4), 1–17.

- Honma, H., Itihara, Y., 1981. Distribution of ammonium in minerals of metamorphic and granitic rocks. *Geochimica et Cosmochimica Acta* 45 (6), 983–988.
- Hyndman, R.D., Peacock, S.M., 2003. Serpentinization of the forearc mantle. *Earth and Planetary Science Letters* 212 (3-4), 417–432.
- Ionov, D.A., Doucet, L.S., Ashchepkov, I.V., 2010. Composition of the lithospheric mantle in the Siberian craton: New constraints from fresh peridotites in the Udachnaya-East kimberlite. *Journal of Petrology* 51 (11), 2177–2210.
- Itihara, Y., Honma, H., 1979. Ammonium in biotite from metamorphic and granitic rocks of Japan. *Geochimica et Cosmochimica Acta* 43 (4), 503–509.
- Israeli, E.S., Harris, J.W., Navon, O., 2001. Brine inclusions in diamonds: A new upper mantle fluid. *Earth and Planetary Science Letters* 187 (3-4), 323–332.
- Jablon, B.M., Navon, O., 2016. Most diamonds were created equal. *Earth and Planetary Science Letters* 443, 41–47.
- Jacob, D., Jagoutz, E., Lowry, D., Matthey, D., Kudrjavitseva, G., 1994. Diamondiferous eclogites from Siberia: Remnants of Archean oceanic crust. *Geochimica et Cosmochimica Acta* 58 (23), 5191–5207.
- Jakobsson, S., Oskarsson, N., 1994. The system CO in equilibrium with graphite at high pressure and temperature: An experimental study. *Geochimica et Cosmochimica Acta* 58 (1), 9–17.
- Jaques, A.L., 1986. The kimberlites and lamproites of Western Australia. *Geological Survey of Western Australia Bulletin* 132, 268.
- Jaques, A.L., Foley, S.F., 2018. Insights into the petrogenesis of the West Kimberley lamproites from trace elements in olivine. *Mineralogy and Petrology* 112 (2), 519–537.
- Jaques, A.L., Green, D.H., 1980. Anhydrous melting of peridotite at 0–15 Kb pressure and the genesis of tholeiitic basalts. *Contributions to Mineralogy and Petrology* 73 (3), 287–310.
- Jarrard, R.D., Abrams, L.J., Pockalny, R., Larson, R.L., Hirono, T., 2003. Physical properties of upper oceanic crust: Ocean Drilling Program Hole 801C and the waning of hydrothermal circulation. *Journal of Geophysical Research: Solid Earth* 108 (B4), 1–27.
- Jaupart, C., Vergnolle, S., 1989. The generation and collapse of a foam layer at the roof of a basaltic magma chamber. *Journal of Fluid Mechanics* 203, 347–380.
- Javoy, M., Pineau, F., Delorme, H., 1986. Carbon and nitrogen isotopes in the mantle. *Chemical Geology* 57 (1-2), 41–62.
- Jia, Y., Kerrich, R., Gupta, A.K., Fyfe, W.S., 2003. <sup>15</sup>N-enriched Gondwana lamproites, eastern India: Crustal N in the mantle source. *Earth and Planetary Science Letters* 215 (1-2), 43–56.

- Jochum, K.P., Nohl, U., Herwig, K., Lammel, E., Stoll, B., Hofmann, A.W., 2005. GeoReM: A new geochemical database for reference materials and isotopic standards. *Geostandards and Geoanalytical Research* 29 (3), 333–338.
- Jochum, K.P., Weis, U., Stoll, B., Kuzmin, D., Yang, Q., Raczek, I., Jacob, D.E., Stracke, A., Birbaum, K., Frick, D.A., Günther, D., Enzweiler, J., 2011. Determination of Reference Values for NIST SRM 610-617 Glasses Following ISO Guidelines. *Geostandards and Geoanalytical Research* 35 (4), 397–429.
- John, T., Scherer, E.E., Haase, K., Schenk, V., 2004. Trace element fractionation during fluid-induced eclogitization in a subducting slab: Trace element and Lu–Hf–Sm–Nd isotope systematics. *Earth and Planetary Science Letters* 227 (3-4), 441–456.
- Johnson, B., Goldblatt, C., 2015. The nitrogen budget of Earth. *Earth-Science Reviews* 148, 150–173.
- Johnson, B.W., Goldblatt, C., 2018. EarthN: A new Earth system nitrogen model. *Geochemistry, Geophysics, Geosystems* 19 (8), 1–27.
- Johnson, K.T.M., 1998. Experimental determination of partition coefficients for rare earth and high-field-strength elements between clinopyroxene, garnet, and basaltic melt at high pressures. *Contributions to Mineralogy and Petrology* 133 (1-2), 60–68.
- Johnston, A.D., Schwab, B.E., 2004. Constraints on clinopyroxene/melt partitioning of REE, Rb, Sr, Ti, Cr, Zr, and Nb during mantle melting: First insights from direct peridotite melting experiments at 1.0 GPa. *Geochimica et Cosmochimica Acta* 68 (23), 4949–4962.
- Kadik, A.A., Kurovskaya, N.A., Ignat'ev, Y.A., Kononkova, N.N., Koltashev, V.V., Plotnichenko, V.G., 2011. Influence of oxygen fugacity on the solubility of nitrogen, carbon, and hydrogen in FeO-Na<sub>2</sub>O-SiO<sub>2</sub>-Al<sub>2</sub>O<sub>3</sub> melts in equilibrium with metallic iron at 1.5 GPa and 1400 C. *Geochemistry International* 49 (5), 429.
- Kamenetsky, V.S., Golovin, A.V., Maas, R., Giuliani, A., Kamenetsky, M.B., Weiss, Y., 2014. Towards a new model for kimberlite petrogenesis: Evidence from unaltered kimberlites and mantle minerals. *Earth-Science Reviews* 139, 145–167.
- Kamenetsky, V.S., Kamenetsky, M.B., Golovin, A.V., Sharygin, V.V., Maas, R., 2012. Ultrafresh salty kimberlite of the Udachnaya–East pipe (Yakutia, Russia): A petrological oddity or fortuitous discovery? *Lithos* 152, 173–186.
- Kavanagh, L., Goldblatt, C., 2015. Using raindrops to constrain past atmospheric density. *Earth and Planetary Science Letters* 413, 51–58.



- Kawamoto, T., Yoshikawa, M., Kumagai, Y., Mirabueno, M.H.T., Okuno, M., Kobayashi, T., 2013. Mantle wedge infiltrated with saline fluids from dehydration and decarbonation of subducting slab. *Proceedings of the National Academy of Sciences* 110 (24), 9663–9668.
- Kelemen, P.B., Johnson, K.T.M., Kinzler, R.J., Irving, A.J., 1990. High-field-strength element depletions in arc basalts due to mantle–magma interaction. *Nature* 345 (6275), 521–524.
- Kelly, J.F., 2000. Stable isotopes of carbon and nitrogen in the study of avian and mammalian trophic ecology. *Canadian journal of zoology* 78 (1), 1–27.
- Kennedy, A.K., Lofgren, G.E., Wasserburg, G.J., 1993. An experimental study of trace element partitioning between olivine, orthopyroxene and melt in chondrules: Equilibrium values and kinetic effects. *Earth and Planetary Science Letters* 115 (1-4), 177–195.
- Khan, A.A., Baur, W.H., 1972. Salt hydrates. VII. The crystal structures of sodium ammonium orthochromate dihydrate and magnesium diammonium bis (hydrogen orthophosphate) tetrahydrate and a discussion of the ammonium ion. *Acta Crystallographica Section B* 28 (3), 683–693.
- Kjarsgaard, B.A., Pearson, D.G., Tappe, S., Nowell, G.M., Dowall, D.P., 2009. Geochemistry of hypabyssal kimberlites from Lac de Gras, Canada: Comparisons to a global database and applications to the parent magma problem. *Lithos* 112, 236–248.
- Konzett, J., Sweeney, R.J., Thompson, A.B., Ulmer, P., 1997. Potassium Amphibole Stability in the Upper Mantle: An Experimental Study in a Peralkaline KNCMASH System to 8.5 GPa. *Journal of Petrology* 38 (5), 537–568.
- Kopylova, M.G., Kostrovitsky, S.I., Egorov, K.N., 2013. Salts in southern Yakutian kimberlites and the problem of primary alkali kimberlite melts. *Earth-Science Reviews* 119, 1–16.
- Korenaga, J., 2011. Thermal evolution with a hydrating mantle and the initiation of plate tectonics in the early Earth. *Journal of Geophysical Research: Solid Earth* 116 (B12403), 1–20.
- Lambert, I.B., Wyllie, P.J., 1970. Melting in the deep crust and upper mantle and the nature of the low velocity layer. *Physics of the Earth and Planetary Interiors* 3, 316–322.
- Lassiter, J.C., Hauri, E.H., Reiners, P.W., Garcia, M.O., 2000. Generation of Hawaiian post-erosional lavas by melting of a mixed lherzolite/pyroxenite source. *Earth and Planetary Science Letters* 178 (3-4), 269–284.
- LaTourrette, T., Hervig, R.L., Holloway, J.R., 1995. Trace element partitioning between amphibole, phlogopite, and basanite melt. *Earth and Planetary Science Letters* 135 (1-4), 13–30.

- Le Huong, T.-T., Otter, L.M., Förster, M.W., Hauzenberger, C.A., Krenn, K., Alard, O., Macholdt, D.S., Weis, U., Stoll, B., Jochum, K.P., 2018. Femtosecond Laser Ablation-ICP-Mass Spectrometry and CHNS Elemental Analyzer Reveal Trace Element Characteristics of Danburite from Mexico, Tanzania, and Vietnam. *Minerals* 8 (234), 1–15.
- Le Losq, C., Neuville, D.R., Florian, P., Henderson, G.S., Massiot, D., 2014. The role of Al<sup>3+</sup> on rheology and structural changes in sodium silicate and aluminosilicate glasses and melts. *Geochimica et Cosmochimica Acta* 126, 495–517.
- Le Maitre, R.W., Streckeisen, A., Zanettin, B., Le Bas, M.J., Bonin, B., Bateman, P., 2005. Igneous rocks: A classification and glossary of terms: recommendations of the International Union of Geological Sciences Subcommittee on the Systematics of Igneous Rocks. Cambridge University Press.
- Leeman, W.P., Scheidegger, K.F., 1977. Olivine/liquid distribution coefficients and a test for crystal-liquid equilibrium. *Earth and Planetary Science Letters* 35 (2), 247–257.
- Li, C., Ripley, E.M., 2010. The relative effects of composition and temperature on olivine-liquid Ni partitioning: Statistical deconvolution and implications for petrologic modeling. *Chemical Geology* 275 (1-2), 99–104.
- Li, Y., Huang, R., Wiedenbeck, M., Keppler, H., 2015. Nitrogen distribution between aqueous fluids and silicate melts. *Earth and Planetary Science Letters* 411, 218–228.
- Li, Y., Keppler, H., 2014. Nitrogen speciation in mantle and crustal fluids. *Geochimica et Cosmochimica Acta* 129, 13–32.
- Li, Y., Wiedenbeck, M., Shcheka, S., Keppler, H., 2013. Nitrogen solubility in upper mantle minerals. *Earth and Planetary Science Letters* 377, 311–323.
- Libourel, G., Marty, B., Humbert, F., 2003. Nitrogen solubility in basaltic melt. Part I. Effect of oxygen fugacity. *Geochimica et Cosmochimica Acta* 67 (21), 4123–4135.
- Lindgren, W., 1912. The nature of replacement. *Economic Geology* 7 (6), 521–535.
- Luhr, J.F., Carmichael, I.S.E., 1985. Jorullo Volcano, Michoacán, Mexico (1759–1774): The earliest stages of fractionation in calc-alkaline magmas. *Contributions to Mineralogy and Petrology* 90 (2), 142–161.
- Lustrino, M., 2011. What ‘anorogenic’ igneous rocks can tell us about the chemical composition of the upper mantle: Case studies from the circum-Mediterranean area. *Geological Magazine* 148 (2), 304–316.

- Mallik, A., Dasgupta, R., Tsuno, K., Nelson, J., 2016. Effects of water, depth and temperature on partial melting of mantle-wedge fluxed by hydrous sediment-melt in subduction zones. *Geochimica et Cosmochimica Acta* 195, 226–243.
- Mallik, A., Li, Y., Wiedenbeck, M., 2018. Nitrogen evolution within the Earth's atmosphere–mantle system assessed by recycling in subduction zones. *Earth and Planetary Science Letters* 482, 556–566.
- Mallik, A., Nelson, J., Dasgupta, R., 2015. Partial melting of fertile peridotite fluxed by hydrous rhyolitic melt at 2–3 GPa: Implications for mantle wedge hybridization by sediment melt and generation of ultrapotassic magmas in convergent margins. *Contributions to Mineralogy and Petrology* 169 (48), 1–24.
- Marschall, H.R., Schumacher, J.C., 2012. Arc magmas sourced from mélange diapirs in subduction zones. *Nature Geoscience* 5 (12), 862–867.
- Martirosyan, N.S., Yoshino, T., Shatskiy, A., Chanyshhev, A.D., Litasov, K.D., 2016. The CaCO<sub>3</sub>–Fe interaction: Kinetic approach for carbonate subduction to the deep Earth's mantle. *Physics of the Earth and Planetary Interiors* 259, 1–9.
- Marty, B., 1995. Nitrogen content of the mantle inferred from N<sub>2</sub>–Ar correlation in oceanic basalts. *Nature* 377 (6547), 326.
- Marty, B., 2012. The origins and concentrations of water, carbon, nitrogen and noble gases on Earth. *Earth and Planetary Science Letters* 313, 56–66.
- Marty, B., Humbert, F., 1997. Nitrogen and argon isotopes in oceanic basalts. *Earth and Planetary Science Letters* 152 (1), 101–112.
- Marty, B., Zimmermann, L., 1999. Volatiles (He, C, N, Ar) in mid-ocean ridge basalts: Assessment of shallow-level fractionation and characterization of source composition. *Geochimica et Cosmochimica Acta* 63 (21), 3619–3633.
- Marty, B., Zimmermann, L., Pujol, M., Burgess, R., Philippot, P., 2013. Nitrogen isotopic composition and density of the Archean atmosphere. *Science* 342 (6154), 101–104.
- Massonne, H.-J., 1992. Evidence for low-temperature ultrapotassic siliceous fluids in subduction zone environments from experiments in the system K<sub>2</sub>O • MgO • Al<sub>2</sub>O<sub>3</sub> • SiO<sub>2</sub> • H<sub>2</sub>O (KMASH). *Lithos* 28 (3-6), 421–434.
- Matzen, A.K., Baker, M.B., Beckett, J.R., Stolper, E.M., 2013. The Temperature and Pressure Dependence of Nickel Partitioning between Olivine and Silicate Melt. *Journal of Petrology* 54 (12), 2521–2545.

- Matzen, A.K., Baker, M.B., Beckett, J.R., Wood, B.J., Stolper, E.M., 2017. The effect of liquid composition on the partitioning of Ni between olivine and silicate melt. *Contributions to Mineralogy and Petrology* 172 (3), 1–18.
- McGary, R.S., Evans, R.L., Wannamaker, P.E., Elsenbeck, J., Rondenay, S., 2014. Pathway from subducting slab to surface for melt and fluids beneath Mount Rainier. *Nature* 511 (7509), 338–340.
- McKeown, D.A., Bell, M.I., Etz, E.S., 1999. Raman spectra and vibrational analysis of the trioctahedral mica phlogopite. *American Mineralogist* 84 (5-6), 970–976.
- Médard, E., Grove, T.L., 2008. The effect of H<sub>2</sub>O on the olivine liquidus of basaltic melts: Experiments and thermodynamic models. *Contributions to Mineralogy and Petrology* 155 (4), 417–432.
- Meen, J.K., 1987. Mantle metasomatism and carbonatites; An experimental study of a complex relationship. In: *Mantle metasomatism and alkaline magmatism*, vol. 215. Geological Society of America, Boulder, Colo., pp. 91–100.
- Mernagh, T.P., Kamenetsky, V.S., Kamenetsky, M.B., 2011. A Raman microprobe study of melt inclusions in kimberlites from Siberia, Canada, SW Greenland and South Africa. *Spectrochimica Acta Part A: Molecular and Biomolecular Spectroscopy* 80 (1), 82–87.
- Mertes, H., Schmincke, H.-U., 1985. Mafic potassic lavas of the Quaternary West Eifel volcanic field. *Contributions to Mineralogy and Petrology* 89 (4), 330–345.
- Mikhail, S., Sverjensky, D.A., 2014. Nitrogen speciation in upper mantle fluids and the origin of Earth's nitrogen-rich atmosphere. *Nature Geoscience* 7 (11), 816–819.
- Mirnejad, H., Bell, K., 2006. Origin and Source Evolution of the Leucite Hills Lamproites: Evidence from Sr-Nd-Pb-O Isotopic Compositions. *Journal of Petrology* 47 (12), 2463–2489.
- Mitchell, A.L., Grove, T.L., 2015. Melting the hydrous, subarc mantle: The origin of primitive andesites. *Contributions to Mineralogy and Petrology* 170 (13), 1–23.
- Mitchell, E.C., Fischer, T.P., Hilton, D.R., Hauri, E.H., Shaw, A.M., Moor, J.M. de, Sharp, Z.D., Kazahaya, K., 2010. Nitrogen sources and recycling at subduction zones: Insights from the Izu-Bonin-Mariana arc. *Geochemistry, Geophysics, Geosystems* 11 (2), 1–24.
- Mitchell, R.H., 2004. Experimental studies at 5–12 GPa of the Ondermatjie hypabyssal kimberlite. *Lithos* 76 (1-4), 551–564.
- Mitchell, R.H., 2013. *Kimberlites: Mineralogy, geochemistry, and petrology*. Springer Science & Business Media.

- Mitchell, R.H., Bergman, S.C., 1991. Petrology of lamproites. Springer Science & Business Media.
- Mitchell, R.H., Edgar, A.D., 2002. Melting experiments on SiO<sub>2</sub>-rich lamproites to 6.4 GPa and their bearing on the sources of lamproite magmas. *Mineralogy and Petrology* 74 (2-4), 115–128.
- Morimoto, N., 1988. Nomenclature of pyroxenes. *Mineralogy and Petrology* 39 (1), 55–76.
- Morrison, G. W. (1980). Characteristics and tectonic setting of the shoshonite rock association. *Lithos*, 13(1), 97-108.
- Mühe, R., Bohrmann, H., Garbe-Schönberg, D., Kassens, H., 1997. E-MORB glasses from the Gakkel Ridge (Arctic Ocean) at 87°N: Evidence for the Earth's most northerly volcanic activity. *Earth and Planetary Science Letters* 152 (1-4), 1–9.
- Murphy, D.T., Collerson, K.D., Kamber, B.S., 2002. Lamproites from Gaussberg, Antarctica: Possible transition zone melts of Archaean subducted sediments. *Journal of Petrology* 43 (6), 981–1001.
- Nash, W.P., Crecraft, H.R., 1985. Partition coefficients for trace elements in silicic magmas. *Geochimica et Cosmochimica Acta* 49 (11), 2309–2322.
- Nelson, D.R., 1992. Isotopic characteristics of potassic rocks: Evidence for the involvement of subducted sediments in magma genesis. *Lithos* 28 (3-6), 403–420.
- Nixon, P.H., 1987. Mantle xenoliths. John Wiley and Sons Inc., New York, NY.
- Novella, D., Frost, D.J., 2014. The composition of hydrous partial melts of garnet peridotite at 6 GPa: Implications for the origin of group II Kimberlites. *Journal of Petrology* 55 (11), 2097–2124.
- Novella, D., Frost, D.J., Hauri, E.H., Bureau, H., Raepsaet, C., Roberge, M., 2014. The distribution of H<sub>2</sub>O between silicate melt and nominally anhydrous peridotite and the onset of hydrous melting in the deep upper mantle. *Earth and Planetary Science Letters* 400, 1–13.
- O'Reilly, S.Y., Griffin, W.L., 2013. Mantle metasomatism. In: *Metasomatism and the chemical transformation of rock*. Springer, pp. 471–533.
- Pal'Yanov, Y.N., Sokol, A.G., Borzdov, Y.M., Khokhryakov, A.F., Sobolev, N.V., 1999. Diamond formation from mantle carbonate fluids. *Nature* 400 (6743), 417–418.
- Pearce, J.A., Peate, D.W., 1995. Tectonic implications of the composition of volcanic arc magmas. *Annual Review of Earth and Planetary Sciences* 23 (1), 251–285.

- Pearson, V.K., Sephton, M.A., Franchi, I.A., Gibson, J.M., Gilmour, I., 2006. Carbon and nitrogen in carbonaceous chondrites: Elemental abundances and stable isotopic compositions. *Meteoritics & Planetary Science* 41 (12), 1899–1918.
- Peccerillo, A., 2017. The Roman Province. In: *Cenozoic Volcanism in the Tyrrhenian Sea Region*. Springer, pp. 81–124.
- Peccerillo, A., Martinotti, G., 2006. The Western Mediterranean lamproitic magmatism: Origin and geodynamic significance. *Terra Nova* 18 (2), 109–117.
- Pelton, A.D., Gabriel, A., Sangster, J., 1985. Liquidus measurements and coupled thermodynamic–phase-diagram analysis of the NaCl–KCl system. *Journal of the Chemical Society, Faraday Transactions 1: Physical Chemistry in Condensed Phases* 81 (5), 1167–1172.
- Pertermann, M., Hirschmann, M.M., Hametner, K., Günther, D., Schmidt, M.W., 2004. Experimental determination of trace element partitioning between garnet and silica-rich liquid during anhydrous partial melting of MORB-like eclogite. *Geochemistry, Geophysics, Geosystems* 5 (5), 1–23.
- Plank, T., Langmuir, C.H., 1998. The chemical composition of subducting sediment and its consequences for the crust and mantle. *Chemical Geology* 145 (3), 325–394.
- Pommier, A., Evans, R.L., 2017. Constraints on fluids in subduction zones from electromagnetic data. *Geosphere* 13 (4), 1026–1041.
- Prelević, D., Foley, S. F., Romer, R. L., Cvetković, V., & Downes, H. (2005). Tertiary ultrapotassic volcanism in Serbia: constraints on petrogenesis and mantle source characteristics. *Journal of Petrology*, 46(7), 1443–1487.
- Prelevic, D., Foley, S., 2007. Accretion of arc-oceanic lithospheric mantle in the Mediterranean: Evidence from extremely high-Mg olivines and Cr-rich spinel inclusions in lamproites. *Earth and Planetary Science Letters* 256 (1-2), 120–135.
- Prelević, D., Akal, C., Foley, S.F. (Eds.), 2008a. Orogenic vs anorogenic lamproites in a single volcanic province: Mediterranean-type lamproites from Turkey. IOP Publishing, 012024 pp.
- Prelević, D., Akal, C., Foley, S.F., Romer, R.L., Stracke, A., van den Bogaard, P., 2012. Ultrapotassic mafic rocks as geochemical proxies for post-collisional dynamics of orogenic lithospheric mantle: The case of southwestern Anatolia, Turkey. *Journal of Petrology* 53 (5), 1019–1055.
- Prelević, D., Akal, C., Romer, R.L., Foley, S.F., 2010. Lamproites as indicators of accretion and/or shallow subduction in the assembly of south-western Anatolia, Turkey. *Terra Nova* 22 (6), 443–452.

- Prelević, D., Foley, S.F., Romer, R., Conticelli, S., 2008b. Mediterranean Tertiary lamproites derived from multiple source components in postcollisional geodynamics. *Geochimica et Cosmochimica Acta* 72 (8), 2125–2156.
- Prelević, D., Jacob, D.E., Foley, S.F., 2013. Recycling plus: A new recipe for the formation of Alpine–Himalayan orogenic mantle lithosphere. *Earth and Planetary Science Letters* 362, 187–197.
- Prouteau, G., Scaillet, B., Pichavant, M., Maury, R., 2001. Evidence for mantle metasomatism by hydrous silicic melts derived from subducted oceanic crust. *Nature* 410 (6825), 197–200.
- Pu, X., Lange, R.A., Moore, G., 2017. A comparison of olivine-melt thermometers based on DMg and DN<sub>i</sub>: The effects of melt composition, temperature, and pressure with applications to MORBs and hydrous arc basalts. *American Mineralogist* 102 (4), 750–765.
- Putirka, K.D., 2008. Thermometers and Barometers for Volcanic Systems. *Reviews in Mineralogy and Geochemistry* 69 (1), 61–120.
- Rapp, R.P., Shimizu, N., Norman, M.D., Applegate, G.S., 1999. Reaction between slab-derived melts and peridotite in the mantle wedge: Experimental constraints at 3.8 GPa. *Chemical Geology* 160 (4), 335–356.
- Rapp, R.P., Watson, E.B., 1995. Dehydration melting of metabasalt at 8–32 kbar: Implications for continental growth and crust-mantle recycling. *Journal of Petrology* 36 (4), 891–931.
- Ringwood, A.E., Kesson, S.E., Hibberson, W., Ware, N., 1992. Origin of kimberlites and related magmas. *Earth and Planetary Science Letters* 113 (4), 521–538.
- Rosenthal, A., Foley, S.F., Pearson, D.G., Nowell, G.M., Tappe, S., 2009. Petrogenesis of strongly alkaline primitive volcanic rocks at the propagating tip of the western branch of the East African Rift. *Earth and Planetary Science Letters* 284 (1), 236–248.
- Roskosz, M., Bouhifd, M.A., Jephcoat, A.P., Marty, B., Mysen, B.O., 2013. Nitrogen solubility in molten metal and silicate at high pressure and temperature. *Geochimica et Cosmochimica Acta* 121, 15–28.
- Russell, J.K., Porritt, L.A., Lavallée, Y., Dingwell, D.B., 2012. Kimberlite ascent by assimilation-fuelled buoyancy. *Nature* 481 (7381), 352–357.
- Ryan, W.B.F., Carbotte, S.M., Coplan, J.O., O'Hara, S., Melkonian, A., Arko, R., Weissel, R.A., Ferrini, V., Goodwillie, A., Nitsche, F., 2009. Global multi-resolution topography synthesis. *Geochemistry, Geophysics, Geosystems* 10 (3), 1–9.



- Sato, K., 1997. Melting experiments on a synthetic olivine lamproite composition up to 8 GPa: Implication to its petrogenesis. *Journal of Geophysical Research: Solid Earth* 102 (B7), 14751–14764.
- Sawyer, E.W., 1991. Disequilibrium melting and the rate of melt–residuum separation during migmatization of mafic rocks from the Grenville Front, Quebec. *Journal of Petrology* 32 (4), 701–738.
- Schmidt, M.W., Poli, S., 1998. Experimentally based water budgets for dehydrating slabs and consequences for arc magma generation. *Earth and Planetary Science Letters* 163 (1-4), 361–379.
- Schmincke, H.-U., 2007. The Quaternary volcanic fields of the east and west Eifel (Germany). In: *Mantle plumes*. Springer, pp. 241–322.
- Scott, H.P., Hemley, R.J., Mao, H.-k., Herschbach, D.R., Fried, L.E., Howard, W.M., Bastea, S., 2004. Generation of methane in the Earth's mantle: In situ high pressure–temperature measurements of carbonate reduction. *Proceedings of the National Academy of Sciences* 101 (39), 14023–14026.
- Sekine, T., Wyllie, P.J., 1982a. Phase relationships in the system  $\text{KAlSiO}_4\text{--Mg}_2\text{SiO}_4\text{--SiO}_2\text{--H}_2\text{O}$  as a model for hybridization between hydrous siliceous melts and peridotite. *Contributions to Mineralogy and Petrology* 79 (4), 368–374.
- Sekine, T., Wyllie, P.J., 1982b. The system granite-peridotite- $\text{H}_2\text{O}$  at 30 kbar, with applications to hybridization in subduction zone magmatism. *Contributions to Mineralogy and Petrology* 81 (3), 190–202.
- Sekine, T., Wyllie, P.J., 1983. Experimental simulation of mantle hybridization in subduction zones. *The Journal of Geology* 91 (5), 511–528.
- Selway, K., Ford, H., Kelemen, P., 2015. The seismic mid-lithosphere discontinuity. *Earth and Planetary Science Letters* 414, 45–57.
- Shannon, R.D., 1976. Revised effective ionic radii and systematic studies of interatomic distances in halides and chalcogenides. *Acta crystallographica Section A: crystal physics, diffraction, theoretical and general crystallography* 32 (5), 751–767.
- Sharygin, I.S., Litasov, K.D., Shatskiy, A., Golovin, A.V., Ohtani, E., Pokhilenko, N.P., 2015. Melting phase relations of the Udachnaya-East group-I kimberlite at 3.0–6.5 GPa: Experimental evidence for alkali-carbonatite composition of primary kimberlite melts and implications for mantle plumes. *Gondwana Research* 28 (4), 1391–1414.

- Shaw, D.M., 1970. Trace element fractionation during anatexis. *Geochimica et Cosmochimica Acta* 34 (2), 237–243.
- Shimizu, N., Kushiro, I., 1975. The partitioning of rare earth elements between garnet and liquid at high pressures: Preliminary experiments. *Geophysical Research Letters* 2 (10), 413–416.
- Snyder, D.A., Carmichael, I.S.E., 1992. Olivine-liquid equilibria and the chemical activities of FeO, NiO, Fe<sub>2</sub>O<sub>3</sub>, and MgO in natural basic melts. *Geochimica et Cosmochimica Acta* 56 (1), 303–318.
- Sobolev, A.V., Hofmann, A.W., Sobolev, S.V., Nikogosian, I.K., 2005. An olivine-free mantle source of Hawaiian shield basalts. *Nature* 434 (7033), 590–597.
- Sokol, A.G., Kupriyanov, I.N., Palyanov, Y.N., Kruk, A.N., Sobolev, N.V., 2013. Melting experiments on the Udachnaya kimberlite at 6.3–7.5 GPa: Implications for the role of H<sub>2</sub>O in magma generation and formation of hydrous olivine. *Geochimica et Cosmochimica Acta* 101, 133–155.
- Sokol, A.G., Palyanov, Y.N., Kupriyanov, I.N., Litasov, K.D., Polovinka, M.P., 2010. Effect of oxygen fugacity on the H<sub>2</sub>O storage capacity of forsterite in the carbon-saturated systems. *Geochimica et Cosmochimica Acta* 74 (16), 4793–4806.
- Som, S.M., Buick, R., Hagadorn, J.W., Blake, T.S., Perreault, J.M., Harnmeijer, J.P., Catling, D.C., 2016. Earth's air pressure 2.7 billion years ago constrained to less than half of modern levels. *Nature Geoscience* 9 (6), 448–451.
- Som, S.M., Catling, D.C., Harnmeijer, J.P., Polivka, P.M., Buick, R., 2012. Air density 2.7 billion years ago limited to less than twice modern levels by fossil raindrop imprints. *Nature* 484 (7394), 359–362.
- Spandler, C., Hermann, J., Arculus, R., Mavrogenes, J., 2003. Redistribution of trace elements during prograde metamorphism from lawsonite blueschist to eclogite facies; implications for deep subduction-zone processes. *Contributions to Mineralogy and Petrology* 146 (2), 205–222.
- Spandler, C., Mavrogenes, J., Hermann, J., 2007. Experimental constraints on element mobility from subducted sediments using high-P synthetic fluid/melt inclusions. *Chemical Geology* 239 (3–4), 228–249.
- Stamm, N., Schmidt, M.W., 2017. Asthenospheric kimberlites: Volatile contents and bulk compositions at 7 GPa. *Earth and Planetary Science Letters* 474, 309–321.

- Stolz, A.J., Jochum, K.P., Spettel, B., Hofmann, A.W., 1996. Fluid-and melt-related enrichment in the subarc mantle: Evidence from Nb/Ta variations in island-arc basalts. *Geology* 24 (7), 587–590.
- Su, H.-M., Jiang, S.-Y., Zhang, D.-Y., Wu, X.-K., 2017. Partial Melting of Subducted Sediments Produced Early Mesozoic Calc-alkaline Lamprophyres from Northern Guangxi Province, South China. *Scientific Reports* 7 (4864), 1–9.
- Sun, S.-S., McDonough, W.-S., 1989. Chemical and isotopic systematics of oceanic basalts: Implications for mantle composition and processes. Geological Society, London, Special Publications 42 (1), 313–345.
- Sweeney, R.J., Thompson, A.B., Ulmer, P., 1993. Phase relations of a natural MARID composition and implications for MARID genesis, lithospheric melting and mantle metasomatism. *Contributions to Mineralogy and Petrology* 115 (2), 225–241.
- Syracuse, E.M., van Keken, P.E., Abers, G.A., 2010. The global range of subduction zone thermal models. *Physics of the Earth and Planetary Interiors* 183 (1-2), 73–90.
- Tappe, S., Foley, S. F., & Pearson, D. G. (2003). The kamafugites of Uganda: a mineralogical and geochemical comparison with their Italian and Brazilian analogues. *Periodico di Mineralogia*, 72, 51-77.
- Tappe, S., Foley, S.F., Kjarsgaard, B.A., Romer, R.L., Heaman, L.M., Stracke, A., Jenner, G.A., 2008. Between carbonatite and lamproite—diamondiferous Torngat ultramafic lamprophyres formed by carbonate-fluxed melting of cratonic MARID-type metasomes. *Geochimica et Cosmochimica Acta* 72 (13), 3258–3286.
- Tartèse, R., Chaussidon, M., Gurenko, A., Delarue, F., Robert, F., 2017. Warm Archean oceans reconstructed from oxygen isotope composition of early-life remnants. *Geochemical Perspectives Letters* 3, 55–65.
- Thornber, C.R., Heliker, C., Sherrod, D.R., Kauahikaua, J.P., Miklius, A., Okubo, P.G., Trusdell, F.A., Budahn, J.R., Ridley, W.I., Meeker, G.P., 2003. Kilauea east rift zone magmatism: An episode 54 perspective. *Journal of Petrology* 44 (9), 1525–1559.
- Tomlinson, E.L., Jones, A.P., Harris, J.W., 2006. Co-existing fluid and silicate inclusions in mantle diamond. *Earth and Planetary Science Letters* 250 (3-4), 581–595.
- Tommasini, S., Avanzinelli, R., Conticelli, S., 2011. The Th/La and Sm/La conundrum of the Tethyan realm lamproites. *Earth and Planetary Science Letters* 301 (3-4), 469–478.

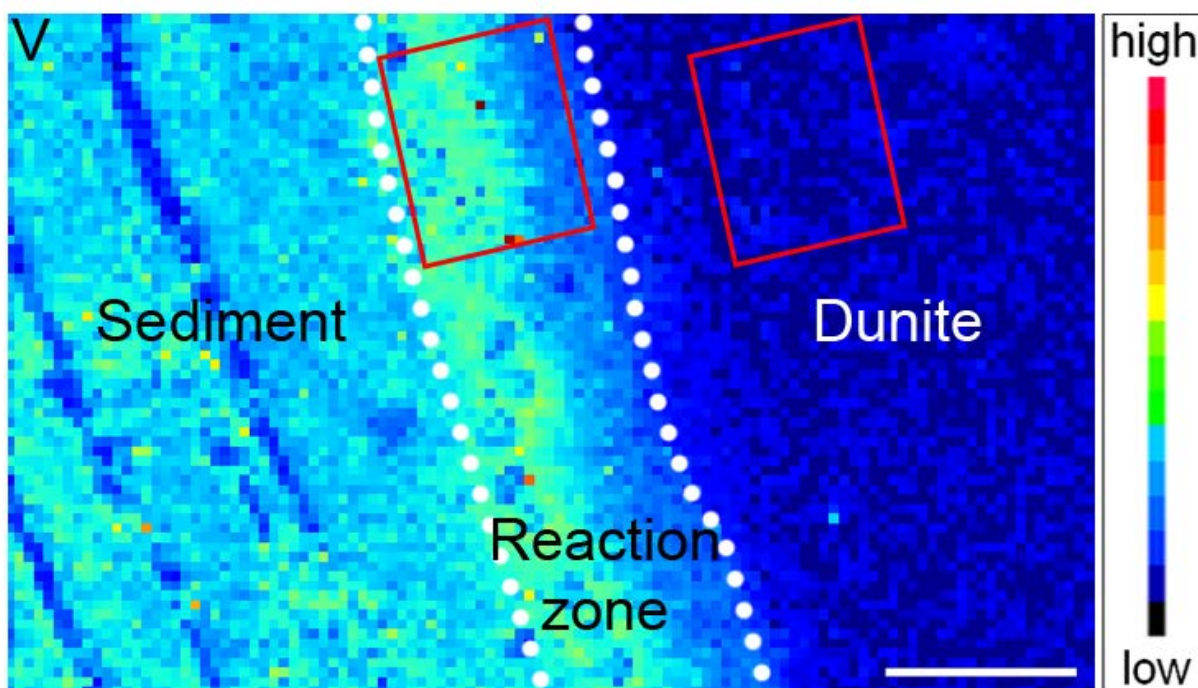
- Ueno, Y., Johnson, M.S., Danielache, S.O., Eskebjerg, C., Pandey, A., Yoshida, N., 2009. Geological sulfur isotopes indicate elevated OCS in the Archean atmosphere, solving faint young sun paradox. *Proceedings of the National Academy of Sciences* 106 (35), 14784–14789.
- Ulmer, P., 1989. The dependence of the Fe<sup>2+</sup>-Mg cation-partitioning between olivine and basaltic liquid on pressure, temperature and composition. *Contributions to Mineralogy and Petrology* 101 (3), 261–273.
- van Westrenen, W., Blundy, J.D., Wood, B.J., 2001. High field strength element/rare earth element fractionation during partial melting in the presence of garnet: Implications for identification of mantle heterogeneities. *Geochemistry, Geophysics, Geosystems* 2 (7), 1–19.
- Veter, M., Foley, S. F., Mertz-Kraus, R., & Groschopf, N. (2017). Trace elements in olivine of ultramafic lamprophyres controlled by phlogopite-rich mineral assemblages in the mantle source. *Lithos*, 292, 81–95.
- Vigouroux, N., Wallace, P.J., Kent, A., JR, 2008. Volatiles in high-K magmas from the western Trans-Mexican Volcanic Belt: Evidence for fluid fluxing and extreme enrichment of the mantle wedge by subduction processes. *Journal of Petrology* 49 (9), 1589–1618.
- Vitousek, P.M., Aber, J.D., Howarth, R.W., Likens, G.E., Matson, P.A., Schindler, D.W., Schlesinger, W.H., Tilman, D.G., 1997. Human alteration of the global nitrogen cycle: Sources and consequences. *Ecological applications* 7 (3), 737–750.
- Wang, A., Pasteris, J.D., Meyer, H.O.A., Dele-Duboi, M.L., 1996. Magnesite-bearing inclusion assemblage in natural diamond. *Earth and Planetary Science Letters* 141 (1-4), 293–306.
- Wang, Y., Foley, S.F., 2018. Hybridization Melting Between Continent-Derived Sediment and Depleted Peridotite in Subduction Zones. *Journal of Geophysical Research: Solid Earth* 123 (5), 3414–3429.
- Wang, Y., Foley, S.F., Prelević, D., 2017a. Potassium-rich magmatism from a phlogopite-free source. *Geology* 45 (5), 467–470.
- Wang, Y., Prelević, D., Buhre, S., Foley, S.F., 2017b. Constraints on the sources of post-collisional K-rich magmatism: The roles of continental clastic sediments and terrigenous blueschists. *Chemical Geology* 455, 192–207.
- Wang, Z., Gaetani, G.A., 2008. Partitioning of Ni between olivine and siliceous eclogite partial melt: Experimental constraints on the mantle source of Hawaiian basalts. *Contributions to Mineralogy and Petrology* 156 (5), 661–678.

- Watenphul, A., Wunder, B., Heinrich, W., 2009. High-pressure ammonium-bearing silicates: Implications for nitrogen and hydrogen storage in the Earth's mantle. *American Mineralogist* 94 (2-3), 283–292.
- Watenphul, A., Wunder, B., Wirth, R., Heinrich, W., 2010. Ammonium-bearing clinopyroxene: A potential nitrogen reservoir in the Earth's mantle. *Chemical Geology* 270 (1-4), 240–248.
- Waters, F.G., 1987. A suggested origin of MARID xenoliths in kimberlites by high pressure crystallization of an ultrapotassic rock such as lamproite. *Contributions to Mineralogy and Petrology* 95 (4), 523–533.
- Watson, E.B., 1982. Melt infiltration and magma evolution. *Geology* 10 (5), 236–240.
- Weiss, Y., Griffin, W.L., Bell, Navon, O., 2011. High-Mg carbonatitic melts in diamonds, kimberlites and the sub-continental lithosphere. *Earth and Planetary Science Letters* 309 (3-4), 337–347.
- Weiss, Y., McNeill, J., Pearson, D.G., Nowell, G.M., Ottley, C.J., 2015. Highly saline fluids from a subducting slab as the source for fluid-rich diamonds. *Nature* 524 (7565), 339–342.
- Weiss, Y., Navon, O., Goldstein, S.L., Harris, J.W., 2018. Inclusions in diamonds constrain thermo-chemical conditions during Mesozoic metasomatism of the Kaapvaal cratonic mantle. *Earth and Planetary Science Letters* 491, 134–147.
- Whittaker, E.J.W., Muntus, R., 1970. Ionic radii for use in geochemistry. *Geochimica et Cosmochimica Acta* 34 (9), 945–956.
- Woodhead, J., Eggins, S., Gamble, J., 1993. High field strength and transition element systematics in island arc and back-arc basin basalts: Evidence for multi-phase melt extraction and a depleted mantle wedge. *Earth and Planetary Science Letters* 114 (4), 491–504.
- Woodland, A.B., Bulatov, V.K., Brey, G.P., Girnis, A.V., Höfer, H.E., Gerdes, A., 2018. Subduction factory in an ampoule: Experiments on sediment–peridotite interaction under temperature gradient conditions. *Geochimica et Cosmochimica Acta* 223, 319–349.
- Worzewski, T., Jegen, M., Kopp, H., Brasse, H., Castillo, W.T., 2011. Magnetotelluric image of the fluid cycle in the Costa Rican subduction zone. *Nature Geoscience* 4 (2), 108–111.
- Wyllie, P.J., Sekine, T., 1982. The formation of mantle phlogopite in subduction zone hybridization. *Contributions to Mineralogy and Petrology* 79 (4), 375–380.
- Xiong, X.-L., 2006. Trace element evidence for growth of early continental crust by melting of rutile-bearing hydrous eclogite. *Geology* 34 (11), 945–948.

- Xu, B., Griffin, W.L., Xiong, Q., Hou, Z.-Q., O'Reilly, S.Y., Guo, Z., Pearson, N.J., Gréau, Y., Yang, Z.-M., Zheng, Y.-C., 2017. Ultrapotassic rocks and xenoliths from South Tibet: Contrasting styles of interaction between lithospheric mantle and asthenosphere during continental collision. *Geology* 45 (1), 51–54.
- Zhang, Y., Zindler, A., 1993. Distribution and evolution of carbon and nitrogen in Earth. *Earth and Planetary Science Letters* 117 (3-4), 331–345.
- Zhang, Y.-L., Liu, C.-Z., Ge, W.-C., Wu, F.-Y., Chu, Z.-Y., 2011. Ancient sub-continental lithospheric mantle (SCLM) beneath the eastern part of the Central Asian Orogenic Belt (CAOB): Implications for crust–mantle decoupling. *Lithos* 126 (3-4), 233–247.
- Ziaja, K., Foley, S.F., White, R.W., Buhre, S., 2014. Metamorphism and melting of picritic crust in the early Earth. *Lithos* 189, 173–184.

# Appendices

## Appendix 1: Supplementary materials



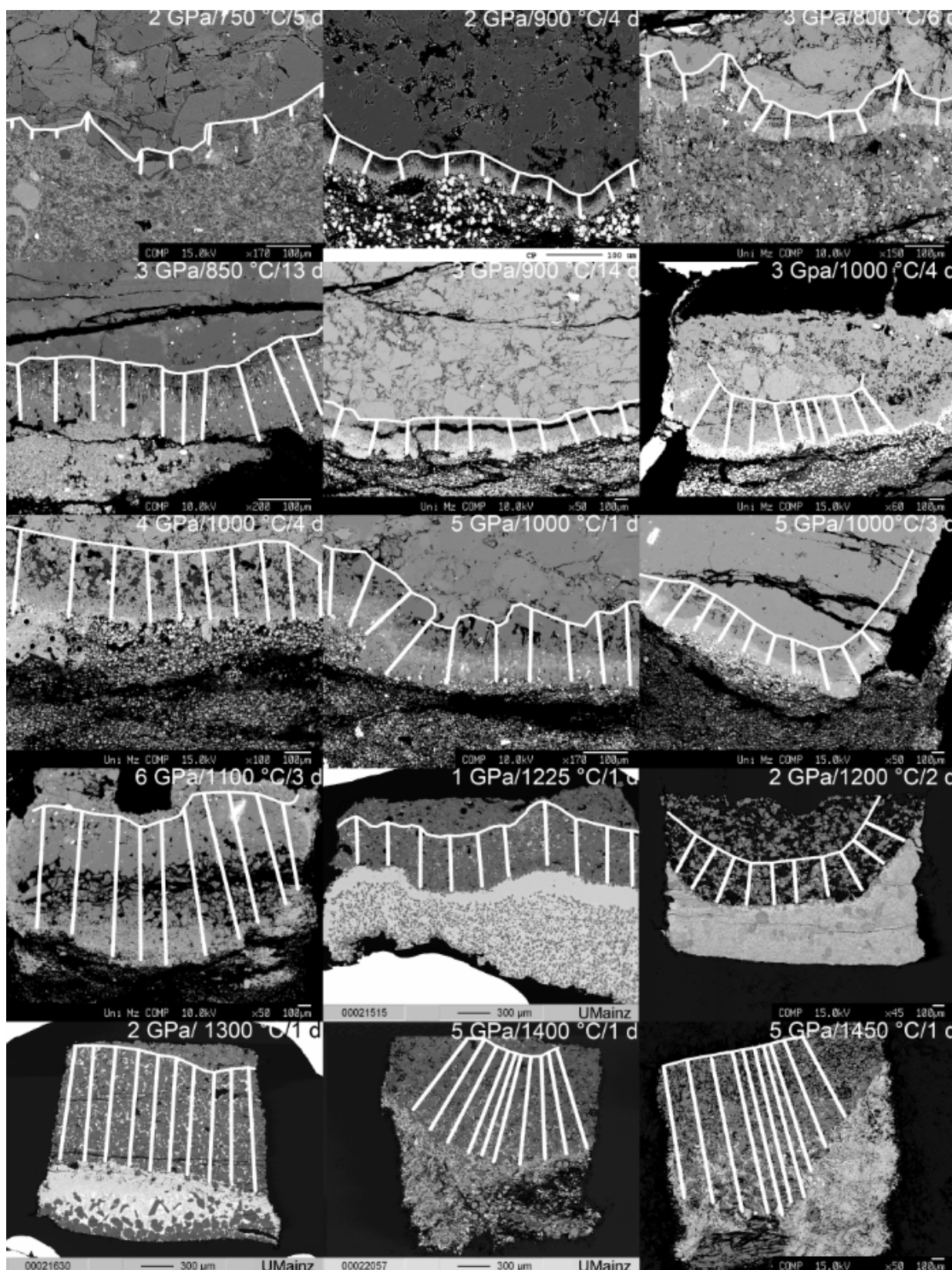
**Supplementary Fig. 1.1:** LA-ICP-TOFMS map of vanadium. Scale bar corresponds to 100  $\mu\text{m}$ . The map depicts two areas of 10,000  $\mu\text{m}^2$  within the reaction zone and within the dunite. The location of the marked area is chosen to represent the most homogeneous part of the reaction zone, while cracks and holes disturb the image in the lower half. The count rates were taken from both areas and used to calculate the enrichment factor of the reaction zone.



**Supplementary Table 1.1:** Phase relations of reaction experiments using marine sediment+H<sub>2</sub>O+CO<sub>2</sub> with dunite.

#	T [°C]	P [GPa]	Duration [d]	% Melt	Assemblage in former sediment	Reaction zone composition of layers 1-3	Reaction zone thickness [μm]	SDEV [μm]	growth rate [μm/d]
1	750	2	4	0	Cpx + Coe + Cc + Phe	Phl + Cpx (+ Opx)	31	10	6
2	900	2	4	~20	Cpx + Gt + glass	Phl + Cpx + Opx + Mgs	53	4	13
3	800	3	6	~10	Cpx + Gt + Coe + Cc + Phe + glass	Cpx + Opx + Dol + Mgs (+Phl)	79	14	13
4	850	3	13	~10	Cpx + Gt + Phe + glass	Phl + Cpx + Opx + Mgs	137	19	11
5	900	3	14	~10	Cpx + Gt + glass	Phl + Cpx + Opx (+ Mgs)	248	11	18
6	1000	3	4	~40	Cpx + Gt + glass	Opx + Cpx (+ Phl)	302	48	76
7	900	4	2	0	Cpx + Gt	Cpx + Opx + Mgs + Chlr	-	-	-
8	1000	4	3	0	Cpx + Gt	Cpx + Opx + Mgs + Chlr	271	32	90
9	1100	4	3	~20	Gt + Phl + glass	Cpx + Opx (+ Phl)	-	-	-
10	1000	5	1	0	Cpx + Gt	Cpx + Opx + Mgs + Chlr	147	19	147
11	1000	5	3	0	Cpx + Gt	Cpx + Opx + Mgs + Chlr	272	52	91
12	1100	6	3	0	Cpx + Gt	Cpx + Opx + Mgs + Chlr	980	133	327

P – pressure, T – temperature, SDEV – 1. Standard deviation, Phases: Chlr – Chloride, Cc – Calcite, Coe – Coesite, Cpx – Clinopyroxene, Dol – Dolomite, Gt – Garnet, Mgs – Magnesite, Opx – Orthopyroxene, Phe – Phengite, Phl – phlogopite



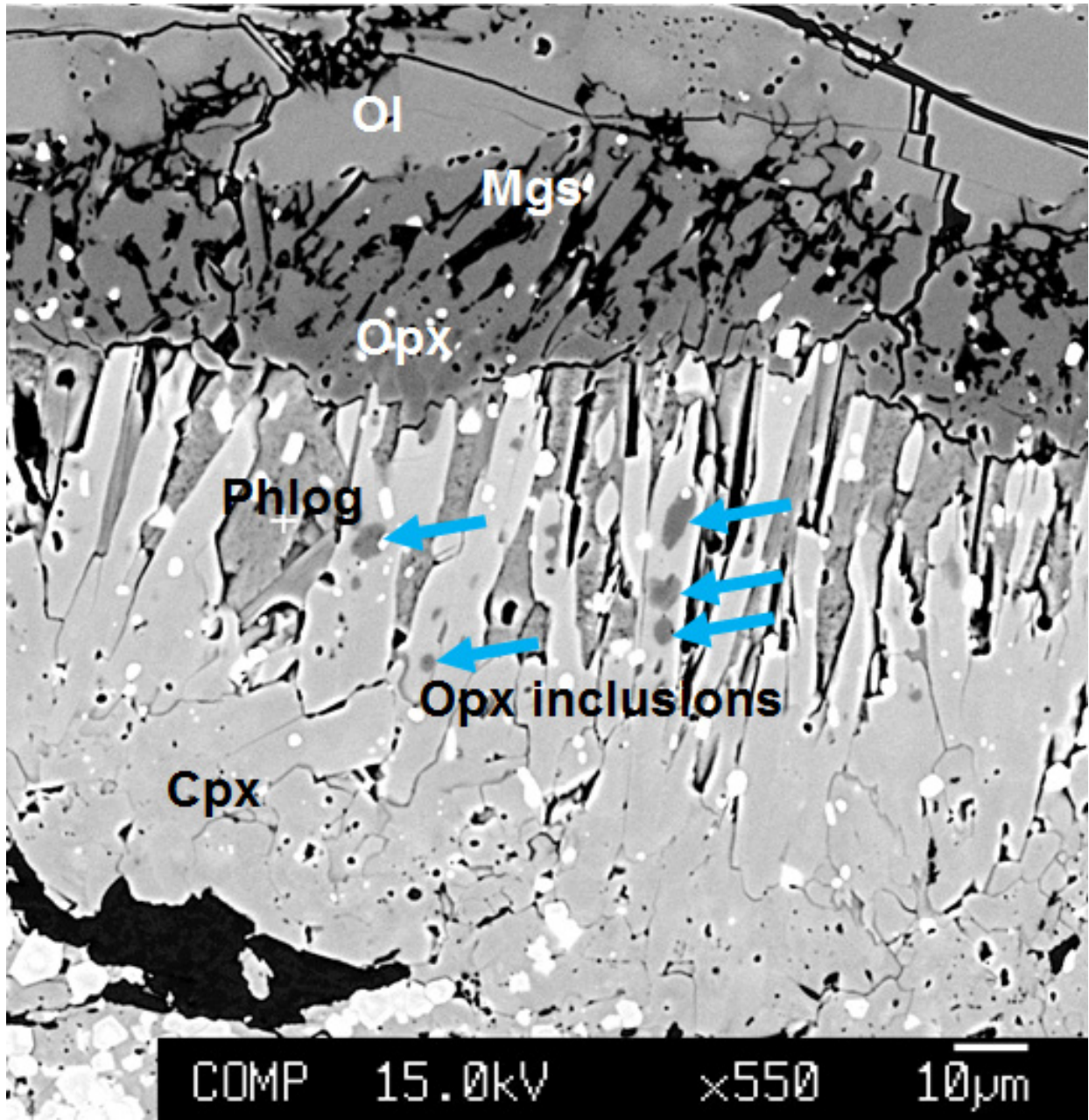
**Supplementary Fig. 1.2:** Metasome thicknesses and infiltrated melt distances. Each reaction zone was measured 10 times (along white line) to calculate the growth rate of the reaction zone (Table 1).

Experiments using ultrapotassic melt<sup>40,41</sup> show infiltration distances of  $505 \pm 60 \mu\text{m}$  (1225 °C),  $371 \pm 24 \mu\text{m}$  (1200 °C),  $1039 \pm 31 \mu\text{m}$  (1300 °C),  $983 \pm 44 \mu\text{m}$  (1400 °C),  $1127 \pm 187 \mu\text{m}$  (1450 °C).

**Supplementary Table 1.2:** Major element composition of starting materials [wt%].

Sample	LOI	Sum	SiO <sub>2</sub>	Al <sub>2</sub> O <sub>3</sub>	Na <sub>2</sub> O	Fe <sub>2</sub> O <sub>3</sub>	MgO	P <sub>2</sub> O <sub>5</sub>	SO <sub>3</sub>	TiO <sub>2</sub>	CaO	K <sub>2</sub> O	MnO	Cl	F
Sediment	15.34	100.5	42.29	14.08	1.55	5.17	3.01	0.16	2.33	0.59	11.16	2.57	1.63	0.42	0.18
Dunite	-1.66	99.54	40.44	0.08	0.03	11.19	49.08	0.00	0.12	0.01	0.13	0.01	0.13	0.00	0.00

Supplementary Tables 1.3 and 1.4: Separate excel-spreadsheet.



**Supplementary Fig. 1.3:** Reaction zone phases. Orthopyroxene inclusions within clinopyroxene reveal growth of the metasome layer at the expense of dunite.

Supplementary Tables 2.1-2.11: Separate excel-spreadsheet.

**Supplementary Table 2.12:** Phase relations of experiments.

#	Composition	T [°C]	P [GPa]	% Melt	Phases formed by reaction	Duration [d]
1	Sediment	1000	4	~65	Gt + Coes + Mg-Cc + Ky + silicate melt	3
2	Sediment/Peridotite Reaction	800	3	~10	Phl + Cpx + Opx + Mg-Cc + Gt + silicate melt	6
3	Sediment/Peridotite Reaction	850	3	~15	Phl + Mgs + Cpx + Opx + Gt + silicate melt	13
4	Sediment/Peridotite Reaction	900	3	~20	Phl + Mgs + Cpx + Opx + Gt + silicate melt	14
5	Sediment/Peridotite Reaction	1000	3	~25	Phl + Cpx + Opx + Gt + silicate melt	4
6	Sediment/Peridotite Reaction	900	4	0	Cpx + Opx + Mgs + Gt + Na-K chloride	2
7	Sediment/Peridotite Reaction	1000	4	0	Cpx + Opx + Mgs + Gt + Na-K chloride	3
8	Sediment/Peridotite Reaction	1100	4	~25	Phl + Gt + Opx + silicate melt	3
9	Sediment/Peridotite Reaction	1000	5	0	Cpx + Opx + Mgs + Gt + Na-K chloride	3
10	Sediment/Peridotite Reaction	1100	6	0	Cpx + Opx + Mgs + Gt + Na-K chloride	3

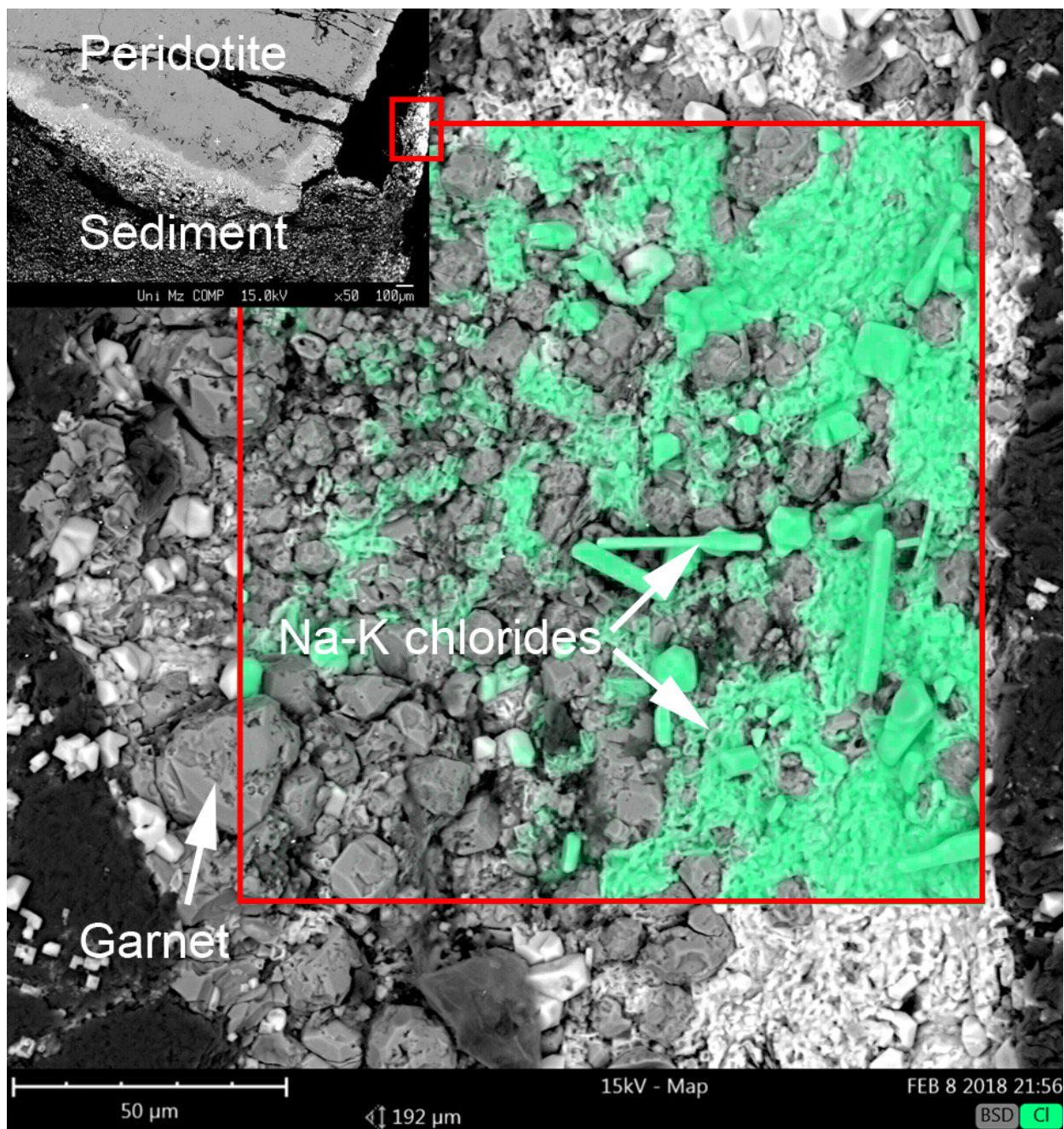
Supplementary Tables 2.13-2.18: Separate excel-spreadsheet.

Supporting information of preparation and measurement of Na-K chlorides:

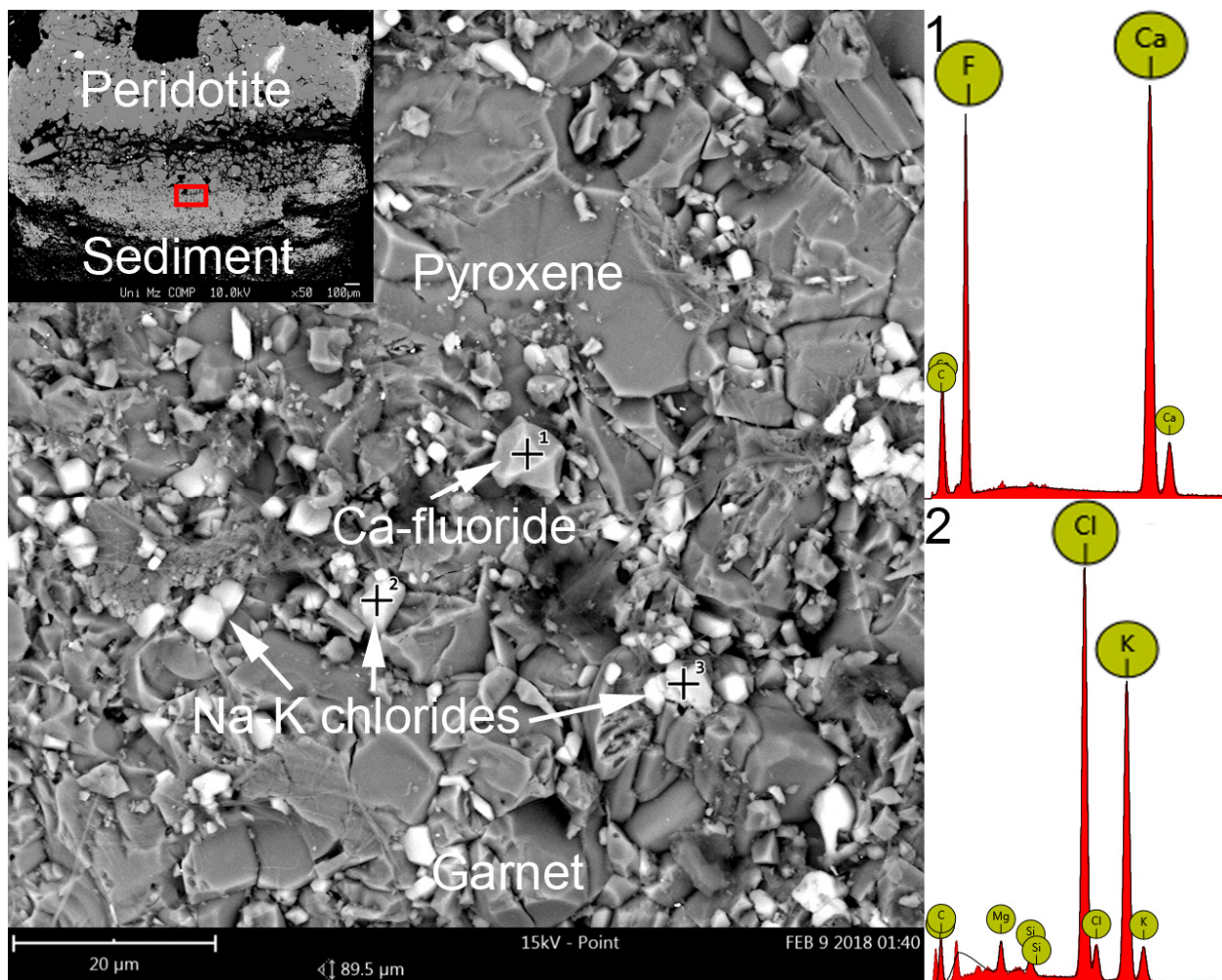
In this part we present additional information to demonstrate the authenticity of Na-K chlorides forming at 4-6 GPa:

1. All experiments from 3-6 GPa used the same starting materials and capsule materials. Mount preparation was identical for all samples, which were cut using a Struers low-speed saw with water-free cutting fluid and polished using water-free Struers DP-Suspension A.
2. The unpolished sample ([Supplementary Fig. 2.2](#)) contains Na-K chlorides.
3. Chlorides are distributed interstitially within the crystal assemblage ([Fig. 2.1 C,D](#), [Supplementary Fig. 2.1, 2.2](#)) and are accompanied by subsidiary amounts of other halides such as Ca-fluoride ([Supplementary Fig. 2.2](#)).
4. Quantitative EPMA and semi-quantitative EDX measurements and maps show that chlorides crystallized as NaCl-KCl solid solution with K/Na of 1-9 ([Fig. 2.2](#)), which requires a minimum crystallization temperature of  $T > 500$  °C at ambient pressure (Pelton et al., 1985). The idiomorphic appearance of Na-K chlorides in this study shows that they crystallized, slowly at high T rather than during quenching after the experiments ([Fig. 1](#), [fig. S3, S4](#)).
5. K/Na ratios of Na-K chlorides are similar to those in silicate melts of experiments at 3 GPa. The separation of Na from K thus followed the same mechanism by crystallizing Na-rich clinopyroxene ([Fig. 2.5 A](#)).
6. Chloride-bearing experiments are devoid of silicate melt and hydrous phases that accommodated K and Cl in reaction and melting experiments at 3 GPa and 4 GPa.





**Supplementary Fig. 2.1:** Chloride map of 5 GPa/1000 °C experiment. A chlorine EDX map (green) is superimposed on a backscattered electron image of chlorides (white) at the inner carbon capsule wall next to garnet crystals of the reaction zone.

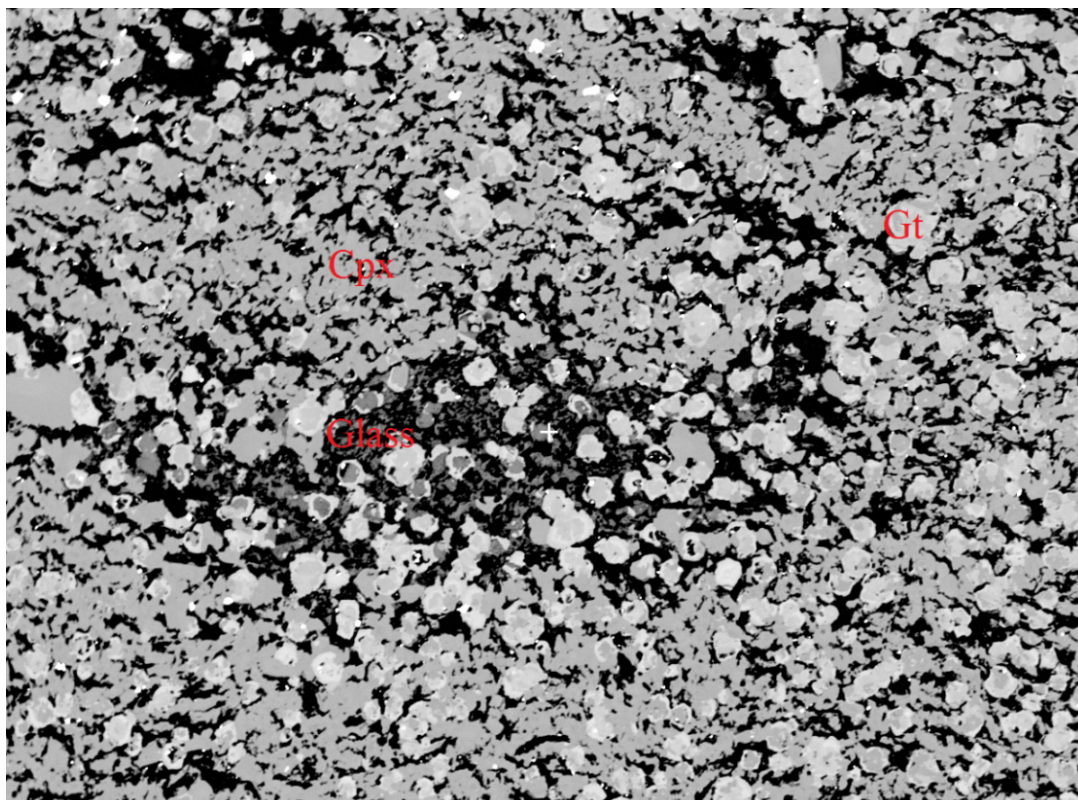


**Supplementary Fig. 2.2:** Backscattered electron image of the 6 GPa/1100 °C experiment showing an unpolished capsule half. The image shows the reaction zone with silicate phases (garnet and pyroxene), with the corresponding EDX spectra for Na-K chlorides (bottom) and Ca-fluoride (top).

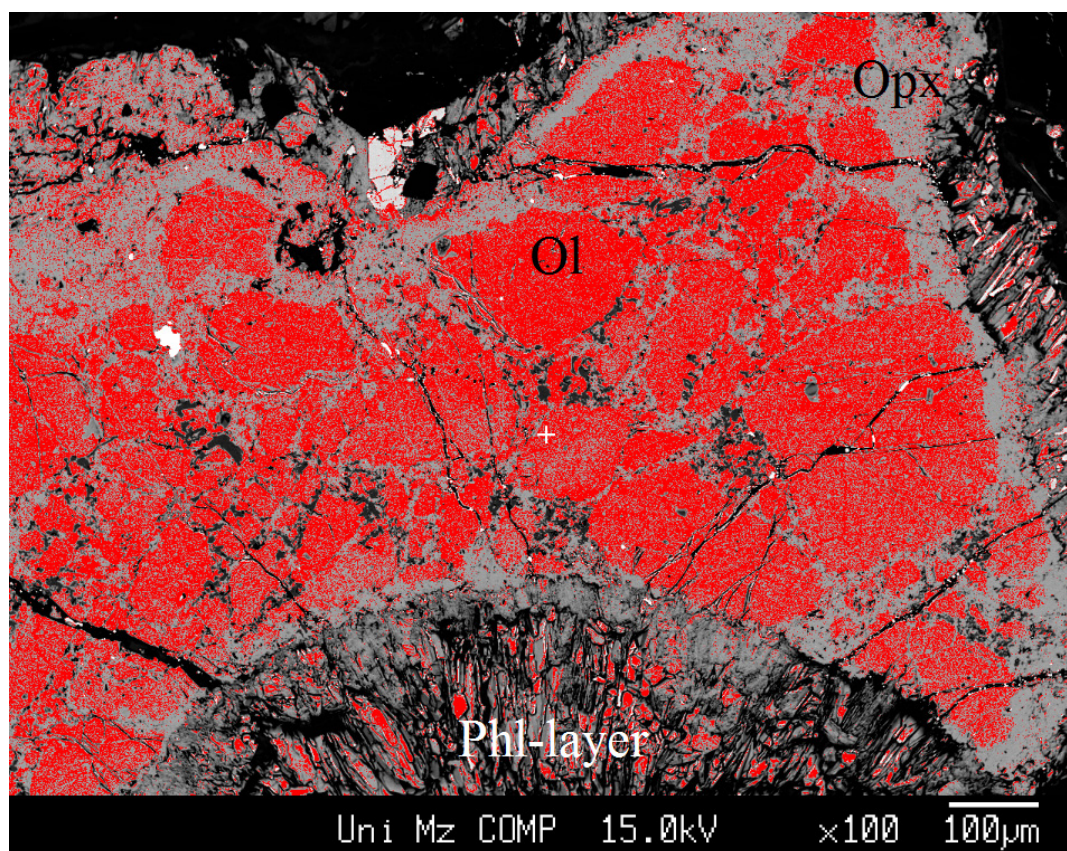
Supplementary Tables 3.1-3.10: Separate excel-spreadsheet.

Supplementary Tables 3.11-3.14: Separate excel-spreadsheet.





**Supplementary Fig. 3.1:** Residual sediment of the 3 GPa/900 °C experiment containing ~60 % clinopyroxene (grey), ~40 % garnet (light grey), and interstitial glass (dark grey) as estimated by Fiji (imagej).



**Supplementary Fig. 3.2:** Orthopyroxene-veins in dunite of the 3 GPa/900 °C experiment containing 22 % orthopyroxene (grey) and 78 % olivine (red) as estimated by Fiji (imagej). The metasomatized sediment is located below the phlogopite layer.



Supplementary Tables 4.1-4.6: Separate excel-spreadsheet.

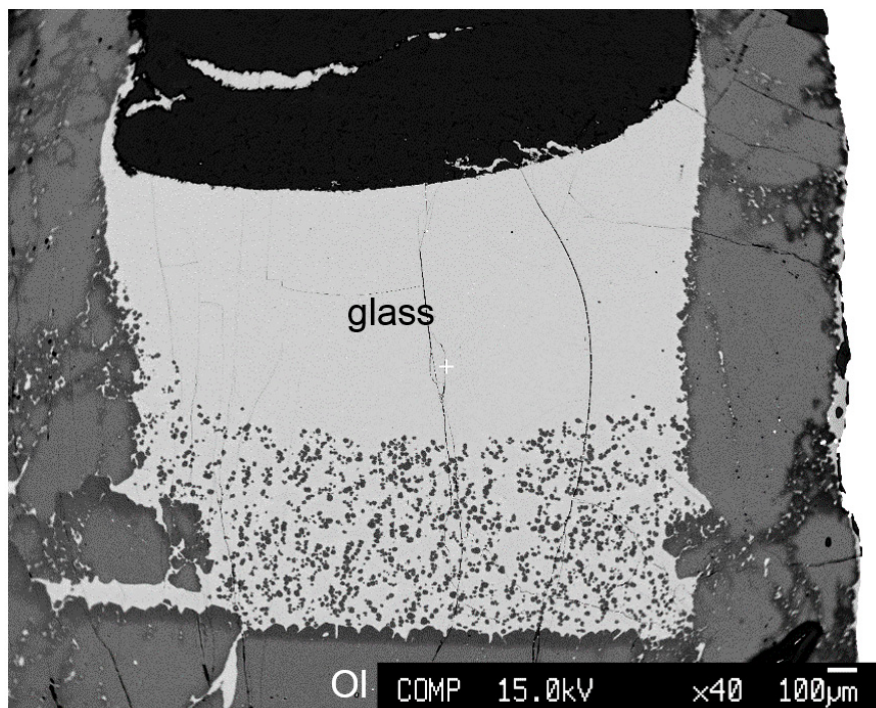
Supplementary Tables 4.6-4.17: Separate excel-spreadsheet.

**Supplementary Table 5.1:** Reference materials for electron-microprobe routines.

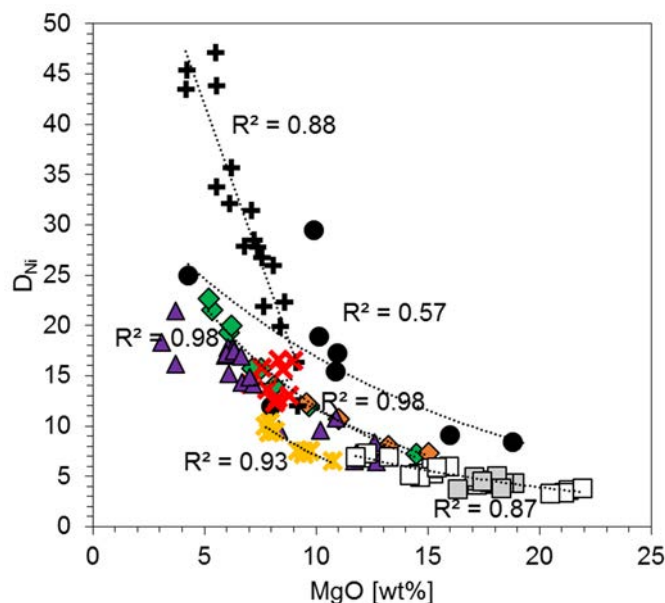
<b>Routine:</b>	<b>silicates</b>	<b>olivine</b>	<b>mica</b>	<b>volcanic glass</b>
Accelerating Voltage	15 kV	20 kV	15 kV	15 kV
Beam Current	12 nA	30 nA	12 nA	12 nA
Spot-size	2 $\mu\text{m}$	2 $\mu\text{m}$	2 $\mu\text{m}$	5-10 $\mu\text{m}$
Elements:	11	10	14	13
Na	Albite	-	Albite	Albite
Al	Al <sub>2</sub> O <sub>3</sub>	Al <sub>2</sub> O <sub>3</sub>	Al <sub>2</sub> O <sub>3</sub>	VG-2
Cr	Cr <sub>2</sub> O <sub>3</sub>	Cr <sub>2</sub> O <sub>3</sub>	Cr <sub>2</sub> O <sub>3</sub>	-
Fe	Fe <sub>2</sub> O <sub>3</sub>	Fe <sub>2</sub> O <sub>3</sub>	Fe <sub>2</sub> O <sub>3</sub>	VG-2
Mg	MgO	Olivine	MgO	VG-A9
Mn	MnTiO <sub>3</sub>	Rhodonite	MnTiO <sub>3</sub>	MnTiO <sub>3</sub>
Ti	MnTiO <sub>3</sub>	TiO <sub>2</sub>	MnTiO <sub>3</sub>	MnTiO <sub>3</sub>
K	Orthoclase	-	Orthoclase	Orthoclase
Si	Wollastonite	Olivine	Orthoclase	VG-2
Ca	Wollastonite	Wollastonite	Wollastonite	VG-A9
Ni	NiO	NiO	-	-
Zn	-	-	ZnS	-
Co	-	Cobaltine	-	-
Ba	-	-	BaSO <sub>4</sub>	-
P	-	-	-	Apatite
F	-	-	SrF <sub>2</sub>	SrF <sub>2</sub>
Cl	-	-	KCl	KCl

Supplementary Tables 5.2: Separate excel-spreadsheet.

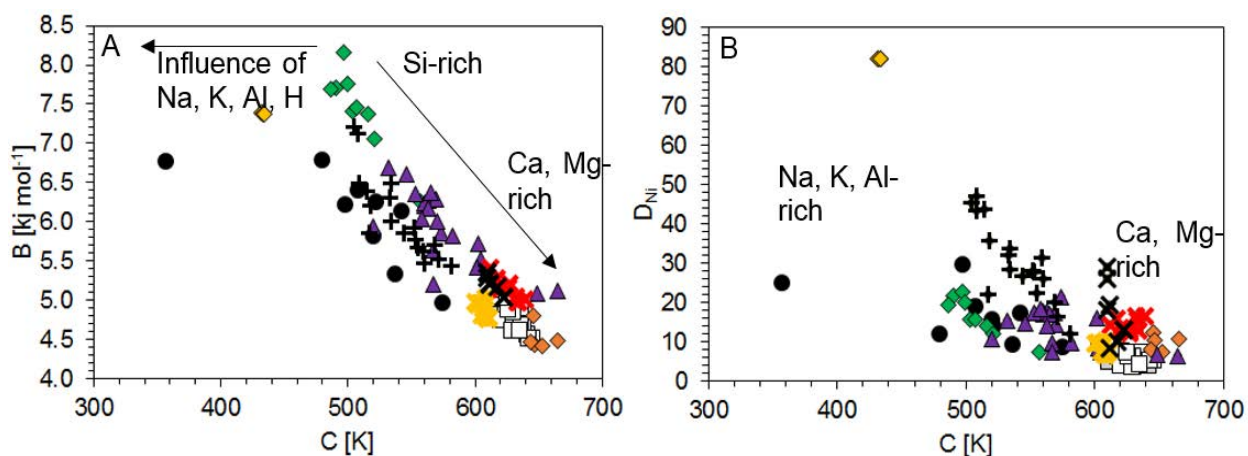
Supplementary Tables 5.3-5.11: Separate excel-spreadsheet.



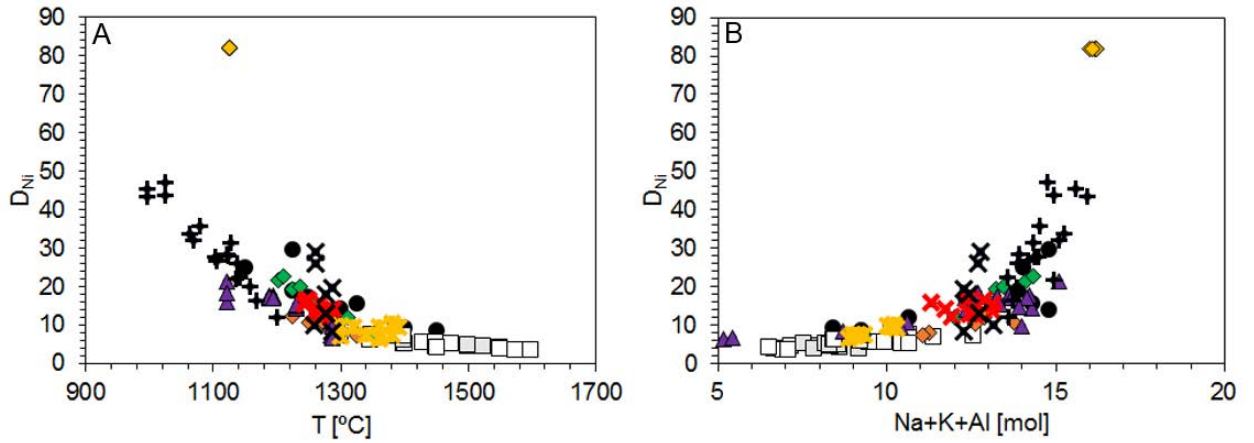
**Supplementary Fig. 5.1:** Synthetic MARID glass in San Carlos Olivine capsule at 1 GPa/1300 °C. Olivine of the capsule wall shows zonation due to equilibration with the MARID melt.



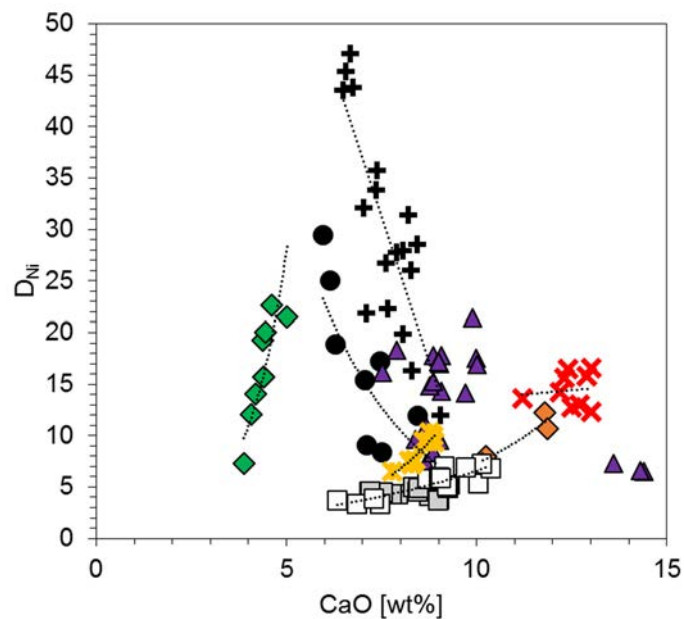
**Supplementary Fig. 5.2:** A) Correlation of  $D_{Ni}$  in olivine/melt *versus* MgO-content of the experimental melts compared with literature data: red crosses – East Pacific Rise/MORB (Allan et al., 1989); black plusses – Mexico/calc-alkaline (Luhr and Carmichael, 1985); purple triangles – alkaline-basaltic melt (Snyder and Carmichael, 1992); orange diamonds – basaltic, and green diamonds – eclogite melt (Wang and Gaetani, 2008); yellow crosses – Fe-rich basaltic melt (Filiberto et al., 2009); white and grey squares – basaltic melt (Matzen et al., 2013; 2017).



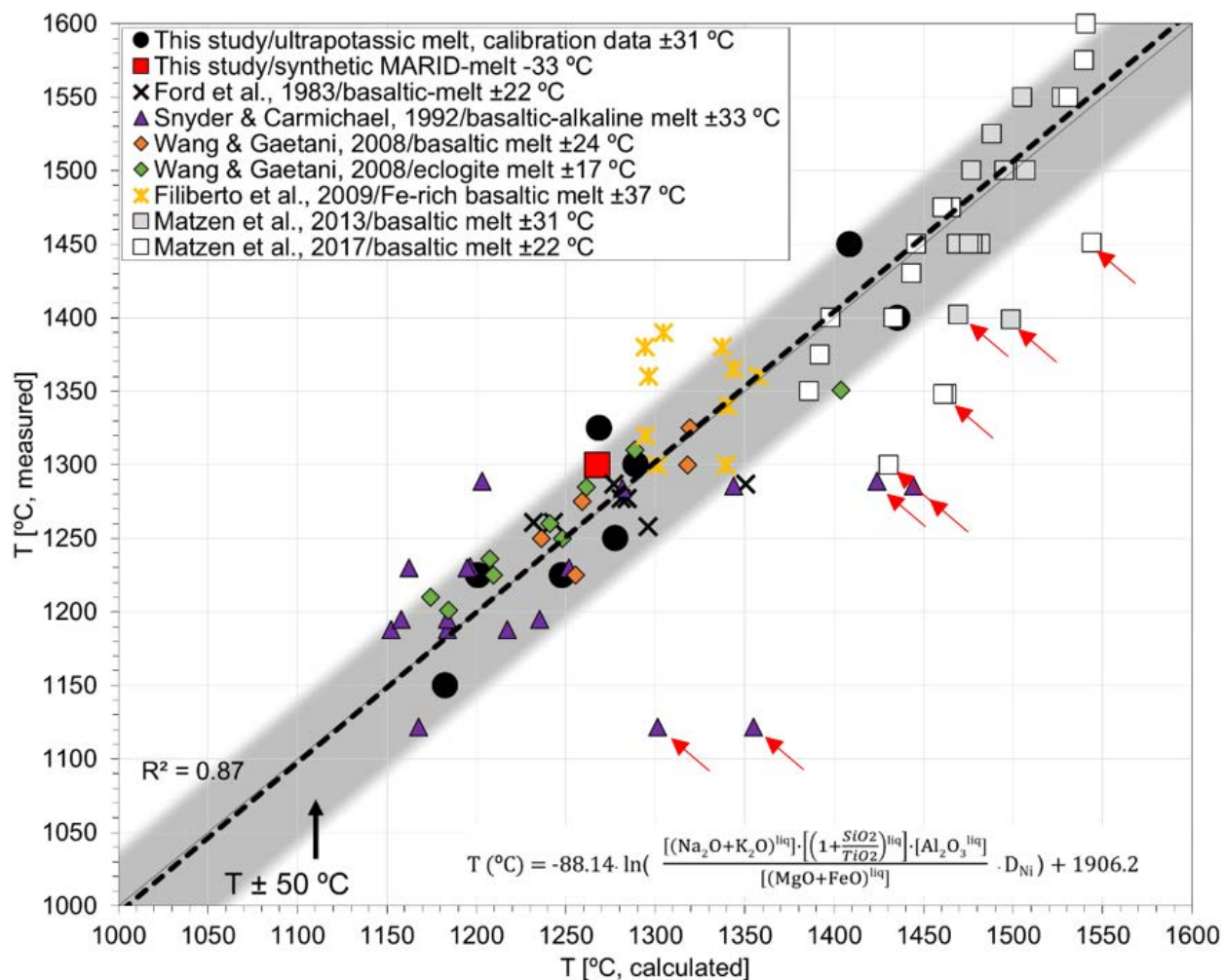
**Supplementary Fig. 5.3:** A) Model parameters B *versus* C of melt-viscosity model (Giordano et al., 2008) applied to experimental melts (black circles) and literature data: black crosses – basaltic-melt (Ford et al., 1983); red crosses – East Pacific Rise/MORB (Allan et al., 1989); black plusses – Mexico/calc-alkaline (Luhr and Carmichael, 1985); purple triangles – alkaline-basaltic melt (Snyder and Carmichael, 1992); orange diamonds – basaltic, and green diamonds – eclogite melt (Wang and Gaetani, 2008); yellow crosses – Fe-rich basaltic melt (Filiberto et al., 2009); white and grey squares – basaltic melt (Matzen et al., 2013; 2017). Increasing proportions of network-modifier cations (Na, K, Ca, Mg) decrease B, whereas values of C show a positive correlation. Volatile elements (H) slightly decrease values of B whereas values of C are strongly decreased. B)  $D_{Ni}$  *versus* model value C. Primitive, magnesian melts plot at low  $D_{Ni}$  olivine/melt and comprise low C-values due to high contents of the network modifier-cations Ca and Mg.



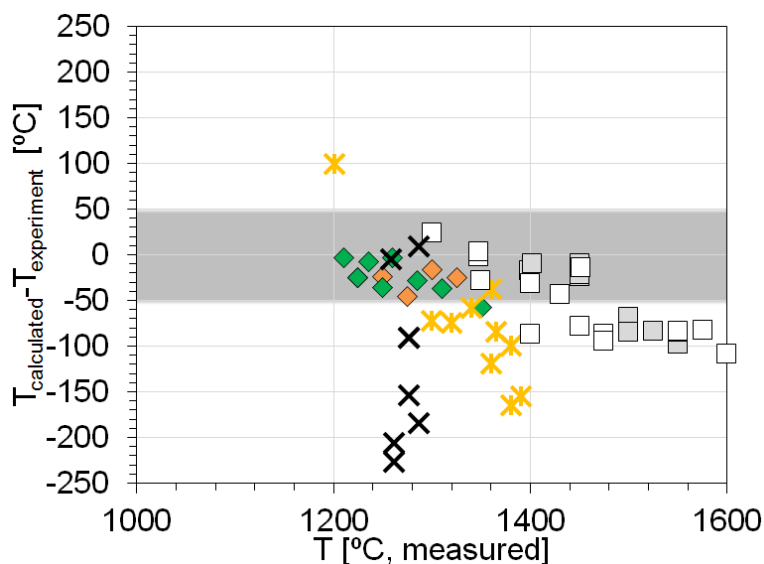
**Supplementary Fig. 5.4:** A)  $D_{Ni}$  versus temperature and B)  $D_{Ni}$  versus molar contents of Na, K, and Al.  $D_{Ni}$  shows a strong correlation with temperature, however  $D_{Ni}$  it is highest for compositions with highest contents of Na, K, and Al (symbols as in Supplementary Fig. 5.3).



**Supplementary Fig. 5.5:** Correlation of  $D_{Ni}$  in olivine/melt versus CaO-content (symbols as in Supplementary Fig. 5.3). The direction of the trend-line dip depends on whether olivine alone fractionates (positive correlation) or together with clinopyroxene (negative correlation).

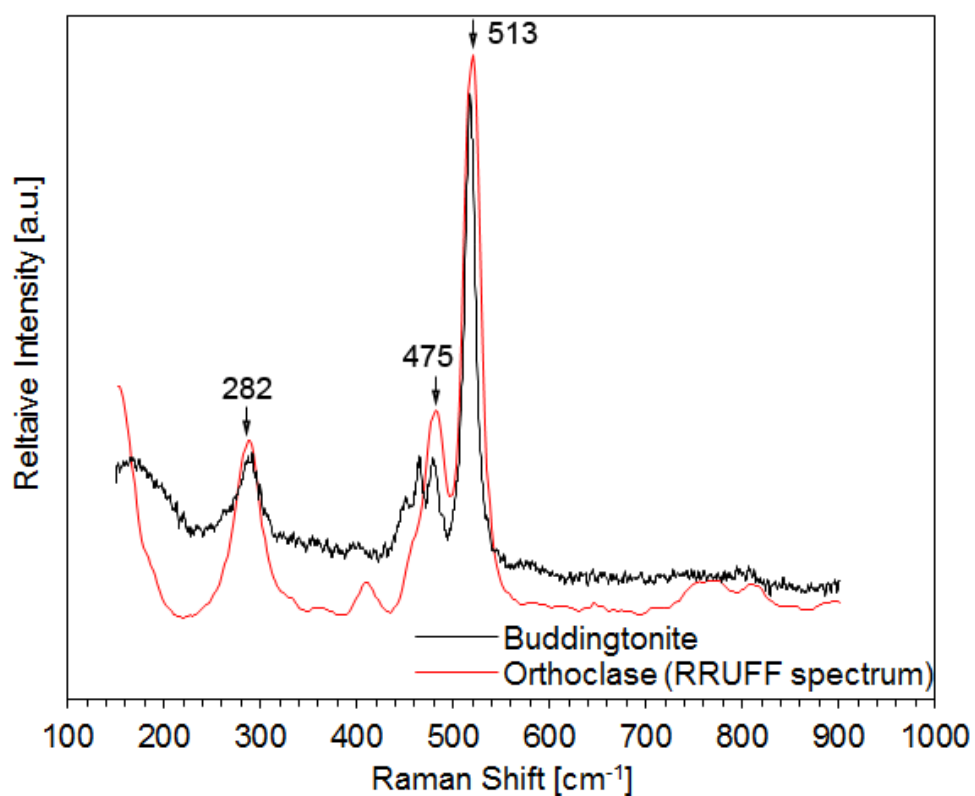


**Supplementary Fig. 5.6:** Calculated temperature *versus* measured temperature (symbols as in Supplementary Fig. 5.3). Red arrows mark literature data obtained at ambient pressure and experienced loss of Na, K, and Fe during the experiment.



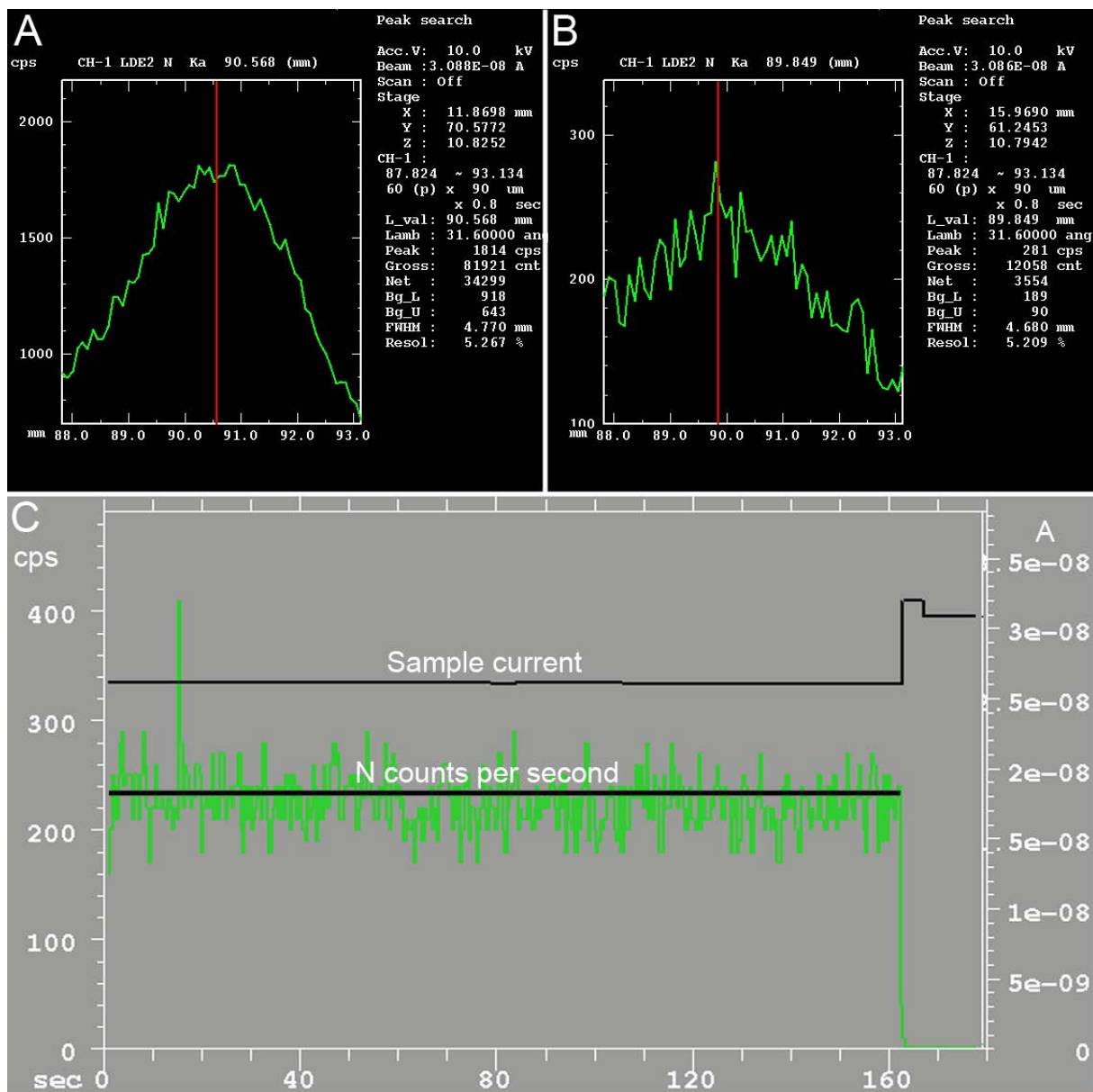
**Supplementary Fig. 5.7:** Thermometer based on Ni-partitioning and molar constituents of melt and olivine (symbols as in Supplementary Fig. 5.3) from Pu et al. (2017). This thermometer can reproduce temperatures of experiments conducted at 1 atmosphere but shows deviations  $> 50$  °C for experiments at high pressure.

Supplementary Tables 6.1-6.10: Separate excel-spreadsheet.

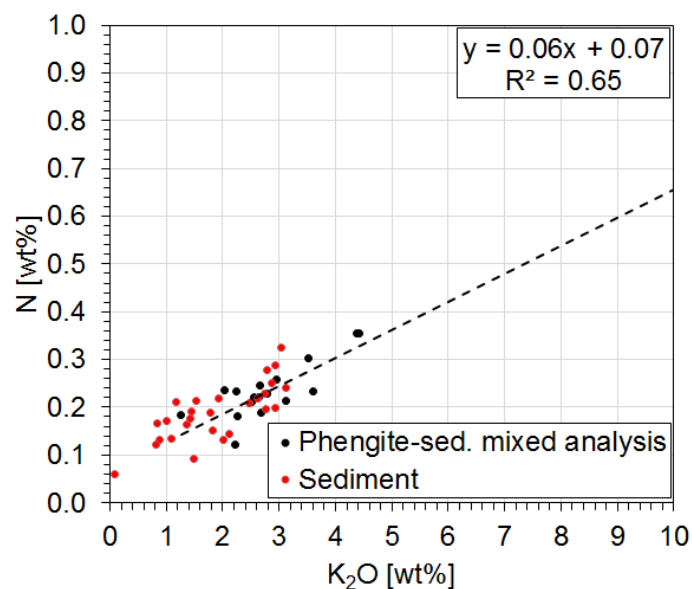


**Supplementary Fig. 6.1:** Raman spectra of NH<sub>4</sub>-feldspar (buddingtonite) compared to orthoclase (spectra from RRUFF database: <http://rruff.info/>, Armbruster and Danisi, 2016). Buddingtonite has the same lattice mode as K-feldspar, despite K<sup>+</sup> being replaced by NH<sub>4</sub><sup>+</sup> in buddingtonite.

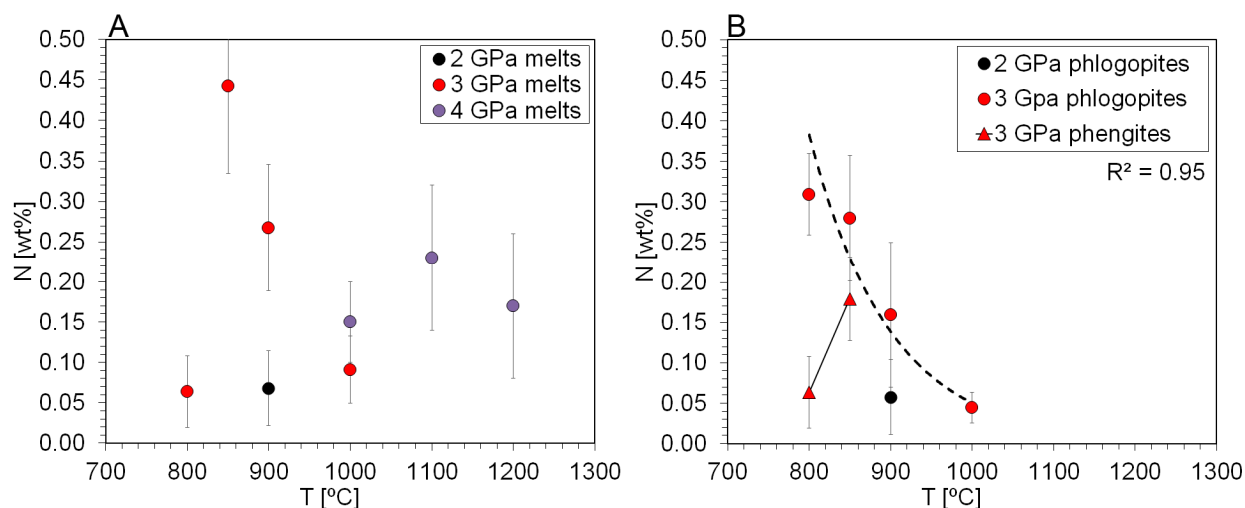




**Supplementary Fig. 6.2:** Measurement parameters for N at the EPMA (10 kV, 30 nA, 10-20  $\mu$ m spot size). A) Nitrogen peak on boron nitride (1814 counts per second [cps]). B) Nitrogen peak on buddingtonite (281 cps). C) Chart recorder showing N signal stability on buddingtonite for 160 s.

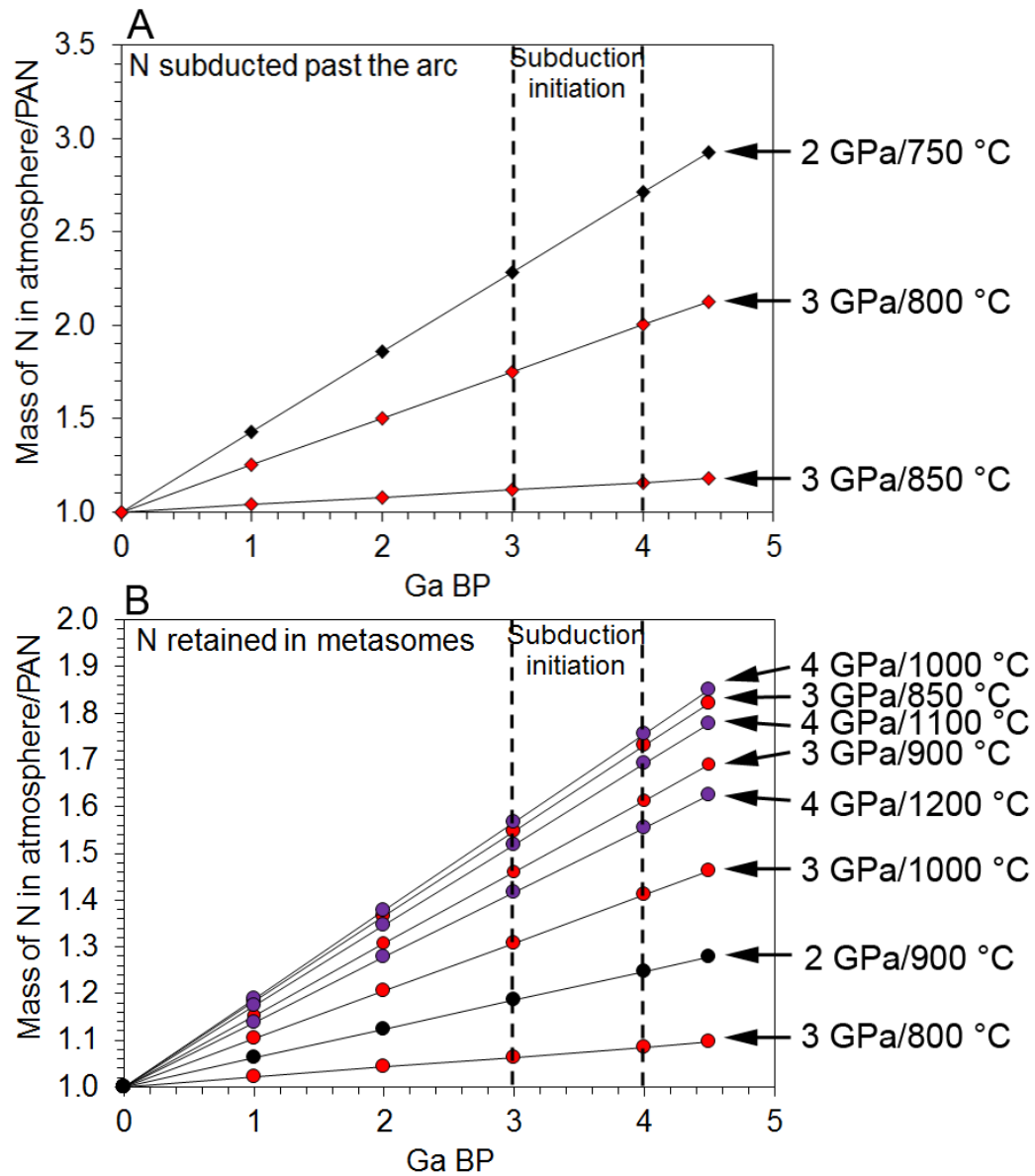


**Supplementary Fig. 6.3:** Linear correlation of N versus K<sub>2</sub>O in phengite of the experiment at 2 GPa/750 °C. Since the crystal size is smaller than the defocused beam (10 μm) used to measure N, only mixed phase analysis are possible for phengite. However, the linear correlation between N and K<sub>2</sub>O enables an extrapolation of the true mass fraction of N in phengite at 10 wt% K<sub>2</sub>O.

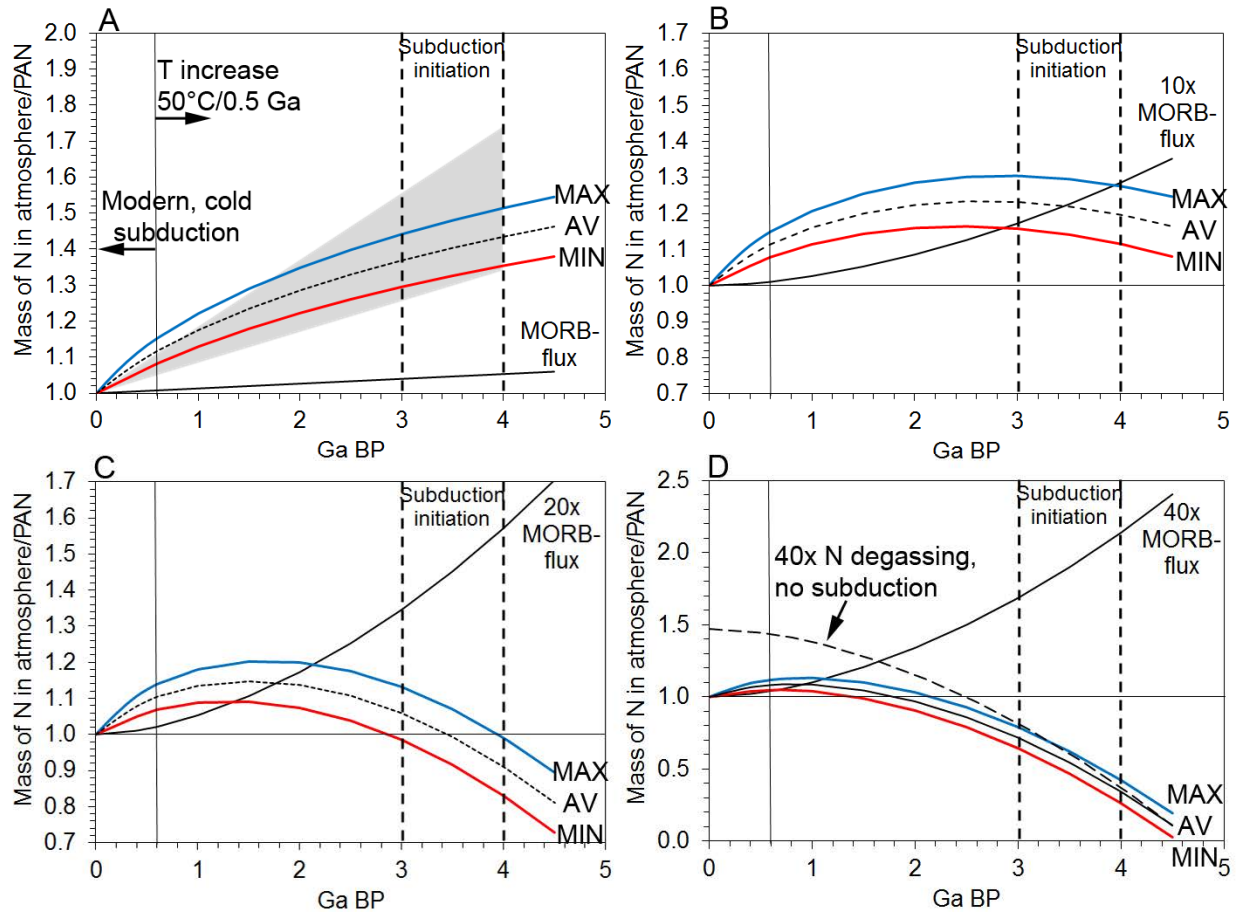


**Supplementary Fig. 6.4:** (A) Nitrogen mass fraction of measured glasses *versus* experimental run temperature. (B) Nitrogen mass fraction of phlogopite and phengite *versus* experimental run temperature. Nitrogen mass fraction of phlogopite at 3 GPa/800-1000 °C correlates negative exponentially with temperature.





**Supplementary Fig. 6.5:** Mass fraction of atmospheric nitrogen *versus* time normalized to present-day atmospheric nitrogen (PAN). (A) The subduction of nitrogen decreases with temperature and is highest in the experiment at 750 °C. (B) The mass of nitrogen metasomatized to the (lithospheric) mantle increases with temperature and pressure and peaks at 3 GPa/850°C and 4 GPa/1000 °C.



**Supplementary Fig. 6.6:** The N retention within subduction zone is plotted according to a dynamic increase of subduction temperature with time from 0-4 Ga BP (MIN scenario: 850-1200 °C, MAX scenario: 750-1100 °C). From 0-0.6 Ga, modern, cold subduction zones with blueschist-facies metamorphism are apparent (Condie and Kröner, 2008). The different pathways of N within Earth's atmosphere in A)-D) correspond to N degassing fluxes rising to 1x MORB values at 4.5 Ga in A), 10x in B), 20x in C), and 40x in D).

## **Appendix 2: Published paper in journal format**



# Melting phlogopite-rich MARID: Lamproites and the role of alkalis in olivine-liquid Ni-partitioning

Michael W. Förster<sup>a,\*</sup>, Dejan Prelević<sup>b,c</sup>, Harald R. Schmück<sup>b</sup>, Stephan Buhre<sup>b</sup>,  
Horst R. Marschall<sup>d</sup>, Regina Mertz-Kraus<sup>b</sup>, Dorrit E. Jacob<sup>a</sup>

<sup>a</sup> Australian Research Council Centre of Excellence for Core to Crust Fluid Systems (CCFS) and GEMOC, Macquarie University, NSW 2109, Sydney, Australia

<sup>b</sup> Institute for Geosciences, Johannes Gutenberg University, 55099 Mainz, Germany

<sup>c</sup> Faculty of Mining and Geology, University Belgrade, 11000 Belgrade, Serbia

<sup>d</sup> Institute for Geosciences, Goethe University, 60438 Frankfurt am Main, Germany

## ARTICLE INFO

Editor: D.B. Dingwell

### Keywords:

Lamproite  
High-pressure experiments  
Metasomatism  
Ni-partitioning  
Geothermometry

## ABSTRACT

In this study, we show how veined lithospheric mantle is involved in the genesis of ultrapotassic magmatism in cratonic settings. We conducted high pressure experiments to simulate vein + wall rock melting within the Earth's lithospheric mantle by reacting assemblages of harzburgite and phlogopite-rich hydrous mantle xenoliths. These comprised a mica-, amphibole-, rutile-, ilmenite-, diopside (MARID) assemblage at 3–5 GPa and 1325–1450 °C. Melting of the MARID assemblages results in infiltration of melt through the harzburgite, leading to its chemical alteration. At 3 and 4 GPa, melts are high in K<sub>2</sub>O (> 9 wt%) with K<sub>2</sub>O/Na<sub>2</sub>O > 2 comparable to anorogenic lamproites. Higher pressures and temperatures (5 GPa/1450 °C) lead to increasing MgO contents of the melt and to some extent lower K<sub>2</sub>O contents (5–7 wt%) at equally high K<sub>2</sub>O/Na<sub>2</sub>O ratios. Our experiments provide insights into the role of alkalis in nickel-partitioning ( $D_{Ni}$ ) between olivine and ultrapotassic melt. We observe that the high contents of Na, K, and Al are indicative of high  $D_{Ni}$  values, implying that the melt polymerization is the dominant factor influencing the olivine/melt nickel partitioning. The change of  $D_{Ni}$  as a function of melt composition results in a pressure independent, empirical geothermometer:

$$T (^{\circ}\text{C}) = -88.14 \cdot \ln \left( \frac{[\text{liq}(\text{Na}_2\text{O} + \text{K}_2\text{O})] \cdot \left[ \text{liq} \left( 1 + \frac{\text{SiO}_2}{\text{TiO}_2} \right) \right] \cdot [\text{liq}(\text{Al}_2\text{O}_3)]}{[\text{liq}(\text{MgO} + \text{FeO})]} \right) \cdot D_{Ni} + 1906.2$$

Element oxides represent the composition of the glass (in wt%), and  $D_{Ni}$  is the liquid/olivine Ni-partitioning coefficient. We propose that this geothermometer is applicable to all natural silicate melts that crystallized olivine in a temperature interval between 1000 and 1600 °C. Application to glass-olivine pairs from calc-alkaline settings (Mexico), MORB (East Pacific Rise), and OIB (Hawaii) yielded reasonable values of 996–1199 °C, 1265 °C, and 1330 °C, respectively.

## 1. Introduction

Basaltic magmas are traditionally viewed to be generated in a homogeneous peridotitic upper mantle (Jaques and Green, 1980). An increasing number of petrological studies challenge this view, as they suggest that melting in the upper mantle in many cases begins with melting of mixed source regions that consist of fertile olivine-free ultramafic lithologies within peridotite (Meen, 1987; Foley, 1992; Hirschmann and Stolper, 1996; Lassiter et al., 2000; Sobolev et al.,

2005; Prelević et al., 2008). This scenario is particularly applicable for K-alkaline and ultrapotassic melt compositions like lamproites (Foley, 1992), which cannot be explained by the low extent of partial melting of a homogeneously metasomatized peridotite (e.g. Green and Falloon, 2005; Green et al., 2014; Novella and Frost, 2014; Novella et al., 2014) because the experimental studies of low degrees (< 1%) of partial melting of phl-bearing peridotite never yielded sufficiently high K-contents (> 5 wt%) and K<sub>2</sub>O/Na<sub>2</sub>O ratios (> 2) to explain ultrapotassic magmatism (Novella and Frost, 2014 and references therein).

\* Corresponding author.

E-mail address: [michael.forster@mq.edu.au](mailto:michael.forster@mq.edu.au) (M.W. Förster).

<https://doi.org/10.1016/j.chemgeo.2017.11.039>

Received 13 July 2017; Received in revised form 21 November 2017; Accepted 26 November 2017

Available online 28 November 2017

0009-2541/ © 2017 Elsevier B.V. All rights reserved.



The inability of low-degree melting experiments to produce melts with high contents of K and the fact that liquidus experiments failed to produce multiple saturation points that include olivine, orthopyroxene, clinopyroxene and garnet/spinel (Edgar and Mitchell, 1997; Foley and Peccerillo, 1992; Foley, 1992; Foley et al., 2012; Mitchell and Edgar, 2002; Sato, 1997) led to an alternative model explaining lamproitic magmatism as being sourced from mantle veined by fertile phlogopite-rich clinopyroxenites, so-called metasomes (Foley, 1992). The wall-rock peridotite is usually of harzburgitic composition as it underwent previous melt extraction and contains high-Fo olivine and Cr-rich spinel (Prelević and Foley, 2007). Vein wall-rock reactions in this system are thought to produce melts of lamproitic compositions with a characteristically high  $K_2O$ , and low  $CaO$  and  $Al_2O_3$ .

Recent experimental studies found that hybridization of depleted mantle with K-rich metasomes is a robust process to explain the source rock of ultrapotassic magmatism (Förster et al., 2017; Mallik et al., 2015, 2016; Wang et al., 2017a; Wang et al., 2017b). Furthermore, phlogopite-rich mantle xenoliths and abundant phlogopite-xenocrysts are associated with the ultrapotassic volcanics (Downes et al., 2002; Prelević et al., 2010; Zhang et al., 2011; Fritschle et al., 2013) suggesting a genetic link.

Mica-amphibole-rutile-ilmenite-diopside (MARID)-type mantle xenoliths from the Kaapvaal craton (RSA) are phlogopite-rich xenoliths typical for cratonic settings (Harte, 1987). Their phlogopite-rich end-member is also referred to as glimmerite. MARID-type xenoliths are either mantle metasomatic assemblages or represent cumulates from ultrapotassic rocks that crystallized from hydrous melts similar to lamproites or kimberlites (Dawson and Smith, 1977; Erlank et al., 1982; Waters, 1987; Sweeney et al., 1993). MARID assemblages are stable over a wide range of pressure and temperatures, including those of the cratonic lithosphere of 3–8 GPa/900–1300 °C (Konzett et al., 1997), thus it is conceivable that they take part in partial melting of the lithospheric mantle.

Numerous recent studies established source–melt kinship between heterogeneously metasomatized lithospheric mantle and ultrapotassic lavas through a complex vein-wall rock melting relationship (Foley, 1992; Tappe et al., 2008; Rosenthal et al., 2009; Giuliani et al., 2015). The vein component in this setting is thought to consist of metasomes similar to MARID xenoliths that explain the extreme variations in isotopic and chemical compositions of the hybrid melts. However, the application of these models faces a significant obstacle due to the lack of comprehensive experimental studies that constrain melting and dynamic metasomatism of a source consisting of mixed peridotite and MARID assemblages.

In this study we discuss the melting of a mixed MARID-glimmerite plus harzburgite source rock at 3–5 GPa, which corresponds to cratonic lithospheric depths of 90 to 150 km. It is a follow up study to Förster et al. (2017) which presented results for similar compositions at low pressures of < 2 GPa corresponding to post-collisional geodynamic settings.

Our study follows a twofold approach: firstly, we use high-pressure experiments to determine the melting reactions of MARID-glimmerites with wall-rock harzburgite and investigate the composition of the produced glass and mineral assemblages. The experiments are carried out in order to provide new insights into the role of veined-peridotites

in the generation of ultrapotassic magmas. Secondly, we determine the Ni-partitioning between olivine and melt over a range of 1–5 GPa and 1150–1450 °C. Partitioning of nickel in olivine/melt ( $D_{Ni}$ ) pairs is known to vary from 2 to 20 in basaltic melts (Hart and Brooks, 1974; Ulmer, 1989; Snyder and Carmichael, 1992; Kennedy et al., 1993; Beattie, 1994; Dunn and Sen, 1994; Wang and Gaetani, 2008; Matzen et al., 2013, 2017), to values of up to 80 in highly alkaline melts (Foley et al., 2011, 2013).  $D_{Ni}$  shows significant exponential correlations with  $MgO$ , whereas pressure and temperature could primarily influence the melt composition (Wang and Gaetani, 2008; Li and Ripley, 2010; Foley et al., 2011, 2013). However, recent studies on experimental compositions with constant melt compositions at changing thermobaric conditions show a significant influence of temperature on  $D_{Ni}$  (Matzen et al., 2013, 2017). The high variability of our melt compositions also enables the definition of a new empirical pressure-independent geothermometer applicable to basaltic, alkaline, and ultrapotassic melts, which correctly reproduced temperatures in the range of 1000–1600 °C.

## 2. Materials and methods

### 2.1. Starting materials

MARID samples were collected from the Boshof Road Dump at the De Beers diamond mine in Kimberley, South Africa. The samples are coarse-grained sub-rounded xenoliths of about 10 cm in diameter. The mineral assemblage is dominated by ca. 90 vol% mm-sized phlogopites. Other phases in descending order of abundance are: diopside, K-rich-terite, rutile, and ilmenite. Calcite and barite occur as accessories. Two samples (DJ0227, DJ0228A) were used to produce thin sections (100  $\mu m$  thickness) and agate milled powders. The full dataset of mineral composition data, including major and trace element data, as well as details on the electron-probe micro analyser (EPMA)-routine is provided in Supplementary File 1–11.

Synthetic harzburgite and MARID compositions were synthesized to provide mantle wall-rock clean of trace elements for the layered reaction experiments, as well as MARID melt clean of trace elements for one Ni-partitioning experiment. They were produced from metal-oxides and carbonates (SIGMA-ALDRICH®) to match the composition of AVX-51 (Rapp et al., 1999) and the bulk analysis of the natural MARID samples, respectively. After grinding and mixing in an agate mortar using acetone, the mixtures were oven-dried and decarbonized. The AVX-51 mix was transformed to harzburgite at 1200 °C, 1 GPa over 10 days.

### 2.2. Experimental techniques

Experiments were carried out at 1 and 3 GPa using a Piston Cylinder Apparatus at the University of Mainz, and at 4–5 GPa using a Belt Apparatus at the University of Frankfurt. Natural MARID and synthetic harzburgite powders were placed in a capsule as a two-layer charge (Table 1). The experimental charge was filled into a carbon capsule to control  $fO_2$  via the C + CO equilibrium which, in turn, was placed into a platinum capsule. The synthetic MARID powder was placed into a capsule made of a San Carlos olivine encased in platinum capsule. The capsules were fitted into a pressure cell consisting of  $Al_2O_3$  spacers, a graphite furnace, b-type thermocouple, and a  $CaF_2$  spacer on the

**Table 1**  
Composition, temperature, pressure, and duration of each experiment.

#	Composition	T [°C]	P [GPa]	% Melt	Phases	Duration [h]
1	MARID/Harzb. Reaction	1325	3	~50	Ol + Opx + Cpx + melt	24
2	MARID/Harzb. Reaction	1360	4	~20	Ol + Opx + Cpx + Phlog + melt	48
3	MARID/Harzb. Reaction	1400	5	~30	Ol + Opx + Cpx + Garnet + Phlog + melt	48
4	MARID/Harzb. Reaction	1450	5	~50	Ol + Opx + Cpx + Phlog + melt	48
5	Synthetic MARID	1300	1	~90	Ol + melt	24



outside of the assemblage for the piston cylinder experiments. For the experiments using the Belt apparatus, the spacer and capsule holder consisted of natural calcium-fluoride, while other materials were identical to those used in the piston-cylinder experiments. The cell assemblies were first pressurized and subsequently heated at a rate of 50 °C/min. Both the Piston cylinder- and Belt-apparatus were continuously water-cooled (water temperature ca. 13 °C) and pressure and temperature were kept constant for 24–48 h. All charges were quenched to temperatures below 500 °C within 8 s in the Piston-cylinder runs, and within 10 s in the Belt runs. The position of the cooling plates in the Belt Apparatus, which are further away from the high-pressure, result in lower quench rates compared to the Piston Cylinder Apparatus.

### 2.3. Analytical techniques

Major element contents in the experimental run products were measured using a JEOL JXA 8200 Superprobe electron-microprobe analyser (EMPA) equipped with 5 wavelength dispersive spectrometers at the University of Mainz, Germany. Micas, silicates, and glasses were analysed with 15 kV accelerating voltage and a beam current of 12 nA, except for the olivines which were analysed at 20 kV and 30 nA. Peak counting times were 20–30 s for melts, silicates, and micas, and 150 s for olivines. The beam diameter was set to 2 µm in the 3 and 4 GPa experiments, and to 20 µm in the experiments at 5 GPa, to average quench phases. A range of synthetic materials were used as reference materials (Supplementary 1). Trace element analyses were carried out by laser ablation-inductively coupled plasma mass spectrometry (LA-ICP-MS) at the University of Mainz. An ESI NWR193 ArF Excimer laser ablation system (193 nm wavelength) equipped with a TwoVol2 ablation cell was used for the formation of a dry aerosol from the samples. After ablation with a repetition rate of 10 Hz at 3 J/cm<sup>2</sup>, the dry aerosol was transferred to an Agilent 7500ce mass spectrometer by a He-Ar

mixed gas flow. Synthetic NIST SRM 612 was used as calibration material with values from Jochum et al. (2011) and <sup>29</sup>Si was selected as internal standard using the SiO<sub>2</sub> data determined by electron-microprobe. For quality control, basaltic USGS BCR-2G was measured as an unknown in each run (Supplementary File 3). Results for USGS BCR-2G were within 10% of the data tabulated in the GeoReM database (<http://georem.mpch-mainz.gwdg.de/>, Jochum et al., 2005). For each analysis, background signals were acquired for 20 s, followed by a dwell time of 30 s with spot sizes of 20 or 50 µm. Where possible, laser ablation spots were co-located with the electron-microprobe analyses. Data processing was carried out using the commercial software GLITTER 4.4.1 (Griffin et al., 2008).

### 3. Results

#### 3.1. Textural observations

The experiments using synthetic MARID powder consisted of glass, free-floating olivines, and capsule-wall olivine (Supplementary 12). All reaction experiments comprised two layers with a melted vein that infiltrated the harzburgite and originated from the former MARID layer of the sample charge. The experiment at 3 GPa contained glass as well as an accumulation of clinopyroxene and olivine crystals at the bottom of the capsule (Fig. 1a). We observed the clinopyroxenes to occur both as euhedral grains and as inclusions in olivine, emphasizing that clinopyroxene crystallized prior to olivine. The harzburgite showed patches of glass, as well as phlogopite and clinopyroxene. We observed less glass in the MARID part at 4 GPa, however, this layer had completely recrystallized to contain 50 vol% rounded olivine and idiomorphic clinopyroxene (Supplementary 2). No glass was observable in the harzburgite part, while phlogopite and clinopyroxene were found in patchy occurrences. At 5 GPa, the MARID part contained an

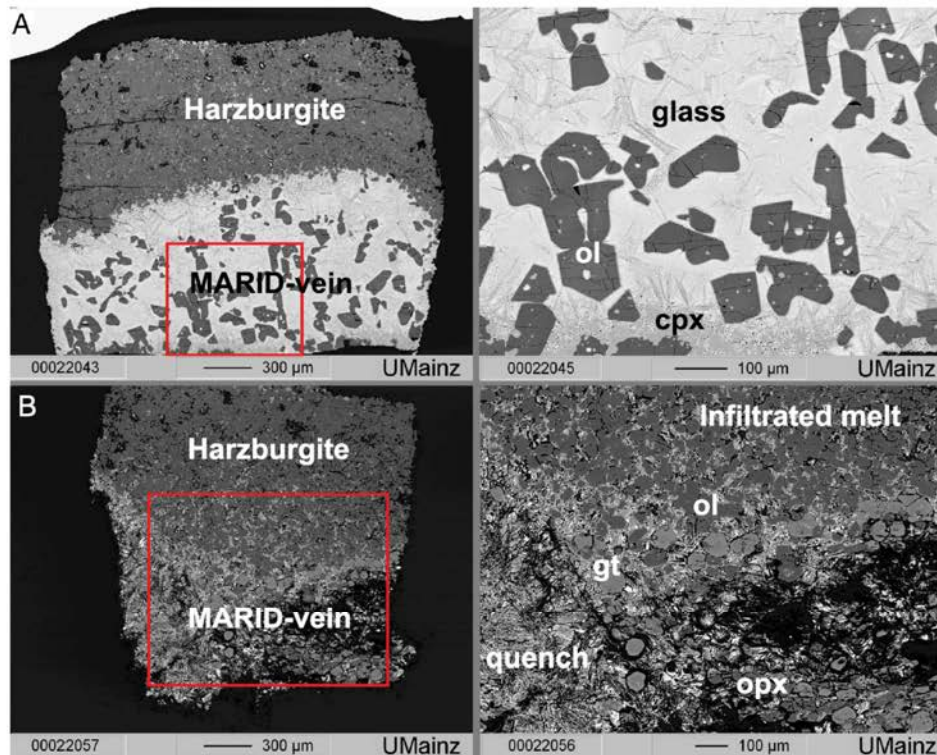


Fig. 1. Composition (Backscattered electron – BSE) images of polished sectioned capsules showing typical textures of the experimental charges. Labels are laid on top of phases: ol – olivine, cpx – clinopyroxene, gt – garnet, glass – quenched melt, quench – quench phases of former melt. A) Experiment at 3 GPa/1325 °C. B) at 5 GPa/1400 °C.



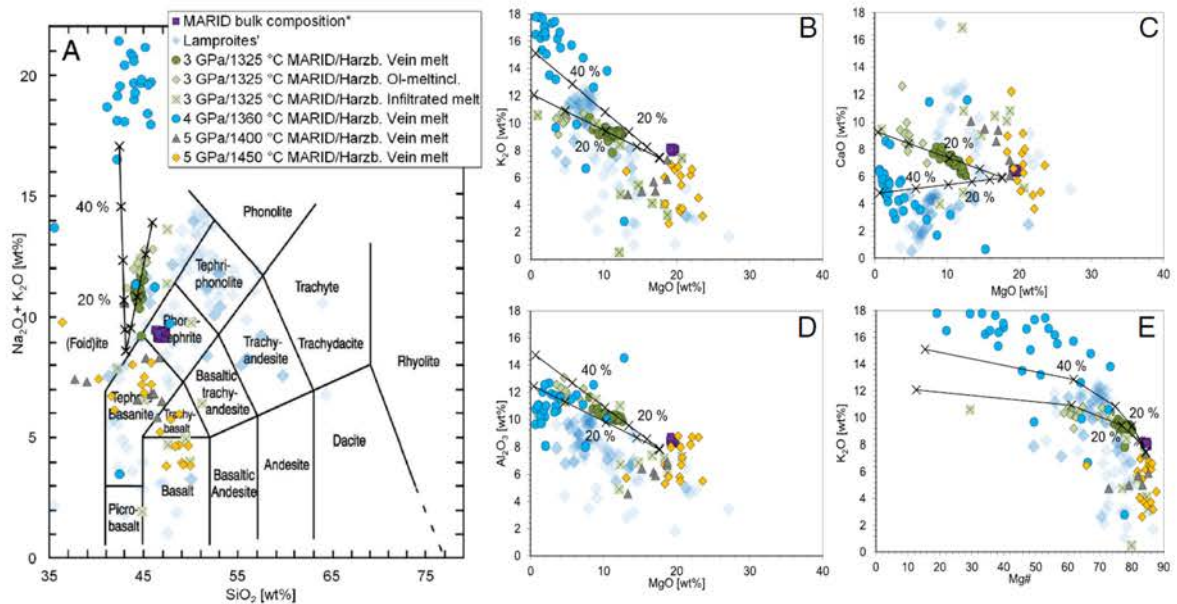


Fig. 2. Major element composition of melts in the experimental charges (3 GPa/1325 °C – green circles/diamonds/squares, 4 GPa/1360 °C – blue circles, 5 GPa/1400 °C – grey triangles, 5 GPa/1450 °C – orange diamonds) compared to lamproites (blue diamonds). A) shows total alkali versus silica, B)  $K_2O$  versus  $MgO$ , C)  $CaO$  versus  $MgO$ , D)  $Al_2O_3$  versus  $MgO$ , and E)  $K_2O$  versus  $Mg\#$ . Melts from the reaction of MARID with harzburgite comprise a wide range of composition depending on the PT-conditions of the experiment. Fractionation pathways with 10% increments were modelled for vein melts of the 3 and 4 GPa experiments starting from the bulk MARID composition normalized to 95 wt%, accounting for 5 wt% volatiles. Residues were calculated by mass balance and comprise 21 wt% olivine and 2 wt% clinopyroxene at 3 GPa as well as 28 wt% olivine and 19 wt% clinopyroxene at 4 GPa. The experimental melts broadly overlap with natural lamproite compositions except the experiment at 4 GPa/1360 °C (blue circles) which shows strong olivine and clinopyroxene fractionation. (Lamproite data: Fraser et al., 1985, Jaques et al., 1986, Murphy et al., 2002, Mirnejad and Bell, 2006 and Davies et al., 2006) (Bulk rock data: Förster et al., 2017).

accumulation of garnet and orthopyroxene, whereas the harzburgite contained phlogopite- and clinopyroxene-bearing veins (Fig. 1b). No glass could be observed in the MARID part of the capsule, but 2  $\mu m$  quench-lamellae of clinopyroxene and phlogopite were evident (Fig. 1). In the harzburgite part of the sample, an interconnected network of clinopyroxene and phlogopite covered the lower half.

### 3.2. Melt compositions in the reaction experiments

The 3 GPa experiment comprised three different melt-types (Table 2): (1) Incongruent melting of the MARID domain produced a melt by crystallizing clinopyroxene and olivine (Fig. 2). The glass reached < 45 wt%  $SiO_2$ , 12 wt%  $MgO$ ,  $Mg\#$  of 75–80, and 9 wt%  $K_2O$  (Fig. 2b, c, e). (2) Melt-inclusions in olivine comprised 11 wt%  $K_2O$ , 13 wt%  $Al_2O_3$ , 8 wt%  $CaO$ , < 5 wt%  $MgO$ , and  $Mg\#$  of 65–70 (Fig. 2d, e). (3) A heterogeneous melt with 45–50 wt%  $SiO_2$  (Table 2) that infiltrated the harzburgite with domains showing > 10 wt%  $CaO$  and < 6 wt%  $K_2O$ , as well as domains < 5 wt%  $CaO$  and > 8  $K_2O$  wt% (Fig. 2 b, d).

The glass of the 4 GPa experiment exhibited  $K_2O$  values between 14

and 18 wt% and total alkalis of about 20 wt% plotting mostly above the foidite-field in the total alkali versus silicate diagram (Fig. 2a). The high  $K_2O$ -content is accompanied by  $MgO$  values of 0.5–4.0 wt% and  $Mg\#$  of 30–60 at 43–45 wt%  $SiO_2$  and  $Al_2O_3$  of 10–13 wt% (Fig. 2b–e).

The melts in the 5 GPa experiments consisted of < 2  $\mu m$  phlogopite-clinopyroxene quench lamellae, but no glass was observed. EPMA analyses were therefore carried out with a large beam diameter of 20  $\mu m$  to average across the quench phases and to yield approximate melt compositions. The melts in these experiments comprise 5–7 wt%  $K_2O$  at > 15 wt%  $MgO$  and  $Mg\#$  of 75–85, while  $Al_2O_3$  and  $CaO$  reach 5–8 wt% and 5–10 wt%, respectively (Fig. 2b–e, Table 2).

### 3.3. Trace element composition of melts and olivine

Trace elements were measured for the 3 and 5 GPa experiments (Fig. 3, Supplementary Files 3–11). All melts are enriched in LILE, HFSE, and LREE (La to Eu), with a positive Ti anomaly (Fig. 3). For determining Ni partitioning between olivine and liquid ( $D_{Ni}$ ), the Ni-content of adjacent olivine-melt pairs of 8 experiments with natural MARID-composition at 1–5 GPa/1150–1450 °C and one synthetic

Table 2  
Representative analysis for bulk MARID composition and high-pressure experiment melts (oxides in wt%).

Melt	$SiO_2$	$TiO_2$	$Al_2O_3$	FeO	MnO	MgO	CaO	Na <sub>2</sub> O	$K_2O$	$P_2O_5$	$SO_3$	Total	$Mg\#$
MARID bulk composition*	47.37	3.17	8.56	6.29	0.05	19.41	6.47	1.30	8.03	0.11	0	101.0	85
Synthetic MARID melt 1 GPa/1300 °C	47.06	4.12	11.18	4.36	0.05	10.98	5.87	1.62	9.50	–	–	94.82	82
3 GPa 1325 °C MARID/Harz. Vein melt	44.65	3.62	10.11	5.39	0.14	12.08	6.53	1.61	9.16	0.10	0.14	93.91	80
3 GPa/1325 °C MARID/Harz. Infiltrated melt	43.01	4.63	10.18	6.23	0.09	15.82	2.63	0.72	10.12	0.08	0.13	94.37	82
3 GPa/1325 °C MARID/Harz. Ol-Melt inclusions	46.02	4.22	13.09	4.45	0.09	4.58	7.86	2.03	10.80	0.12	0.16	93.97	65
4 GPa/1360 °C MARID/Harz. Vein melt	44.72	4.97	11.89	5.10	0.09	2.82	2.91	2.38	17.33	0.24	0.18	93.05	50
5 GPa/1400 °C MARID/Harz. Vein melt	45.28	3.47	6.92	6.15	0.08	18.70	6.08	1.00	7.33	–	–	95.35	84
5 GPa/1450 °C MARID/Harz. Vein melt	43.84	2.56	7.99	7.13	0.06	19.21	6.61	1.08	6.97	0.54	0.08	96.16	83

\* refers to publication Förster et al. (2017).



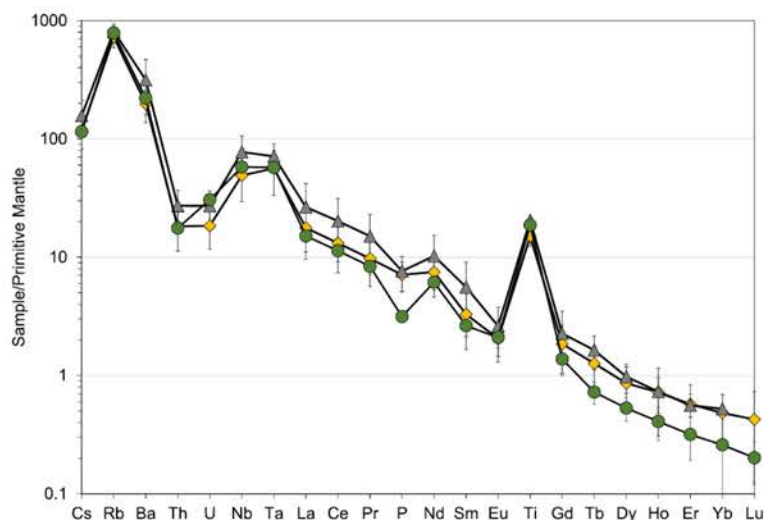


Fig. 3. Trace element composition of melts 3 GPa/1325 °C – green circles, 5 GPa/1400 °C – grey triangles, 5 GPa/1450 °C – orange diamonds) normalized to primitive mantle composition. All experimental charges show a steep trace element pattern containing positive Rb and Ti anomalies due to the high content of phlogopite in the MARID starting material.

MARID composition at 1 GPa/1300 °C yielded 37–2550  $\mu\text{g g}^{-1}$  for olivine and 4.4–127  $\mu\text{g g}^{-1}$  for adjacent glass (Table 3).

### 3.4. Composition of the mineral phases

All experimental melts were found to have crystallized mineral phases that were either not present in the starting material (olivine, orthopyroxene, and pyrope-rich garnet) or that had a distinctly different major and trace element composition (clinopyroxene and phlogopite).

Major elements in olivines were analysed from the experiments at 3 and 5 GPa. The experiments contain two sources for olivine, the harzburgite and the MARID vein. The 3 GPa experiment shows groups from both sources: The first group consists of olivine crystallized after the incongruent breakdown of phlogopite in the MARID part and shows Fo contents of 92 and [NiO] of 0.1–0.2 wt% (Table 4). The reaction olivine in the infiltrated harzburgitic part of the charge contains 0.25–0.35 wt % NiO at similar Fo contents of approximately 92 (Table 4). The 5 GPa experiments contain reaction olivine that must have settled from the harzburgite, since the MARID vein crystallized orthopyroxene instead of olivine. This reaction olivine shows [NiO] of 0.05 wt% at Fo contents of 92, and [MgO] of 51–52 wt% (Table 4).

Clinopyroxene separate into two groups based on their  $\text{Cr}_2\text{O}_3$  content (Table 4). The harzburgite contains clinopyroxene with a  $\text{Cr}_2\text{O}_3$ -rich composition (1.2–2.3 wt%), while the MARID vein part comprises those of  $\text{Cr}_2\text{O}_3$ -poor compositions (< 0.8 wt%) (Table 4). Both compositions are abundant in the experiment at 3 GPa, whereby the  $\text{Cr}_2\text{O}_3$ -poor clinopyroxenes are found in the cumulate part (Fig. 1a). This clinopyroxene is higher in MgO (20 wt%),  $\text{Al}_2\text{O}_3$  (2–3 wt%), and lower in CaO (15–17 wt%) and  $\text{Na}_2\text{O}$  (< 1 wt%) compared to the diopside of the MARID starting material, which presents an MgO content of approximately 15 wt% and [CaO] of approximately 20 wt% (Table 4). The reaction clinopyroxene in the harzburgite is similar to the diopside in the harzburgite starting material, however, it shows lower contents for  $\text{Cr}_2\text{O}_3$  (1.2–2.3 wt%). The 5 GPa experiment only contains reaction clinopyroxene with high contents of  $\text{Cr}_2\text{O}_3$  (1.0–1.6 wt%) and  $\text{Al}_2\text{O}_3$  (2.2–4.0 wt%).

Phlogopite is abundant in all experiments. It shows a gradual increase in  $\text{TiO}_2$  (2–8 wt%) and decrease in  $\text{SiO}_2$  (43–35 wt%) as well as  $\text{Al}_2\text{O}_3$  (10–4 wt%), with rising pressure and temperature (Fig. 4a, b). Remarkably, all Ti-rich and Al-poor phlogopite is higher in FeO (15–20 wt%) compared to the phlogopite in the MARID starting material (6–7 wt% FeO) (Table 4).

Table 3  
Ni-contents of melt and olivine and  $D_{\text{Ni}}$  of experimental charges.

Experiment	Average Ni contents [ $\mu\text{g g}^{-1}$ ]		$D_{\text{Ni}}$
	Olivine	Glass	
1 GPa/1225 °C MARID*	1104	37.5	29.5
1 GPa/1300 °C Synthetic MARID	989	68.3	14.5
1 GPa/1225 °C MARID/Harz. experiment*	848	44.9	18.9
2 GPa/1150 °C MARID/Harz. experiment*	255	102	25.0
2 GPa/1250 °C MARID/Harz. experiment*	141	81.8	17.2
2 GPa/1300 °C MARID/Harz. experiment*	177	14.8	11.9
3 GPa/1325 °C MARID/Harz. experiment	1962	127	15.4
5 GPa/1400 °C MARID/Harz. experiment	103	11.4	9.1
5 GPa/1450 °C MARID/Harz. experiment	36.7	4.4	8.4

\*Data from Förster et al. (2017)

## 4. Discussion

### 4.1. Constraints on the formation of cratonic ultrapotassic magmas

Our experimental charges contain melts of contrasting composition, which are the consequence of an intended disequilibrium between the two parts of the layered sample. The MARID-part in the 3 GPa experiment melted incongruently and comprises a melt with high  $\text{K}_2\text{O}$  and moderate MgO contents with values of 9 and 12 wt%, respectively (Fig. 2b). Fractionation curves, calculated from mass balance calculations (Supplementary 2), show that the melt evolved from the bulk MARID composition by fractionating 21 wt% olivine and 2 wt% clinopyroxene. Small amounts of melt penetrated the harzburgitic part of the sample charge and reacted upon infiltration (Fig. 1a). This infiltrated melt shows a higher variability of  $\text{K}_2\text{O}$  compared to the vein melt due to the small size of individual melt pockets and is generally lower in  $\text{Al}_2\text{O}_3$  (Fig. 1d). The vein melt in the 4 GPa experiment is similar to the vein melt in the 3 GPa experiment, but is of a more evolved composition (Fig. 2a–e). The melt of the 4 GPa experiments shows fractionation of 28 wt% olivine and 19 wt% clinopyroxene as evident from mass balance (Supplementary 2). Melts in the 5 GPa experiments

Table 4

Representative analyses for silicate phases in the experiments (oxides in wt%).

Olivine	SiO <sub>2</sub>	TiO <sub>2</sub>	Al <sub>2</sub> O <sub>3</sub>	FeO	MnO	MgO	CaO	Cr <sub>2</sub> O <sub>3</sub>	NiO	P <sub>2</sub> O <sub>5</sub>	SO <sub>3</sub>	Total	Mg#
Synthetic Harzburgite-olivine*	40.33	0	0.06	8.81	0.15	50.72	0.18	0.13	0.46	–	–	100.84	91
3 GPa/1325 °C Vein olivine	41.85	0.16	0.04	7.50	0.07	50.67	0.16	0.15	0.20	–	–	100.73	92
3 GPa/1325 °C Reaction olivine	41.75	0.03	0.04	7.53	0.08	50.76	0.15	0.18	0.32	–	–	100.83	92
5 GPa/1400 °C Reaction olivine	40.93	0.04	0.07	7.83	0.12	51.22	0.13	0.09	0.05	–	–	100.54	92
Phlogopite	SiO <sub>2</sub>	TiO <sub>2</sub>	Al <sub>2</sub> O <sub>3</sub>	FeO	MnO	MgO	CaO	Na <sub>2</sub> O	K <sub>2</sub> O	Cr <sub>2</sub> O <sub>3</sub>	NiO	Total	Mg#
MARID phlogopite*	42.07	2.58	9.59	6.58	0.06	22.05	0	0.15	10.01	0.29	–	93.89	86
3 GPa/1325 °C Reaction phlogopite	42.30	4.98	11.24	5.17	0.04	20.59	0.16	0.11	10.11	–	–	95.51	88
5 GPa/1400 °C Vein phlogopite	41.35	3.78	11.42	7.46	0.06	19.59	0.15	0.20	10.40	–	–	95.25	82
5 GPa/1400 °C Vein Fe-phlogopite	38.26	6.84	6.05	20.59	0.20	6.41	1.41	0.86	9.11	–	–	90.76	36
5 GPa/1450 °C Vein phlogopite	41.31	3.39	10.87	5.03	0.05	22.35	1.27	0.19	9.65	–	–	94.72	89
5 GPa/1450 °C Vein Fe-phlogopite	42.03	6.14	4.44	17.00	0.11	11.20	0.46	0.19	9.65	–	–	91.78	54
Clinopyroxene	SiO <sub>2</sub>	TiO <sub>2</sub>	Al <sub>2</sub> O <sub>3</sub>	FeO	MnO	MgO	CaO	Na <sub>2</sub> O	K <sub>2</sub> O	Cr <sub>2</sub> O <sub>3</sub>	NiO	Total	Mg#
MARID clinopyroxene*	55.31	0.10	0.65	5.38	0.18	15.88	20.49	1.40	0.02	0.48	–	99.89	75
Synthetic Harzburgite-clinopyroxene*	55.71	0.02	1.23	3.45	0.12	19.75	16.35	1.46	0.02	2.24	0.09	100.44	91
3 GPa/1325 °C Vein-clinopyroxene	54.79	0.40	2.07	3.35	0.04	21.01	16.08	0.77	0.08	0.60	0.02	99.21	92
3 GPa/1325 °C Reaction-clinopyroxene	55.14	0.21	1.70	3.64	0.13	21.49	14.65	0.95	0.06	2.06	0.06	100.09	91
5 GPa/1400 °C Reaction-clinopyroxene	54.99	0.22	2.47	3.50	0.07	22.10	13.64	1.18	0.14	1.36	0	99.66	92
Orthopyroxene	SiO <sub>2</sub>	TiO <sub>2</sub>	Al <sub>2</sub> O <sub>3</sub>	FeO	MnO	MgO	CaO	Na <sub>2</sub> O	K <sub>2</sub> O	Cr <sub>2</sub> O <sub>3</sub>	NiO	Total	Mg#
Synthetic Harzburgite-opx*	58.58	0.01	0.49	3.12	0.12	36.68	1.18	0.01	0.01	0.16	0.14	100.51	95
3 GPa/1325 °C Reaction-orthopyroxene	58.16	0.03	0.28	3.03	0.14	36.33	1.75	0.16	0.02	0.23	0.12	100.25	96
5 GPa/1400 °C Reaction-orthopyroxene	56.35	0.15	1.97	4.39	0.09	34.21	1.74	0.21	0.03	0.35	0.05	99.54	93
Garnet	SiO <sub>2</sub>	TiO <sub>2</sub>	Al <sub>2</sub> O <sub>3</sub>	FeO	MnO	MgO	CaO	Na <sub>2</sub> O	K <sub>2</sub> O	Cr <sub>2</sub> O <sub>3</sub>	NiO	Total	Mg#
5 GPa/1400 °C Vein-garnet	42.53	0.68	20.86	5.11	0.14	22.87	4.83	0.03	0.02	2.78	0	99.85	89

are lower in K<sub>2</sub>O (3–6 wt%) since higher temperatures led to intense harzburgite melting and consequently decreasing K, Al, and Ca, and increased Mg# in the melt (Fig. 2, Table 2). Their quench textures are likely a result of the Mg-rich melt composition that provides all constituents for the rapid growth of phlogopite and clinopyroxene.

Melt compositions of the reaction experiments from 3 to 5 GPa are similar to anorogenic lamproites (Fig. 2). Anorogenic lamproites are primitive, ultrapotassic, mantle-derived lavas that are common to cratons and stabilized terranes. Their petrogenesis is highly complex since their mantle source is enriched in high LILE and REE, while simultaneously depleted in CaO, Al<sub>2</sub>O<sub>3</sub> (Mitchell and Bergman, 1991). The composition of anorogenic lamproites comprises K<sub>2</sub>O > 8 wt% and K<sub>2</sub>O/Na<sub>2</sub>O > 2 at MgO of 10 to 20–25 wt% (olivine-lamproites) and SiO<sub>2</sub> of generally < 50 wt% (Fraser et al., 1985; Jaques et al., 1986; Murphy et al., 2002; Mirnejad and Bell, 2006; Davies et al., 2006). Lower contents of SiO<sub>2</sub> (41–45 wt% in primary melts) and higher contents of MgO separate them from orogenic lamproites that show overall lower MgO (< 10 wt%) and higher contents of SiO<sub>2</sub>, ranging from 46 to 60 wt% (Förster et al., 2017 and references therein). Lamproites are also very low in Na<sub>2</sub>O, CaO and Al<sub>2</sub>O<sub>3</sub>, which favours a depleted, harzburgitic source over a lherzolitic one (Mitchell and Bergman, 1991 and references therein). Nevertheless, high K-contents in lamproites demands enrichment in phlogopite of this source.

When compared with bulk rock analyses of lamproites (Fraser et al., 1985; Jaques et al., 1986; Murphy et al., 2002; Mirnejad and Bell, 2006; Davies et al., 2006), vein melts in the 3 GPa experiment plot near the anorogenic lamproite composition in Fig. 2. However, at similar MgO

contents, they reach about 2 wt% higher Al<sub>2</sub>O<sub>3</sub> contents. The infiltrated melts at 3 GPa, in turn, are lower in Al<sub>2</sub>O<sub>3</sub> and CaO due to their reaction with the harzburgite (Table 2) and thus resemble anorogenic lamproites more closely. Their lower contents of K<sub>2</sub>O and Al<sub>2</sub>O<sub>3</sub> can be explained by crystallization of phlogopite. These phlogopites comprise higher Al<sub>2</sub>O<sub>3</sub>-contents (12 wt%) compared to MARID phlogopites (10 wt%, Fig. 4b) and lie within the range of compositions observed in lamproites (Fig. 4a, b).

Crystallization of garnet and orthopyroxene (Fig. 1b) at 5 GPa/1400 °C led to lower Al and Si compared to the experiment at 1450 °C (Table 2). The overall major element chemistry of the infiltrated melts plot at the MgO-rich end of the lamproite array (Fig. 2), and thus, is comparable to olivine lamproites. The experimental melts are low in SiO<sub>2</sub> (< 45 wt%) due to the crystallization of clinopyroxene in addition to olivine. This complements the findings of (Förster et al., 2017) where experimental conditions of 1–2 GPa resulted in melts high in SiO<sub>2</sub> (up to 60 wt%). At low pressures, only olivine fractionates, which leads to a strong SiO<sub>2</sub> increase of the reaction melts, and thus, silica-rich orogenic lamproites (Prelević et al., 2008).

#### 4.2. Ni-partitioning in olivine and ultrapotassic melts

The reaction experiments of MARID and depleted peridotite comprised D<sub>Ni</sub> of 8.4–29.5 at 6–12 wt% Na<sub>2</sub>O + K<sub>2</sub>O. We propose that this “wide” range in total alkali content can be used to probe the influence of Na and K variations on D<sub>Ni</sub>. Experimental durations of 24–48 h ensured Ni to equilibrate between olivine and liquid. Additionally, one



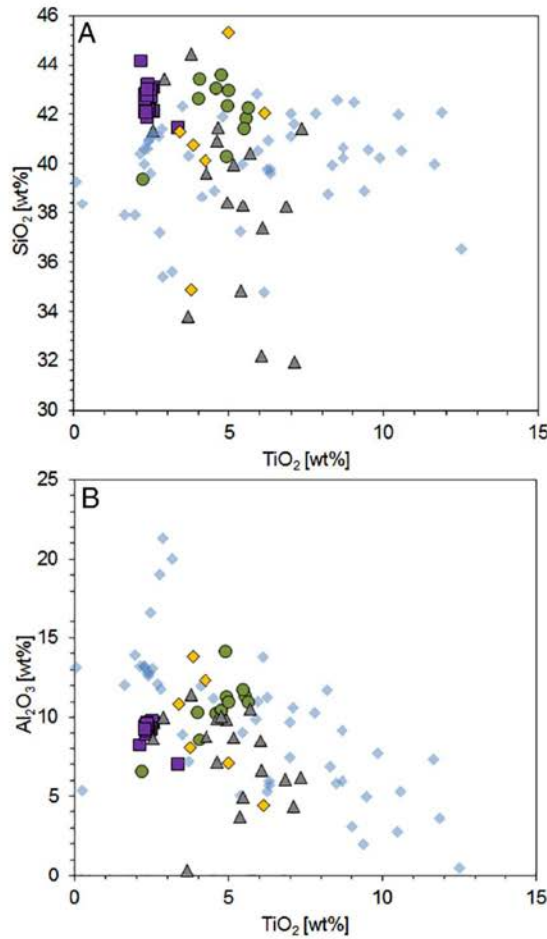


Fig. 4. Major element composition of phlogopites from start materials (MARID phlogopites – purple squares) and experiments (3 GPa/1325 °C – green circles, 5 GPa/1400 °C – grey triangles, 5 GPa/1450 °C – orange diamonds) compared to lamproites phlogopites (blue diamonds). A)  $\text{SiO}_2$  versus  $\text{TiO}_2$ , B)  $\text{Al}_2\text{O}_3$  versus  $\text{TiO}_2$ . \* (MARID phlogopite data: Förster et al., 2017) (Lamproite phlogopite: Carmichael, 1967; Barton and van Bergen, 1981; Jaques et al., 1986 and Hwang et al., 1994).

Table 5

Correlation coefficients of various combinations of constituents versus  $D_{\text{Ni}}$  and T.

Combination of constituents:	Coefficient of determination, $R^2$ :
$D_{\text{Ni}}$ versus $\frac{(\text{Na}_2\text{O} + \text{K}_2\text{O}) \cdot (\text{SiO}_2 + \text{TiO}_2) \cdot \text{Al}_2\text{O}_3}{(\text{MgO} + \text{FeO}) \cdot \text{CaO}}$	0.94
T versus $\frac{(\text{Na}_2\text{O} + \text{K}_2\text{O}) \cdot (\text{SiO}_2 + \text{TiO}_2) \cdot \text{Al}_2\text{O}_3}{(\text{MgO} + \text{FeO}) \cdot \text{CaO}}$	0.84
$D_{\text{Ni}}$ versus $\text{Na}_2\text{O} + \text{K}_2\text{O}$	0.83
$D_{\text{Ni}}$ versus T	0.83
$D_{\text{Ni}}$ versus FeO	0.82
$D_{\text{Ni}}$ versus P	0.73
$D_{\text{Ni}}$ versus $\text{K}_2\text{O}$	0.70
$D_{\text{Ni}}$ versus MgO	0.57
$D_{\text{Ni}}$ versus CaO	0.53
$D_{\text{Ni}}$ versus $\text{Al}_2\text{O}_3$	0.29
$D_{\text{Ni}}$ versus $\text{Na}_2\text{O}$	0.28
$D_{\text{Ni}}$ versus $\text{TiO}_2$	0.18
$D_{\text{Ni}}$ versus $\text{SiO}_2$	0.10

inverse experiment was conducted consisting of synthetic MARID melt in an inner capsule made of San Carlos olivine with  $D_{\text{Ni}}$  of 14.5 at 11 wt %  $\text{Na}_2\text{O} + \text{K}_2\text{O}$  (Supplementary 12). The observed range in total alkali-content underlines the earlier findings of Foley et al. (2013), who demonstrated that alkaline melts show  $D_{\text{Ni}}$  (olivine/melt) twice as high compared to basaltic compositions. A plot of  $D_{\text{Ni}}$  versus  $\text{K}_2\text{O}$  and total alkalis of the melts from the experimental charges shows positive exponential correlations ( $R^2 = 0.70$  for  $\text{K}_2\text{O}$  and  $R^2 = 0.83$  for  $\text{Na}_2\text{O} + \text{K}_2\text{O}$ ) (Fig. 5). The well-known exponential correlation of  $D_{\text{Ni}}$  versus MgO achieves an  $R^2$  of only 0.57 in our experiments (Supplementary 13), whereas low alkaline compositions with similar contents of MgO achieve a high  $R^2$  of 0.9 (Wang and Gaetani, 2008; Li and Ripley, 2010). This means that the influences of MgO and total alkalis in the partitioning between Ni and the alkaline melt are superimposed. Accordingly, the coefficient of determination ( $R^2$ ) is highest for  $D_{\text{Ni}}$  versus a constituent that dominates the partitioning process for each melt composition (Table 5).

The dependence of  $D_{\text{Ni}}$  on the total alkali content suggests that the change in melt structure affects the solubility of Ni. This structural change also affects the melt-viscosity, since Na and K are large cations, and thus, strong modifiers of the melts' silicate network. The melts' viscosity therefore may be indicative for structural changes of the melts' network. Giordano et al. (2008) presented an empirical melt-viscosity model that is based on an optimized version of the equation of Fulcher (1925). It can predict the viscosity of silicate melts based on the melts' composition and temperature:

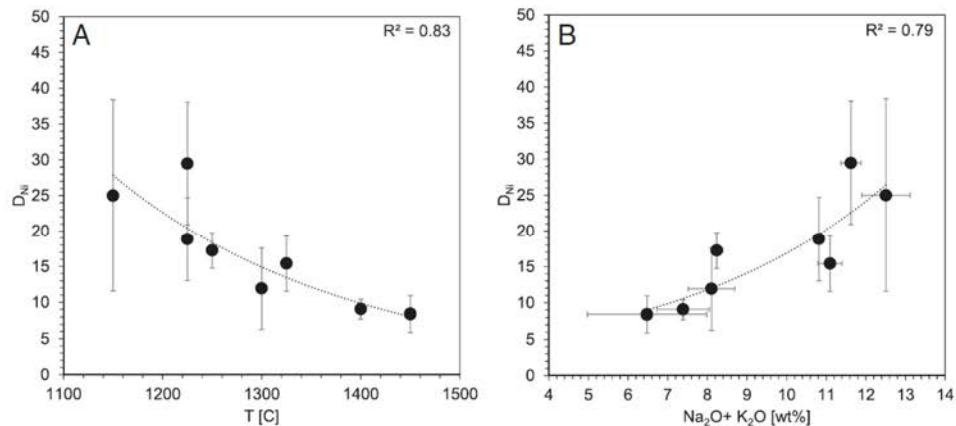


Fig. 5. Ni-partitioning of melt/olivine ( $D_{\text{Ni}}$ ) of experiments from this study (1325–1450 °C) and data from Förster et al. (2017) for experiments from 1150 to 1300 °C. A) shows  $D_{\text{Ni}}$  versus temperature, B)  $D_{\text{Ni}}$  versus total alkalis.

$$\log \eta = A + \frac{B}{T[K] - C}$$

Parameter A is defined by the viscosity of a silicate melt at infinite temperature and independent of the composition. B and C are compositional parameters that account for the influence of silicate network formers (e.g. Si, Fe) and network modifiers (Ca, Mg, Na, K, Al). Aluminium is known to act as a network former when present as  $\text{Al}^{[4]}$ , however, high temperature, as present in mantle-derived melts, increases the abundance of  $\text{Al}^{[5]}$ , which reduces melt viscosity (Le Losq et al., 2014). Since this study is confined to primitive mantle derived melts, Al is treated as network modifier, while it likely could be a transient species, aiding in melt-network formation at temperatures close to 1000 °C. Volatiles act as network modifiers, and strongly influence the parameter C and  $\log \eta$  in the melt-viscosity model, while parameter B is less influenced (Giordano et al., 2008). Since our experimental melts contain volatiles, they were included as difference of EPMA totals from 100 wt%, while the literature data sets resemble dry melts with totals close to 100 wt%.

We applied this model to melts from experimental charges of this study and literature datasets (Supplementary 14), which resulted in a positive exponential correlation of  $D_{\text{Ni}}$  versus melt viscosity (Fig. 6a). This correlation is strongly influenced by temperature in two ways: First, low temperature leads to increased cohesive forces between molecules, and therefore, viscosity increase. Second, fractionation results in loss of the melt modifiers Ca and Mg, which relatively increases the abundance of the network former Si. Nevertheless, fractionation also increases the concentration of the network modifiers Na, K, and volatiles, which delays increase in viscosity (Giordano et al., 2008).

Melts rich in Na, K, and Al are vertically offset towards higher  $D_{\text{Ni}}$ , when compared to basaltic compositions at similar temperature and viscosity (Fig. 6a). This finding is enhanced in a plot of  $D_{\text{Ni}}$  versus the compositional parameter B, since it excludes the effect of temperature and volatiles on the viscosity (Fig. 6b). However, Na, K, and Al-rich melts are also Si-rich, indicating that melt polymerization is crucial for the partitioning process. At similar temperature, eclogite melts (Wang and Gaetani, 2008) show higher  $D_{\text{Ni}}$  (12–23) when compared to basaltic melts of the same study (7–12), since the latter reach ~10 wt% higher contents of  $\text{SiO}_2$ . Eclogite melts have similar  $\text{SiO}_2$  contents as andesites (Luhr and Carmichael, 1985), which explains their similar range in melt viscosity (Fig. 6a). However, the andesites achieve twice as high  $D_{\text{Ni}}$  values as the eclogite melts (20–47 versus 12–23). We assume this difference to arise from their ~150 °C lower temperature and significantly higher fraction of  $\text{Al}_2\text{O}_3$  (16.3 versus 13.4 wt%). At low temperatures of ~1000 °C, as achieved by the andesites, Al increases melt viscosity (Le Losq et al., 2014). This implies, that the andesites might have a higher degree of melt polymerization than the eclogite melts. Therefore, we conclude that high fractions of Na, K, and Al are characteristic for high-grade polymerized melts and, therefore, imply also high  $D_{\text{Ni}}$ .

We interpret the Ni-partitioning between olivine and liquid to be dominated by the melt polymerization. Their influence on  $D_{\text{Ni}}$  is stronger than the temperature-influence, since highest  $D_{\text{Ni}}$  are not achieved by the coolest melts, but those with greatest polymerization as evident by high contents of Na, K, and Al (Supplementary 15). Nevertheless, since Matzen et al. (2013, 2017) reported significant influence of temperature on the partitioning process, the combination of  $D_{\text{Ni}}$  and change of melt composition should result in a sensitive geothermometer (4.3).

#### 4.3. Ni-partitioning in olivine/liquid as a geothermometer

To investigate the correlation of  $D_{\text{Ni}}$  (olivine/melt) versus all major constituents, their oxide-wt% were combined in groups of similar charges and ionic-radii ratios and coordination environments. Furthermore, oxides that correlate with  $D_{\text{Ni}}$  positively ( $\text{Na}_2\text{O}$ ,  $\text{K}_2\text{O}$ ,

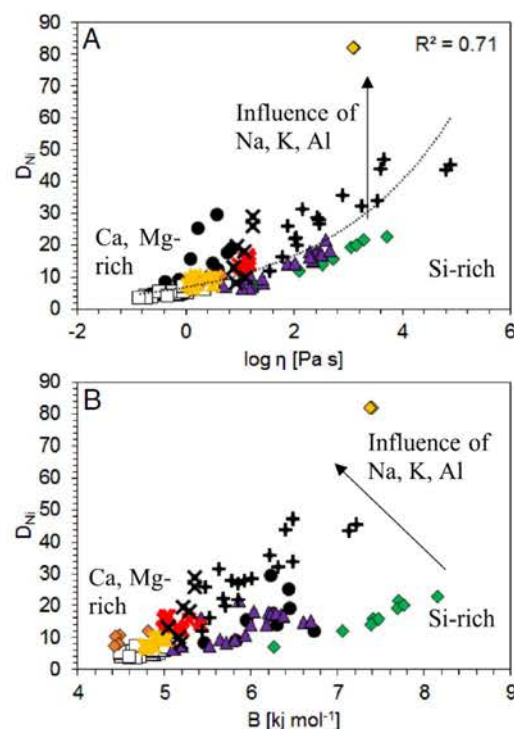


Fig. 6.  $D_{\text{Ni}}$  of olivine/melt versus melt-viscosity calculated with model from Giordano et al. (2008) applied to ultrapotassic melts from this study (black circles) and literature data: red crosses – East Pacific Rise/MORB (Allan et al., 1989); black pluses – Mexico/calc-alkaline basaltic andesite (Luhr and Carmichael, 1985); black crosses – basaltic-melt (Ford et al., 1983); purple triangles – alkaline-basaltic melt (Snyder and Carmichael, 1992); yellow diamond – Gaussberg/leucitite (Foley and Jenner, 2004); orange diamonds – basaltic, and green diamonds – eclogite melt (Wang and Gaetani, 2008); yellow crosses – Fe-rich basaltic melt (Filiberto et al., 2009); white and grey squares – basaltic melt (Matzen et al., 2013, 2017).  $D_{\text{Ni}}$  shows a positive exponential correlation with the melts viscosity ( $\log \eta$ ). Alkali-rich melt compositions are vertically offset (arrow), showing that the melt modifier Na and K strongly influence the partitioning process. B) shows  $D_{\text{Ni}}$  of olivine/melt versus the compositional value B of the melt-viscosity model. Primitive, magnesian melts plot at low  $D_{\text{Ni}}$  olivine/melt and comprise low B-values due to high contents of the network modifier-cations Ca, Mg, and Fe. With increase of B, the  $D_{\text{Ni}}$  of olivine/melt branches into two pathways depending on the content of the volatiles (and network modifiers) Na and K over the network formers Al and Si.

$\text{SiO}_2$ ,  $\text{TiO}_2$ ,  $\text{Al}_2\text{O}_3$ ) were positioned at the numerator, while those groups that correlate negatively ( $\text{MgO}$ ,  $\text{FeO}$ ,  $\text{CaO}$ ), were positioned at the denominator, resulting in [I] (Fig. 7) with  $R^2$  of 0.94:

$$\frac{[\text{liq}(\text{Na}_2\text{O} + \text{K}_2\text{O})] \cdot [\text{liq}(\text{SiO}_2 + \text{TiO}_2)] \cdot [\text{liq}(\text{Al}_2\text{O}_3)]}{[\text{liq}(\text{MgO} + \text{FeO})] \cdot [\text{liq}(\text{CaO})]} \quad (1)$$

We applied this term to datasets of contrasting compositions ranging from basaltic-, Fe-rich basaltic, and alkaline-, to eclogite melts (Ford et al., 1983; Snyder and Carmichael, 1992; Wang and Gaetani, 2008; Filiberto et al., 2009; Matzen et al., 2013, 2017). All datasets show positive exponential fits with  $D_{\text{Ni}}$  (Fig. 7). The  $D_{\text{Ni}}$  of ~80 found in a leucitite from Antarctica (Foley and Jenner, 2004) is close to the extrapolation of the exponential curve fit of our dataset, showing that ultrapotassic melts can reach exceptionally high  $D_{\text{Ni}}$  values.

The relationship of melt composition and nickel partitioning between olivine and liquid is established here as a new geothermometer. The temperature-dependent variation of the melt compositions were used previously to calibrate geothermometers based on glass composition (Helz and Thornber, 1987; Thornber et al., 2003; Putirka, 2008) and olivine/liquid Ni partitioning (Häkli and Wright, 1967; Arndt et al.,



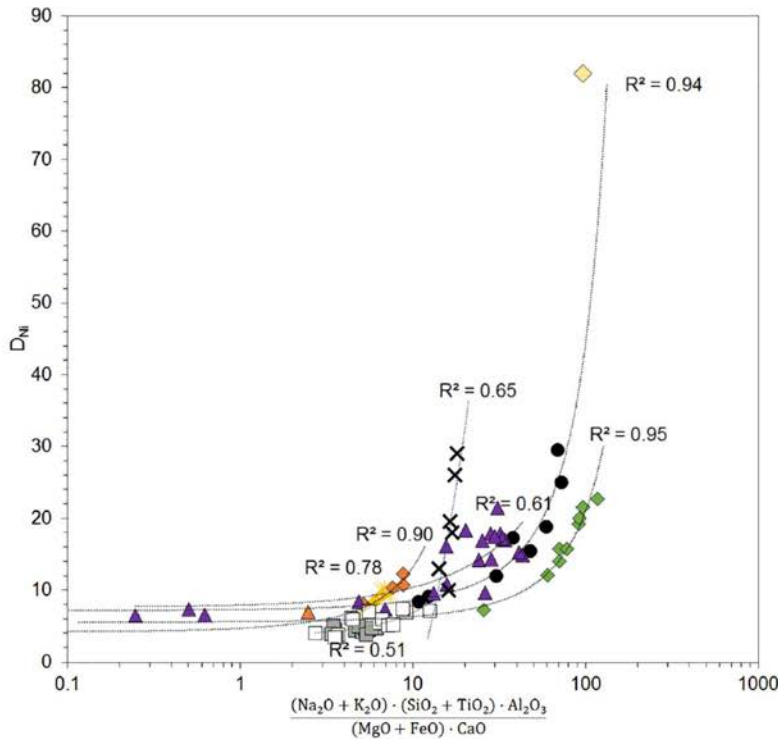


Fig. 7.  $D_{Ni}$  dependencies of our melts (black circles) and test datasets (symbols are the same as in Fig. 6). The large yellow diamond is the Gaussberg datapoint from Foley and Jenner (2004), a leucitite from Antarctica with total alkalis of ~14 wt% which is not included into any regression. It closely plots to the exponential fit of our dataset and shows that ultrapotassic compositions are able to reach exceptionally high  $D_{Ni}$  for olivine/melt.

1977). The new thermometer is derived from [I], whereby CaO is replaced by  $TiO_2$  [II]. The replacement of CaO was necessary since it shows opposed sloping correlations with  $D_{Ni}$  upon test data sets (Supplementary 16). The differences in sloping of CaO versus  $D_{Ni}$  lead to the spread of the literature datasets along the X-axis when [I] is plotted versus  $D_{Ni}$  (Fig. 7). This difference in correlation is only present for CaO and is connected to fractionation: simple olivine fractionation leads to an increase with  $D_{Ni}$ , whereas fractionation of olivine + clinopyroxene (+ plagioclase) removes CaO and leads to a decrease with  $D_{Ni}$ . However, datasets plot in the same range when CaO is replaced by  $TiO_2$ . Rearrangement of the term moves  $TiO_2$  as a denominator to  $SiO_2$ . This term then shows a similar correlation of all test data sets versus  $D_{Ni}$ :

$$\frac{[liq(Na_2O + K_2O)] \cdot \left[ liq \left( 1 + \frac{SiO_2}{TiO_2} \right) \right] \cdot [liq(Al_2O_3)]}{[liq(MgO + FeO)]} \quad (2)$$

For temperature calibration,  $D_{Ni}$  was added to the term and plotted against the experimental run temperature. This yielded a logarithmic dependency, which results in [III]:

$$T(^{\circ}C) = -88.14 \cdot \ln \left( \frac{[liq(Na_2O + K_2O)] \cdot \left[ liq \left( 1 + \frac{SiO_2}{TiO_2} \right) \right] \cdot [liq(Al_2O_3)]}{[liq(MgO + FeO)]} \cdot D_{Ni} \right) + 1906.2 \quad (3)$$

This thermometer is closely aligned to the bisectrix of a 1:1 fit between measured and calculated temperature and shows an  $R^2$  of 0.87 for the calibration dataset of our study (Supplementary 17). It is applicable to temperature ranges of 1000–1600 °C for natural melt

compositions over the range of olivine crystallization (Fig. 8a). The calculated temperatures agree well with the measured temperatures of the test datasets. Average temperature deviations between calculated and measured values range from 17 to 33 °C, compared to 10–87 °C for thermometers that solely use Ni partitioning (Hart and Davis, 1978), as well as 29–67 °C and 38–122 °C for thermometers using glass composition only (Helz and Thornber, 1987; Thornber et al., 2003; Putirka, 2008). While Matzen et al. (2013, 2017) reports an influence of pressure on  $D_{Ni}$  between 2 and 3 GPa, our thermometer reproduces temperatures independent of the experimental pressures (0.0001–5 GPa), suggesting that any influence is a secondary effect of changing melt compositions.

Some data points from Snyder and Carmichael (1992) and Matzen et al. (2013, 2017) show overestimations of > 100 °C for calculated temperatures of experiments conducted at 0.1 MPa (Fig. 8a, Supplementary 17). However, the authors report loss of Na, K, and Fe in these experiments, which likely explains the overestimation of the calculated temperatures as the composition of the liquid changed. Similar experiments, conducted at 0.1 MPa pressure (Wang and Gaetani, 2008), report no element loss and do indeed yield correctly reproducible temperatures.

Recently, Pu et al. (2017) provided a new Ni-partitioning thermometer that calculates temperature based on  $D_{Ni}$  and the molar abundances of major and minor constituents (FeO, MnO, MgO, CaO, CoO, NiO,  $TiO_2$ ,  $Al_2O_3$ ) in melt and olivine and is calibrated on 123 different 1-atm pressure experiments. This thermometer reproduces melt temperatures of experiments at ambient pressures well, however, melt temperatures of high-pressure experiments are underestimated by > 50 °C (Supplementary 18).

Nickel partitioning between olivine and melt and the change of melt composition complement each other well, since both monitor the temperature of the host magma. We encourage researchers to examine this thermometer in further studies to unravel the exact connection between  $D_{Ni}$  and melt composition.

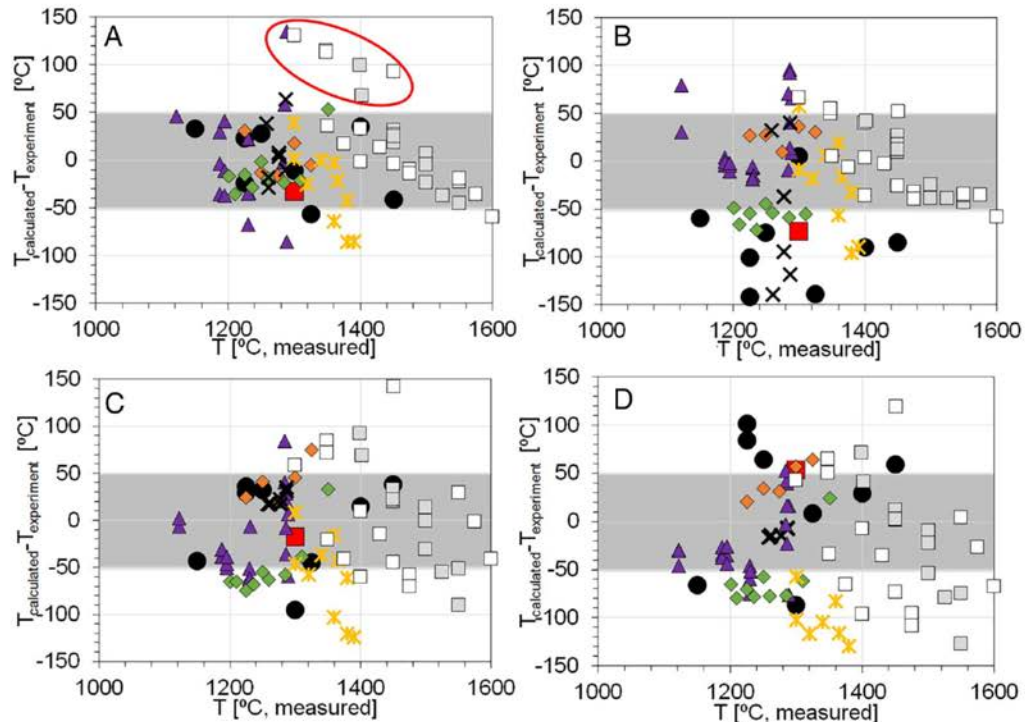


Fig. 8. Glass-based geothermometers showing deviations of calculated- from measured temperatures of ultrapotassic melts from our study (black circles and red square) and literature data: the symbols are the same as in Fig. 6. Grey inlay corresponds to a deviation of  $\pm 50$  °C from the measured temperature. Encircled data points are not included in deviations since they are derived from experiments with significant loss of alkalis and iron. A) shows our new thermometer, comprising average deviations of the test data sets ranging from  $\pm 17$ – $33$  °C. B) is a pure Ni-partitioning based geothermometer from Hart and Davis (1978), which gives deviations from measured values ranging from  $\pm 10$ – $87$  °C. C) and D) are thermometers from Putirka (2008), based on the glass composition with average deviations of  $\pm 29$ – $67$  °C and  $\pm 38$ – $122$  °C, respectively.

#### 4.4. Geothermometry on natural glass-olivine pairs

Figs. 8 and 9 give an application of our thermometer with calculated temperatures versus  $D_{Ni}$  to datasets of various composition ranging from calc-alkaline to ultrapotassic to MORB to OIB (Hawaii) compositions. Our aim here is to test if the thermometer is applicable to natural

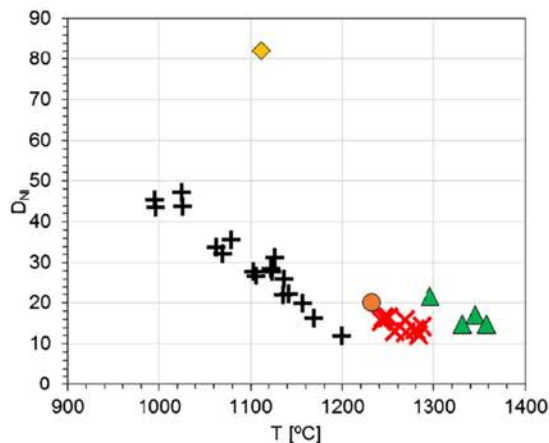


Fig. 9. Application of the thermometer to olivine-glass pairs from lavas of different geologic settings: orange diamond – Gaussberg(Antarctica)/leucite (Foley and Jenner, 2004), black pluses – Mexico/calc-alkaline basaltic-andesite (Luhr and Carmichael, 1985), red crosses – East Pacific Rise/MORB (Allan et al., 1989), orange circle – Gakkel-Ridge/MORB (Mühe et al., 1997), green triangles – Hawaii/olivine-tholeiite (Leeman and Scheidegger, 1977).

olivine/liquid pairs.

The reproducibility of temperatures from melts in high- and ambient pressure experiments (Fig. 8) suggests considerable agreement with our calculations for the majority of the melt compositions. Calculated temperatures (996–1199 °C) for calc-alkaline basalts and andesites from Mexico (Luhr and Carmichael, 1985) agree well with calculated temperatures (1020–1177 °C) from Pu et al. (2017). However, the calculated temperature for MORB compositions ( $\sim 1265$  °C) from the East Pacific Rise (Allan et al., 1989) exceeds that calculated by Pu et al. (2017) ( $\sim 1177$  °C). Nevertheless, the average for East Pacific Rise-MORB and the temperature of 1232 °C calculated for Gakkel-ridge MORB (Mühe et al., 1997) are within the range of temperatures (1218–1336 °C) that were experimentally determined for dry crystallizing MORB-magma (Almeev et al., 2007; Falloon et al., 2007a). An average calculated temperature of 1330 °C for glasses from Hawaii (Leeman and Scheidegger, 1977) is also close to the temperature (1365 °C) of Hawaiian primary magmas (Green et al., 2001), however, highest observed eruption temperatures of Hawaiian lavas are lower at about 1190 °C (Ault et al., 1961). Erupted Hawaiian glass also contains 0.93 wt%  $H_2O$  (Falloon et al., 2007b), which is 3-times higher than basalt intruding into the summit magma-chambers (0.32 wt%: Greenland et al., 1985). In addition, the Kilauea glass has a  $K_2O/H_2O$  ratio of 2, while olivine fractionation should increase both species on a 1:1 line (Falloon et al., 2007b). Small amounts of  $H_2O$  ( $< 1$  wt%) significantly depress the liquidus of basalt by  $< 100$  °C, an effect that is less-pronounced in silicic magmas (Médard and Grove, 2008). The enrichment of  $H_2O$  takes place at the roof of the magma-chamber prior to the eruption (Jaupart and Vergnolle, 1989), thereby reducing the liquidus of the basalt and enabling the overheated magma to cool to the measured eruption temperature.



Accordingly, this thermometer [III] calculates magma-chamber temperatures of the last equilibration of olivine with melt, rather than eruption temperatures that are lower due to cooling prior to eruption.

## 5. Conclusion

1. Incongruent melting of MARID glimmerites produces melts with  $K_2O$  of 8–10 wt%, 11–12 wt%  $Al_2O_3$  at  $MgO$  values of 10–15 wt% and  $SiO_2$  of < 45 wt%. Upon reaction with harzburgite, these melts crystallize clinopyroxene and phlogopite, lowering  $Al_2O_3$  and  $K_2O$  of the melt. Thus, incongruent and reaction melts of MARID glimmerites are capable of explaining the composition of various ultrapotassic magmas.
2. The ultrapotassic melt compositions show that olivine/liquid Ni-partitioning is dominated by the melts polymerization as expressed by high contents Na, K, and Al.
3. The change in melt composition and influence of temperature on nickel-partitioning complements to a new pressure-independent geothermometer. It yields precise melt temperatures in the range of 1000–1600 °C and is applicable for basaltic, alkaline, and ultrapotassic melts.
4. Geothermometry on natural olivine-liquid pairs shows that calculated temperatures likely represent magma-chamber temperatures of the last olivine-liquid equilibration. We estimate temperatures of 997–1199 °C for calc-alkaline magmas (Mexico), 1265 °C for MORB (East Pacific Rise), and 1330 °C for Hawaiian magma (Kilauea).

## Acknowledgements

This work is part of the lead authors PhD thesis and is supported by an Australian Government International Postgraduate Research Scholarship (IPRS). This project was also financed by the “Internal University Research Funding” program of the Johannes-Gutenberg University, Mainz. DP was supported through the Deutsche Forschungsgemeinschaft (DFG) within the project PR 1072/9-1. Thomas Kautz and Fabian Schroeder-Frerkes of the Goethe University, Frankfurt are thanked for assistance with the Belt-apparatus. Jennifer Rowland is gratefully acknowledged for proof-reading the manuscript and language improvement. Ananya Mallik and Cliff Shaw are gratefully acknowledged for providing reviews that significantly improved this manuscript. This is contribution 1032 from the ARC Centre of Excellence for Core to Crust Fluid Systems (<http://www.ccfsc.mq.edu.au>) and 1191 in the GEMOC Key Centre (<http://www.gemoc.mq.edu.au>).

## Appendix A. Supplementary data

Supplementary data to this article can be found online at <https://doi.org/10.1016/j.chemgeo.2017.11.039>.

## References




- Allan, J.F., Batiza, R., Perfit, M.R., Fornari, D.J., Sack, R.O., 1989. Petrology of lavas from the Lamont seamount chain and adjacent East Pacific Rise, 10 N. *J. Petrol.* 30 (5), 1245–1298.
- Almeev, R.R., Holtz, F., Koepke, J., Parat, F., Botcharnikov, R.E., 2007. The effect of  $H_2O$  on olivine crystallization in MORB: experimental calibration at 200 MPa. *Am. Mineral.* 92 (4), 670–674.
- Arndt, N.T., Naldrett, A.J., Pyke, D.R., 1977. Komatiitic and iron-rich tholeiitic lavas of Munro Township, northeast Ontario. *J. Petrol.* 18 (2), 319–369.
- Ault, W.U., Eaton, J.P., Richter, D.H., 1961. Lava temperatures in the 1959 Kilauea eruption and cooling lake. *Geol. Soc. Am. Bull.* 72 (5), 791–794.
- Barton, M., van Bergen, M.J., 1981. Green clinopyroxenes and associated phases in a potassium-rich lava from the Leucite Hills, Wyoming. *Contrib. Mineral. Petrol.* 77 (2), 101–114.
- Beattie, P., 1994. Systematics and energetics of trace-element partitioning between olivine and silicate melts: implications for the nature of mineral/melt partitioning. *Chem. Geol.* 117 (1), 57–71.
- Carmichael, I.S., 1967. The mineralogy and petrology of the volcanic rocks from the Leucite Hills, Wyoming. *Contrib. Mineral. Petrol.* 15 (1), 24–66.
- Davies, G.R., Stolz, A.J., Mahotkin, I.L., Nowell, G.M., Pearson, D.G., 2006. Trace element and Sr–Pb–Nd–Hf isotope evidence for ancient, fluid-dominated enrichment of the source of Aldan Shield lamproites. *J. Petrol.* 47, 1119–1146.
- Dawson, J.B., Smith, J.V., 1977. The MARID (mica-amphibole-rutile-ilmenite-diopside) suite of xenoliths in kimberlite. *Geochim. Cosmochim. Acta* 41 (2), 309–323.
- Downes, H., Kostoula, T., Jones, A.P., Beard, A.D., Thirlwall, M.F., Bodinier, J.L., 2002. Geochemistry and Sr–Nd isotopic compositions of mantle xenoliths from the Monte Vulture carbonatite-melilitite volcano, central southern Italy. *Contrib. Mineral. Petrol.* 144, 78–92.
- Dunn, T., Sen, C., 1994. Mineral/matrix partition coefficients for orthopyroxene, plagioclase, and olivine in basaltic to andesitic systems: a combined analytical and experimental study. *Geochim. Cosmochim. Acta* 58 (2), 717–733.
- Edgar, A.D., Mitchell, R.H., 1997. Ultra high pressure-temperature melting experiments on an  $SiO_2$ -rich lamproite from Smoky Butte, Montana: derivation of siliceous lamproite magmas from enriched sources deep in the continental mantle. *J. Petrol.* 38 (4), 457–477.
- Erlank, A.J., Allsopp, H.L., Hawkesworth, C.J., Menzies, M.A., 1982. Chemical and isotopic characterization of upper mantle metasomatism in peridotite nodules from the Montfontein kimberlite. *Terra Cognita* 2 (3).
- Falloon, T.J., Danyushevsky, L.V., Ariskin, A., Green, D.H., Ford, C.E., 2007a. The application of olivine geothermometry to infer crystallization temperatures of parental liquids: implications for the temperature of MORB magmas. *Chem. Geol.* 241 (3), 207–233.
- Falloon, T.J., Green, D.H., Danyushevsky, L.V., 2007b. Crystallization temperatures of tholeiitic parental liquids: implications for the existence of thermally driven mantle plumes. *Geol. Soc. Am. Spec. Pap.* 430, 235–260.
- Filiberto, J., Jackson, C., Le, L., Treiman, A.H., 2009. Partitioning of Ni between olivine and an iron-rich basalt: experiments, partition models, and planetary implications. *Am. Mineral.* 94 (2–3), 256–261.
- Foley, S., 1992. Vein-plus-wall-rock melting mechanisms in the lithosphere and the origin of potassic alkaline magmas. *Lithos* 28 (3–6), 435–453.
- Foley, S.F., Jenner, G.A., 2004. Trace element partitioning in lamproitic magmas—the Gaussberg olivine leucite. *Lithos* 75 (1), 19–38.
- Foley, S., Peccerillo, A., 1992. Potassic and ultrapotassic magmas and their origin. *Lithos* 28 (3–6), 181–185.
- Foley, S.F., Jacob, D.E., O'Neill, H.S.C., 2011. Trace element variations in olivine phenocrysts from Ugandan potassic rocks as clues to the chemical characteristics of parental magmas. *Contrib. Mineral. Petrol.* 162 (1), 1–20.
- Foley, S.F., Link, K., Tiberindwa, J.V., Barfaijo, E., 2012. Patterns and origin of igneous activity around the Tanzanian craton. *J. Afr. Earth Sci.* 62 (1), 1–18.
- Foley, S.F., Prelevic, D., Rehfeldt, T., Jacob, D.E., 2013. Minor and trace elements in olivines as probes into early igneous and mantle melting processes. *Earth Planet. Sci. Lett.* 363, 181–191.
- Ford, C.E., Russell, D.G., Craven, J.A., Fisk, M.R., 1983. Olivine-liquid equilibria: temperature, pressure and composition dependence of the crystal/liquid cation partition coefficients for Mg, Fe<sup>2+</sup>, Ca and Mn. *J. Petrol.* 24 (3), 256–266.
- Förster, M.W., Prelevic, D., Schmucke, H.R., Buhre, S., Vetter, M., Mertz-Kraus, R., Foley, S.F., Jacob, D.E., 2017. Melting and dynamic metasomatism of mixed harzburgite + glimmerite mantle source: implications for the genesis of orogenic potassic magmas. *Chem. Geol.* 455, 182–191.
- Fraser, K., Hawkesworth, C., Erlank, A., Mitchell, R., Scott-Smith, B., 1985. Sr, Nd and Pb isotope and minor element geochemistry of lamproites and kimberlites. *Earth Planet. Sci. Lett.* 76, 57–70.
- Fritschle, T., Prelevic, D., Foley, S.F., Jacob, D.E., 2013. Petrological characterization of the mantle source of Mediterranean lamproites: indications from major and trace elements of phlogopite. *Chem. Geol.* 353, 267–279.
- Fulcher, G.S., 1925. Analysis of recent measurements of the viscosity of glasses. *J. Am. Ceram. Soc.* 8 (6), 339–355.
- Giordano, D., Russell, J.K., Dingwell, D.B., 2008. Viscosity of magmatic liquids: a model. *Earth Planet. Sci. Lett.* 271 (1), 123–134.
- Giuliani, A., Phillips, D., Woodhead, J.D., Kamenetsky, V.S., Fiorentini, M.L., Maas, R., Soltys, A., Armstrong, R.A., 2015. Did diamond-bearing orangeites originate from MARID-veined peridotites in the lithospheric mantle? *Nat. Commun.* 6 (6837), 1–10.
- Green, D.H., Falloon, T.J., 2005. Primary magmas at mid-ocean ridges, “hotspots” and other intraplate settings: Constraints on mantle potential temperature. *Geol. Soc. Am. Spec. Pap.* 388, 217–247.
- Green, D.H., Falloon, T.J., Eggins, S.M., Yaxley, G.M., 2001. Primary magmas and mantle temperatures. *Eur. J. Mineral.* 13 (3), 437–452.
- Green, D.H., Hiberson, W.O., Rosenthal, A., Kovács, I., Yaxley, G.M., Falloon, T.J., Brink, F., 2014. Experimental study of the influence of water on melting and phase assemblages in the upper mantle. *J. Petrol.* 55 (10), 207–209.
- Greenland, L.P., Rose, W.I., Stokes, J.B., 1985. An estimate of gas emissions and magmatic gas content from Kilauea volcano. *Geochim. Cosmochim. Acta* 49 (1), 125–129.
- Griffin, W.L., Powell, W.J., Pearson, N.J., O'Reilly, S.Y., 2008. Glitter: data reduction software for laser ablation ICP-MS. In: Sylvester, P. (Ed.), *Laser Ablation-ICP-MS in the Earth Sciences. Current Practices and Outstanding Issues*. Mineral. Assoc. Can. Short Course Series 40, pp. 308–311.
- Häklil, T.A., Wright, T.L., 1967. The fractionation of nickel between olivine and augite as a geothermometer. *Geochim. Cosmochim. Acta* 31 (5), 877–884.
- Hart, S.E., Brooks, C., 1974. Clinopyroxene-matrix partitioning of K, Rb, Cs, Sr and Ba. *Geochim. Cosmochim. Acta* 38 (12), 1799–1806.
- Hart, S.R., Davis, K.E., 1978. Nickel partitioning between olivine and silicate melt. *Earth Planet. Sci. Lett.* 40 (2), 203–219.
- Harte, B., 1987. Metasomatic events recorded in mantle xenoliths: an overview. *Mantle Xenoliths* 625–640.
- Helz, R.T., Thornber, C.R., 1987. Geothermometry of Kilauea Iki lava lake, Hawaii. *Bull.*



- Volcanol. 49 (5), 651–668.
- Hirschmann, M.M., Stolper, E.M., 1996. A possible role for garnet pyroxenite in the origin of the “garnet signature” in MORB. *Contrib. Mineral. Petrol.* 124 (2), 185–208.
- Hwang, P., Taylor, W.R., Rocky, N.M.S., Ramsay, R.R., 1994. Mineralogy, geochemistry and petrogenesis of the Metters Bore No. 1 lamproite pipe, Calwinyardah Field, West Kimberley Province, Western Australia. *Mineral. Petrol.* 51 (2–4), 195–226.
- Jaques, A.L., Green, D.H., 1980. Anhydrous melting of peridotite at 0–15 kb pressure and the genesis of tholeiitic basalts. *Contrib. Mineral. Petrol.* 73 (3), 287–310.
- Jaques, A.L., Lewis, J.D., Smith, B.D., 1986. The Kimberlites and Lamproites of Western Australia. *Geol. Surv. W. Aust. Dep. Mines Bull.* 132.
- Jaupart, C., Vergnolle, S., 1989. The generation and collapse of a foam layer at the roof of a basaltic magma chamber. *J. Fluid Mech.* 203, 347–380.
- Jochum, K.P., Nohl, U., Herwig, K., Lammel, E., Stoll, B., Hofmann, A.W., 2005. GeoReM: a new geochemical database for reference materials and isotopic standards. *Geostand. Geoanal. Res.* 29 (3), 333–338.
- Jochum, K.P., Weis, U., Stoll, B., Kuzmin, D., Yang, Q., Raczek, I., Jacob, D.E., Stracke, A., Birbaum, K., Frick, D.A., Günther, D., Enzweiler, J., 2011. Determination of reference values for NIST SRM 610–617 glasses following ISO guidelines. *Geostand. Geoanal. Res.* 35 (4), 397–429.
- Kennedy, A.K., Lofgren, G.E., Wasserburg, G.J., 1993. An experimental study of trace element partitioning between olivine, orthopyroxene and melt in chondrules: equilibrium values and kinetic effects. *Earth Planet. Sci. Lett.* 115 (1), 177–195.
- Konzett, J., Sweeney, R.J., Thompson, A.B., Ulmer, P., 1997. Potassium amphibole stability in the upper mantle: an experimental study in a peralkaline KNCMASH system to 8.5 GPa. *J. Petrol.* 38 (5), 537–568.
- Lassiter, J.C., Hauri, E.H., Reiners, P.W., García, M.O., 2000. Generation of Hawaiian post-erosional lavas by melting of a mixed lherzolite/pyroxenite source. *Earth Planet. Sci. Lett.* 178 (3), 269–284.
- Le Losq, C., Neuville, D.R., Florian, P., Henderson, G.S., Massiot, D., 2014. The role of Al<sup>3+</sup> on rheology and structural changes in sodium silicate and aluminosilicate glasses and melts. *Geochim. Cosmochim. Acta* 126, 495–517.
- Leeman, W.P., Scheidegger, K.F., 1977. Olivine/liquid distribution coefficients and a test for crystal-liquid equilibrium. *Earth Planet. Sci. Lett.* 35 (2), 247–257.
- Li, C., Ripley, E.M., 2010. The relative effects of composition and temperature on olivine-liquid Ni partitioning: statistical deconvolution and implications for petrologic modeling. *Chem. Geol.* 275 (1), 99–104.
- Lühr, J.F., Carmichael, I.S., 1985. Jorullo Volcano, Michoacán, Mexico (1759–1774): the earliest stages of fractionation in calc-alkaline magmas. *Contrib. Mineral. Petrol.* 90 (2–3), 142–161.
- Mallik, A., Nelson, J., Dasgupta, R., 2015. Partial melting of fertile peridotite fluxed by hydrous rhyolitic melt at 2–3 GPa: implications for mantle wedge hybridization by sediment melt and generation of ultrapotassic magmas in convergent margins. *Contrib. Mineral. Petrol.* 169 (5), 1–24.
- Mallik, A., Dasgupta, R., Tsuno, K., Nelson, J., 2016. Effects of water, depth and temperature on partial melting of mantle-wedge fluxed by hydrous sediment-melt in subduction zones. *Geochim. Cosmochim. Acta* 195, 226–243.
- Matzen, A.K., Baker, M.B., Beckett, J.R., Stolper, E.M., 2013. The temperature and pressure dependence of nickel partitioning between olivine and silicate melt. *J. Petrol.* 54 (12), 2521–2545.
- Matzen, A.K., Baker, M.B., Beckett, J.R., Wood, B.J., Stolper, E.M., 2017. The effect of liquid composition on the partitioning of Ni between olivine and silicate melt. *Contrib. Mineral. Petrol.* 172 (1), 3.
- Médard, E., Grove, T.L., 2008. The effect of H<sub>2</sub>O on the olivine liquidus of basaltic melts: experiments and thermodynamic models. *Contrib. Mineral. Petrol.* 155 (4), 417–432.
- Meen, J., 1987. Mantle metasomatism and carbonatites: an experimental study of a complex relationship. *Geol. Soc. Am. Spec. Pap.* 215, 91–100.
- Mirnejad, H., Bell, K., 2006. Origin and source evolution of the Leucite Hills lamproites: evidence from Sr–Nd–Pb–O isotopic compositions. *J. Petrol.* 47, 2463–2489.
- Mitchell, R.H., Bergman, S.C., 1991. *Petrology of Lamproites*. Springer Science & Business Media.
- Mitchell, R.H., Edgar, A.D., 2002. Melting experiments on SiO<sub>2</sub>-rich lamproites to 6.4 GPa and their bearing on the sources of lamproite magmas. *Mineral. Petrol.* 74 (2–4), 115–128.
- Mühe, R., Bohrmann, H., Garbe-Schönberg, D., Kassens, H., 1997. E-MORB glasses from the Gakkel Ridge (Arctic Ocean) at 87°N: evidence for the Earth's most northerly volcanic activity. *Earth Planet. Sci. Lett.* 152 (1), 1–9.
- Murphy, D.T., Collerson, K.D., Kamber, B.S., 2002. Lamproites from Gaussberg, Antarctica: possible transition zone melts of Archaean subducted sediments. *J. Petrol.* 43, 981–1001.
- Novella, D., Frost, D.J., 2014. The composition of hydrous partial melts of garnet peridotite at 6 GPa: implications for the origin of group II kimberlites. *J. Petrol.* 55 (11), 2097–2124.
- Novella, D., Frost, D.J., Hauri, E.H., Bureau, H., Raepsaet, C., Roberge, M., 2014. The distribution of H<sub>2</sub>O between silicate melt and nominally anhydrous peridotite and the onset of hydrous melting in the deep upper mantle. *Earth Planet. Sci. Lett.* 400, 1–13.
- Prelević, D., Foley, S.F., 2007. Accretion of arc-oceanic lithospheric mantle in the Mediterranean: evidence from extremely high-Mg olivines and Cr-rich spinel inclusions in lamproites. *Earth Planet. Sci. Lett.* 256 (1), 120–135.
- Prelević, D., Foley, S.F., Romer, R., Conticelli, S., 2008. Mediterranean Tertiary lamproites derived from multiple source components in postcollisional geodynamics. *Geochim. Cosmochim. Acta* 72 (8), 2125–2156.
- Prelević, D., Akal, C., Romer, R.L., Foley, S.F., 2010. Lamproites as indicators of accretion and/or shallow subduction in the assembly of south-western Anatolia, Turkey. *Terra Nova* 22 (6), 443–452.
- Pu, X., Lange, R.A., Moore, G., 2017. A comparison of olivine-melt thermometers based on DMg and DNi: the effects of melt composition, temperature, and pressure with applications to MORBs and hydrous arc basalts. *Am. Mineral.* 102 (4), 750–765.
- Putirka, K.D., 2008. Thermometers and barometers for volcanic systems. *Rev. Mineral. Geochem.* 69 (1), 61–120.
- Rapp, R.P., Shimizu, N., Norman, M.D., Applegate, G.S., 1999. Reaction between slab-derived melts and peridotite in the mantle wedge: experimental constraints at 3.8 GPa. *Chem. Geol.* 160 (4), 335–356.
- Rosenthal, A., Foley, S.F., Pearson, D.G., Nowell, G.M., Tappe, S., 2009. Petrogenesis of strongly alkaline primitive volcanic rocks at the propagating tip of the western branch of the East African Rift. *Earth Planet. Sci. Lett.* 284 (1), 236–248.
- Sato, K., 1997. Melting experiments on a synthetic olivine lamproite composition up to 8 GPa: implication to its petrogenesis. *J. Geophys. Res.* Solid Earth 102 (B7), 14751–14764.
- Snyder, D.A., Carmichael, I.S., 1992. Olivine-liquid equilibria and the chemical activities of FeO, NiO, Fe<sub>2</sub>O<sub>3</sub>, and MgO in natural basic melts. *Geochim. Cosmochim. Acta* 56 (1), 303–318.
- Sobolev, A.V., Hofmann, A.W., Sobolev, S.V., Nikogosian, I.K., 2005. An olivine-free mantle source of Hawaiian shield basalts. *Nature* 434 (7033), 590–597.
- Sweeney, R.J., Thompson, A.B., Ulmer, P., 1993. Phase relations of a natural MARID composition and implications for MARID genesis, lithospheric melting and mantle metasomatism. *Contrib. Mineral. Petrol.* 115 (2), 225–241.
- Tappe, S., Foley, S.F., Kjarsgaard, B.A., Romer, R.L., Heaman, L.M., Stracke, A., Jenner, G.A., 2008. Between carbonatite and lamproite—diamondiferous Torngat ultramafic lamprophyres formed by carbonate-fluxed melting of cratonic MARID-type metasomes. *Geochim. Cosmochim. Acta* 72 (13), 3258–3286.
- Thorner, C.R., Heliker, C., Sherrod, D.R., Kauahikaua, J.P., Miklius, A., Okubo, P.G., Trusdell, F.A., Budahn, J.R., Ridley, W.I., Meeker, G.P., 2003. Kilauea east rift zone magmatism: an episode 54 perspective. *J. Petrol.* 44 (9), 1525–1559.
- Ulmer, P., 1989. The dependence of the Fe<sup>2+</sup>–Mg cation-partitioning between olivine and basaltic liquid on pressure, temperature and composition. *Contrib. Mineral. Petrol.* 101 (3), 261–273.
- Wang, Z., Gaetani, G.A., 2008. Partitioning of Ni between olivine and siliceous eclogite partial melt: experimental constraints on the mantle source of Hawaiian basalts. *Contrib. Mineral. Petrol.* 156 (5), 661–678.
- Wang, Y., Prelević, D., Buhre, S., Foley, S.F., 2017a. Constraints on the sources of post-collisional K-rich magmatism: the roles of continental clastic sediments and terrigenous blueschists. *Chem. Geol.* 455, 192–207.
- Wang, Y., Foley, S.F., Prelević, D., 2017b. Potassium-rich magmatism from a phlogopite-free source. *Geology* 45 (5), 467–470.
- Waters, F.G., 1987. A suggested origin of MARID xenoliths in kimberlites by high pressure crystallization of an ultrapotassic rock such as lamproite. *Contrib. Mineral. Petrol.* 95 (4), 523–533.
- Zhang, Y.L., Liu, C.Z., Ge, W.C., Wu, F.Y., Chu, Z.Y., 2011. Ancient sub-continental lithospheric mantle (SCLM) beneath the eastern part of the Central Asian Orogenic Belt (CAOB): implications for crust-mantle decoupling. *Lithos* 126, 233–247.

## Article

# Femtosecond Laser Ablation-ICP-Mass Spectrometry and CHNS Elemental Analyzer Reveal Trace Element Characteristics of Danburite from Mexico, Tanzania, and Vietnam

Le Thi-Thu Huong <sup>1,\*</sup> , Laura M. Otter <sup>2,3,\*</sup> , Michael W. Förster <sup>3</sup>,  
Christoph A. Hauzenberger <sup>1</sup>, Kurt Krenn <sup>1</sup>, Olivier Alard <sup>3,4</sup>, Dorothea S. Macholdt <sup>2</sup>,  
Ulrike Weis <sup>2</sup>, Brigitte Stoll <sup>2</sup> and Klaus Peter Jochum <sup>2</sup> 

<sup>1</sup> NAWI Graz Geocentre, University of Graz, 8010 Graz, Austria;

christoph.hauzenberger@uni-graz.at (C.A.H.); kurt.krenn@uni-graz.at (K.K.)

<sup>2</sup> Climate Geochemistry Department, Max Planck Institute for Chemistry, 55128 Mainz, Germany;  
d.macholdt@mpic.de (D.S.M.); ulrike.weis@mpic.de (U.W.); Brigitte.stoll@mpic.de (B.S.);  
k.jochum@mpic.de (K.P.J.)

<sup>3</sup> Department of Earth and Planetary Sciences, Macquarie University, Sydney NSW 2109, Australia;  
michael.forster@hdr.mq.edu.au (M.W.F.); olivier.alard@mq.edu.au (O.A.)

<sup>4</sup> Géosciences Montpellier, UMR 5243, CNRS & Université Montpellier, 34095 Montpellier, France

\* Correspondence: thi.le@uni-graz.at (L.T.-T.H.); laura.otter@hdr.mq.edu.au (L.M.O.)

Received: 7 May 2018; Accepted: 28 May 2018; Published: 29 May 2018



**Abstract:** Danburite is a calcium borosilicate that forms within the transition zones of metacarbonates and pegmatites as a late magmatic accessory mineral. We present here trace element contents obtained by femtosecond laser ablation-inductively coupled plasma (ICP)-mass spectrometry for danburite from Mexico, Tanzania, and Vietnam. The Tanzanian and Vietnamese samples show high concentrations of rare earth elements ( $\Sigma\text{REEs}$  1900  $\mu\text{g}\cdot\text{g}^{-1}$  and 1100  $\mu\text{g}\cdot\text{g}^{-1}$ , respectively), whereas Mexican samples are depleted in REEs ( $<1.1 \mu\text{g}\cdot\text{g}^{-1}$ ). Other traces include Al, Sr, and Be, with Al and Sr dominating in Mexican samples (325 and 1611  $\mu\text{g}\cdot\text{g}^{-1}$ , respectively). Volatile elements, analyzed using a CHNS elemental analyzer, reach  $<3000 \mu\text{g}\cdot\text{g}^{-1}$ . Sr and Al are incorporated following  $\text{Ca}^{2+} = \text{Sr}^{2+}$  and  $2 \text{B}^{3+} + 3 \text{O}^{2-} = \text{Al}^{3+} + 3 \text{OH}^- + \square$  (vacancy). REEs replace  $\text{Ca}^{2+}$  with a coupled substitution of  $\text{B}^{3+}$  by  $\text{Be}^{2+}$ . Cerium is assumed to be present as  $\text{Ce}^{4+}$  in Tanzanian samples based on the observed Be/REE molar ratio of 1.5:1 following  $2 \text{Ca}^{2+} + 3 \text{B}^{3+} = \text{Ce}^{4+} + \text{REE}^{3+} + 3 \text{Be}^{2+}$ . In Vietnamese samples, Ce is present as  $\text{Ce}^{3+}$  seen in a Be/REE molar ratio of 1:1, indicating a substitution of  $\text{Ca}^{2+} + \text{B}^{3+} = \text{REE}^{3+} + \text{Be}^{2+}$ . Our results imply that the trace elements of danburite reflect different involvement of metacarbonates and pegmatites among the different locations.

**Keywords:** danburite; trace elements; REE; femtosecond LA-ICP-MS; CHNS elemental analyzer; pegmatites; skarn

## 1. Introduction

Danburite crystallizes in the orthorhombic system and has the formula  $\text{CaB}_2\text{Si}_2\text{O}_8$ . Its structure consists of a tetrahedral framework with boron and silicon orderly distributed in different tetrahedral sites. The framework of corner-sharing  $\text{Si}_2\text{O}_7$  and  $\text{B}_2\text{O}_7$  groups are interconnected by Ca atoms [1,2]. According to previous studies [3,4], the structural unit of danburite contains two tetrahedrally coordinated cations (T1: B and T2: Si), one calcium, and five oxygen atoms, among which O1, O2, and O3 are bonded to both B and Si, while O4 and O5 are bridging oxygens of the  $\text{Si}_2\text{O}_7$  and  $\text{B}_2\text{O}_7$  groups, respectively.



Danburite is one of the few boron minerals that are valued as gemstones. After its discovery in Danbury, Connecticut, USA, colorless gem-quality danburite has been subsequently found in Japan, Mexico, Russia, Sri Lanka, and Switzerland [5]. Exceptionally rare is yellow danburite, which so far has been reportedly found only in Madagascar, Tanzania, Myanmar, and Vietnam [6,7]. The important geological environments that are known to have produced gem-quality danburite specimens include pegmatites and metacarbonates associated with hydrothermal activity [8–10].

Previous studies presenting danburite compositions were generally limited to its major element geochemistry (e.g., [11,12]) due to the lack of microanalytical reference materials for boron minerals. While Huong et al. [7] overcame this issue by applying femtosecond laser ablation-inductively coupled plasma-mass spectrometry (LA-ICP-MS), which allows virtually matrix-independent calibration, their study was confined to a regional scale. Here, we present state-of-the-art femtosecond LA-ICP-MS determination of major and trace element concentrations in danburite from three distinct worldwide distributed occurrences (Tanzania, Vietnam, and Mexico). The aims of this study are (1) to investigate the geochemical differences of danburites from different locations (Tanzania, Vietnam, and Mexico) and rock types (pegmatites and skarn), (2) to elucidate their potential for further provenance discrimination, and (3) to understand the incorporation of trace elements into the danburite structure.

## 2. Materials and Methods

### 2.1. Sample Material

For this study, we selected 6 danburite samples from 3 deposits in Mexico, Tanzania, and Vietnam (2 samples from each deposit), representing different geological environments. The Mexican danburites were collected from the polymetallic skarn deposit (sulfides of Ag, Pb, Cu, and Zn) in the Charcas mining district, San Luis Potosi. The area is characterized by marine siliciclastic and volcanoclastic rocks, with 2 domains (east and west) separated by a regional fault [9]. In the region of San Luis Potosi, numerous volcanic systems and igneous rocks are associated with different mineral deposits. The Charcas deposit has a large Ca–B metasomatic envelope composed of early datolite and later danburite. Other minerals associated with danburite include calcite, apophyllite, stilbite, chalcophyllite, sphalerite, and citrine. The samples appear as colorless, transparent, prismatic euhedral crystals and are up to 6 cm in length.

The Tanzanian danburite originates from the central zone of a pegmatite mostly as yellowish, fine-grained, massive, opaque aggregates, but occasionally also as larger single crystals with color and transparency. The mine is referred to by the locals as “Munaraima” and is situated in Eastern Tanzania, at the edge of the Uluguru Mountains [10] near the village of Kivuma. The region around Kivuma is dominated by a metasedimentary sequence including metapelites, gneisses, and spinel and ruby-bearing marbles, which underwent granulite facies metamorphism during the East African Orogen at ~640 Ma [13,14]. Tonalitic dikes and pegmatites, commonly found in this area, intruded the basement rocks during slow cooling of the whole area. The contact zone of marble and pegmatite is dominated by a mineral assemblage consisting of microcline (variety amazonite), blue quartz, kyanite, and dravite, while the core complex is mainly composed of massive quartz and schörl [10]. For this study, small, anhedral, transparent yellow danburite crystals ranging from 0.5 to 1 cm in size were selected.

The Vietnamese danburite samples (1–1.5 cm) appear as yellow, transparent, broken, and slightly rounded crystals and have been found in a placer deposit (Bai Cat) in the Luc Yen mining area, Yen Bai province, Northern Vietnam [7,15]. The geology of Luc Yen is dominated by metamorphic rocks, mainly granulitic gneisses, mica schists, and marbles, which are associated with the large-scale Ailao Shan–Red River shear zone. Locally, aplitic and pegmatitic dykes occur [16]. Danburite crystals are associated with ruby, sapphire, spinel, topaz, and tourmaline in the Bai Cat placer deposit, which is surrounded by marble units. While the primary formations of ruby, sapphire, and spinel in Luc Yen are associated with metamorphosed limestones, those of tourmaline and topaz originate from pegmatite



bodies. Besides tourmaline and topaz, these pegmatites contain orthoclase, smoky quartz, lepidolite, and beryl. Danburite crystals have not yet been discovered in situ, hence their genetic relationship with the Luc Yen pegmatites is not verified. However, fluid inclusion studies of Luc Yen danburites indicate a pegmatitic origin [15].

## 2.2. Analytical Methods

Chemical data for major elements were obtained by electron microprobe at the Institute of Geosciences, Johannes Gutenberg University Mainz, by laser ablation-inductively coupled plasma-mass spectrometry (LA-ICP-MS) at the Max Planck Institute for Chemistry, Mainz, and by CHNS Elemental Analyzer at Macquarie University.

Electron probe micro-analysis (EPMA) was performed at the University of Mainz with a JEOL JXA 8200 Superprobe instrument equipped with 5 wavelength-dispersive spectrometers, using 15 kV acceleration voltage and 12 nA filament current. Calcium and silicon were analyzed with wollastonite as a standard material.

LA-ICP-MS data for a total of 55 elements were obtained using an NWR Femto femtosecond laser operating at a wavelength of 200 nm in combination with a ThermoFisher Element2 single-collector sector-field ICP mass spectrometer (see Table 1). Pre-ablation cleaning was performed using a spot size of 65  $\mu\text{m}$ , 80  $\mu\text{m/s}$  scan speed, and 50 Hz pulse repetition rate at 100% energy output to remove any superficial surface residue. Thereafter, samples were ablated using line scans of 300  $\mu\text{m}$  length at a spot size of 55  $\mu\text{m}$  and a scan speed of 5  $\mu\text{m/s}$ . These parameters resulted in an energy density of ca. 0.51 J/cm<sup>2</sup> at the sample surface, and the pulse repetition rate was set to 50 Hz. Since there is no matrix-matched calibration material for Ca–B silicates available, we applied a laser device that produces pulses at 150 fs, enabling virtually matrix-independent calibration [17]. The glass microanalytical reference material NIST SRM 610 was used as calibration material in the evaluation process, where <sup>43</sup>Ca was used as internal standard. Reduction of data and elimination of obvious outliers were performed following a programmed routine in Microsoft Excel described in Jochum et al. [18].

All samples were additionally analyzed for their H, C, N, and S contents in a vario EL cube elemental analyzer (Elementar, Langenselbold, Germany). For analysis, 50 to 100 mg samples were packed in Sn-foils (no flux added) and were ignited in an oxygen–He gas atmosphere furnace at around 1150 °C. The produced gases were then trapped and released in a set of chromatographic columns for the sequential analysis of N (no trapping), then C, H, and S. Each sample was measured for 9 min, and released gases were sequentially analyzed with a thermal conductivity detector. Sample measurements were repeated 3 times for each sampling location, and all values were calibrated against the reference materials BAM-U110, JP-1, and CRPG BE-N (Table 2). Analytical uncertainties were evaluated from reference material values, which were found to lie within 16% and 25% for C and H of the data tabulated in the GeoReM database [19].

Table 1. Operating conditions of the femtosecond laser ablation-inductively coupled plasma-mass spectrometry (fs-LA-ICP-MS) system.

Operating Conditions of NWR Femto200 Laser System	
Wavelength $\lambda$ (nm)	200
Fluence (J·cm <sup>−2</sup> )	0.51
Pulse length (fs)	150
Pulse repetition rate (Hz)	50
Laser energy output (%)	100
Spot size ( $\mu\text{m}$ )	55
Line length ( $\mu\text{m}$ )	300
Scan speed ( $\mu\text{m} \cdot \text{s}^{-1}$ )	5
Warm-up time (s)	28
Dwell time (s)	60
Washout time (s)	30

Table 1. Cont.

Operating Conditions of the Element2 Mass Spectrometer	
RF power (W)	1055
Cooling gas (Ar) flow rate (L·min <sup>−1</sup> )	16
Auxiliary gas (Ar) flow rate (L·min <sup>−1</sup> )	1.19
Additional gas (He) flow rate (L·min <sup>−1</sup> )	0.7
Sample gas (Ar) flow rate (L·min <sup>−1</sup> )	0.7
Sample time (s)	0.002
Samples per peak	100
Mass window (%)	10
Time per pass (s)	2
Scan mode (Escan/Bscan)	both
Mass resolution	300

Table 2. Reference materials for CHNS analyzer.

BE-N Altered Basalts (SARM)	H TCD	C TCD	N TCD	S TCD	S IR
<i>n</i>	14	20	17	21	8
Average (μg·g <sup>−1</sup> )	2771 ± 534	2301 ± 147	197 ± 42	301 ± 37	298 ± 23
RSD %	19	6	21	12	8
BAM-U110					
<i>n</i>	13	18	18	17	—
Average (μg·g <sup>−1</sup> )	12,258 ± 1758	72,340 ± 2640	4237 ± 165	9114 ± 1082	—
RSD %	14	4	4	12	—
JP-1 Peridotite massif (JGS)					
<i>n</i>	4	12	14	14	14
Average (μg·g <sup>−1</sup> )	3195 ± 170	763 ± 82	91 ± 23	27 ± 14	26 ± 7
RSD %	5	11	26	51	27

*n* denotes the number of measurement performed; average refers to arithmetic means of the *n* values measured; RSD % is relative standard deviation expressed in %. “TCD” refers to the thermal conductivity detector and “IR” to the infrared detector devices.

### 3. Results

The chemical composition of the danburite samples from Mexico, Tanzania, and Vietnam are presented in Table 3. The major element mass fractions of B, Ca, and Si are close to the stoichiometric composition, i.e., 28.32 wt % B<sub>2</sub>O<sub>3</sub> (calculated from 87,890 ppm B obtained by ICP-MS), 22.81 wt % CaO, and 48.88 wt % SiO<sub>2</sub>, respectively.

The trace elements Li, Sc, Ga, Se, Rb, Zr, Nb, Ag, Cd, Sn, Cs, Hf, Ta, W, Ir, Pt, Au, Tl, Bi, and U have concentrations below the detection limit in all samples (see detection limits in footnote of Table 3). A C1-chondrite-normalized plot of rare earth element (REE) mass fractions (normalizing data from [20]) displays a strong enrichment of light rare earth elements (LREEs: La, Ce, Pr, Nd, Sm, Eu) compared to heavy rare earth elements (HREEs: Gd, Tb, Dy, Ho, Er, Tm, Yb, Lu) in danburite from Tanzania and Vietnam, while the samples from Mexico are mostly below detectability (Figure 1). Europium shows a negative anomaly of the same order for samples from Tanzania and Vietnam, while no other strong anomaly is observed (e.g., Ce). Total lanthanide content of Tanzanian samples is up to 1900 μg·g<sup>−1</sup>, hence the mass fractions of LREE exceed those of HREE by a 500-fold enrichment. The Vietnamese samples are different, with a total REE content of around 1000 μg·g<sup>−1</sup>, hence the mass fractions of LREE exceed those of HREE by a 200-fold enrichment. The Mexican danburites appear to be REE-poor, with total REE contents below 1 μg·g<sup>−1</sup> for La and Ce, while the remaining REEs from Nd to Lu are below the detection limits. Possible quadrivalent trace elements such as Ti, Hf, and Zr were also below the detection limits. Thorium and Pb show low mass fractions of 0.1 and 11 μg·g<sup>−1</sup> in the Mexican danburites, and 0.6 and 8 μg·g<sup>−1</sup> in the Vietnamese and Tanzanian danburites, respectively.



The trivalent element Al shows highly varying concentrations among the different deposits and is anti-correlated with  $\Sigma\text{REE}$ , thus also with Be (see Figure 2A,B), while no correlation was observed between Al and Sr (Figure 2C). The highest mass fractions of Al are found in the Mexican samples ( $325 \mu\text{g}\cdot\text{g}^{-1}$ ) and the lowest in the Tanzanian samples ( $84 \mu\text{g}\cdot\text{g}^{-1}$ ) (Table 3). Strontium is highest ( $1611 \mu\text{g}\cdot\text{g}^{-1}$ ) in the Mexican samples and lowest ( $66 \mu\text{g}\cdot\text{g}^{-1}$ ) in the Vietnamese samples (Figure 2D). Manganese yields up to  $18 \mu\text{g}\cdot\text{g}^{-1}$  in the Vietnamese danburites, while the Mexican and Tanzanian samples have Mn contents below the detection limits. In general, transition metals (e.g., Fe and Ni) have extremely low concentrations in all danburite samples. The three danburite origins can also be separated from each other using the mass fractions of Y (Figure 2E). Beryllium is found to be highest in the Tanzanian danburite (up to  $178 \mu\text{g}\cdot\text{g}^{-1}$ ) and lowest in the Mexican samples ( $3 \mu\text{g}\cdot\text{g}^{-1}$ ). In addition, low concentrations of less than 1, 9, and  $2 \mu\text{g}\cdot\text{g}^{-1}$  of the elements Ba, Mg, and Cu, respectively, are identified in all samples regardless of their origin. The positive correlation between Be and  $\Sigma\text{REE}$  is exceptionally strong for all three deposits (Figure 3A), and due to varying mass fractions of all shown elements, this plot enables excellent discrimination among the three deposits. Univalent elements such as Li, Na, and, K fall below the detection limits.

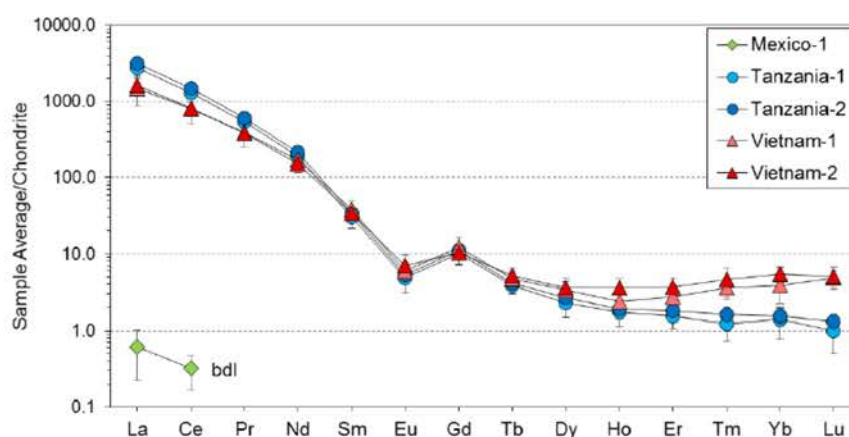


Figure 1. Rare earth element (REE) mass fractions in danburite from Mexico, Tanzania, and Vietnam. All values are presented as averages and normalized to C1-chondrite (data from [20]). Samples from Tanzania and Vietnam have a high abundance of REEs, especially LREEs, while samples from Mexico are largely devoid of these elements (bd, below detection limit, from Pr to Lu).

The contents of the light volatile elements H, C, N, and S are generally low for both unpowdered and powdered samples (see Table 4). Samples from both Tanzania and Mexico exhibit mass fractions of H, C, N, and S of  $<10$ ,  $<200$ ,  $<100$ , and  $<15 \mu\text{g}\cdot\text{g}^{-1}$ , respectively. The samples from Vietnam show significantly higher mass fractions for H, C, N, and S in unpowdered specimens, reaching values of up to 300, 5600, 1000, and  $15 \mu\text{g}\cdot\text{g}^{-1}$ , respectively. However, most elements are present in lower concentrations in the powdered sample set (H, C, and N of 40, 3000, and  $520 \mu\text{g}\cdot\text{g}^{-1}$ , respectively). Higher values for powdered samples from Mexico and Tanzania are likely attributed to the significantly increased surface-to-volume ratio facilitating higher adhesion of atmospheric gases. Significantly higher values for H and C in all Vietnamese samples agree well with a previous study by Huong et al. [15], who characterized a high abundance of primary  $\text{CO}_2$ -bearing fluid inclusions in these samples, which likely accounts for the elevated concentrations of both elements, while fluid inclusion is not present in the Mexican or Tanzanian specimens. High N mass fractions are in the expected range of metamorphosed sediments, which are involved in danburite formation and are known to contain  $\sim 200\text{--}3000 \mu\text{g}\cdot\text{g}^{-1}$  N for a typical metamorphic gradient of  $500\text{--}700^\circ\text{C}$  (e.g., [21]). Overall lower values of H, C, and N in the powdered Vietnamese sample set support the observation

that these elements are derived from fluid inclusions and were lost during crushing in the agate mortar. Nevertheless, powdered samples were still found to contain up to  $40 \mu\text{g}\cdot\text{g}^{-1}$  structurally bound H (equivalent to 0.036 wt %  $\text{H}_2\text{O}^+$ ), which is close to the value of 0.04 wt %  $\text{H}_2\text{O}^+$  determined by IR spectroscopy as published in [4].

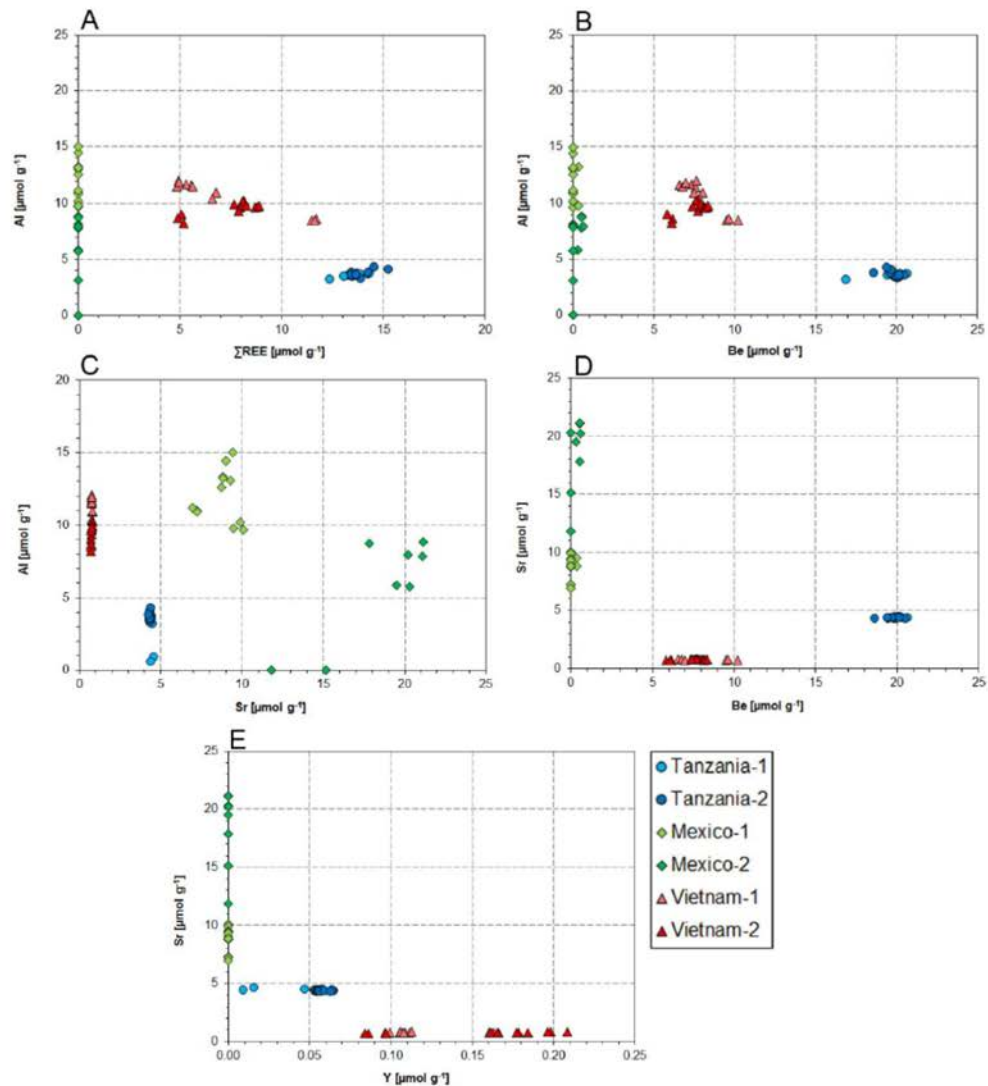


Figure 2. Molar abundance of Al versus (A)  $\Sigma\text{REE}$ , (B) Be, and (C) Sr, and Sr versus (D) Be and (E) Y. Aluminum is negatively correlated with (A) REEs, (B) Be, and (D) partly Sr, while Sr correlates negatively with (D) Be and (E) Y.

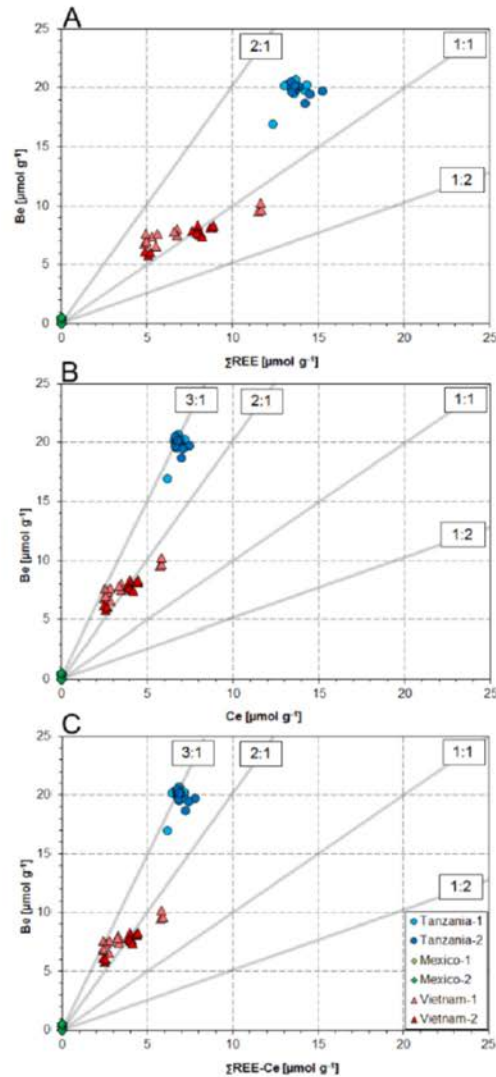


Figure 3. (A) Molar abundance of Be shows a linear correlation with  $\Sigma\text{REE}$  and illustrates that incorporation of REEs in the danburite structure is accompanied by Be. The Be/ $\Sigma\text{REE}$  ratio in Tanzanian samples is approximately 1.5:1, while it varies in Vietnamese samples from ca. 1:1 to ca. 1.5:1. Correlations between Be and  $\Sigma\text{REE}$  are ideally suited to distinguish danburite sampling locations. However, the simple substitution equation  $\text{Ca}^{2+} + \text{B}^{3+} = \text{REE}^{3+} + \text{Be}^{2+}$ , where the Be/ $\Sigma\text{REE}$  ratio is 1:1, is not sufficient to explain the varying ratios of Be and  $\Sigma\text{REE}$ . (B) Molar abundance of Be and Ce shows a linear correlation, implying that incorporation of Ce into the danburite structure is accompanied by Be. The Be/Ce ratio in Tanzanian samples is approx. 3:1, while in Vietnamese samples it varies from ca. 2:1 to ca. 3:1. The equation  $2\text{Ca}^{2+} + 3\text{B}^{3+} = \text{Ce}^{4+} + \text{REE}^{3+} + 3\text{Be}^{2+}$ , where the Be/Ce ratio is 3:1, explains the Tanzanian and most of the Vietnamese cases very well. Therefore, we argue here that Ce occurs not only as  $\text{Ce}^{3+}$ , but also as  $\text{Ce}^{4+}$  in Tanzanian and Vietnamese danburite and the substitution mechanism  $2\text{Ca}^{2+} + 3\text{B}^{3+} = \text{Ce}^{4+} + \text{REE}^{3+} + 3\text{Be}^{2+}$  takes place in these samples. (C) Be/( $\Sigma\text{REE} - \text{Ce}$ ) ratios show similar behavior to Be/Ce ratios. As the Be/( $\Sigma\text{REE} - \text{Ce}$ ) ratios vary from 2:1 to 3:1, both substitution mechanisms should take place:  $\text{Ca}^{2+} + \text{B}^{3+} = \text{REE}^{3+} + \text{Be}^{2+}$ ,  $2\text{Ca}^{2+} + 3\text{B}^{3+} = \text{Ce}^{4+} + \text{REE}^{3+} + 3\text{Be}^{2+}$ .



**Table 3.** Average chemical composition (in  $\mu\text{g}\cdot\text{g}^{-1}$  and  $\mu\text{mol}\cdot\text{g}^{-1}$ ) and relative standard deviation (RSD, %) obtained from danburite of three different occurrences. All concentrations were obtained by fs LA-ICP-MS ( $n = 12$  line scans), except CaO and  $\text{SiO}_2$ , which were evaluated with Electron Probe Microanalyzer (EPMA) (averaged from  $n = 20$  spot analyses per sample).

Element	Isotope Used	L.O.D.	Charcas, San Luis Potosi, Mexico						Morogoro, Tanzania						Luc Yen, Vietnam					
			Mex-1			Mex-2			Tanz-1			Tanz-2			Viet-1			Viet-2		
			O ( $\mu\text{g}\cdot\text{g}^{-1}$ )	RSD (%)	O ( $\mu\text{g}\cdot\text{g}^{-1}$ )	O ( $\mu\text{g}\cdot\text{g}^{-1}$ )	RSD (%)	O ( $\mu\text{g}\cdot\text{g}^{-1}$ )	O ( $\mu\text{mol}\cdot\text{g}^{-1}$ )	RSD (%)	O ( $\mu\text{g}\cdot\text{g}^{-1}$ )	O ( $\mu\text{mol}\cdot\text{g}^{-1}$ )	RSD (%)	O ( $\mu\text{g}\cdot\text{g}^{-1}$ )	O ( $\mu\text{mol}\cdot\text{g}^{-1}$ )	RSD (%)	O ( $\mu\text{g}\cdot\text{g}^{-1}$ )	O ( $\mu\text{mol}\cdot\text{g}^{-1}$ )	RSD (%)	O ( $\mu\text{mol}\cdot\text{g}^{-1}$ )
CaO*	-	-	22.47	0.04	0.49	22.43	0.71	22.63	0.04	0.60	22.48	0.04	0.57	22.32	0.03	0.51	22.40	0.03	0.37	
B	11	10	86218	7975	6.67	90471	4.05	86280	7981	1.56	87270	8072	2.69	85698	7927	3.13	89138	8245	3.19	
$\text{SiO}_2$ *	-	-	48.31	0.8	0.40	48.81	0.33	48.80	0.8	0.36	48.88	0.8	0.38	48.81	0.8	0.43	48.43	0.8	0.37	
La	139	0.01	0.15	0.0011	63.5	0.01	0.0001	675	4.9	35.3	807	5.8	4.7	368	2.7	42.3	400	2.9	22.0	
Ce	140	0.01	0.20	0.0014	48.1	0.05	0.0004	827	5.9	34.7	964	6.9	3.4	508	3.6	36.9	525	3.8	19.6	
Pr	141	0.03	<0.03	-	-	<0.03	-	51.4	0.37	35.1	59.5	0.42	4.0	37.4	0.27	35.3	36.5	0.26	17.5	
Nd	143	0.08	<0.08	-	-	<0.08	-	91.1	0.63	34.5	106	0.74	4.9	80.9	0.56	32.2	72.8	0.51	16.2	
Sm	147	0.05	<0.05	-	-	<0.05	-	4.65	0.03	28.7	5.68	0.04	9.6	5.94	0.04	27.1	5.23	0.03	18.7	
Eu	151	0.05	<0.05	-	-	<0.05	-	0.28	0.002	37.7	0.31	0.002	14.1	0.34	0.002	28.5	0.41	0.003	38.2	
Gd	157	0.04	<0.04	-	-	<0.04	-	2.05	0.013	28.1	2.38	0.015	10.9	2.46	0.016	37.1	2.13	0.014	28.3	
Tb	159	0.01	<0.01	-	-	<0.01	-	0.15	0.001	22.4	0.16	0.001	15.5	0.18	0.001	29.5	0.20	0.001	26.1	
Dy	163	0.05	<0.05	-	-	<0.05	-	0.58	0.004	35.7	0.68	0.004	7.80	0.85	0.005	30.5	0.92	0.006	33.7	
Ho	165	0.01	<0.01	-	-	<0.01	-	0.10	0.001	35.9	0.11	0.001	11.3	0.13	0.001	40.3	0.20	0.001	31.1	
Er	167	0.04	<0.04	-	-	<0.04	-	0.25	0.001	30.0	0.28	0.002	38.6	0.46	0.003	41.0	0.61	0.004	33.3	
Tm	169	0.02	<0.02	-	-	<0.02	-	0.03	0.0002	40.5	0.04	0.0002	49.3	0.09	0.0005	31.4	0.12	0.0007	40.1	
Yb	173	0.04	<0.04	-	-	<0.04	-	0.23	0.0013	44.4	0.26	0.0015	32.5	0.64	0.0037	42.1	0.90	0.0052	22.4	
Lu	175	0.02	<0.02	-	-	<0.02	-	0.02	0.0001	50.3	0.03	0.0002	43.5	0.12	0.0007	23.7	0.13	0.0007	32.2	
Al	27	10	325	120	14.9	171	40.5	84.3	3.1	36.2	101	3.7	7.58	288	10.7	12.8	257	9.5	6.41	
As	69	1	46.6	0.6	8.74	7.05	19.0	<1	0.01	56.5	<1	0.01	67.8	1.13	0.02	103	1.10	0.01	46.0	
Ba	135, 137	0.1	0.50	0.004	54.1	0.19	36.60	0.29	0.002	25.06	0.22	0.002	14.77	0.48	0.003	89.66	0.63	0.005	27.03	
Be	9	3	3.06	0.3	12.5	4.94	26.0	156	17.4	32.8	178	19.8	242	71.7	8.0	14.09	67.0	7.4	12.2	
Cr	53	5	<5	-	-	<5	-	<5	-	-	<5	-	-	6.44	0.12	43.8	<5	-	-	
Cu	65	1	1.56	0.02	65.3	<1	-	<1	-	-	<1	-	-	1.10	0.02	78.2	2.00	0.03	56.4	
Fe	57	20	<20	-	-	<20	-	<20	-	-	<20	-	-	<20	-	-	<20	-	-	
K	39	7	<7	-	-	<7	-	<7	-	-	<7	-	-	<7	-	-	<7	-	-	
Mg	25	9	<9	-	-	<9	-	<9	-	-	<9	-	-	<9	-	-	<9	-	-	
Mn	55	1	<1	-	-	<1	-	<1	-	-	<1	-	-	18.4	0.34	8.93	14.57	0.27	14.3	
Na	23	50	<50	-	-	<50	-	<50	-	-	<50	-	-	<50	-	-	<50	-	-	
Ni	62	18	<18	-	-	<18	-	<18	-	-	<18	-	-	<18	-	-	<18	-	-	
Pb	207, 208, 209	0.1	0.27	0.0013	49.2	0.23	0.0011	7.46	0.0360	33.8	8.05	0.0389	8.94	11.1	0.0534	5.05	10.6	0.0514	5.60	

Table 3. Cont.

Element	Isotope Used	Charcas, San Luis Potosi, Mexico						Morogoro, Tanzania						Luc Yen, Vietnam					
		Mex-1			Mex-2			Tanz-1			Tanz-2			Viet-1			Viet-2		
		O ( $\mu\text{g}\cdot\text{g}^{-1}$ )	RSD (%)	O ( $\mu\text{g}\cdot\text{g}^{-1}$ )	RSD (%)	O ( $\mu\text{g}\cdot\text{g}^{-1}$ )	RSD (%)	O ( $\mu\text{mol}\cdot\text{g}^{-1}$ )	RSD (%)	O ( $\mu\text{g}\cdot\text{g}^{-1}$ )	RSD (%)	O ( $\mu\text{g}\cdot\text{g}^{-1}$ )	RSD (%)	O ( $\mu\text{mol}\cdot\text{g}^{-1}$ )	RSD (%)	O ( $\mu\text{g}\cdot\text{g}^{-1}$ )	RSD (%)	O ( $\mu\text{mol}\cdot\text{g}^{-1}$ )	RSD (%)
Sb	<sup>121</sup> , <sup>123</sup>	13.0	0.1	81.9	35.8	0.3	75.6	<1	-	-	-	<1	-	-	-	<1	-	-	-
Sr	88	767	8.8	12.09	1611	14.8	40.6	387	4.4	1.44	4.4	381	4.4	1.02	66.5	66.1	0.8	5.08	5.08
Th	232	<0.01	-	-	<0.01	-	-	0.47	0.0020	41.3	8.45	0.66	0.0028	8.45	0.11	0.11	0.0005	44.6	44.6
Ti	49	<3	-	-	<3	-	-	<3	-	-	-	<3	-	-	<3	<3	-	-	-
V	51	0.5	0.01	36.54	0.98	0.02	19.1	0.84	0.02	10.8	11.3	0.83	0.02	11.3	0.73	0.95	0.02	22.5	22.5
Y	89	<0.1	-	-	<0.1	-	-	4.21	0.05	35.1	6.19	5.23	0.1	6.19	10.6	14.1	0.2	27.9	27.9
Zn	67	59.6	0.9	34.6	27.5	0.4	53.1	15.8	0.2	32.5	41.7	15.5	0.2	41.7	63.2	89.9	1.4	49.0	49.0

\* (wt %), excluded due to concentrations below limits of detection (L.O.D.) in  $\mu\text{g}\cdot\text{g}^{-1}$  in all samples: Li (<5), Sc (<1), Ga (<0.5), Se (<10), Rb (<0.5), Zr (<0.1), Nb (<0.01), Ag (<0.1), Cd (<1), Sn (<1), Cs (<0.1), Hf (<0.01), Ta (<0.01), W (<0.01), Ir (<0.01), Pt (<0.01), Au (<0.1), Tl (<0.1), Bi (<0.01), and U (<0.01).



**Table 4.** Light volatile elements in unpowdered and powdered danburite samples provided as  $\mu\text{g}\cdot\text{g}^{-1}$ ; calculated  $\text{H}_2\text{O}^+$  values are given in wt %.

Sample Location	Unpowdered Samples					Powdered Samples				
	H	eq. $\text{H}_2\text{O}^+$ (wt %)	C	N	S	H	eq. $\text{H}_2\text{O}^+$ (wt %)	C	N	S
Mexico	<10	<0.01	200 $\pm$ 5	50 $\pm$ 10	13 $\pm$ 1	31 $\pm$ 10	0.028	130 $\pm$ 50	230 $\pm$ 130	25 $\pm$ 7
Tanzania	<10	<0.01	120 $\pm$ 40	100 $\pm$ 50	8 $\pm$ 1	14 $\pm$ 1	0.012	70 $\pm$ 40	100 $\pm$ 50	22 $\pm$ 3
Vietnam	300 $\pm$ 50	0.244	5600 $\pm$ 20	1000 $\pm$ 10	15 $\pm$ 3	40 $\pm$ 10	0.036	3000 $\pm$ 40	520 $\pm$ 20	19 $\pm$ 11

## 4. Discussion

### 4.1. Substitution Mechanisms of REEs, Be, and Sr in Danburite Structure

Referring to the similarity in ionic size and charge, eightfold-coordinated  $\text{Ca}^{2+}$  (1.12 Å) can be replaced to a certain extent by  $\text{Sr}^{2+}$  (1.26 Å). This substitution commonly takes place in danburite from all deposits and is mostly observed in the Mexican samples, where the concentration of Sr reaches 1611  $\mu\text{g}\cdot\text{g}^{-1}$ , followed by the Tanzanian and Vietnamese samples, with Sr concentrations up to 387  $\mu\text{g}\cdot\text{g}^{-1}$  and 66  $\mu\text{g}\cdot\text{g}^{-1}$ , respectively (Table 3).



Another substitution in danburite is the replacement of  $\text{Ca}^{2+}$  by  $\text{REE}^{3+}$  (here we presume that all REEs are trivalent, with the exception of Ce, which can be quadrivalent under strongly oxidizing conditions). It is obvious that danburite from all deposits prefer to incorporate LREE over HREE by a 200- to 500-fold enrichment. The  $\text{REE}^{3+}$  have decreasing radii with respect to increasing atomic number, i.e., from La (1.16 Å) to Ce (1.15 Å) to Lu (0.98 Å). Moreover, LREE radii are more compatible with the eightfold-coordinated  $\text{Ca}^{2+}$  lattice site. This explains why LREEs, especially La and Ce, are preferentially incorporated in the danburite lattice. The negative Eu anomaly observed in the Vietnamese and Tanzanian danburite is in accordance with a general depletion of Eu in highly oxidized magma, such as granites and pegmatites [22].

The substitution of  $\text{Ca}^{2+}$  by a  $\text{REE}^{3+}$  requires charge compensation and is therefore coupled with the substitution of  $\text{B}^{3+}$  (0.11 Å) by  $\text{Be}^{2+}$  (0.27 Å) and/or  $\text{Si}^{4+}$  (0.26 Å) by  $\text{Al}^{3+}$  (0.39 Å). These coupled substitutions theoretically allow all sites to be filled and charges to be balanced accordingly:

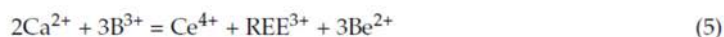


An omission-style substitution of  $\text{Ca}^{2+}$  by a trivalent  $\text{REE}^{3+}$  is also suitable to gain charge balance:



However, the positive correlation of molar abundance of REE and Be suggests that Equation (2) is the dominating process of REE incorporation into the danburite lattice (Figure 3A). The remaining substitution Equations (3) and (4) are theoretically possible, but are not supported by the datasets, which show, e.g., a negatively correlated relationship of Al with  $\Sigma\text{REE}$  (Figure 2A). In the Vietnamese samples, the Be/REE ratio is at an approximate 1:1 trend. In the Tanzanian samples, all the values are approximately equal to 1.5:1 (Figure 3A). A Be/REE ratio that is equal to or higher than 1:1 indicates that REEs are fully coupled with Be; subsequently, the two other forms of substitution,  $\text{Ca}^{2+} + \text{Si}^{4+} = \text{REE}^{3+} + \text{Al}^{3+}$  (3) and  $3\text{Ca}^{2+} = 2\text{REE}^{3+} + \square$  (4), are subordinate mechanisms. However, Equation (2) implies a Be/REE ratio equal to 1:1, rather than the 1.5:1 ratio measured in the Tanzanian samples. Hence, the excessive molar abundance of Be over REE in the Tanzanian samples needs to be explained by another substitution process with different ratios for Be and REEs or by an REE-independent substitution mechanism. This first hypothesis leads to the suggestion that

Ce occurs not only as  $\text{Ce}^{3+}$ , but also  $\text{Ce}^{4+}$  in the samples (with ionic sizes of 1.15 Å and 0.97 Å, respectively). The existence of  $\text{Ce}^{4+}$  in geological materials has been observed in various studies [23–26]. Hence, we extend substitution mechanism (2) to account for the probable presence of quadrivalent Ce:



Equation (5) is an example of a substitution mechanism where the ratio of  $\Sigma\text{REEs}$  (all  $\text{REE}^{3+}$  and  $\text{Ce}^{4+}$ ) to Be is equal to 3:2 (or 1.5:1). According to Equation (5), the ratios Be/Ce and Be/( $\Sigma\text{REEs} - \text{Ce}$ ) are both 3:1. Our chemical data (Figure 3B,C) show that the Be/Ce and Be/( $\Sigma\text{REEs} - \text{Ce}$ ) ratios in the Tanzanian samples are approximately 3:1 and 1.5:1. Therefore, we assume that mechanisms (2) and (5) take place predominantly in the Vietnamese and Tanzanian samples, respectively, with Ce likely present as  $\text{Ce}^{3+}$  and  $\text{Ce}^{4+}$ , respectively. This might suggest that REE uptake into Tanzanian danburite occurs at elevated oxygen fugacity compared to Mexican and Vietnamese danburite.

#### 4.2. Substitution Mechanisms Involving OH and Al in the Danburite Lattice

The presence of Be may also be the result of a REE-independent substitution of  $\text{B}^{3+}$  by  $\text{Be}^{2+}$  coupled with the substitution of  $\text{O}^{2-}$  by  $\text{OH}^-$ :



The presence of  $\text{OH}^-$  species in the danburite lattice was indicated in [4,7] by means of FTIR spectroscopy. The bridging oxygen O5 in the  $\text{B}_2\text{O}_7$  group is an ideal candidate for partial  $\text{OH}^-$  replacement, which allows the presence of low amounts of  $\text{OH}^-$  in danburite. However, a coupled incorporation of  $\text{Be}^{2+}$  and  $\text{OH}^-$  was not observed in our study (Figure 4A). Beran [4] proposed a coupled 1:1 substitution of  $\text{Si}^{4+}$  and  $\text{O}^{2-}$  by  $\text{Al}^{3+}$  and  $\text{OH}^-$  to charge balance OH incorporation. However, a direct substitution (1:1) was not confirmed by either dataset in the present study. Instead, we observed a positive correlation of  $\text{Al}^{3+}$  with  $\text{OH}^-$  (Figure 4B) in a 1:3 ratio, which suggests a coupled incorporation of  $\text{Al}^{3+}$  and  $\text{OH}^-$ , substituting for  $\text{B}^{3+}$  and  $\text{O}^{2-}$ , respectively:



Regarding the possibility of Al incorporation into danburite, it should be noted that the geochemical behavior of  $\text{B}^{3+}$  and  $\text{Al}^{3+}$  is very similar; however, they differ in radius size, with 0.11 Å for  $\text{B}^{3+}$  and 0.39 Å for  $\text{Al}^{3+}$  when in a tetrahedral coordination environment. Hence, a simple substitution mechanism such as  $\text{B}^{3+} = \text{Al}^{3+}$  would not be possible. Although a substitution of  $\text{Al}^{3+}$  with  $\text{B}^{3+}$  has been observed in the system albite  $\text{NaAlSi}_3\text{O}_8$  -  $\text{NaBSi}_3\text{O}_8$  reedmergnerite [27], as well as in a synthetic phlogopite  $\text{KMg}_3(\text{BSi}_3)\text{O}_{10}(\text{OH})_2$  [28], this process seems not to be valid for the danburite datasets (Figure 4A,B). Substitution mechanism (7) explains the Mexican samples as well, where the Al concentration is high and both REE and Be concentrations are low.

In general, the four main substitution mechanisms discussed above take place with different priority in the three studied locations. The substitutions of  $\text{Ca}^{2+}$  by  $\text{Sr}^{2+}$  and  $2\text{B}^{3+}$  by  $\text{Al}^{3+}$  are more common in the Mexican samples, while the substitutions of  $\text{Ca}^{2+}$  by REEs in the forms  $\text{Ca}^{2+} + \text{B}^{3+} = \text{REE}^{3+} + \text{Be}^{2+}$  and  $2\text{Ca}^{2+} + 3\text{B}^{3+} = \text{Ce}^{4+} + \text{REE}^{3+} + 3\text{Be}^{2+}$  are more common in the Vietnamese and Tanzanian samples, respectively.



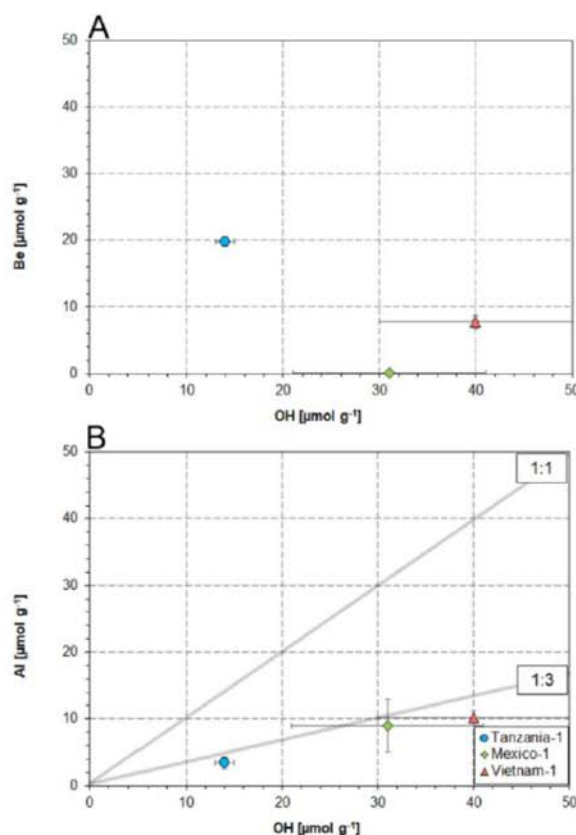


Figure 4. (A) Beryllium and OH correlate negatively, which suggests that incorporation into the danburite structure is not coupled. (B) However, Al shows a positive correlation with OH at a 1:3 ratio for all sampling locations, making a coupled incorporation of Al with OH likely.

#### 4.3. Constraints on the Geochemical Formation Environment of Danburite

Since danburite samples from Tanzania and Vietnam show a similar strong enrichment in LREE, the reported low values in the Mexican samples must therefore mean either a deficit of REE in the source material or REEs were already sequestered in datolite, which co-occurs with Mexican danburite. However, the depletion of REEs in the Mexican samples is accompanied by exceedingly high amounts of Sr (ca.  $1000 \mu\text{g}\cdot\text{g}^{-1}$  on average), which is an independent indicator of a different source composition with a higher component of biogenic calcareous sediments in the source material of this location. Biogenic limestone is known to contain high Sr values by being virtually free of REE [29,30]. In comparison, samples from Vietnam and Tanzania exhibit high REE, Y, and Be coupled with low Sr, thereby representing a composition that results from the involvement of highly differentiated late-stage silicic magmas (i.e., pegmatites). This is in agreement with the observed negative Eu anomalies in these samples, which are characteristic for late magmas, where the depletion in Eu is driven by fractional crystallization of plagioclase, which is commonly found to incorporate high amounts of  $\text{Eu}^{2+}$  [22]. This is in agreement with the nature of the outcrop and mineral assemblage in which the danburite was found. The high compatibility of LREE in the danburite lattice must therefore only be limited by the availability from the source material (i.e., highest in Tanzanian and lowest in Mexican samples). High contents of REE are in accordance with the significantly low amounts of N in the Tanzanian samples, due to the incompatibility of N in highly fractionated magmatic rocks, indicating a strong pegmatite component in the Tanzanian samples. Charge compensation and a

Be/ $\Sigma$ REEs ratio of 1.5:1 indicate the presence of  $\text{Ce}^{4+}$  (Equation (5)), additionally supporting a highly oxidized pegmatitic source for the Tanzanian samples. Nitrogen mass fractions generally increase with decreasing temperature and increasing involvement of metamorphic rocks (e.g., [21]), which suggests that the Vietnamese and Mexican samples were either formed at greater distance from the pegmatite or sourced from a higher proportion of recycled metamorphic rocks. Hence, we conclude that even though danburite always forms in a transition zone of metacarbonates and pegmatites, there are significant geochemical differences, i.e.,  $\Sigma$ REE, Be, Sr, Al, and OH in danburite, that directly reflect the different proportions and compositions of these source materials. Thus, our results suggest that trace element concentrations are suitable for determining the origins and locations of danburite crystals (i.e., for gem-testing laboratories).

## 5. Conclusions

In this study, we investigated trace element variations of danburite from three different locations in Mexico, Tanzania, and Vietnam. The most important trace elements in danburite that reflect their provenance include REEs, Sr, Al, Be, and, to a lesser extent, Mn, Zn, and Y. Mexican samples are fairly devoid of REEs, while Tanzanian samples contain up to  $1900 \mu\text{g}\cdot\text{g}^{-1}$  and Vietnamese samples have intermediate total values of around  $1100 \mu\text{g}\cdot\text{g}^{-1}$ . LREEs are more abundant than HREEs in all danburite samples, showing a 200- to 500-fold relative enrichment. Strontium and Al are more enriched in Mexican danburite than in Tanzanian and Vietnamese danburite, with mass fractions up to 1611 and  $325 \mu\text{g}\cdot\text{g}^{-1}$ , respectively.

Based on fs-LA-ICP-MS and CHNS analysis, we identified four mechanisms of trace element substitution in danburite: Two replacements of  $\text{Ca}^{2+}$  by  $\text{Sr}^{2+}$  ( $\text{Ca}^{2+} = \text{Sr}^{2+}$ ) and of  $\text{B}^{3+}$  by  $\text{Al}^{3+}$ , which are coupled with an incorporation of  $\text{OH}^-$  for  $\text{O}^{2-}$ :  $2\text{B}^{3+} + 3\text{O}^{2-} = \text{Al}^{3+} + 3\text{OH}^- + \square$ , are dominant in the Mexican samples. The incorporation of  $\text{REE}^{3+}$  for  $\text{Ca}^{2+}$  coupled with a simultaneous replacement of  $\text{B}^{3+}$  by  $\text{Be}^{2+}$  is present in the Vietnamese and Tanzanian samples. Different valance states of Ce are present in the Vietnamese and Tanzanian samples, leading to two different substitutions:  $\text{Ca}^{2+} + \text{B}^{3+} = \text{REE}^{3+} + \text{Be}^{2+}$  and  $2\text{Ca}^{2+} + 3\text{B}^{3+} = \text{Ce}^{4+} + \text{REE}^{3+} + 3\text{Be}^{2+}$ , respectively.

The observed significant differences in trace element abundance not only suggest a high potential for provenance discrimination, but also provide information on the contrasting source compositions of the three deposits. The formation of danburite generally involves both metacarbonates and pegmatites as source materials. Different proportions of these two source components were involved in the formation of danburite at the three locations, and likely explain the observed trace element variations. Low REE and Be coupled with high Sr, Al, N, and OH in the Mexican samples indicate a dominant biogenic metacarbonate component, while the Vietnamese and Tanzanian samples show high REE and Be coupled with low Sr, Al, N, and OH, characteristic of a predominantly pegmatitic source. The 200- to 500-fold enrichment of LREE over HREE in the Tanzanian and Vietnamese samples results from the preferential replacement of Ca ions by similarly sized LREE ions. The negative Eu anomaly, which is characteristic of highly fractionated igneous rocks, is characteristic of Vietnamese and Tanzanian danburite and supports the predominance of the pegmatitic source at these locations.

**Author Contributions:** L.T.-T.H., L.M.O., K.P.J., C.A.H., and K.K. designed and coordinated the study. K.P.J. and C.A.H. supervised the project. L.T.-T.H., L.M.O., and K.K. collected and prepared the samples. M.W.F. prepared epoxy mounts and performed electron probe microanalyses. L.M.O., D.S.M., B.S., and U.W. collected and evaluated trace element concentrations. M.W.F. and O.A. collected and evaluated light volatile element concentrations and calibrated the CHNS analyzer. L.T.-T.H., L.M.O., and M.W.F. wrote the first drafts of the manuscript. K.P.J., C.A.H., K.K., and O.A. carefully edited the final version. All authors contributed to the final version and gave their approval for submission.

**Funding:** Vietnamese danburite samples were collected during a field trip funded by a NAFOSTED Project, grant number 1055.99-2013.13. L.T.-T.H. is grateful to the ASEAN-European Academic University Network, the Austrian Federal Ministry of Science, Research and Economy, and the Austrian Agency for International Cooperation in Education and Research for financial support.

**Acknowledgments:** Lauren Gorojovsky is acknowledged for preparation and analyses of reference materials for the CHNS elemental analyzer, and we kindly acknowledge the insightful comments by two anonymous reviewers.



**Conflicts of Interest:** The authors declare no conflict of interest.

## References

1. Lindbloom, J.T.; Gibbs, G.V.; Ribbe, P.H. Crystal Structure of Hurlbutite—Comparison with Danburite and Anorthite. *Am. Mineral.* **1974**, *59*, 1267–1271.
2. Best, S.P.; Clark, R.J.H.; Hayward, C.L.; Withnall, R. Polarized single-crystal Raman spectroscopy of danburite,  $\text{CaB}_2\text{Si}_2\text{O}_8$ . *J. Raman Spectrosc.* **1994**, *25*, 557–563. [[CrossRef](#)]
3. Sugiyama, K.; Takéuchi, Y. Unusual thermal expansion of a B–O bond in the structure of danburite  $\text{CaB}_2\text{Si}_2\text{O}_8$ . *Z. Kristallogr. -Cryst. Mater.* **1985**, *173*, 293–304. [[CrossRef](#)]
4. Beran, A. OH groups in nominally anhydrous framework structures: An infrared spectroscopic investigation of danburite and labradorite. *Phys. Chem. Miner.* **1987**, *14*, 441–445. [[CrossRef](#)]
5. Hurwit, K.N. Gem Trade Lab Notes: Golden yellow danburite from Sri Lanka. *Gems Gemol.* **1986**, *22*, 47.
6. Chadwick, K.M.; Laurs, B.M. Gem News International: Yellow danburite from 346 Tanzania. *Gems Gemol.* **2008**, *44*, 169–171.
7. Huong, L.T.-T.; Otter, L.M.; Häger, T.; Ullmann, T.; Hofmeister, W.; Weis, U.; Jochum, K.P. A New Find of Danburite in the Luc Yen Mining Area, Vietnam. *Gems Gemol.* **2016**, *52*. [[CrossRef](#)]
8. De Vito, C.; Pezzotta, F.; Ferrini, V.; Aurisicchio, C. Nb–Ti–Ta oxides in the gem-mineralized and “hybrid” Anjanabonoina granitic pegmatite, central Madagascar: A record of magmatic and postmagmatic events. *Can. Mineral.* **2006**, *44*, 87–103. [[CrossRef](#)]
9. Cook, R.B. Connoisseur’s: Danburite, Charcas, San Luis Potosí, Mexico. *Rocks Miner.* **2003**, *78*, 400–403. [[CrossRef](#)]
10. Hintze, J. Safari njema—AFRIKANISCHES TAGEBUCH (I): Reise zu den gelben Danburiten von Morogoro, Tansania. *Lapis Die Aktuelle Monatsschrift Fuer Liebhaber Und Sammler Von Mineralien Und* **2010**, *35*, 25.
11. Dyar, M.D.; Wiedenbeck, M.; Robertson, D.; Cross, L.R.; Delaney, J.S.; Ferguson, K.; Francis, C.A.; Grew, E.S.; Guidotti, C.V.; Hervig, R.L. Reference minerals for the microanalysis of light elements. *Geostand. Geoanal. Res.* **2001**, *25*, 441–463. [[CrossRef](#)]
12. Ottolini, L.; Cámara, F.; Hawthorne, F.C.; Stirling, J. SIMS matrix effects in the analysis of light elements in silicate minerals: Comparison with SREF and EMPA data. *Am. Mineral.* **2002**, *87*, 1477–1485. [[CrossRef](#)]
13. Balmer, W.A.; Hauzenberger, C.A.; Fritz, H.; Sutthirath, C. Marble-hosted ruby deposits of the Morogoro Region, Tanzania. *J. Afr. Earth Sci.* **2017**, *134*, 626–643. [[CrossRef](#)]
14. Möller, A.; Mezger, K.; Schenk, V. U–Pb dating of metamorphic minerals: Pan-African metamorphism and prolonged slow cooling of high pressure granulites in Tanzania, East Africa. *Precambrian Res.* **2000**, *104*, 123–146. [[CrossRef](#)]
15. Huong, L.T.-T.; Krenn, K.; Hauzenberger, C. Sassolite- and  $\text{CO}_2$ - $\text{H}_2\text{O}$ -bearing Fluid Inclusions in Yellow Danburite from Luc Yen, Vietnam. *J. Gemmol.* **2017**, *35*, 544–550. [[CrossRef](#)]
16. Garnier, V.; Ohnenstetter, D.; Giuliani, G.; Maluski, H.; Deloule, E.; Trong, T.P.; Van, L.P.; Quang, V.H. Age and significance of ruby-bearing marble from the Red River Shear Zone, northern Vietnam. *Can. Mineral.* **2005**, *43*, 1315–1329. [[CrossRef](#)]
17. Jochum, K.P.; Stoll, B.; Weis, U.; Jacob, D.E.; Mertz-Kraus, R.; Andreae, M.O. Non-Matrix-Matched Calibration for the Multi-Element Analysis of Geological and Environmental Samples Using 200 nm Femtosecond LA-ICP-MS: A Comparison with Nanosecond Lasers. *Geostand. Geoanal. Res.* **2014**, *38*, 265–292. [[CrossRef](#)]
18. Jochum, K.P.; Stoll, B.; Herwig, K.; Willbold, M. Validation of LA-ICP-MS trace element analysis of geological glasses using a new solid-state 193 nm Nd: YAG laser and matrix-matched calibration. *J. Anal. At. Spectrom.* **2007**, *22*, 112–121. [[CrossRef](#)]
19. Jochum, K.P.; Nohl, U.; Herwig, K.; Lammel, E.; Stoll, B.; Hofmann, A.W. GeoReM: A new geochemical database for reference materials and isotopic standards. *Geostand. Geoanal. Res.* **2005**, *29*, 333–338. [[CrossRef](#)]
20. Palme, H.; Jones, A. Solar system abundances of the elements. *Treat. Geochem.* **2003**, *1*, 711.
21. Plessen, B.; Harlov, D.E.; Henry, D.; Guidotti, C.V. Ammonium loss and nitrogen isotopic fractionation in biotite as a function of metamorphic grade in metapelites from western Maine, USA. *Geochim. Cosmochim. Acta* **2010**, *74*, 4759–4771. [[CrossRef](#)]
22. Fowler, A.D.; Doig, R. The significance of europium anomalies in the REE spectra of granites and pegmatites, Mont Laurier, Quebec. *Geochim. Cosmochim. Acta* **1983**, *47*, 1131–1137. [[CrossRef](#)]



23. Braun, J.-J.; Pagel, M.; Muller, J.-P.; Bilong, P.; Michard, A.; Guillet, B. Cerium anomalies in lateritic profiles. *Geochim. Cosmochim. Acta* **1990**, *54*, 781–795. [[CrossRef](#)]
24. Takahashi, Y.; Shimizu, H.; Kagi, H.; Yoshida, H.; Usui, A.; Nomura, M. A new method for the determination of CeIII/CeIV ratios in geological materials; application for weathering, sedimentary and diagenetic processes. *Earth Planet. Sci. Lett.* **2000**, *182*, 201–207. [[CrossRef](#)]
25. Taunton, A.E.; Welch, S.A.; Banfield, J.F. Microbial controls on phosphate and lanthanide distributions during granite weathering and soil formation. *Chem. Geol.* **2000**, *169*, 371–382. [[CrossRef](#)]
26. Bao, Z.; Zhao, Z. Geochemistry of mineralization with exchangeable REY in the weathering crusts of granitic rocks in South China. *Ore Geol. Rev.* **2008**, *33*, 519–535. [[CrossRef](#)]
27. Wunder, B.; Stefanski, J.; Wirth, R.; Gottschalk, M. Al-B substitution in the system albite (NaAlSi<sub>3</sub>O<sub>8</sub>)-reedmergnerite (NaBSi<sub>3</sub>O<sub>8</sub>). *Eur. J. Mineral.* **2013**, *25*, 499–508. [[CrossRef](#)]
28. Stubican, V.; Roy, R. Boron substitution in synthetic micas and clays. *Am. Mineral.* **1962**, *47*, 1166.
29. Chen, C.; Liu, Y.; Foley, S.F.; Ducea, M.N.; He, D.; Hu, Z.; Chen, W.; Zong, K. Paleo-Asian oceanic slab under the North China craton revealed by carbonatites derived from subducted limestones. *Geology* **2016**, *44*, 1039–1042. [[CrossRef](#)]
30. Gozzi, F.; Gaeta, M.; Freda, C.; Mollo, S.; Di Rocco, T.; Marra, F.; Dallai, L.; Pack, A. Primary magmatic calcite reveals origin from crustal carbonate. *Lithos* **2014**, *190*, 191–203. [[CrossRef](#)]



© 2018 by the authors. Licensee MDPI, Basel, Switzerland. This article is an open access article distributed under the terms and conditions of the Creative Commons Attribution (CC BY) license (<http://creativecommons.org/licenses/by/4.0/>).



## Full length article

An experimental study of the role of partial melts of sediments *versus* mantle melts in the sources of potassic magmatismMichael W. Förster<sup>a,\*</sup>, Dejan Prelević<sup>b,c</sup>, Stephan Buhre<sup>b</sup>, Regina Mertz-Kraus<sup>b</sup>, Stephen F. Foley<sup>a</sup><sup>a</sup> ARC Centre of Excellence of Core to Crust Fluid Systems and Department of Earth and Planetary Sciences, Macquarie University, NSW 2109, Sydney, Australia<sup>b</sup> Institute of Geosciences, Johannes Gutenberg University, 55099 Mainz, Germany<sup>c</sup> Faculty of Mining and Geology, University Belgrade, Djusina 7, 11000 Belgrade, Serbia

## ARTICLE INFO

## Keywords:

Lamproite  
High-pressure experiments  
Metasomatism  
Post-collisional magmatism  
Mediterranean magmatism  
High-K lavas

## ABSTRACT

Potassium-rich lavas with K/Na of  $> 2$  are common in orogenic and anorogenic intraplate magmatic provinces. However, in the primitive mantle, the concentration of Na exceeds that of K by 10 times. The source of K-rich lavas thus needs to be either K-enriched or Na-depleted to account for high K/Na ratios. The geochemical and isotopic compositions of high  $^{87}\text{Sr}/^{86}\text{Sr}$  post-collisional lavas show that their mantle source contains a recycled crustal component. These highly K-enriched lavas with crustal like trace element patterns are termed “orogenic lamproites” and are compositionally distinct from K-rich “anorogenic lamproites” that show lower  $^{87}\text{Sr}/^{86}\text{Sr}$  and a trace element pattern that resembles that of primary mantle melts. For both groups the processes of K-enrichment within their source are uncertain and are thought to be linked to melts of sedimentary rocks for “orogenic lamproites” and low-degree melts of ultramafic mantle rocks for “anorogenic lamproites”. In both cases, metasomatism of the mantle lithosphere is the precursor to K-rich magmatism. In this study we experimentally determine the effects of mantle metasomatism by sediment- and hydrous mantle melts. The experiments simulate the interaction of refractory lithospheric mantle and metasomatizing melt in a 2-layer reaction experiment. The sediment/dunite reaction experiments lead to formation of a strongly K-enriched phlogopite-pyroxenite layer sandwiched between the two starting materials. The low temperature of the sediment/dunite reaction runs at  $< 1000^\circ\text{C}$  simulates a fore-arc subduction environment, in which the melts of sediment are consumed during interaction with dunite as the temperature is below the solidus of the produced phlogopite-pyroxenites. The hydrous mantle melt/dunite reaction run is simulated by reacting a hydrated basanite with dunite. Since the temperature of the reaction is higher than the solidus of the resulting phlogopite-pyroxenites ( $1200^\circ\text{C}$ ), the hydrous melt is not consumed but flows further, increasing in  $\text{K}_2\text{O}$  and K/Na as it reacts with the refractory peridotite. In both cases, melts are enriched in K and K/Na increases by crystallizing a low K and low K/Na eclogitic residue. Compositions of glass and phlogopite from both types of reactions are comparable to glasses and phlogopites found within post-collisional lavas. Since the enrichment of K within the reaction zone is strongly controlled by the formation of low K/Na and low-K residues, metasomatic enrichment of the mantle lithosphere in K does not need a highly K-enriched metasomatic agent.

## 1. Introduction

Lavas formed in post-collisional settings are geochemically extremely heterogeneous and show Si-undersaturated to Si-oversaturated compositions. Within the Alpine-Himalayan belt, post-collisional lavas usually have  $> 4 \text{ wt}\%$   $\text{K}_2\text{O}$  to up to  $9 \text{ wt}\%$  and  $\text{K/Na} > 2$ . The array of lavas present within the Alpine-Himalayan belt comprise all four major groups of K-rich rock compositions including shoshonites, voluminous Roman-type lavas, as well as lamproites and kamafugites (Foley et al., 1987). Since low-degree melting experiments of peridotite have not

been able to produce high contents of K and high K/Na, and liquidus experiments have not produced multiple saturation points for olivine, orthopyroxene, clinopyroxene and garnet/spinel (Edgar and Mitchell, 1997; Foley, 1992; Mitchell and Edgar, 2002; Sato, 1997), an alternative explanation for K-rich magmatism has been established that involves the presence of phlogopite pyroxenites (“metasomes”) in the lithospheric mantle (Foley, 1992). While lavas with  $\text{K}_2\text{O} < 5 \text{ wt}\%$  and  $\text{SiO}_2 > 55 \text{ wt}\%$  may form by direct melting of mixed crustal/mantle rocks without phlogopite in the source (Campbell et al., 2014; Mallik et al., 2016; Mallik et al., 2015; Wang et al., 2017b; Wang et al., 2017a;

\* Corresponding author.

E-mail address: [michael.forster@mq.edu.au](mailto:michael.forster@mq.edu.au) (M.W. Förster).<https://doi.org/10.1016/j.jseas.2019.03.014>

Received 14 September 2018; Received in revised form 19 March 2019; Accepted 21 March 2019

Available online 21 March 2019

1367-9120/ © 2019 Elsevier Ltd. All rights reserved.



Wang and Foley, 2018), extremely K-enriched lavas are thought to require modally metasomatized mantle, enriched in phlogopite (Conticelli et al., 2015; Conticelli et al., 2007; Conticelli and Peccerillo, 1992; Lustrino, 2011; Prelević et al., 2008b). Experimental studies of melting of phlogopite-veined refractory peridotite and phlogopite-peridotite successfully produced melts with  $K_2O$  of 8–12 wt% and indicate the importance of phlogopite within the source of ultrapotassic lavas (Condamine et al., 2016; Condamine and Médard, 2014; Förster et al., 2018; Förster et al., 2017). Phlogopite-enriched metasomatized mantle is generally thought to be formed when K-enriched liquids percolate and react with refractory peridotite, re-fertilizing it and producing veins (Conticelli et al., 2013; Foley, 1992; Prelević et al., 2013; Tappe et al., 2008). The source of the K-enriched liquids comprises recycled materials, including blueschists (Tommasini et al., 2011), terrigenous siliciclastic sediments (Prelević et al., 2008b), and marly sediments (Avanzinelli et al., 2007). Recycling and metasomatism take place during subduction, where sediments melt at temperatures as low as 675 °C, depending on pressure and volatile contents and metasomatize the mantle wedge (Hermann et al., 2006; Hermann and Spandler, 2007). Melts of sediment, which are strongly enriched in Si, react with Si-poor peridotites to form phlogopite pyroxenites (Sekine and Wyllie, 1983; Wyllie and Sekine, 1982). The phlogopite pyroxenites which are formed at low temperatures within a subduction setting are able to produce K-enriched melts if they are activated by a temperature increase which might be induced by asthenospheric upwelling i.e. by slab rollback or detachment (Gülmez et al., 2016; Vigouroux et al., 2008).

All previously presented rocks share an ‘orogenic’ origin, which is characteristic of strong crustal isotopic signatures (e.g. high  $^{87}Sr/^{86}Sr$ ) and geochemical signatures of recycled crustal materials. However, there are also ‘anorogenic’ K-rich rocks, which show low  $^{87}Sr/^{86}Sr$  isotopic and geochemical signatures of a mantle origin (Prelević et al., 2008a; Tappe et al., 2007). These ‘anorogenic lamproites’ suggest that besides metasomatism induced by melting of recycled crustal lithologies, metasomatism by low-degree mantle melts may also lead to K-enrichment of the lithospheric mantle. While the recycling of crustal lithologies brings K-rich rocks into the mantle, melts of peridotites are generally enriched in Na over K, given the composition of primitive mantle, which contains only 0.026 wt% K but 0.246 wt% Na, resulting in a K/Na of ~0.1 (Hofmann, 1988). In the presence of volatiles such as  $CO_2$  and  $H_2O$ , the melting point of peridotite is depressed to up to 400 °C and forms low-degree melts. Low-degree ‘incipient’ melts of peridotite are, depending on the presence and amount of volatiles, highly alkaline and Si-poor with compositions such as melilitites, kimberlites, lamprophyres, and carbonatites (Foley and Pintér, 2018; Vetter et al., 2017). At < 1% melting of a phlogopite-free garnet-peridotite,  $K_2O$  is enriched to up to 2 wt% while  $Na_2O$  attains ~3 wt% (Erlank, 1987; Novella and Frost, 2014). While these low-degree melts are only rarely erupted due to their overall low volume, they are certainly suitable agents for metasomatism of the lithospheric mantle (Tappe et al., 2018). The Quaternary Eifel Volcanic Fields is an example of ‘anorogenic’ mildly potassic intraplate magmatism (K/Na ~ 1) that is interpreted as a result of partially melting of a metasomatized lithospheric mantle enriched in phlogopite (Mertes and Schmincke, 1985; Schmincke, 2007). Particularly for the Quaternary Eifel volcanic fields is a spatial overlap with the older Eocene Hoheifel volcanic fields which comprised sodic magmatism with low K/Na of < 0.5 (Fekiacova et al., 2007).

In this study we react layered sediment/dunite and hydrous basanite/dunite in high-pressure experiments to investigate the behaviour of major and trace elements during mantle metasomatism. The sediment/dunite reaction experiments were performed at thermobaric conditions of 1–4 GPa/800–1000 °C that correspond to the fore-arc setting of a subduction zone. A melting experiment of pure sediment was performed at 4 GPa/1000 °C to examine phases that crystallize in absence of the reacting dunite. The hydrous basanite/dunite reaction

experiment was performed at 3 GPa/1200 °C and represents an environment within the lithospheric mantle unrelated to subduction zone metasomatism. Both reaction experiments lead to the growth of metasomatic phases in a layer between the starting materials.

## 2. Materials and methods

### 2.1. Experimental techniques

Experiments were performed with a piston cylinder apparatus at the University of Mainz for experiments performed at 1–3 GPa and a belt apparatus at the University of Frankfurt for experiments at 4 GPa. The experimental charges consisted of layers of dunite (sample ZD11–53) and either sediment (ODP 161-976B 18 X3 105–106.5; a siliciclastic marine sediment with < 10% carbonate and 5–10 wt%  $H_2O$  as estimated by difference to 100 wt% in glasses and a melt fraction of ~40%) or a sodic basanite (Arensberg, Hoheifel, Germany). The basanite has K/Na ~ 0.4 and plots on the border between basanite and trachybasaltic compositions (Fig. 2A). The basanite was powdered and mixed with 10 wt% oxalic acid ( $C_2H_2O_4$ ) as a volatile source for 4 wt%  $H_2O$ . Experimental charges were filled into a carbon capsules to control  $fO_2$  via the C + CO equilibrium, and these were placed into platinum capsules. The assemblies of the piston cylinder experiments consisted of  $Al_2O_3$  spacers, a graphite furnace, b-type thermocouple, and a sintered  $CaF_2$  outer spacer. At the belt apparatus, the spacer and capsule holder consisted of natural polycrystalline calcium fluoride, while other materials were identical to those used in the piston-cylinder experiments. All assemblies were pressurized first and heated at a rate of 50 °C/min. Both apparatuses were cooled by a water circuit at approximately 13 °C and pressure and temperature were kept constant for 2–14 days. All charges were quenched to temperatures below 500 °C within 8 s in the piston-cylinder runs (Ziaja et al., 2014), and within 10 s in the belt runs.

### 2.2. Analytical techniques

Major element mass fractions of experimental phases were acquired using a JEOL JXA 8200 Superprobe electron-probe micro-analyser (EPMA) equipped with five wavelength dispersive spectrometers at the University of Mainz, Germany. All samples were measured using 15 kV accelerating voltage, a spot size of 2  $\mu m$ , and a beam current of 12 nA with peak counting times of 20–30 s. A range of synthetic materials were used as reference materials. Major element analysis of experimental charges are presented in supplementary Tables 1–6. Trace element concentrations have been obtained by laser ablation-inductively coupled plasma mass spectrometry (LA-ICP-MS) at the University of Mainz. Using an ESI NWR193 ArF Excimer laser ablation system (193 nm wavelength) equipped with a TwoVol2 ablation cell, samples were ablated to a dry aerosol. Following ablation at 10 Hz and 3 J/cm<sup>2</sup>, the dry aerosol was transferred to an Agilent 7500ce mass spectrometer by a He-Ar mixed gas flow. Synthetic NIST SRM 610 was used with published values (Jochum et al., 2011) for external calibration material. As internal standard  $^{29}Si$  was used by applying  $SiO_2$  mass fractions which were determined by EPMA. For quality control, USGS BCR-2G was analysed as an unknown in each run and measured values were within 10% of the data tabulated in the GeoReM database (Jochum et al., 2005). Background signals were acquired for 20 s, followed by a dwell time of 30 s with spot sizes of 20  $\mu m$  at each analysed spot. Data processing and reduction was carried out using the commercial software GLITTER 4.4.1 (Griffin, 2008). The whole dataset of reference material- and sample analysis can be found in supplementary Tables 7–14.



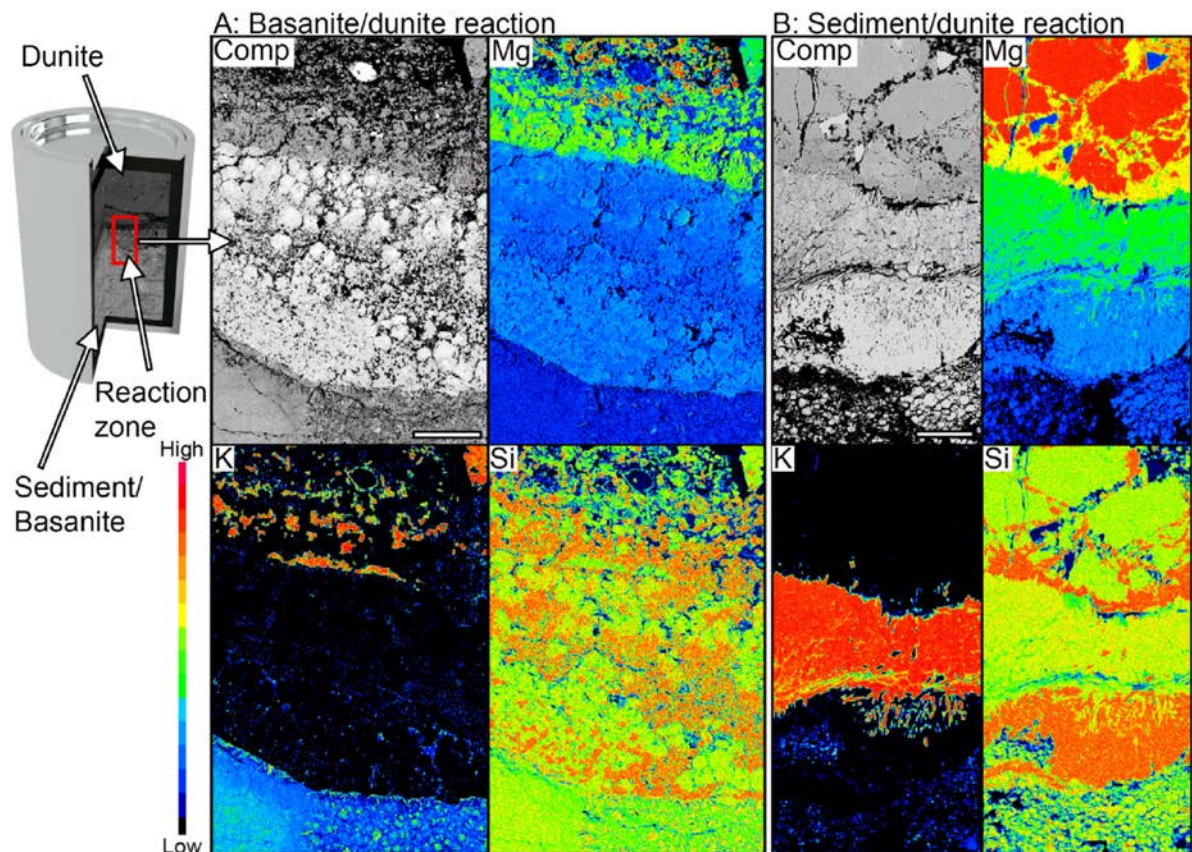


Fig. 1. Backscattered electron images (Comp) and WDX elemental maps of Mg, K, and Si of (A) basanite/dunite reaction at 3 GPa/1200 °C and (B) sediment/dunite reaction at 3 GPa/900 °C. The basanite/dunite reaction experiment (A) consists of three compositionally distinct layers, the uppermost is the former dunite, enriched in phlogopite and orthopyroxene as seen by the red colour in the K and Si maps. The middle layer consists of clinopyroxene and garnet, has the brightest grey scale in the backscattered electron image (Comp) and appears blue in the Mg map. Domains of garnet (green) and clinopyroxene (red) can be distinguished in the Si map. The lowermost layer is composed of glass and appears blue in the K map; the green needles are phlogopite crystals that formed during quenching. The sediment/dunite reaction experiment (B) shows four compositionally distinct layers: the uppermost represents the metasomatized dunite, enriched in orthopyroxene only (red in the Si map). The second layer forms a belt solely composed of phlogopite (red in K map) and is followed by a pure clinopyroxene layer (blue on Mg, red on Si map). The lowermost layer is composed of garnet, clinopyroxene, and interstitial melt (blue on K map). Scale bar 500  $\mu\text{m}$  (A) and 100  $\mu\text{m}$  in (B). (For interpretation of the references to colour in this figure legend, the reader is referred to the web version of this article.)

### 3. Results

#### 3.1. Textural observations

The reaction experiments of sediment/dunite and basanite/dunite show strong enrichment of K, Al, and Si in a reaction zone within the original dunite half of the capsule (Fig. 1A, B). Generally, WDX-maps reveal the metasomatic growth of phlogopite, clinopyroxene, and orthopyroxene at the expense of olivine. Metasomatic phases generally show grain sizes of 20–50  $\mu\text{m}$ . The basanite/dunite reaction experiment, which was performed at 3 GPa/1200 °C (Fig. 1A), shows 3 compositionally distinct layers. The uppermost layer is dunite, which is metasomatically enriched in orthopyroxene, clinopyroxene, and phlogopite. Beneath the contact zone, the basanite crystallized to a layer of clinopyroxene and garnet, which forms the central part of the map images. Individual clinopyroxene and garnet grains attain sizes of < 50  $\mu\text{m}$ . The lowermost layer consists of quenched basanitic glass with needles of quenched phlogopite, which is recognizable by its higher content of K and Mg when compared to the surrounding glass. The sediment/dunite experiment shown in Fig. 1B was performed at 3 GPa/900 °C and shows 4 compositionally distinct layers. The dunite is

metasomatically enriched in orthopyroxene, which is recognizable in veins along olivine grain boundaries. The second layer is nearly entirely composed of phlogopite with a small amount of clinopyroxene. Beneath the phlogopite layer follows a layer nearly entirely composed of clinopyroxene. Some of these clinopyroxenes show inclusions of orthopyroxene. Since orthopyroxene formed by reaction with olivine, the dunite layer extended to layer 3 clinopyroxenes as the reaction started. The lowermost layer consists of clinopyroxene and garnet and shows interstitial glass. The sediment melting experiment at 4 GPa/1000 °C is devoid of layering and comprises glass, garnet, kyanite, Mg-calcite, and coesite.

#### 3.2. Major element compositions

Melts formed during the reaction of sediment and dunite are moderate to high in  $\text{SiO}_2$  (50–76 wt%) with moderate  $\text{K}_2\text{O}$  contents of 3–6 wt% and K/Na of 1–5 (Table 2, Fig. 2A–C). The melts from basanite/dunite reaction are lower in  $\text{SiO}_2$ , have  $\text{K}_2\text{O}$  of 2.5–3.5 wt%, and low K/Na of 0.5–1.2 but higher than the bulk basanite starting composition with K/Na of 0.4 at  $\text{K}_2\text{O}$  of 1.4 wt%. Experimental clinopyroxene shows a zonation towards omphacite (Fig. 3A) across the reaction



**Table 1**  
Composition, temperature, pressure, and duration of each experiment.

#	Experiment	P [GPa]	T [°C]	% Melt	Phases	Duration
1	Sediment/dunite reaction	1	900	~40	Ol + Opx + Cpx + melt	4 d
2	Sediment/dunite reaction	2	900	~40	Ol + Opx + Cpx + Gt + melt	4 d
3	Sediment/dunite reaction	3	800	~10	Ol + Opx + Cpx + Phl + Mgs + Gt + Phe + Coe + melt	7 d
4	Sediment/dunite reaction	3	900	~20	Ol + Opx + Phl + Cpx + Mgs + Gt + melt	14 d
5	Sediment/dunite reaction	3	1000	~30	Ol + Opx + Cpx + Gt + (Phl) + melt	4 d
6	Sediment melting	4	1000	~70	Ky + Gt + Cc + Coe + melt	4 d
7	Basanite/dunite reaction	3	1200	~40	Ol + Opx + Cpx + Gt + Phl + melt	2 d

**Table 2**  
Average composition of starting materials and high-pressure experiment melts normalized to 100% (oxides in wt%).

Sample	Na <sub>2</sub> O	K <sub>2</sub> O	MnO	SiO <sub>2</sub>	MgO	FeO	Al <sub>2</sub> O <sub>3</sub>	Cr <sub>2</sub> O <sub>3</sub>	CaO	TiO <sub>2</sub>	Total
Sediment bulk	1.78(6)	2.46(9)	2.17(9)	54.9(4)	3.93(6)	3.6(2)	17.8(1)	–	13.5(2)	0.82(3)	101
Basanite bulk	3.9(1)	1.46(7)	0.21(5)	46.5(4)	9.3(6)	10.6(2)	13.9(3)	–	12.0(3)	2.54(9)	100
1 GPa/900 °C Sediment/Dunite reaction	2.4(6)	3.3(9)	1.4(6)	54(1)	4(1)	3(1)	19(4)	0.10(1)	13(1)	0.5(2)	100
2 GPa/900 °C Sediment/Dunite reaction	1.7(5)	5.4(0.6)	0.1(1)	69(1)	0.4(1)	0.8(2)	17.4(5)	0.01(2)	3.0(7)	0.30(2)	100
4 GPa/1000 °C Sediment melting	2(1)	4.2(3)	0.5(1)	64(2)	1.6(4)	1.9(4)	14.3(6)	–	10(2)	0.9(2)	100
3 GPa/1200 °C Basanite/Dunite reaction	2.8(4)	2.6(4)	0.18(4)	46(1)	11(1)	7.1(6)	14.4(5)	0.03(2)	13(2)	3.3(2)	100

The number in parentheses is the first standard deviation on the last digit.

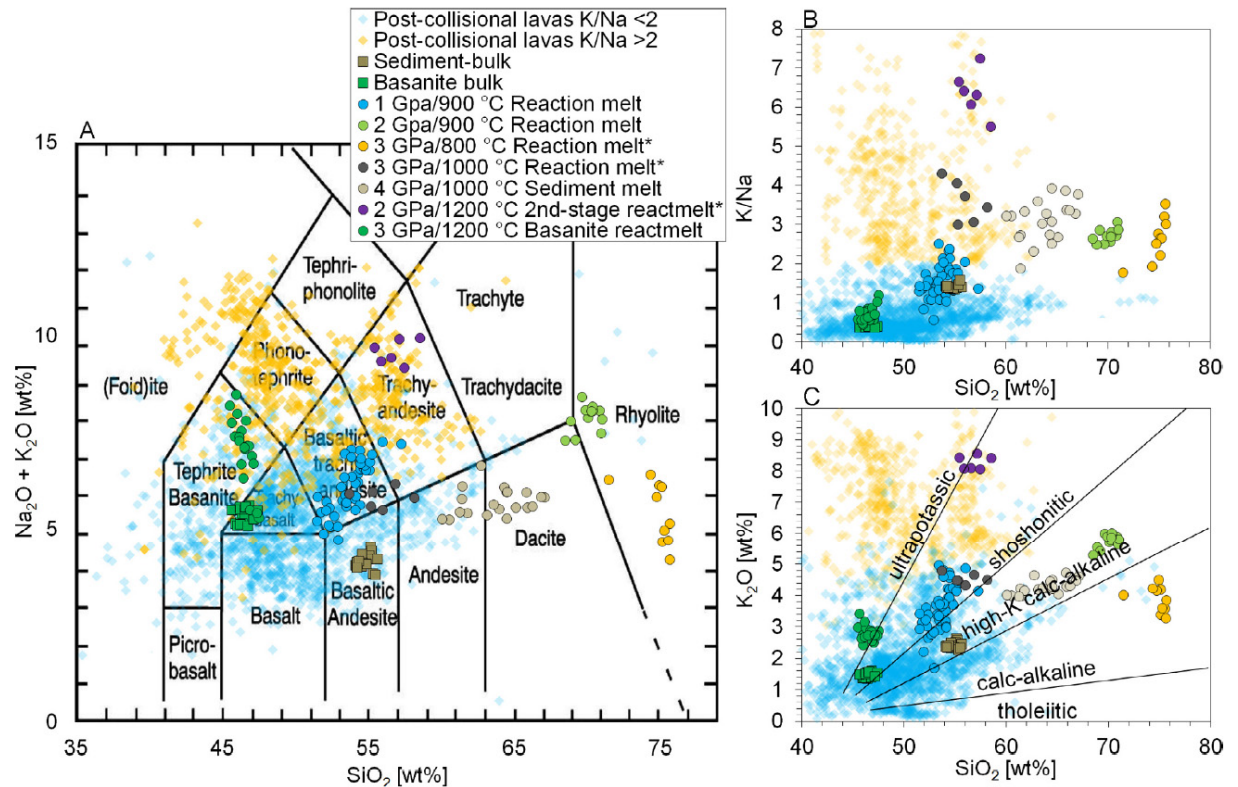


**Fig. 2.** Total alkali versus silica (A) K/Na versus SiO<sub>2</sub> (B), and K<sub>2</sub>O versus SiO<sub>2</sub> (C) for experimental melts (coloured squares: brown, sediment bulk; green, basanite bulk). Coloured circles: blue 1 GPa/900 °C; lime 2 GPa/900 °C; yellow 3 GPa/800 °C; grey 3 GPa/1000 °C; brown 4 GPa/1000 °C; purple 2 GPa/1200 °C; green 3 GPa/1200 °C. Compositions are compared to post-collisional lavas with K/Na > 2 (faint yellow diamonds) and K/Na < 2 (blue diamonds) (Prelević et al., 2008b). Generally, melts of sediment and basanite increase in K/Na as reaction proceeds. Sediment/dunite reaction melts are generally high in SiO<sub>2</sub> and total alkalis (A) and only show similarities to post-collisional lavas at T > 900 °C, while melts of phlogopite-enriched dunite, which formed by sediment/dunite reaction (termed 2nd-stage melt, \*Förster et al., submitted), are comparable to post-collisional lavas with K/Na > 2. The basanite/dunite reaction melts (green circles) attain K<sub>2</sub>O contents of 3 wt% and K/Na of 0.5–1.2 (B, C). (For interpretation of the references to colour in this figure legend, the reader is referred to the web version of this article.)



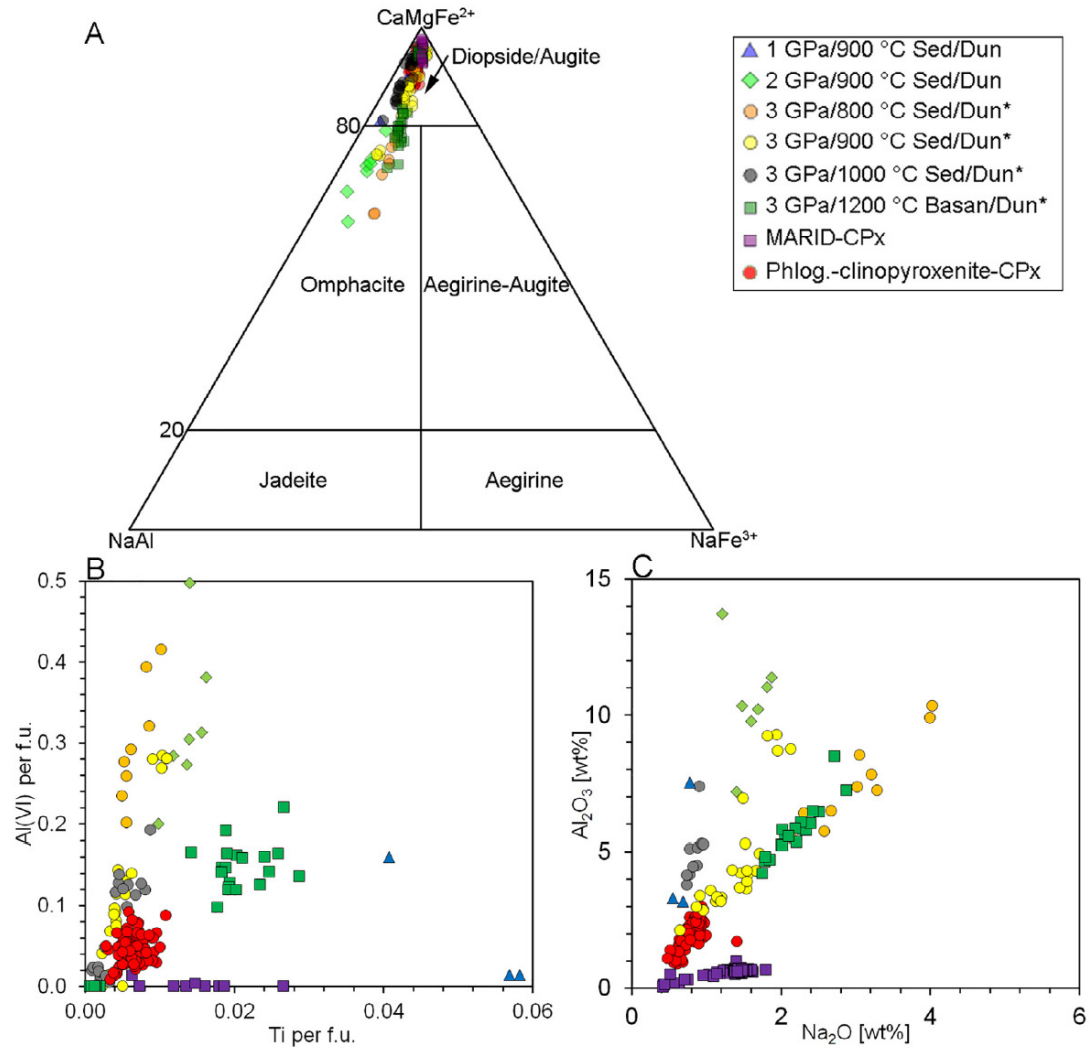


Fig. 3. Compositions of pyroxenes from reaction experiments (blue triangles 1 GPa/900 °C; lime diamonds 2 GPa/900 °C; orange circles 3 GPa/800 °C; yellow circles 3 GPa/900 °C; grey circles 3 GPa/1000 °C; green squares 3 GPa/1200 °C) compared to MARID-type clinopyroxenes (purple squares) and phlogopite clinopyroxenite xenoliths from post-collisional settings (red circles). (A) The  $\text{CaMgFe}^{2+}$ - $\text{NaAl}$ - $\text{NaFe}^{3+}$  diagram (Morimoto, 1988) shows that clinopyroxenes compositionally vary from the diopside/augite field towards omphacitic composition. The Al (VI) versus Ti (a.f.u.) plot (B) show that clinopyroxenes associated with melts of sediment trend to higher Al(VI) at given Ti compared to those from basanite melts. While clinopyroxenes from phlogopite clinopyroxenite xenoliths plot with experimental samples, MARID clinopyroxenes are devoid of Al(VI) and plot at very low  $\text{Al}_2\text{O}_3$  at given  $\text{Na}_2\text{O}$  (C). (For interpretation of the references to colour in this figure legend, the reader is referred to the web version of this article.)

zone towards the sediment and basanite capsule half. Omphacitic clinopyroxene from the sediment shows higher Al(VI) per f.u. (formula unit) (0.2–0.5) at lower Ti per f.u. (< 0.015) than those from basanite which attain Al(VI) per f.u. of 0.1–0.2 at Ti per f.u. of 0.01–0.03 (Fig. 3B), while total contents of  $\text{Al}_2\text{O}_3$  and  $\text{Na}_2\text{O}$  are similar between sediment and basanite clinopyroxenes across the reaction zone (Fig. 3C). Phlogopite formed by sediment/dunite reaction shows > 8 wt %  $\text{K}_2\text{O}$  and 0.1–0.5 wt%  $\text{Na}_2\text{O}$  as well as 10–17 wt%  $\text{Al}_2\text{O}_3$  and 0.1–1.4 wt%  $\text{TiO}_2$ , while those from basanite/dunite reaction have higher  $\text{Na}_2\text{O}$  of 0.8–1.7 wt% and 2.2–2.6 wt%  $\text{TiO}_2$  (Fig. 4A, B). Experimental phlogopite has compositions similar to those from post-collisional lavas but show generally higher contents of  $\text{Al}_2\text{O}_3$  similar to those in phlogopite of phl-clinopyroxenites xenoliths (Fig. 4B). Garnet from sediment/dunite reaction is lower in MgO (< 13 wt%) and higher in MnO (> 3 wt%), compared to that from basanite/dunite reaction,

which attains > 21 wt% MgO (Table 3).

### 3.3. Trace element composition

N-MORB normalized trace element pattern of sediment/dunite reaction melts are high in large ion lithophile elements (LILE), high field strength elements (HFSE), and show pronounced negative anomalies at Nb, P, and Ti (Fig. 5A). The pattern overall follows that of post-collisional lavas with  $\text{K/Na} > 2$  (Conticelli et al., 2007; Prelević et al., 2013; Prelević et al., 2008b), while the starting bulk sediment composition shows higher heavy rare earth elements (REE) and lower LILE. The N-MORB normalized trace element patterns of basanite/dunite reaction melts (Fig. 5B) show lower mass fractions for LILE and a slight negative anomaly for Ti. The reaction melts fall broadly within the array found for post-collisional lavas showing low  $\text{K/Na}$  of 0.5–1

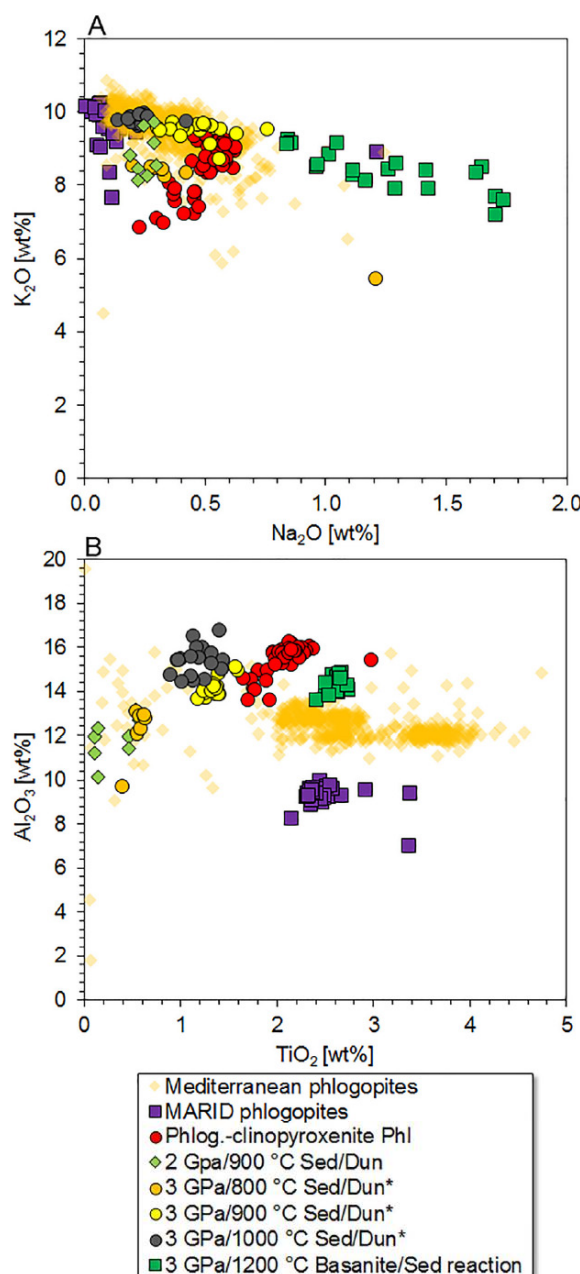


Fig. 4. Compositions of phlogopites from experiments (lime diamonds 2 GPa/ 900 °C; orange circles 3 GPa/800 °C; yellow circles 3 GPa/900 °C; grey circles 3 GPa/1000 °C; green squares 3 GPa/1200 °C) compared to phlogopites in post-collisional lavas (Fritschle et al., 2013), phlogopite clinopyroxenite xenoliths (red circles), and MARID phlogopites (purple squares) (Förster et al., 2018; Förster et al., 2017). (A) K<sub>2</sub>O versus Na<sub>2</sub>O shows that experimental phlogopites from sediment/dunite reaction (circles) plot at Na<sub>2</sub>O < 0.5 wt%, while those from basanite/dunite reaction (green squares) attain 0.8–1.7 wt% Na<sub>2</sub>O. (B) Al<sub>2</sub>O<sub>3</sub> versus TiO<sub>2</sub> shows that experimental phlogopites attain 10–17 wt% Al<sub>2</sub>O<sub>3</sub> and 0.2–1.5 wt% TiO<sub>2</sub> for sediment/dunite reaction and 2–2.5 wt% for basanite/dunite reaction. Phlogopites from post-collisional lavas show a wide range with most data points at 12–14 wt% Al<sub>2</sub>O<sub>3</sub> and 2–4 wt% TiO<sub>2</sub>, while phlogopites from phlogopite clinopyroxenite xenoliths attain higher Al<sub>2</sub>O<sub>3</sub> of 13–16 wt % at 1.5–2.2 wt% TiO<sub>2</sub>. MARID-phlogopites show overall lower Al<sub>2</sub>O<sub>3</sub> values at similar TiO<sub>2</sub>. (For interpretation of the references to colour in this figure legend, the reader is referred to the web version of this article.)

(Prelević et al., 2013; Prelević et al., 2008b). K-rich lavas with K/Na of 1–2 show both geochemical signatures as present in rocks with K/Na of 0.5–1 and K/Na > 2 (Fig. 5) and thus form a transient group where rocks can be formed by ‘orogenic’ and ‘anorogenic’ processes. CI-Chondrite normalized REE of clinopyroxene are steeper for sediment/dunite reaction experiments compared to basanite/dunite reaction (Fig. 6A), while CI-Chondrite normalized garnet of both reaction experiments are nearly identical in composition (Fig. 6B). Garnet that crystallized from the sediment melting experiment, however, has lower mass fractions of light REE (Fig. 6B). The mass fractions of compatible trace elements within phlogopite (Fig. 7) of both experiments from sediment/dunite and basanite/dunite reaction fall within the broad range reported for phlogopites in post-collisional lavas (Fritschle et al., 2013). Partitioning coefficients for clinopyroxene/melt, garnet/melt, and phlogopite/melt for both sediment/dunite and basanite/dunite reaction are generally < 1 except the heavy REE in garnet and LILE in phlogopite (Fig. 8A–C). Trace element distribution between clinopyroxene and garnet are largely controlled by the strong differences in trace element partitioning in clinopyroxene/melt which reaches higher values for sediment/dunite reaction (Fig. 8D). Ratios of Th/La versus Sm/La, Th/Yb versus Nb/Yb, and Sm/Nd versus Rb/Sr show that sediment/dunite reaction melts plot with post-collisional lavas (Prelević et al., 2008b) (Fig. 9A–C). Those from basanite/dunite reaction attain the lowermost ratios of Th/La, Rb/Sr, and high Nb/Yb at the end of the spectrum found within post-collisional lavas. Lithium is generally enriched in sediments as well as melts of sediment and phlogopites that form from sediment-melt/dunite reaction (Fig. 9D). In contrast, basanite/dunite reaction melts and phlogopites are very low in Li.

#### 4. Discussion

##### 4.1. Sediment/dunite reaction

The reaction of melts of sediment with refractory mantle (dunite) generally lead to the formation of a strongly layered reaction zone and the reorganization of elements from both domains into metasomatic phases (Fig. 1B). Silica is the most mobile element as evident from orthopyroxene veins on olivine grain boundaries, followed by K and Al in phlogopite, and Ca in clinopyroxene. The infiltrating reaction melts show a general trend of decrease in SiO<sub>2</sub> with increasing temperature and melt fraction, thus diluting SiO<sub>2</sub> within the liquid (Fig. 2, Table 1). Generally, K<sub>2</sub>O is enriched and K/Na ratios are higher in melts compared to the starting sediment composition (Fig. 2B, C). The trace element concentrations of experimental glasses show a steepened pattern from LILE, HFSE, and light REE to heavy REE when compared to the starting sediment composition (Fig. 5A). Bulk sediment trace element contents are too low in LILE and too high in heavy REE to satisfy the values observed for post-collisional lavas, while experimental melt compositions fall within the range of natural rocks with K/Na > 2 (Prelević et al., 2008b). The mass fraction of K in the melt is controlled by the composition of the phases in the residue of the reacted sediment, which are clinopyroxene and garnet, and thus devoid of K (Fig. 3, Table 1). Clinopyroxene shows a strong zonation across the reaction zone from a diopsidic end-member within the dunite towards an omphacitic composition within the reacted sediment (Fig. 3A), thus transforming the residual sediment to an eclogite-like assemblage. The K-rich, rhyolitic melt formed from the sediment infiltrates and reacts with olivine following the reaction: Si-rich melt + olivine → phlogopite + pyroxene + garnet. This reaction takes place in all sediment/dunite reaction experiments. Since the solidus increases from 800 °C for the sediment to ~1150 °C for phlogopite-pyroxenite (Förster et al., 2017), the melt is gradually consumed. Phlogopite formed during this reaction shares strong similarities to that occurring in metasomatic phlogopite clinopyroxenite mantle xenoliths (Fig. 4), while they possess slightly higher Al<sub>2</sub>O<sub>3</sub> than those in post-collisional lavas (Fritschle et al., 2013). However, compatible trace elements are within the range



Table 3

Average analyses for silicate phases in the experiments (oxides in wt%).

Olivine	Na <sub>2</sub> O	K <sub>2</sub> O	MnO	SiO <sub>2</sub>	MgO	FeO	Al <sub>2</sub> O <sub>3</sub>	Cr <sub>2</sub> O <sub>3</sub>	CaO	TiO <sub>2</sub>	Total
1 GPa/900 °C Sediment/Dunite reaction	0.01(1)	0.01(1)	0.17(2)	40.3(1)	50.5(2)	8.6(1)	0.01(1)	0.03(2)	0.06(1)	0.01(1)	99.7(2)
2 GPa/900 °C Sediment/Dunite reaction	0.02(2)	0.01(1)	0.13(2)	40.5(1)	50.5(1)	8.61(4)	0.02(1)	0.03(2)	0.04(1)	0.01(1)	99.8(3)
3 GPa/1200 °C Basanite/Dunite reaction	0.01(1)	0.01(1)	0.35(9)	41.4(6)	55(1)	5(2)	0.03(2)	0.05(3)	0.06(4)	0.02(1)	102(1)
<i>Phlogopite</i>											
2 GPa/900 °C Sediment/Dunite reaction	0.25(5)	9.6(4)	0.06(6)	41(1)	25(2)	3.2(5)	13(1)	0.5(4)	0.2(4)	0.5(4)	94(1)
3 GPa/1200 °C Basanite/Dunite reaction	1.1(3)	8.8(6)	0.03(3)	39.6(9)	23.7(8)	4.4(4)	15.1(3)	0.2(2)	0.09(5)	2.2(5)	96(1)
<i>Clinopyroxene</i>											
1 GPa/900 °C Sediment/Dunite reaction	0.7(1)	0.12(6)	0.6(4)	49.0(7)	11(1)	9.7(1)	5(2)	0.04(2)	21.2(6)	1.8(3)	99.24(6)
2 GPa/900 °C Sediment/Dunite reaction	1.6(2)	0.4(7)	0.9(4)	50(2)	11(2)	4(1)	11(2)	0.04(2)	18(2)	0.48(7)	97(1)
3 GPa/1200 °C Basanite/Dunite reaction	2.2(3)	0.01(1)	0.10(3)	53.3(6)	15.9(8)	4.5(5)	6(1)	0.13(9)	18.2(5)	0.8(1)	100.9(6)
<i>Orthopyroxene</i>											
3 GPa/1200 °C Basanite/Dunite reaction	0.07(3)	0.01(2)	0.48(3)	58.2(4)	38.8(6)	2.1(8)	1.4(1)	0.12(4)	0.59(5)	0.05(1)	101.9(4)
<i>Garnet</i>											
2 GPa/900 °C Sediment/Dunite reaction	0.3(2)	0.2(1)	6(2)	40(1)	7.3(5)	10.4(4)	20(1)	0.06(4)	13.7(6)	1.4(4)	99(1)
4 GPa/1000 °C Sediment melting	0.14(2)	0.01(1)	3(2)	42.0(7)	13(5)	8(3)	21.9(4)	–	12(3)	0.8(2)	101(2)
3 GPa/1200 °C Basanite/Dunite reaction	0.08(8)	0.01(2)	0.8(4)	42(1)	21(4)	8(4)	22(2)	2(3)	5(2)	0.7(6)	101.6(5)

The number in parentheses is the first standard deviation on the last digit.

reported for phlogopite phenocrysts and xenocrysts in post-collisional lavas (Fritschle et al., 2013) (Fig. 7). Re-melting of the metasomatized dunite in a 2nd-stage capsule experiment produced melts with K<sub>2</sub>O mass fractions of 8–9 wt% (Fig. 2) and demonstrated that high-K lavas can form in a multi-stage metasomatism and melting process (Förster et al., submitted).

#### 4.2. Hydrous-basanite/dunite reaction

The reaction of melt of hydrous basanite with dunite also leads to strong layering and re-organization of elements from both domains into metasomatic phases. Silicon, K, Al, and Ca are the most mobile elements and caused the crystallisation of a phlogopite-bearing pyroxenite in place of dunite (Fig. 1A). Between melt and dunite, an eclogite layer formed, solely composed of garnet and clinopyroxene. Clinopyroxene shows a trend from diopside composition within the dunite to omphacite within the garnet-clinopyroxene layer (Fig. 3A). Analogous to the sediment/dunite reaction, melts in the basanite/dunite reaction show higher K<sub>2</sub>O and K/Na than the starting composition and plot within the array of post-collisional lavas with K/Na < 2 (Fig. 2). Trace element compositions of both the basanite starting composition and melts formed in the reaction zone fall within the range for post-collisional lavas with K/Na 0.5–1 (Prelević et al., 2008b). In contrast to the sediment/dunite reaction, the melt in the basanite/dunite reaction experiments is SiO<sub>2</sub>-undersaturated, yet the reaction leads to the formation of phlogopite pyroxenites (Hirschmann et al., 2003). Since the experiment is conducted above the solidus of phlogopite pyroxenite and phlogopite peridotite (Condamine et al., 2016; Förster et al., 2017), the melt present in the capsule is not consumed by the reaction, thus: hydrous basanite + dunite → phlogopite + pyroxene + garnet + melt. While the melt on the product side still corresponds to basanite according to the total alkali versus silica diagram (Fig. 1A), it is more foiditic in composition and contains higher alkalis than the starting basanite which lies at the border to trachybasalt. Phlogopites are higher in Na<sub>2</sub>O and TiO<sub>2</sub> compared to those from melts of sediment/dunite reaction (Fig. 4) and reflect higher Na<sub>2</sub>O partitioning and content of the basanitic melt. However, compatible trace elements of phlogopites (Fig. 7) are similar to those within post-collisional lavas and show lower Cs, and higher Ni compared to those from melts of sediment/dunite reaction (Fritschle et al., 2013).

#### 4.3. Trace element partitioning

For both starting materials, sediment and basanite, trace element

contents of reaction melts were enriched in LILE, HFSE, and light REE, while heavy REE were found to be depleted (Fig. 5). Partitioning is controlled by the two main minerals of the residue, clinopyroxene and garnet, which incorporate mainly light REE and heavy REE, respectively (Fig. 6). Partition coefficients for clinopyroxene/melt are generally below unity except for Nd-Eu and slightly prefers light REE over heavy REE for the sediment/dunite reaction melts (Fig. 8A), while those from the basanite/dunite reaction melt show a preference of heavy REE over light REE, which is in agreement with previous studies (Foley et al., 1996; Hauri et al., 1994; Johnston and Schwab, 2004; Wang and Foley, 2018). Partition coefficients are higher for sediment/dunite reaction melts than basanite/dunite reaction melts as a result of their stronger polymerized Si-rich compositions (Nash and Crecraft, 1985), and are even higher for Si-rich phyllite melts from Wang and Foley (2018). Garnet/melt partitioning is strongly dependant on the garnet composition, which is almandine-rich (Fe-rich) for the sediment/dunite and pyrope-rich (Mg-rich) for the basanite/dunite reaction experiments (Table 3). Heavy REE are strongly compatible in both garnet types (Fig. 6B), while garnet/melt partition coefficients are slightly higher for light REE for the almandine-rich garnet in the sediment/dunite reaction experiments (Fig. 8B). For both garnet types, the slope is clearly positive, denoting their strong preference for heavy REE over light REE (Johnson, 1998; Pertermann et al., 2004; Shimizu and Kushiro, 1975; van Westrenen et al., 2001; Wang and Foley, 2018). For sediment/dunite garnets, partitioning is above unity for elements to the right of Nd, while for basanite/dunite garnets, they are above unity from Dy onwards (Fig. 8B). Partitioning between phlogopite/melt is above unity for Cs-Ba and Ti in the sediment/dunite reaction melts and for Rb, Ba, and Ti for the basanite/dunite reaction melts (Fig. 8C) similar to natural phlogopites in lamprophyre and basanite (Foley et al., 1996; LaTourrette et al., 1995). Distribution between clinopyroxene and garnet shows that within the residue of both sediment/dunite and basanite/dunite reaction pairs, light REE are enriched into clinopyroxene and heavy REE into garnet (Fig. 8D).

#### 4.4. Trace elements as indicators for recycling- and mantle melting processes

Trace element distribution patterns in melts produced by sediment/dunite reaction and basanite/dunite reaction show that both produce distinct signatures that can be found within post-collisional lavas (Fig. 5). While lavas with K/Na > 2 are extremely enriched in LILE and HFSE with pronounced negative anomalies at Nb, P, and Ti, those with K/Na 0.5–1 are less enriched and show a negative Rb, P, and Ti-



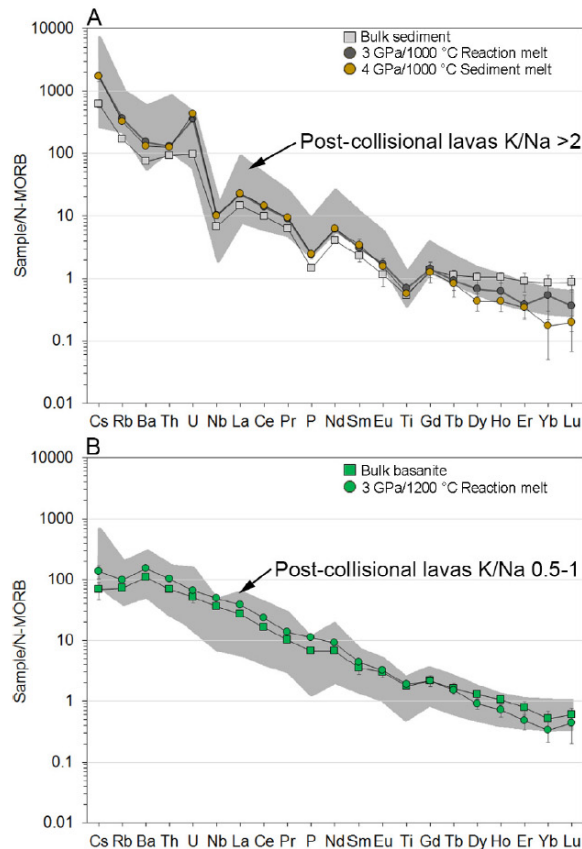


Fig. 5. Trace element compositions of starting materials (grey squares, sediment; green squares, basanite) compared to experimental melts (grey circles 3 GPa/1000 °C; brown circles 4 GPa/1000 °C; green circles 3 GPa/1200 °C) and post-collisional lavas (shaded area) (Prelević et al., 2008b). The sediment/dunite reaction melts (A) are rich in Cs, Rb, Ba, and show negative anomalies at Nb, P, and Ti, similar to post-collisional lavas with  $K/Na > 2$ . The basanite/dunite reaction melt (B) shows lower Cs, Rb, Ba, and is devoid of any pronounced anomaly. The observed pattern plots within post-collisional lavas that overall show lower  $K/Na$  of 0.5–1.0. Normalized to N-MORB (Sun and McDonough, 1989). (For interpretation of the references to colour in this figure legend, the reader is referred to the web version of this article.)

anomaly. Due to enrichment of LILE, HFSE, and light REE over heavy REE during sediment melting and reaction, the negative anomalies at Nb, P, and Ti of the bulk sediment composition are pronounced within the sediment/dunite reaction melts. This strongly suggests that Nb, P, and Ti anomalies within  $K/Na > 2$  post-collisional lavas are inherited from a source mantle that had been metasomatized by a sediment-derived melt (Prelević et al., 2013; Prelević et al., 2008b). The basanite/dunite reaction melt behaves in a similar way to the sediment/dunite reaction melts and LILE, HFSE, and light REE are enriched over heavy REE. However, the basanite/dunite reaction melts show a negative Rb anomaly (Fig. 5B), which results from Rb/Cs fractionation during the formation of phlogopite which has contrasting  $D_{Rb}$  of  $\sim 6.5$  and  $D_{Cs}$  of  $\sim 0.25$ , thus slightly enriching Cs in the melt (Fig. 8 C). The strong enrichment of Th over REE within  $K/Na > 2$  post-collisional lavas is evident in the Th/La versus Sm/La plot and Th/Yb versus Nb/Yb where post-collisional lavas attain high Th/La and Th/Yb (Fig. 9A, B). The grouping of sediment/dunite and basanite/dunite reaction melts around their starting composition at Th/La  $\sim 0.3$ , Sm/Nd 0.1–0.2 and at Th/La  $\sim 0.1$ , Sm/La 0.5–2.0 suggests that variations within post-collisional lavas reflect heterogeneities already within their source

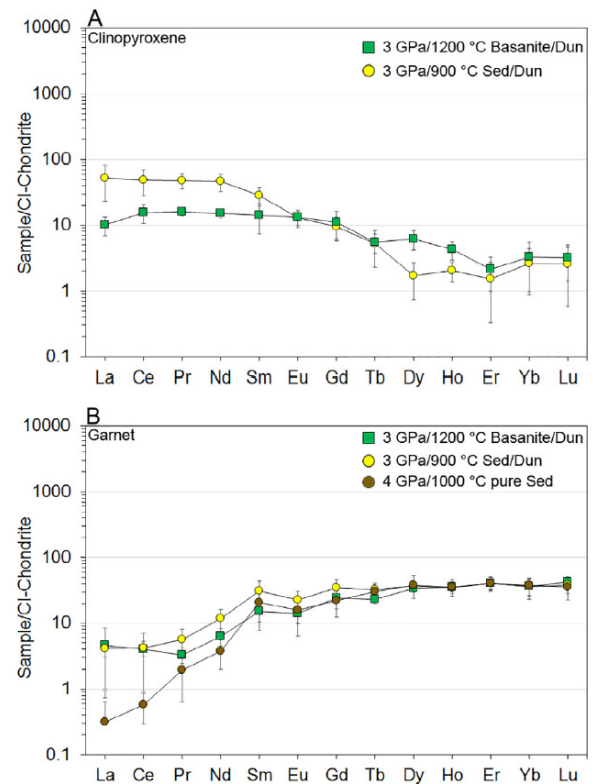


Fig. 6. Chondrite-normalized REE patterns of clinopyroxene (A) and garnet (B) of samples from basanite/dunite (green squares), sediment/dunite reaction (yellow circles), and pure sediment melting (brown circles). Clinopyroxene samples from sediment/dunite reaction show higher light REE to heavy REE fractionation than those from basanite/dunite reaction (A). Garnet samples from sediment/dunite and basanite/dunite reaction experiments are similar in composition and attain higher light REE than those from pure sediment melting experiments (B), while their heavy REE signatures are nearly identical. (For interpretation of the references to colour in this figure legend, the reader is referred to the web version of this article.)

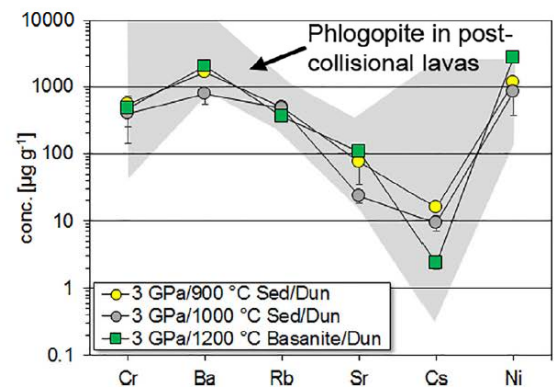


Fig. 7. Concentration of compatible trace elements (Cr, Ba, Rb, Sr, Cs, Ni) in phlogopite from experiments (yellow circles 3 GPa/900 °C; grey circles 3 GPa/1000 °C; green squares 3 GPa/1200 °C) compared to samples from post-collisional lavas (Fritschle et al., 2013). All experimental samples from basanite/dunite and sediment/dunite reaction fall within the range observed for phlogopites in post-collisional lavas regardless of starting material. (For interpretation of the references to colour in this figure legend, the reader is referred to the web version of this article.)

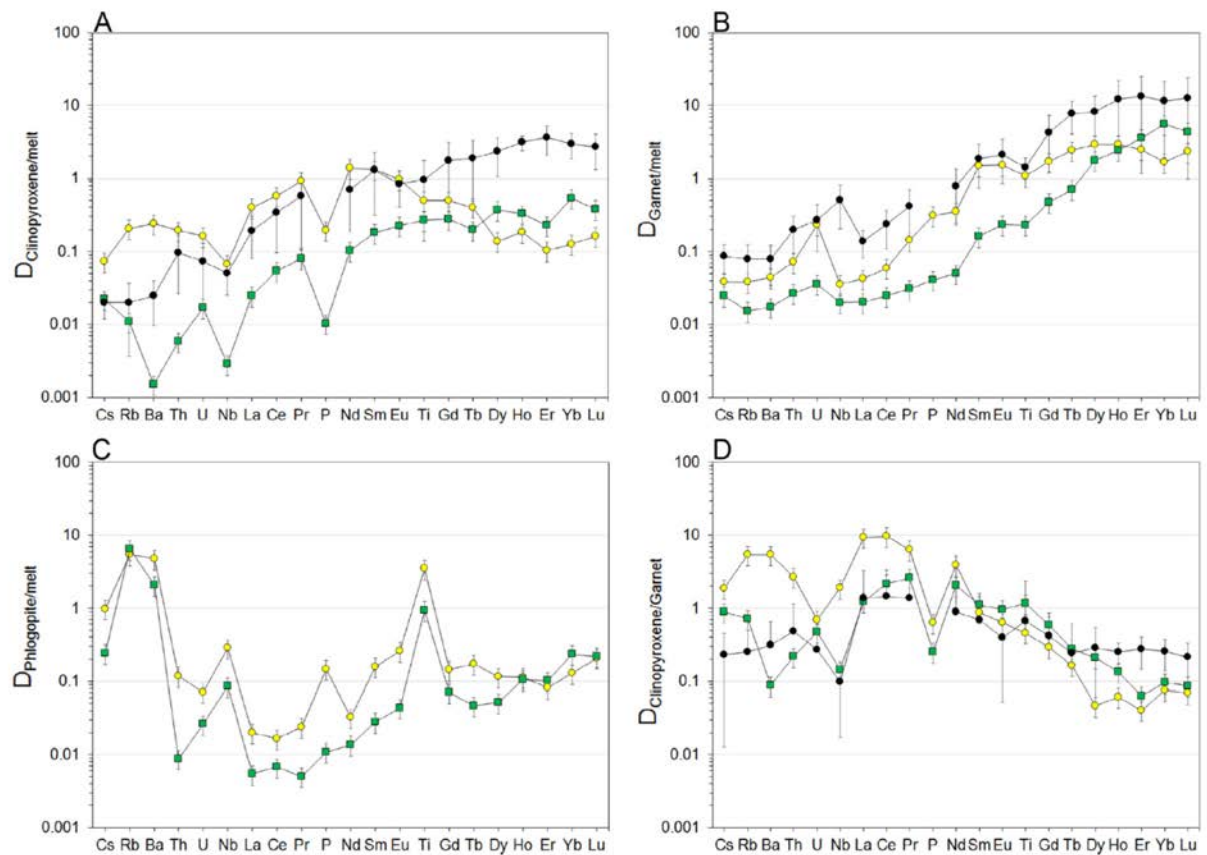


Fig. 8. Partition coefficients for trace elements of (A) clinopyroxene/melt (B) garnet/melt (C) phlogopite/melt pairs, and (D) clinopyroxene/garnet from sediment/dunite experiment at 3 GPa/900 °C (yellow circles) and basanite/dunite reaction at 3 GPa/1200 °C (green circles) compared to values from Wang et al. (2018) (black circles). Generally, partition coefficients are higher for the sediment/dunite experiment than basanite/dunite with the exception of heavy REE. Partition coefficients are generally < 1 for mineral/melt (A–C) except for heavy REE in garnet (B) and Cs, Rb, Ba, and Ti in phlogopite (C). Partitioning of trace elements between clinopyroxene and garnet (D) is mainly influenced by partitioning of clinopyroxene and melt (A). (For interpretation of the references to colour in this figure legend, the reader is referred to the web version of this article.)

components (Fig. 9A). In both experimental samples and post-collisional lavas, Th/Yb versus Nb/Yb are positively correlated (Fig. 9B). Mantle melts attain lowest Th/Yb and high Nb/Yb as evident from the basanite/dunite reaction experiments and MARID compositions (Förster et al., 2018), while those from sediment/dunite reaction attain highest Th/Yb and low Nb/Yb. Since sediment/dunite and basanite/dunite reaction melts form parallel trending lines and overlap with the bulk starting material compositions, differences in Th/Yb versus Nb/Yb are inherited from the composition of the source material. Basanite/dunite reaction melts also attain lowest Rb/Sr, identical with the bulk starting material composition at similar Sm/Nd to the sediment/dunite reaction melts which attain higher Rb/Sr than their starting composition and thus show higher  $D_{Rb}$  than  $D_{Sr}$  during melting and reaction (Fig. 9C). While a small proportion of samples from post-collisional lavas show high Rb/Sr > 0.2 similar to the sediment/dunite reaction melts, most analysed samples plot at Rb/Sr of ~0.1, thus between sediment/dunite and basanite/dunite reaction melts. In the Rb versus Li plot, phlogopites attain highest Rb concentrations in accordance with  $D_{Rb}$  (phlogopite/melt) of ~6.5 for basanite/dunite and ~5 for sediment/dunite reaction experiments (Fig. 9D). Lithium, a generally incompatible element attains  $D_{Li}$  (phlogopite/melt) of ~0.7 for both basanite/dunite and sediment/dunite reaction melts. Lithium concentrations of generally 10–60  $\mu\text{g g}^{-1}$  to up to 220  $\mu\text{g g}^{-1}$  are common within post-collisional lavas (Foley et al., 2013) and can be explained

by concentrations of 15–85  $\mu\text{g g}^{-1}$  to up to 310  $\mu\text{g g}^{-1}$  within recycled sediments.

#### 4.5. Melts of sediment- versus mantle melt-metasomatism

Irrespective of starting composition, the reaction of hydrous melt with refractory peridotite leads to metasomatic overprinting of the peridotite and enrichment in K, Al, Si, LILE, HFSE, and light REE. However, metasomes formed by reaction between melts of sediment/dunite and basanite/dunite pairs show significant differences in major and trace element concentrations. Metasomes formed by melts of sediment are generally more strongly enriched in LILE (especially Cs) with higher Li, Th/La, Th/Yb, and Rb/Sr compared to those formed by mantle melts (Figs. 5, 9), and likely represent the source for post-collisional lavas with high K/Na of > 2 of ‘orogenic’ origin such as shoshonites, Roman-type lavas, and lamproites (Prelević et al., 2008b). Phlogopite formed by melts of sediment/dunite reaction is lower in Na<sub>2</sub>O and TiO<sub>2</sub> than that from basanite/dunite reaction and reflects the low Ti, Na composition of recycled sediments as well as lower  $D_{Na}$  and  $D_{Ti}$  induced by lower temperature (Righter and Carmichael, 1996) (Fig. 4). Additionally, phlogopites formed by hydrous basanite/dunite reaction shows lowest Cs concentrations, which reflect its low concentrations in the basanite starting composition (Fig. 7). While subduction and melts of sediment/dunite reaction generally occurs at



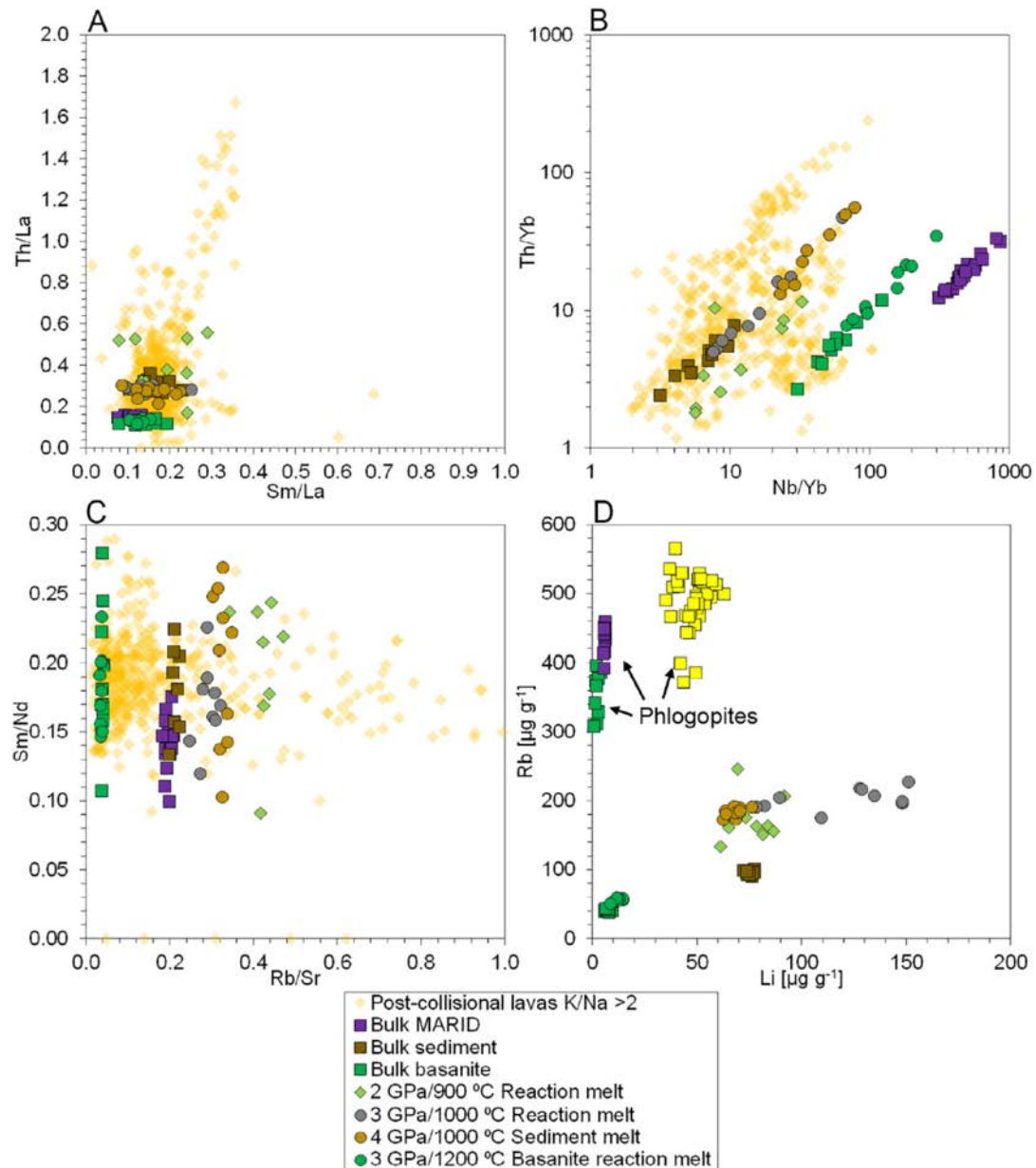


Fig. 9. Trace element compositions of experimental melts (lime diamonds 2 GPa/900 °C; grey circles 3 GPa/1000 °C; brown circles 4 GPa/1000 °C; green squares 3 GPa/1200 °C) compared to post-collisional lavas (yellow diamonds) and MARID xenoliths (purple squares). (A) Th/La versus Sm/La shows experimental sediment/dunite reaction melts at Th/La 0.2–0.6, plotting with the bulk of post-collisional lavas, while basanite/dunite reaction melts plot at Th/La < 0.2 with MARID xenoliths. (B) Th/Yb versus Nb/Yb of sediment/dunite reaction melts plot with post-collisional lavas, while basanite/dunite reaction melts and MARID xenoliths attain higher Nb/Yb ratios and plot largely outside the field of post-collisional lavas. (C) Sm/Nd versus Rb/Sr shows that sediment/dunite reaction melts largely at Rb/Sr > 0.2 while most post collisional lavas plot around Rb/Sr of 0.1. Samples from basanite/dunite reaction are very low in Rb/Sr and attain ratios of 0.04. (D) In the Rb versus Li plot, sediment/dunite reaction melts attain high Li mass fractions of 50–150  $\mu\text{g g}^{-1}$ , while corresponding phlogopites (yellow squares) attain similar mass fractions of Li (50  $\mu\text{g g}^{-1}$ ). Basanite/dunite reaction melts and corresponding phlogopites (green squares) attain low Li mass fractions of < 20  $\mu\text{g g}^{-1}$  similar to MARID phlogopites (purple squares). (For interpretation of the references to colour in this figure legend, the reader is referred to the web version of this article.)

temperatures < 1000 °C, below the solidus of phlogopite pyroxenites (~1150 °C), the metasome formation in this scenario consumes all melt and requires a secondary activation of the metasome by later heat input from the asthenosphere which is enabled by e.g. slab rollback as evident from Turkey and Mexico (Gülmez et al., 2016; Vigouroux et al., 2008). The hydrous basanite/dunite reaction differs from the sediment/dunite

experiments since the reaction takes place above the solidus of phlogopite pyroxenites and phlogopite peridotite (Condamine et al., 2016; Förster et al., 2017), and thus the melt is not completely consumed during the reaction. Instead, the percolating and reacting melt attains a K-rich composition by crystallizing an eclogite-like layer, bearing omphacitic, Na-rich, clinopyroxene in contact with the dunite (Fig. 3A).

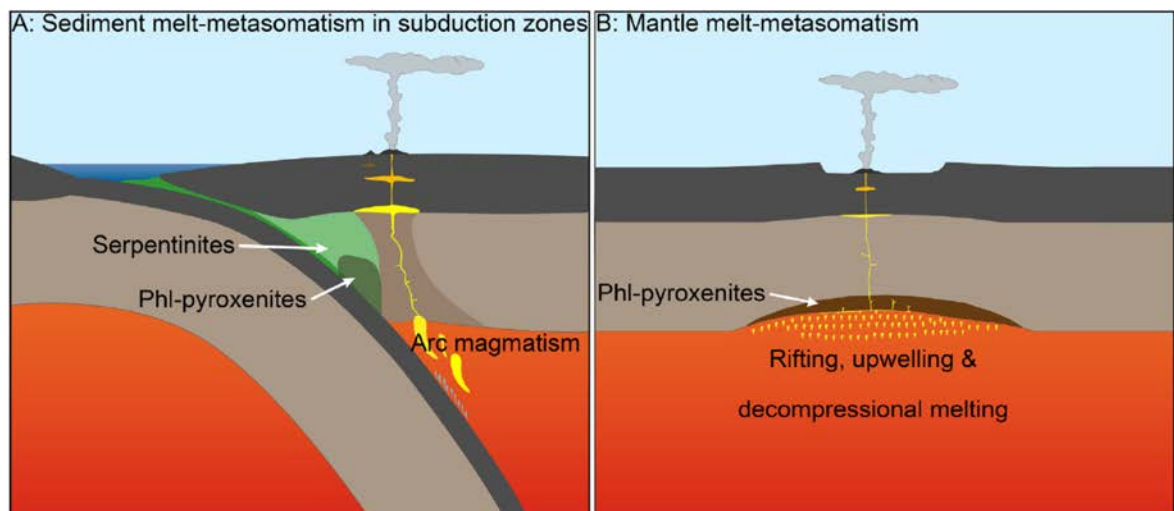


Fig. 10. Melts of sediment- metasomatism in a subduction zone (A) and mantle melt-metasomatism in a rifting & upwelling scenario. In both cases metasomatism leads to the formation of phlogopite pyroxenites and enrichment of the lithospheric mantle in K.

Thus, the melt dynamically increases its K/Na by leaving behind a low K/Na eclogite, while the dunite next to it is strongly enriched in phlogopite and orthopyroxene (Fig. 1A). Since hydrous melting of eclogite leads to the formation of low K/Na tonalitic melt which would dilute high K/Na melt from the phlogopite pyroxenites of the metasomatized dunite, maximum K/Na is limited by equilibrium with eclogite (Lambert and Wyllie, 1970; Xiong, 2006). Thus, the basanite/dunite reaction melts might represent post-collisional lavas with lower K/Na of 0.5–1 of ‘anorogenic’ origin such as melilitites and nephelinites (Tappe et al., 2007), K-rich foidites/basanites (Tappe et al., 2016), ultramafic lamprophyres (Vetter et al., 2017), and kamafugites (Foley et al., 1987; Prelević et al., 2008a; Rosenthal et al., 2009), which is in accordance with the lower content of LILE, HFSE and low Th/La and Th/Nb (Figs. 5, 9). However, if the eclogite-pyroxenite metasome delaminates as a result of the high density of eclogite (Elkins-Tanton and Foulger, 2005), it could lead to melting of the phlogopite pyroxenites and lavas of ‘anorogenic’ origin can reach K/Na > 1 which might explain the mixed appearance of ‘orogenic’ and ‘anorogenic’ rocks at K/Na of 1–2.

## 5. Conclusion

In this study we reacted layered sediment/dunite and hydrous basanite/dunite experiments at thermobaric conditions of 1–4 GPa/800–1200 °C that represent a subduction environment (Fig. 10A) for the sediment/dunite, and a lithospheric mantle environment unrelated to subduction zones (Fig. 10B) for the hydrous basanite/dunite reaction experiments.

- All experiments show the growth of a reaction zone between both starting materials, which is strongly enriched in K, Al, and Si as evident from metasomatically grown phases such as pyroxene and phlogopite (Fig. 1).
- The melt of sediment is highly enriched in LILE, HFSE, and light REE similar to post collisional lavas with K/Na > 2 (Fig. 5A) and shows high Th/La, Th/Yb, and Rb/Sr (Fig. 9).
- Since the products of the reaction of melts of sediment with dunite are below their hydrous solidus, all melt is consumed as it reacts with the refractory peridotite. In a subduction zone scenario this leads to progressive growth of metasomatic phlogopite pyroxenite within the fore-arc (Fig. 10A), which is only activated after the cessation of subduction during asthenospheric upwelling by slab

rollback, tear, or break-off.

- Melts of the hydrous basanite/dunite reaction experiments show LILE, HFSE, and REE patterns similar to lavas in post-collisional settings with K/Na of 0.5–1 (Fig. 5B). In contrast to sediment/dunite reaction melts, the hydrous basanite/dunite reaction melts are low in Th/La, Th/Yb, and Rb/Sr and high in Nb/Yb (Fig. 9).
- Upwelling of asthenospheric mantle due to e.g. stretching and rifting of the lithosphere (Fig. 10B) leads to incipient melting of the asthenosphere and metasomatic growth of phlogopite pyroxenites within the lithospheric mantle. The enrichment of K within the lithospheric mantle is thus not dependent on the migration of liquids that are originally ultrapotassic.

## Declaration of interests

The authors declared that there is no conflict of interest.

## Acknowledgements

We gratefully acknowledge Qing Xiong for providing the dunite sample ZD11–53 used in the experiments. The International Ocean Discovery Project (IODP) supported this study in providing the Mediterranean marine sediment sample from sampling site 161-976. This work is part of the lead author's PhD thesis supported by an Australian Government International Postgraduate Research Scholarship (IPRS) and Postgraduate Research Fund (PGRF). Thomas Kautz of the Goethe University, Frankfurt assisted with the belt apparatus experiments. DP was supported through the Deutsche Forschungsgemeinschaft (DFG) project PR 1072/9-1. This is contribution 1334 from the ARC Centre of Excellence for Core to Crust Fluid Systems (<http://www.ccfsc.mq.edu.au>) and 1307 in the GEMOC Key Centre (<http://www.gemoc.mq.edu.au>).

## Appendix A. Supplementary data

Supplementary data to this article can be found online at <https://doi.org/10.1016/j.jseas.2019.03.014>.

## References

Avanzinelli, R., Elliott, T., Tommasini, S., Conticelli, S., 2007. Constraints on the genesis



- of potassium-rich Italian volcanic rocks from U/Th disequilibrium. *J. Petrol.* 49, 195–223.
- Campbell, I.H., Stepanov, A.S., Liang, H.-Y., Allen, C.M., Norman, M.D., Zhang, Y.-Q., Xie, Y.-W., 2014. The origin of shoshonites: New insights from the Tertiary high-potassium intrusions of eastern Tibet. *Contrib. Miner. Petrol.* 167, 983.
- Condamine, P., Médard, E., 2014. Experimental melting of phlogopite-bearing mantle at 1 GPa: Implications for potassic magmatism. *Earth Planet. Sci. Lett.* 397, 80–92.
- Condamine, P., Médard, E., Devidal, J.-L., 2016. Experimental melting of phlogopite-peridotite in the garnet stability field. *Contrib. Miner. Petrol.* 171, 95.
- Conticelli, S., Avanzinelli, R., Ammannati, E., Casalini, M., 2015. The role of carbon from recycled sediments in the origin of ultrapotassic igneous rocks in the Central Mediterranean. *Lithos* 232, 174–196.
- Conticelli, S., Avanzinelli, R., Poli, G., Brasci, E., Giordano, G., 2013. Shift from lamproite-like to leucititic rocks: Sr–Nd–Pb isotope data from the Monte Cimino volcanic complex vs. the Vico stratovolcano, Central Italy. *Chem. Geol.* 353, 246–266.
- Conticelli, S., Carlson, R.W., Widom, E., Serri, G., 2007. Chemical and isotopic composition (Os, Pb, Nd, and Sr) of Neogene to Quaternary calc-alkalic, shoshonitic, and ultrapotassic mafic rocks from the Italian peninsula: Inferences on the nature of their mantle sources. *Cenozoic Volcanism Mediterranean Area* 418, 171.
- Conticelli, S., Peccerillo, A., 1992. Petrology and geochemistry of potassic and ultrapotassic volcanism in central Italy: Petrogenesis and inferences on the evolution of the mantle sources. *Lithos* 28, 221–240.
- Edgar, A.D., Mitchell, R.H., 1997. Ultra high pressure–temperature melting experiments on an SiO<sub>2</sub>-rich lamproite from Smoky Butte, Montana: Derivation of siliceous lamproite magmas from enriched sources deep in the continental mantle. *J. Petrol.* 38, 457–477.
- Elkins-Tanton, L.T., Foulger, G.R., 2005. Continental magmatism caused by lithospheric delamination. *Spec. Papers-Geol. Soc. Am.* 388, 449.
- Erlank, A.J., 1987. Evidence for mantle metasomatism in peridotite nodules from the Kimberley pipes, South Africa. In: *Mantle metasomatism*, pp. 221–311.
- Fekiacova, Z., Mertz, D.F., Hofmann, A.W., 2007. Geodynamic setting of the Tertiary Hoheifel volcanism (Germany), part II: Geochemistry and Sr, Nd and Pb isotopic compositions. In: *Mantle Plumes*. Springer, pp. 207–239.
- Foley, S., 1992. Vein-plus-wall-rock melting mechanisms in the lithosphere and the origin of potassic alkaline magmas. *Lithos* 28, 435–453.
- Foley, S., Venturelli, G., Green, D.H., Toscani, L., 1987. The ultrapotassic rocks: Characteristics, classification, and constraints for petrogenetic models. *Earth Sci. Rev.* 24, 81–134.
- Foley, S.F., Jackson, S.E., Fryer, B.J., Greenough, J.D., Jenner, G.A., 1996. Trace element partition coefficients for clinopyroxene and phlogopite in an alkaline lamprophyre from Newfoundland by LAM-ICP-MS. *Geochim. Cosmochim. Acta* 60, 629–638.
- Foley, S.F., Pinter, Z., 2018. Primary melt compositions in the Earth's Mantle. In: *Magmas Under Pressure*. Elsevier, pp. 3–42.
- Foley, S.F., Prelević, D., Rehfeldt, T., Jacob, D.E., 2013. Minor and trace elements in olivines as probes into early igneous and mantle melting processes. *Earth Planet. Sci. Lett.* 363, 181–191.
- Förster, M.W., Prelević, D., Schmück, H.R., Buhre, S., Marshall, H.R., Mertz-Kraus, R., Jacob, D.E., 2018. Melting phlogopite-rich MARID: Lamproites and the role of alkalis in olivine-liquid Ni-partitioning. *Chem. Geol.* 476, 429–440.
- Förster, M.W., Prelević, D., Schmück, H.R., Buhre, S., Vetter, M., Mertz-Kraus, R., Foley, S.F., Jacob, D.E., 2017. Melting and dynamic metasomatism of mixed harzburgite + glimmerite mantle source: Implications for the genesis of orogenic potassic magmas. *Chem. Geol.* 455, 182–191.
- Fritschle, T., Prelević, D., Foley, S.F., Jacob, D.E., 2013. Petrological characterization of the mantle source of Mediterranean lamproites: Indications from major and trace elements of phlogopite. *Chem. Geol.* 353, 267–279.
- Griffin, W.L., 2008. GLITTER: Data reduction software for laser ablation ICP-MS. *Laser Ablation ICP-MS in the Earth Sciences: Current practices and outstanding issues*, pp. 308–311.
- Gülmez, F., Genç, Ş.C., Prelević, D., Tüysüz, O., Karacik, Z., Roden, M.F., Billor, Z., 2016. Ultrapotassic volcanism from the waning stage of the Neotethyan subduction: A key study from the Izmir–Ankara–Erzincan Suture Belt, Central Northern Turkey. *J. Petrol.* 57, 561–593.
- Hauri, E.H., Wagner, T.P., Grove, T.L., 1994. Experimental and natural partitioning of Th, U, Pb and other trace elements between garnet, clinopyroxene and basaltic melts. *Chem. Geol.* 117, 149–166.
- Hermann, J., Spandler, C., Hack, A., Korsakov, A.V., 2006. Aqueous fluids and hydrous melts in high-pressure and ultra-high pressure rocks: Implications for element transfer in subduction zones. *Lithos* 92, 399–417.
- Hermann, J., Spandler, C.J., 2007. Sediment melts at sub-arc depths: An experimental study. *J. Petrol.* 49, 717–740.
- Hirschmann, M.M., Kogiso, T., Baker, M.B., Stolper, E.M., 2003. Alkaline magmas generated by partial melting of garnet pyroxenite. *Geology* 31, 481–484.
- Hofmann, A.W., 1988. Chemical differentiation of the Earth: The relationship between mantle, continental crust, and oceanic crust. *Earth Planet. Sci. Lett.* 90, 297–314.
- Jochum, K.P., Nohl, U., Herwig, K., Lammel, E., Stoll, B., Hofmann, A.W., 2005. GeoReM: A new geochemical database for reference materials and isotopic standards. *Geostand. Geoanal. Res.* 29, 333–338.
- Jochum, K.P., Weis, U., Stoll, B., Kuzmin, D., Yang, Q., Raczek, I., Jacob, D.E., Stracke, A., Birbaum, K., Frick, D.A., 2011. Determination of reference values for NIST SRM 610–617 glasses following ISO guidelines. *Geostand. Geoanal. Res.* 35, 397–429.
- Johnson, K.T.M., 1998. Experimental determination of partition coefficients for rare earth and high-field-strength elements between clinopyroxene, garnet, and basaltic melt at high pressures. *Contrib. Miner. Petrol.* 133, 60–68.
- Johnston, A.D., Schwab, B.E., 2004. Constraints on clinopyroxene/melt partitioning of REE, Rb, Sr, Ti, Cr, Zr, and Nb during mantle melting: First insights from direct peridotite melting experiments at 1.0 GPa. *Geochim. Cosmochim. Acta* 68, 4949–4962.
- Lambert, I.B., Wyllie, P.J., 1970. Melting in the deep crust and upper mantle and the nature of the low velocity layer. *Phys. Earth Planet. Inter.* 3, 316–322.
- LaTourrette, T., Hervig, R.L., Holloway, J.R., 1995. Trace element partitioning between amphibole, phlogopite, and basanite melt. *Earth Planet. Sci. Lett.* 135, 13–30.
- Lustrino, M., 2011. What ‘anorogenic’ igneous rocks can tell us about the chemical composition of the upper mantle: Case studies from the circum-Mediterranean area. *Geol. Mag.* 148, 304–316.
- Mallik, A., Dasgupta, R., Tsuno, K., Nelson, J., 2016. Effects of water, depth and temperature on partial melting of mantle-wedge fluxed by hydrous sediment-melt in subduction zones. *Geochim. Cosmochim. Acta* 195, 226–243.
- Mallik, A., Nelson, J., Dasgupta, R., 2015. Partial melting of fertile peridotite fluxed by hydrous rhyolitic melt at 2–3 GPa: Implications for mantle wedge hybridization by sediment melt and generation of ultrapotassic magmas in convergent margins. *Contrib. Miner. Petrol.* 169, 48.
- Mertes, H., Schmincke, H.-U., 1985. Mafic potassic lavas of the Quaternary West Eifel volcanic field. *Contrib. Miner. Petrol.* 89, 330–345.
- Mitchell, R.H., Edgar, A.D., 2002. Melting experiments on SiO<sub>2</sub>-rich lamproites to 6.4 GPa and their bearing on the sources of lamproite magmas. *Mineral. Petrol.* 74, 115–128.
- Morimoto, N., 1988. Nomenclature of pyroxenes. *Mineral. Petrol.* 39, 55–76.
- Nash, W.P., Crecraft, H.R., 1985. Partition coefficients for trace elements in silicic magmas. *Geochim. Cosmochim. Acta* 49, 2309–2322.
- Novella, D., Frost, D.J., 2014. The composition of hydrous partial melts of garnet peridotite at 6 GPa: Implications for the origin of group II Kimberlites. *J. Petrol.* 55, 2097–2124.
- Pertermann, M., Hirschmann, M.M., Hametner, K., Günther, D., Schmidt, M.W., 2004. Experimental determination of trace element partitioning between garnet and silica-rich liquid during anhydrous partial melting of MORB-like eclogite. *Geochim. Cosmochim. Acta* 68, 193–205.
- Prelević, D., Akal, C., Foley, S.F. (Eds.), 2008. Orogenic vs anorogenic lamproites in a single volcanic province: Mediterranean-type lamproites from Turkey. *IOP Publishing* 012024 pp.
- Prelević, D., Foley, S.F., Romer, R., Conticelli, S., 2008b. Mediterranean Tertiary lamproites derived from multiple source components in postcollisional geodynamics. *Geochim. Cosmochim. Acta* 72, 2125–2156.
- Prelević, D., Jacob, D.E., Foley, S.F., 2013. Recycling plus: A new recipe for the formation of Alpine-Himalayan orogenic mantle lithosphere. *Earth Planet. Sci. Lett.* 362, 187–197.
- Righter, K., Carmichael, I.S.E., 1996. Phase equilibria of phlogopite lamprophyres from western Mexico: Biotite-liquid equilibria and P-T estimates for biotite-bearing igneous rocks. *Contrib. Miner. Petrol.* 123, 1–21.
- Rosenthal, A., Foley, S.F., Pearson, D.G., Nowell, G.M., Tappe, S., 2009. Petrogenesis of strongly alkaline primitive volcanic rocks at the propagating tip of the western branch of the East African Rift. *Earth Planet. Sci. Lett.* 284, 236–248.
- Sato, K., 1997. Melting experiments on a synthetic olivine lamproite composition up to 8 GPa: Implication to its petrogenesis. *J. Geophys. Res. Solid Earth* 102, 14751–14764.
- Schmincke, H.-U., 2007. The Quaternary volcanic fields of the east and west Eifel (Germany). In: *Mantle plumes*. Springer, pp. 241–322.
- Sekine, T., Wyllie, P.J., 1983. Experimental simulation of mantle hybridization in subduction zones. *J. Geol.* 91, 511–528.
- Shimizu, N., Kushiro, I., 1975. The partitioning of rare earth elements between garnet and liquid at high pressures: Preliminary experiments. *Geophys. Res. Lett.* 2, 413–416.
- Sun, S.-S., McDonough, W.-S., 1989. Chemical and isotopic systematics of oceanic basalts: Implications for mantle composition and processes. *Geol. Soc., London, Spec. Publ.* 42, 313–345.
- Tappe, S., Foley, S.F., Kjarsgaard, B.A., Romer, R.L., Heaman, L.M., Stracke, A., Jenner, G.A., 2008. Between carbonate and lamproite—diamondiferous Torngat ultramafic lamprophyres formed by carbonate-fluxed melting of cratonic MARID-type metasomes. *Geochim. Cosmochim. Acta* 72, 3258–3286.
- Tappe, S., Foley, S.F., Stracke, A., Romer, R.L., Kjarsgaard, B.A., Heaman, L.M., Joyce, N., 2007. Craton reactivation on the Labrador Sea margins: 40Ar/39Ar age and Sr–Nd–Hf–Pb isotope constraints from alkaline and carbonate intrusives. *Earth Planet. Sci. Lett.* 256, 433–454.
- Tappe, S., Smart, K., Torsvik, T., Massuyeau, M., de Wit, M., 2018. Geodynamics of kimberlites on a cooling Earth: Clues to plate tectonic evolution and deep volatile cycles. *Earth Planet. Sci. Lett.* 484, 1–14.
- Tappe, S., Smart, K.A., Stracke, A., Romer, R.L., Prelević, D., van den Bogaard, P., 2016. Melt evolution beneath a rifted craton edge: 40Ar/39Ar geochronology and Sr–Nd–Hf–Pb isotope systematics of primitive alkaline basalts and lamprophyres from the SW Baltic Shield. *Geochim. Cosmochim. Acta* 173, 1–36.
- Tommasini, S., Avanzinelli, R., Conticelli, S., 2011. The Th/La and Sm/La conundrum of the Tethyan realm lamproites. *Earth Planet. Sci. Lett.* 301, 469–478.
- van Westrenen, W., Blundy, J.D., Wood, B.J., 2001. High field strength element/rare earth element fractionation during partial melting in the presence of garnet: Implications for identification of mantle heterogeneities. *Geochim., Geophys. Geosyst.* 2.
- Veter, M., Foley, S.F., Mertz-Kraus, R., Groschopf, N., 2017. Trace elements in olivine of ultramafic lamprophyres controlled by phlogopite-rich mineral assemblages in the mantle source. *Lithos* 292, 81–95.
- Vigouroux, N., Wallace, P.J., Kent, A.J., 2008. Volatiles in high-K magmas from the western Trans-Mexican Volcanic Belt: Evidence for fluid fluxing and extreme enrichment of the mantle wedge by subduction processes. *J. Petrol.* 49, 1589–1618.
- Wang, Y., Foley, S.F., 2018. Hybridization melting between continent-derived sediment and depleted peridotite in subduction zones. *J. Geophys. Res.: Solid Earth*.

- Wang, Y., Foley, S.F., Prelević, D., 2017a. Potassium-rich magmatism from a phlogopite-free source. *Geology* 45, 467–470.
- Wang, Y., Prelević, D., Buhre, S., Foley, S.F., 2017b. Constraints on the sources of post-collisional K-rich magmatism: The roles of continental clastic sediments and terrigenous blueschists. *Chem. Geol.* 455, 192–207.
- Wyllie, P.J., Sekine, T., 1982. The formation of mantle phlogopite in subduction zone hybridization. *Contrib. Miner. Petrol.* 79, 375–380.
- Xiong, X.-L., 2006. Trace element evidence for growth of early continental crust by melting of rutile-bearing hydrous eclogite. *Geology* 34, 945–948.
- Ziaja, K., Foley, S.F., White, R.W., Buhre, S., 2014. Metamorphism and melting of picritic crust in the early Earth. *Lithos* 189, 173–184.